Galaxy Evolution through the Lens of Stellar Population Synthesis

Eva Maria Theresia Sextl

München 2025

Galaxy Evolution through the Lens of Stellar Population Synthesis

Eva Maria Theresia Sextl

Dissertation
an der Fakultät für Physik
der Ludwig–Maximilians–Universität
München

vorgelegt von
Eva Maria Theresia Sextl
aus Eggenfelden

München, den 6. November 2025

Erstgutachter: Prof. Dr. Rolf-Peter Kudritzki
Zweitgutachter: Prof. Dr. Andreas Burkert
Tag der mündlichen Prüfung: 15. Dezember 2025

I ko‘ mei‘ Heu aa a Stroh hoaß’n!

Elise Beck
Der Niederbayer in seinen Sprüchen und Redensarten,
in ’Das Bayerland’, 1902

Contents

Abstract

The study of galactic evolution remains one of the central questions in modern astronomy. Understanding the governing processes requires careful examination of both the dynamical and chemical evolution of galaxies, as these shape their structure, composition, and long-term behavior. Despite their significance, many previous studies have focused on global indicators or gradients, often assuming strict azimuthal symmetry. Such simplifications overlook that galaxies are complex systems influenced by localized feedback mechanisms and environmental effects that govern their development and diversity.

This thesis investigates these issues through stellar population synthesis (SPS), a spectral analysis technique that decomposes the integrated light of a galaxy region into the contributions from stars of different ages and metallicities. Since individual stars are typically unresolvable beyond the Local Group, SPS is one of the most powerful tools for exploring the stellar content of distant systems. Through a fitting technique, this method determines key physical parameters such as stellar ages, metallicities, star formation histories, and the dust properties of the interstellar medium. Collectively, they provide fundamental insight into the processes that govern galaxy formation and evolution.
Although SPS, including its most popular variant 'full-spectral fitting', has been developed and improved over several decades, a tremendous potential remains untapped. This work aims to refine and extend stellar population synthesis to make it a competitive alternative to established techniques such as HII region emission line studies and the spectral analysis of individual extremely bright stellar sources like supergiant stars and stellar clusters. Ultimately, we improve the methodological framework of SPS to derive robust and physically meaningful stellar population properties within the challenging environment of star-forming nuclear rings.

As a first step, we analyzed stacked spectra constructed from ∼200,000 star-forming galaxies in the Sloan Digital Sky Survey (SDSS) with SPS. By using our own carefully tested spectral fitting algorithm, we measure metallicities, ages, and star formation histories of the young and old stellar populations together with interstellar reddening and extinction. We obtain the mass-metallicity relationship for young and old stellar populations, which

aligns well with analytical look-back evolution models. The focus of this exploratory study extends to underlying assumptions about star formation and dust properties, which have been largely omitted in previous research.
In an interdisciplinary extension to the previous traditional application of SPS, the first results of an ambitious and award-winning AI project are discussed. A generative machine learning framework is trained on SDSS data and capable of predicting optical galaxy spectra from photometric broadband images. We apply SPS to the predicted galaxy spectra to test the AI's capability. With further refinement, this approach could recover key galaxy properties, normally accessible only through spectroscopic observations, from photometric data alone.
Next, we investigated the spatially resolved spectra of galaxies in the TYPHOON survey. In the grand design spiral NGC 1365, the stellar disk grows inside-out, but an unexpected central dip in metallicity signals the inflow of metal-poor gas and interruptions in star formation caused by active galactic nucleus (AGN) feedback. Similarly, M83, a massive barred spiral galaxy with an irregular nuclear region, shows a high and fairly uniform metallicity in its young stars with a localized central decrease linked to gas inflow or AGN effects, alongside a dust cavity correlated with molecular gas.
For the first time, a spatial one-to-one comparison of metallicities derived from full-spectral fitting with those obtained from individual young stellar probes was carried out in the fourth and fifth publication. To do this, we moved beyond common metallicity definitions in the field to obtain a more physically meaningful and robust measure called 'physical metallicity'. This updated definition aligns with the conventions commonly used in chemical evolution studies, and the successful comparison confirms the robustness of our spectral fitting technique.
In the fifth publication, the focus turns to one of the current key instruments for spatially resolved spectroscopy: the MUSE spectrograph at the 8m VLT. This powerful tool delivers high-quality spectroscopic data across a two-dimensional field of view in a single exposure. Applying SPS, we challenge prior interpretations from the flagship MUSE-TIMER survey regarding the chemical evolution of prominent nuclear rings in the local universe. The results reveal that peculiar low-metallicity signatures in NGC 7552, NGC 613, NGC 1097, and NGC 3351 originate from older stellar populations, tracing past inflows of metal-poor gas, followed by normal enrichment to (super)solar levels. By separating young and old stellar contributions, the study avoids biases of conventional averaging methods and highlights the role of very young stars in accurate modeling. The findings, supported by reddening maps, confirm ongoing inflows and show that MUSE's spatial and spectral resolution enables detailed investigations of nuclear star-forming regions despite lacking the blue part of the optical spectrum.

Together, these five studies demonstrate that stellar population synthesis, when refined with physically motivated definitions and applied across statistical, spatially resolved, and machine learning domains, provides a physically grounded and predictive tool for tracing galactic evolution over cosmic time. With the wealth of high-quality data already available, a unique opportunity of investigation in both the local and distant universe lies ahead.

Deutsche Zusammenfassung

Die Erforschung der Evolution von Galaxien stellt eine der zentralen Fragestellungen der modernen Astronomie dar. Das Verständnis dieser Prozesse erfordert eine sorgfältige Untersuchung sowohl der dynamischen als auch der chemischen Entwicklung von Galaxien, da diese Aspekte ihre Struktur, Zusammensetzung und ihren langfristigen Entwicklungsverlauf prägen. Trotz ihrer Bedeutung konzentrieren sich viele Studien in der Fachliteratur auf globale Indikatoren oder Gradienten und gehen dabei häufig von einer perfekten azimutalen Symmetrie aus. Diese Vereinfachungen übersehen jedoch, dass Galaxien komplexe Systeme sind, die von lokalen Rückkopplungsmechanismen und Umwelteinflüssen beeinflusst werden, die eine entscheidende Rolle für ihre Entwicklung und Vielfalt spielen.
Die vorliegende Dissertation versucht sich dieser Fragestellung mit der stellaren Populationssynthese (SPS) zu nähern, einem Verfahren der Spektralanalyse, mit dem das integrierte Licht eines Galaxienbereichs in die Beiträge von Sternen unterschiedlichen Alters und verschiedener Metallizitäten zerlegt wird. Da einzelne Sterne außerhalb der Lokalen Gruppe in der Regel nicht mehr aufgelöst werden können, stellt SPS eines der leistungsfähigsten Verfahren zur Untersuchung der stellaren Populationen solcher Systeme dar. Mithilfe eines Fit-Prozesses erlaubt die Methode die Bestimmung zentraler physikalischer Parameter wie mittleres Sternenalter, Metallizität, Sternentstehungsgeschichte und die Staubeigenschaften des interstellaren Mediums. Diese Größen wiederum liefern grundlegende Erkenntnisse über die Prozesse, die die Entstehung und Entwicklung von Galaxien bestimmen.

Trotz der über Jahrzehnte erfolgten Weiterentwicklung der SPS, insbesondere der sogenannten „Full-Spectral-Fitting“-Technik, bleibt ihr wissenschaftliches Potenzial bislang nicht vollständig ausgeschöpft. Ziel dieser Arbeit ist es, die Methode konzeptionell und technisch weiterzuentwickeln, um sie als präzise und robuste Alternative zu etablierten Verfahren, wie der Emissionslinienanalyse von HII-Regionen oder der Spektralanalyse einzelner heller Sterne und Sternhaufen, zu etablieren. Eine methodische Erweiterung ermöglicht es, selbst unter den komplexen Bedingungen nuklearer Ringe mit aktiver Sternentstehung, physikalisch konsistente Eigenschaften stellarer Populationen abzuleiten.

Im ersten Teil der Arbeit werden aufaddierte Spektren von etwa 200.000 Galaxien mit aktiver Sternentstehung aus dem Sloan Digital Sky Survey mittels SPS analysiert. Unter Verwendung eines eigens entwickelten und umfassend validierten Fitting-Algorithmus werden Metallizitäten, Altersverteilungen und Sternentstehungsgeschichten sowohl junger als auch alter Sternpopulationen sowie interstellare Rötung und Extinktion bestimmt. Auf dieser Basis wird die Massen-Metallizitäts-Beziehung für beide Komponenten abgeleitet, die gut mit analytischen Evolutionsmodellen übereinstimmt. Besondere Aufmerksamkeit gilt dabei grundlegenden Annahmen zur Sternentstehung und zur Staubphysik, die bisher in der Literatur weitgehend unbeachtet geblieben sind.
Im zweiten Teil der Arbeit wird ein preisgekröntes KI-Projekt vorgestellt. Dabei kommt ein Verfahren des Maschinellen Lernens zum Einsatz, das aus mehreren photometrischen Bild-Daten die optischen Spektren von Galaxien vorhersagen kann. Die stellare Populationssynthese wird auf diese künstlich erzeugten Spektren angewendet, um die Zuverlässigkeit der KI zu überprüfen. Eine Weiterentwicklung dieses Ansatzes könnte es in Zukunft ermöglichen, wichtige Eigenschaften von Galaxien, die bisher nur mit aufwendigeren Spektren messbar waren, allein auf Basis großflächiger Bilddurchmusterungen zu bestimmen.
Im dritten Teil werden räumlich aufgelöste Spektren aus dem TYPHOON-Survey untersucht. Für die Spiralgalaxie NGC 1365 zeigt sich ein Scheibenwachstum von innen nach außen, während ein zentraler Einbruch der Metallizität auf den Zufluss metallarmen Gases und eine durch Rückkopplung des aktiven Galaxienkerns (AGN) verursachte Unterbrechung der Sternbildung, hindeutet. Ähnliche Befunde ergeben sich für M83, eine massereiche Balkenspiralgalaxie mit unregelmäßigem Zentralbereich. Die jungen Sterne der Scheibe zeigen insgesamt eine hohe und homogene Metallizität, jedoch ergibt sich wieder ein örtliches zentrales Minimum, das auf Gaszufluss oder AGN-Einflüsse zurückgeführt werden kann. Zusätzlich wird ein fast staubfreier Bereich festgestellt, der mit molekularem Gas korreliert ist.
Erstmals wird ein direkter räumlicher Vergleich zwischen den aus „Full-Spectral-Fitting"-Techniken abgeleiteten Metallizitäten und denjenigen aus unabhängigen stellaren Proben durchgeführt. Hierzu werden geläufige Definitionen der Metallizität im Fachgebiet um eine physikalisch konsistentere Größe, die sogenannte „physikalische Metallizität", in der vierten und fünften Publikation erweitert. Der Vergleich belegt die Zuverlässigkeit der entwickelten spektroskopischen Methodik.
Die fünfte Publikation der Arbeit befasst sich mit dem Einsatz des MUSE-Spektrographen am 8 m-VLT, einem der wichtigsten Instrumente weltweit für räumlich aufgelösten Spektroskopie. Die MUSE-Beobachtungen ermöglichen die Erfassung hochauflösender Spektraldaten über ein zweidimensionales Sichtfeld in nur einer Aufnahme. Frühere Schlussfolgerungen zur chemischen Entwicklung markanter nuklearer Ringe mit Sternentstehung, die in den MUSE-TIMER Studien getroffen wurden, werden kritisch hinterfragt. Unsere Ergebnisse zeigen, dass die beobachteten Signaturen extrem niedriger Metallizität in NGC 7552, NGC 613, NGC 1097 und NGC 3351 auf ältere Sternpopulationen zurückgehen, die frühe Phasen metallarmen Gaszuflusses widerspiegeln, gefolgt von einer Anreicherung auf (über) solare Metallizitäten. Durch die Trennung von jungen und alten Sternkomponenten werden Verzerrungen herkömmlicher Mittelungsverfahren vermieden. Die Bedeutung

sehr junger Sterne für präzise Modellierungen wird hervorgehoben. Räumlich aufgelöste Karten der Extinktion zeigen weiterhin, dass Gas in die zentralen Bereiche einströmt, und unterstreichen die Eignung von MUSE für detaillierte Studien nuklearer Sternentstehungsgebiete. Das trifft sogar zu, obwohl MUSE den blauen Bereich des optischen Spektrums nicht abdeckt.

Die in dieser Arbeit präsentierten fünf Studien zeigen, dass die stellare Populationssynthese eine fundierte und prognosefähige Methode zur Bestimmung der Galaxienentwicklung über kosmische Zeiträume hinweg darstellt. Hierbei ist es von Nutzen, sie in unterschiedlichen Kontexten anzuwenden, beispielsweise in der Statistik unzähliger Galaxien, bei räumlich aufgelösten Spektren oder im Maschinellen Lernen. Die bereits vorhandenen umfangreichen Datensätze eröffnen ein breites zukünftiges Forschungsfeld, um die Entwicklung von Galaxien im nahen und fernen Universum besser verstehen zu können.

1 Introduction

Galaxies are gravitationally bound systems composed of stars, gas, dust, and dark matter that display a variety of morphological features such as bulges, disks, halos, and frequently bars or rings. By carefully examining the light that a galaxy emits across different wavelengths, called the spectral energy distribution (SED), we can begin to uncover the story behind their structure and evolution. Different components imprint distinctive signatures on their spectrum: young, high-mass stars predominantly emit ultraviolet and blue optical radiation, whereas low-mass, older stars contribute primarily at longer wavelengths. Interstellar dust preferentially absorbs UV and optical photons and re-emits mostly in the infrared. Additionally, ionized gas regions produce characteristic emission lines that provide valuable diagnostics of the physical conditions within the interstellar medium. To disentangle these overlapping signals, we must deeply understand the fundamental physical processes that generate and modify a galaxy's spectrum.

Stellar Population Synthesis (SPS) is one of the most powerful tools available for analyzing and deciphering the often subtle contributions present in the integrated spectrum of a galaxy. By combining template spectra of simpler building blocks, called Single Stellar Populations (SSPs), a model for the observed spectrum is created. In the literature, this is also referred to as 'full-spectral fitting'[1]. It is clear that we cannot disentangle individual stellar contributions in a galaxy spectrum composed of millions of stars, but through sophisticated model fitting we can infer the mean ages, metallicities, and relative contributions of distinct stellar populations embedded within a galaxy. In this thesis, we aim to refine and extend SPS as a competitive alternative to established methods like HII region emission line studies and spectral analysis of bright stellar sources such as supergiants and clusters. Ultimately, we improve the SPS framework to derive robust, physically meaningful stellar population properties within the challenging environment of star-forming nuclear rings. These regions contribute significantly to the growth of central stellar mass and play a key role in the secular evolution of galaxies.

[1] An alternative approach within SPS, which we will not address further, is 'Evolutionary Population Synthesis'. The star formation history in this case is assumed a priori (Maraston, 2005). In contrast, full-spectral fitting seeks to reconstruct the star formation history directly from the observational data.

To achieve this ultimate goal, it is first necessary to take a closer look at galaxies and the constituents shaping their spectra. In the following, several introductory sections cover basics and current key challenges in stellar evolution, stellar spectra, and dust treatment. These core concepts provide the necessary framework for developing accurate SSP models, which will act as the fitting templates in SPS. A special focus lies on young stellar components and what can be robustly inferred with existing techniques and identifying the areas where advanced modeling is necessary. Although certain sections may appear trivial to experts, their inclusion is intentional to ensure a more accessible and inclusive introduction to SPS.

1.1 Galaxy Zoo

Already a simple look through field glasses in a clear night sky reveals that galaxies come in a variety of shapes. Since the advent of photographic plates, it has become common to classify them into three main groups: elliptical, spiral, and lenticular (intermediate) galaxies (Wolf, 1908; Hubble, 1926; Lundmark, 1927). Our work aims for a deeper understanding of the evolution of galaxies, so we first have to take a closer look at them.

Elliptical galaxies are characterized by their smooth, featureless light profiles and broadly ellipsoidal or triaxial shapes, lacking the disks, spiral arms, or prominent dust lanes seen in other types (Sandage, 1975). Mostly composed of metal-rich older, reddish stars, these galaxies contain very little gas or dust, resulting in minimal new star formation. This holds at least up to redshifts of $z \sim 2.2$ (Mei et al., 2009; Andreon & Huertas-Company, 2011). Therefore, they are sometimes called 'passive' or 'quiescent' in the literature. The absence of recent star formation in elliptical galaxies originates from the downsizing phenomenon, where the most massive galaxies formed their stars earlier and over shorter periods than less massive ones (Cowie et al., 1996; Neistein et al., 2006; Thomas et al., 2005). During these early epochs, vigorous starburst activity rapidly consumed or expelled the available gas, a process guided by energetic feedback from supernovae and active galactic nuclei (AGN) (Cattaneo et al., 2008). As a result, the remaining cold gas was either exhausted or heated by AGN-driven processes beyond the threshold required for cooling, halting further star formation. Ellipticals obey well-established scaling relations such as the Faber-Jackson relation (Faber & Jackson, 1976) or the Fundamental Plane (Djorgovski & Davis, 1987), which connect their luminosity, effective radius, surface brightness, and stellar velocity dispersion. It is therefore not surprising that these 'easier' galaxies[2] were the first targets of Stellar Population Synthesis (Bacon et al., 2001; Jimenez et al., 2007; Cappellari et al., 2011).
Many of the ideas and popular tools in SPS (especially libraries of stellar spectra) were

[2]Ellipticals are actually far from being structurally simple: Many show evidence for triaxiality (Binney, 1978), kinematic substructure, and remnants of past merger events, especially in the cores of galaxy clusters where they are most commonly found (Merritt, 1993; Aguerri et al., 2012). See also Combes (2021, chapter 3) for further common misconceptions.

primarily designed with such systems in mind. However, SPS becomes significantly more challenging when examining star-forming spiral galaxies, as they display an entirely different range of properties: They normally feature a prominent central bulge surrounded by a flattened disk, from which striking spiral arms extend outward. The bulge is a densely populated, spheroidal region primarily composed of older, metal-rich stars. It is normally a prominent feature in (N)IR images and is defined by kinematics. The rotating disk hosts both thin and thick components. The thin disk is rich in interstellar gas and dust, providing the raw material for ongoing star formation and harboring young, luminous stars, while the thicker disk contains older stellar populations (Bournaud et al., 2009). Winding outward from the bulge, the striking spiral arms stand out as regions of enhanced gas and dust density and active star formation. Systems with arms that can be traced easily over a large radial range are labeled 'grand design'. NGC 1365 (chapter 4) and M83 (chapter 5) are prominent examples. Galaxies showing only patchy, discontinuous spiral features receive the term 'flocculent'.
In addition to these structural components, the interstellar medium within spiral galaxies is dynamically shaped by gas flows: Inflows deliver fresh, often metal-poor gas from the outer disk or circumgalactic medium toward the central regions, sustaining star formation and potentially feeding central black hole activity (see 1.2 for details). Conversely, outflows can expel gas and metals into the halo or intergalactic regime, regulating both the star formation rate and the galaxy's chemical evolution (Zahid et al., 2014).

1.2 Stellar Bars: Prominent Structures in Spiral Galaxies

Stellar bars are among the most dynamically influential substructures in disk galaxies. Roughly two-third of local spiral galaxies show indications of a bar (Menéndez-Delmestre et al., 2007). This structure consists of an elongated, kiloparsec-scale distribution of stars, interstellar gas, and dust, extending from the galactic center and typically connecting with spiral arms at its outer edges. Despite their high number, their precise formation time is still unknown. With the James Webb Space telescope (JWST), stellar bars at redshifts of $z \sim 2.2$ (Guo et al., 2023) and $z \sim 3.8$ (Amvrosiadis et al., 2025) have been found. The latter would correspond to a formation time when the universe was only 1.66 Gyr old[3]. In simulations, bars can form quickly on the timescale of hundreds of Myr (Verwilghen et al., 2024) and remain stable on a Gyr timescale (Bland-Hawthorn et al., 2023; Rosas-Guevara et al., 2025).
The stellar orbits aligned with the bar (so called x_1 orbits) support the bar's elongated structure (Contopoulos & Papayannopoulos, 1980). From a dynamical perspective, the bar's non-axisymmetric gravitational potential induces strong torques that can redistribute the angular momentum of stars within the disk. This redistribution is particularly efficient

[3]calculated using the Cosmology Calculator 1 `https://ned.ipac.caltech.edu/help/cosmology_calc.html`

near resonances, such as the corotation radius, where the angular speed of the bar matches that of the stars in the disk (Daniel & Wyse, 2015). The result is significant radial migration with no associated change to the orbital eccentricity (Sellwood & Binney, 2002). Stars can become displaced over kiloparsec scales away from their original galactocentric radii, moving either inward or outward along the disk (Lépine et al., 2003). Radial migration poses a problem for SPS, as we can only track old stellar populations at their current positions, not their birthplaces. The metallicity gradient for the older population we obtain with our method is therefore probably flatter as it was when these stars were formed (as in Magrini et al. 2016 and section 4.4.3.)

1.2.1 Star-forming Nuclear Rings

One of the bar's most profound effects besides stellar migration is its ability to drive gas inward along its dust lanes towards the center (Bittner, 2021, chapter 1). As the gas travels along these lanes, it accumulates at distinct contact points where it encounters strong dynamical barriers. These points typically correspond to specific resonances, particularly the inner Lindblad resonance (ILR), established by the potential of the bar itself (Buta & Combes, 1996). Here, the inflowing material can no longer move freely inward, instead piling up to form a compact, dense structure known as the nuclear ring (Li et al., 2015; Verwilghen et al., 2024). This region is characterized by so-called x_2 orbits, which are oriented perpendicular to the major axis of the galactic bar. These star-forming rings generally have radii ranging from hundred parsecs to about a kiloparsec, centering tightly around the galactic nucleus (Comerón et al., 2010). They are characterized by exceptionally high rates of ongoing star formation, often surpassing 1 $M_\odot$/yr (Mazzuca et al., 2008), and appear to be long-lived structures (Sarzi et al., 2007; Allard et al., 2006). Observations frequently reveal that these rings are filled with knotty clusters of young, massive stars, as well as an abundance of dust and molecular gas (Emsellem et al., 2022). The stellar populations within nuclear rings can give hints about their formation history. Detailed age dating of clusters reveals sequential bursts of star formation, indicating repeated episodes of gas inflow followed by a starburst activity. This pattern supports a scenario known as 'pearls on a string', in which new clusters of stars form at specific points (often where gas inflow is maximized) and then age as they orbit within the ring on a scale of several million years (Böker et al., 2008). In contrast, the alternative 'popcorn' scenario predicts a more stochastic, global onset of star formation, where clusters form randomly throughout the ring without a discernible age gradient. The two main ideas are compactly illustrated in Falcón-Barroso et al. 2007.

Observations and studies have found not only star-forming nuclear rings but also smooth rings of old stars that are likely the leftovers of past star-forming nuclear rings (Erwin et al., 2001; Bittner et al., 2020). These older nuclear rings are not covered by this thesis but are worthwhile targets on their own in the future.

Although rare exceptions exist in which nuclear rings appear in an unbarred galaxy (some examples in Comerón et al. 2010), in the vast majority of cases both features are present

together. One key question that arises at this point concerns the origin of the transported gas. It could come from the outer regions of the galaxy as a consequence of a (minor) merger (Sparre et al., 2022), or even originate from the cosmic web itself (Galárraga-Espinosa et al., 2023). We will shortly comment on this in chapter 7, but it should be noted that this question requires much additional research.

1.2.2 Secondary Bars

Arsenault (1989) showed that bars and rings are more prevalent in galaxies with AGN and/or starburst. While the main bar shovels the gas to about a few hundred parsecs from the center towards inner resonances, there must exist a further process to produce further gas inflows to about 10 pc from the central supermassive black hole (Emsellem et al., 2015). There exist so called nuclear bars within nuclear disks themselves. An inner bar is basically a secondary, smaller bar nested within the main bar. It can rotate independently, redistributing angular momentum and effectively channeling material inward. This scenario is called "bars-within-bars" (Shlosman et al., 1989). According to Erwin (2024), roughly 20% of barred galaxies exhibit such double-barred systems. One example discussed in this work is NGC 1097 (see chapter 6), where this phenomenon has been clearly observed (Quillen et al., 1995; Prieto et al., 2005).

1.3 Basics of Stellar Evolution

After setting the galactic stage, we can now turn to the key ingredients required for building Stellar Population Synthesis templates. These include isochrones, which trace the evolutionary tracks of stars of different masses at a fixed age; stellar spectral libraries, which provide the spectra associated with each evolutionary phase; and an initial mass function (IMF), which defines the relative number of stars formed at each mass. Together, these components allow us to model the integrated light of a stellar population. Additionally, dust must be considered, as it absorbs and scatters starlight, changing the overall SED. Although these concepts may appear almost trivial at first glance, revisiting them is essential. Without a solid grasp of underlying physics, any attempt to model or interpret a galaxy's spectrum risks oversimplification and misrepresentation of its true nature.
We discuss stellar evolution first: Stars can be modeled as gravitating gas spheres whose evolutionary pathway is determined by stellar mass (and to a lesser extend by the chemical composition and other minor influences like stellar rotation). They originate in subregions of giant molecular clouds, where gravitational instabilities cause localized gas clumps to collapse into protostars (Larson, 1969). These can be induced from gas accretion that exceeds the Jeans mass, or by shock waves from nearby supernovae or by cloud collisions when entering a nuclear ring. As these clumps contract, they form protostars who still gain mass via accretion and radiate gravitational potential energy away in parallel. Initially, they are fully convective and follow the so called Hayashi track on the Hertzsprung-Russell di-

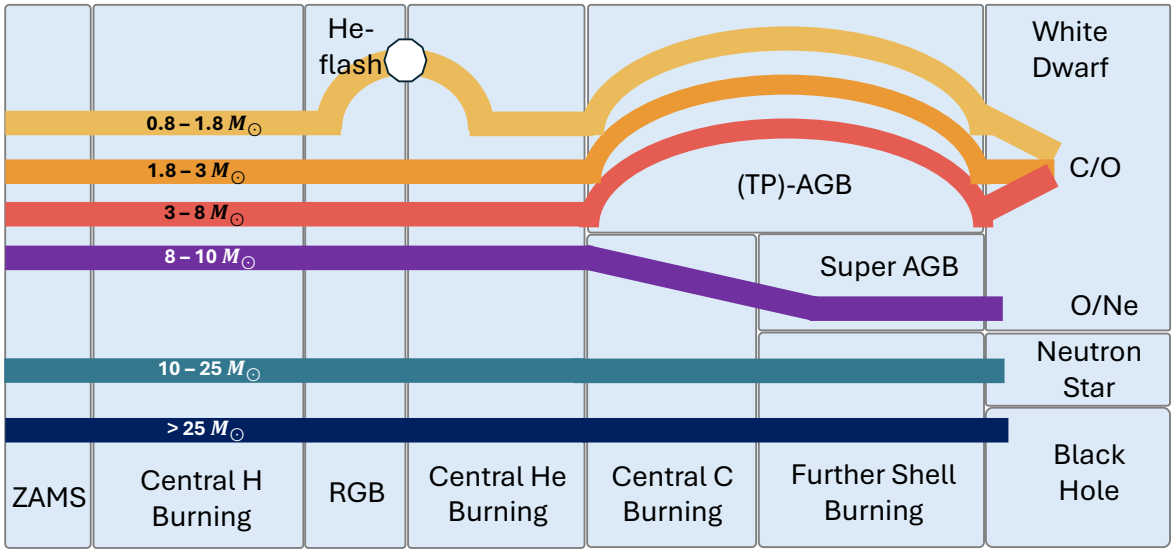

Figure 1.1: Relevant stages of stellar evolution broken down for different initial stellar masses. Adapted from Remple (2025, Chapter 2) and expanded to include additional phases of massive stellar evolution following Salaris & Cassisi (2005, chapter 6,7).

agram, remaining at nearly constant temperature while contracting. Eventually, radiative zones develop inside the protostar and it moves horizontally towards higher temperatures (Henyey track). Above 10^7 K core temperature, central hydrogen fusion is finally ignited and the star arrives on the zero-age main sequence (ZAMS) in hydrostatic equlibrium. The pre-main sequence (pre-MS) evolution is dominated by the Kelvin-Helmholtz timescale and is generally much faster for massive stars than for lower masses. A good approximation is $t_{\rm prems} \sim M^{-2.5}$ (Kippenhahn et al., 2013, chapter 28.2). This has odd consequences for very young star cluster, where the most massive members already leave the main sequence (MS), when solar types stars have not even arrived there yet. This can be seen for instance in Choi et al. (2016, Figure 13) and in Figure 1.2 in the next section.

The main sequence is defined by the stable burning of hydrogen into helium in the core via nuclear fusion, providing the pressure needed to counteract gravitational collapse. The dominant fusion pathway depends on the core temperature, and therefore on mass: stars with masses $\leq 1.3 M_\odot$ primarily utilize the proton-proton (pp) chain, while in more massive stars ($> 1.3 M_\odot$) the CNO cycle dominates, which is more temperature sensitive and requires the presence of heavier nuclei as 'catalysts' (Pagel, 2009, chapter 5.6). Once fusion begins, stars settle into remarkably stable configurations, spending roughly 90% of their total lifetimes on the main sequence. The duration τ of this phase scales with $\tau \sim M^{-2.5}$, meaning high-mass stars burn through their fuel much more rapidly than their low-mass counterparts. For example, a 10 solar mass star may remain on the main sequence for only a few million years, while a 1 solar mass star like the Sun persists for about 10 billion years. The luminosity in contrast roughly scales as $L \sim M^{3.5}$ which results in a 10^4 – 10^5 times

higher energy output in the 10 solar mass star. These trends alone make stellar population synthesis modeling of overwhelmingly young populations challenging (see chapter 6). Due to the rapid speed of evolutionary phases of massive stars, small differences in age can lead to significant differences in observable quantities such as the overall SED shape or certain spectral features. The impact of the age-metallicity degeneracy (section 3.5.5) worsens this problem.
When hydrogen in the core is exhausted, nuclear fusion ceases temporarily in the central region. The core contracts under its own gravity, increasing its temperature, while the outer layers expand and cool, transforming the star into a red (super) giant[4]. The spectra of these stages show significantly different features from MS stars (i.e. prominent lines of neutral metals and molecules Gray & Corbally (2009, chapter 2)). In stars with initial masses $\geq 0.5 M_{\odot}$, the contracting core eventually reaches temperatures ($\sim 10^8$ K) sufficient to ignite helium fusion via the triple-alpha process (Salaris & Cassisi, 2005, chapter 6.1). The next stages differ depending on the initial stellar mass.

In low-mass stars ($\lessapprox 2 M_{\odot}$), this occurs only under degenerate conditions, in a so called helium flash. The degenerate nature of the core causes a rapid temperature increase without immediate pressure increase, leading to intense helium burning until thermal pressure lifts degeneracy and stabilizes the core. Following this, the star settles onto the horizontal branch (typically for Population II stars) or the red clump (for Population I stars). After the core helium fusion into carbon and oxygen is exhausted, stars with initial masses $< 8 M_{\odot}$ do not reach high enough core temperatures to ignite their carbon-oxygen core (Pagel, 2009, chapter 5.10). They undergo significant mass loss during the asymptotic giant branch (AGB) phase, driven by pulsations and stellar winds, ultimately ejecting their outer envelopes to form planetary nebulae (Kippenhahn et al., 2013, chapter 34). Their final life stages are white dwarfs composed primarily of carbon and oxygen.

Intermediate and massive stars ($\gtrapprox 2 M_{\odot}$) will evolve quite differently. First, they avoid the Helium-flash due to their lower core densities and can ignite helium regularly. After the core helium is exhausted, the process repeats: successive contraction and ignition of more advanced burning stages in increasingly hot and dense shells around the core. In stars with sufficient mass ($\geq 8\, M_{\odot}$), post-helium burning stages include carbon, neon, oxygen, and silicon fusion, forming an onion-like structure of concentric shells (Salaris & Cassisi, 2005, chapter 7.5). This sequence of advanced nuclear burning stages continues until iron-group elements form in the core, which cannot generate energy by fusion, leading to the conditions for core collapse and subsequent supernova in the most massive stars.

One of the best summary illustrations on this matter is shown in Remple (2025, chapter 2). An adopted version for our purposes including stellar end-phases is shown here in

[4]This statement holds approximately true, but there does exist an intermediate phase called blue supergiants who are (a) evolving towards the red supergiant stage (RSG) or (b) returning back from it. These extremely luminous stars are some of the brightest stars in the universe, can be individually resolved up to ~ 8 Mpc and can be used as distance indicators (Kudritzki et al., 2024, 2025)

Figure 1.1. It should be emphasized that this section and the summary figure are merely a general overview. There exist rare types of stars that fall outside common classifications. For instance Wolf-Rayet (WR) stars who show emission (not only absorption) lines of highly ionized elements like helium, nitrogen, carbon, and oxygen resulting from the loss of their outer hydrogen layers. Other peculiar exotic and short-lived types are B[e] stars (Aret et al., 2016) or yellow hypergiants (Klochkova, 2019).

1.4 A Word on Binary Evolution and Metallicity Effects

The previous paragraphs covered the well-known phases of stellar evolution of single stars. Today, we know that stellar multiplicity is important (Sana et al., 2012). Popular systems like α Centauri (Innes, 1917), Sirius (Goldschmidt, 1863) or Eta Carinae (Damineli et al., 2000) are multiple systems. The number of multiple systems among solar type stars varies from $\approx 46\%$ (Raghavan et al., 2010) to $\approx 58\%$ (Duchêne & Kraus, 2013; Fuhrmann et al., 2017). For O, B, A spectral types this fraction are probably much higher (González-Payo et al., 2024). Binary evolution is also responsible for a range of intriguing astrophysical phenomena, including gravitational waves, Type Ia supernovae, and X-ray binaries (Han et al., 2020). Even planets can form in multiple systems (Zurlo et al., 2023). From a stellar evolution perspective, systems with wide separations are uncritical, the consequences of mass and angular momentum transfer can only play an important role in *close systems*. Concerning spectra, key spectral indices such as Ca4455, Fe4668, Mgb, and Na D are systematically stronger across all metallicities in populations evolving with tight binary interactions (Zhang et al., 2004). Interactions within binaries can also produce exotic populations of hot, luminous stars (including stripped helium stars and rejuvenated main-sequence stars; Renzo et al. 2023; Götberg et al. 2019) altering both the stellar content and emission properties of galaxies. As a result, the integrated light from these populations remains bluer for longer periods. Luckily for the presented work in this thesis, this seems not to affect very young populations < 10 Myr, and influences mostly the UV-flux and not the optical regime (Götberg et al., 2019).

After a star's mass, its metallicity plays a crucial role in determining its life cycle and development. In astrophysics, metallicity Z refers to the abundance of elements heavier than helium and is mostly given on a logarithmic scale. This is then indicated by rectangular brackets $[\mathrm{Z}] = \log(Z/Z_\odot)$ and represents the metallicity as the logarithm of the ratio of an object's metal fraction Z to the solar bulk metal fraction $Z_\odot = 0.0142$ (Asplund et al., 2009). A more extended analysis on [Z] and how to measure it, is given in section 1.9.

Metallicity influences a star's evolution by affecting both the strength of its (line- and dust-driven) stellar winds and the efficiency of hydrogen fusion. Iron, in particular, is significant because it contributes greatly to the opacity within the star's interior. This increased opacity enhances radiation-driven stellar winds, as described by studies such as in Kudritzki & Puls (2000); Vink et al. (2001); Eldridge & Vink (2006). Additionally,

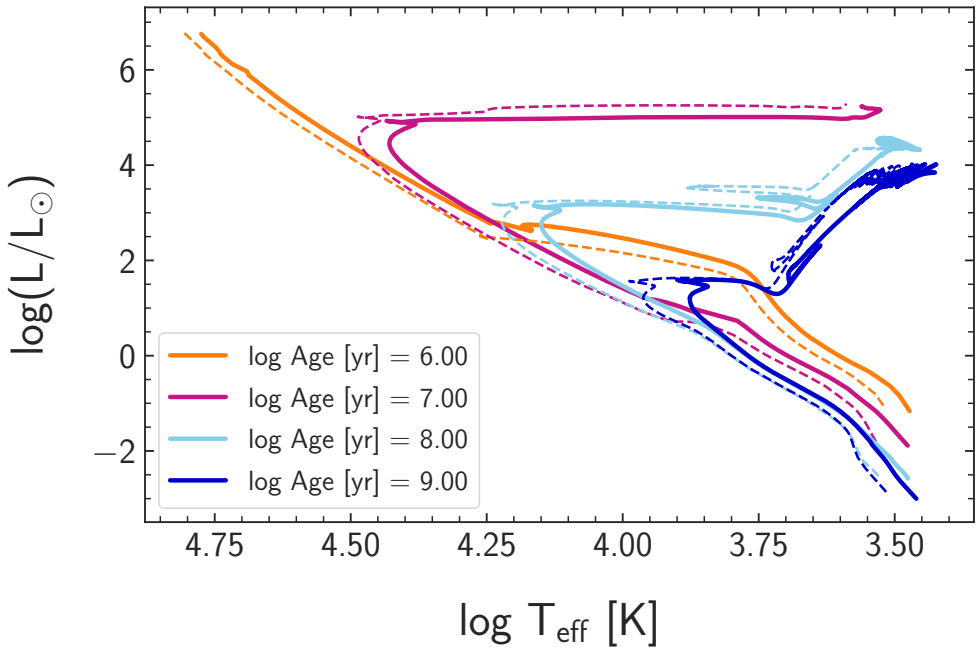

Figure 1.2: Hertzsprung-Russell diagram of MIST-Isochrones at varying ages (1 Myr, 10 Myr, 100 Myr and 1 Gyr). Solid line: [Z] = 0.0 (solar metallicity), dashed line: [Z] = −0.75 (0.18 times solar). The models include stellar rotation ($v_{rot}/v_{crit} = 0.4$) and pre-MS evolution. Evolutionary phases later than the tip of the red giant branch are omitted for clarity.

increased iron content tends to expand the star's radius due to increased photon opacity. As a result, stars with higher metallicity generally experience a slight reduction in surface gravity and show shorter MS lifetimes. This behavior cannot only be shown by studying analytic models (ie polytropes Kippenhahn et al. 2013, chapter 19) but also by solving the stellar structure equations in numerical simulations. Such stellar evolution codes can nowadays simulate stellar structure and evolution across a broad range of masses and chemical compositions. Despite being limited to 1D radial geometry with approximate treatments for multidimensional processes like convection or rotational mixing, remarkable agreement with observations was achieved. Detached eclipsing binaries serve as fundamental empirical benchmarks for these models, since their geometry enables direct, high-precision measurements of both stellar masses and radii (Taormina et al., 2020). Modern models can indeed reproduce observed properties of main-sequence and core-helium-burning stars to within a few percent, but notable discrepancies still exist for more evolved phases, particularly subgiants and red giants (del Burgo & Allende Prieto, 2018). In our following studies we will particularly use the stellar evolution tracks calculated with the stellar evolution code MESA: MIST (MESA Isochrones and Stellar Tracks, Choi et al. 2016; Dotter 2016). These isochrones span a broad range of ages (from log(age) [yr] = 5 to 10.3), metallicities (from [Z] = −4 to +0.5), and different initial stellar rotation rates. As the final template grid in SPS is normally the same grid as the stellar tracks, it is crucial to have broad ranges already at this stage. MIST isochrones at different stellar ages and with stellar rotation

are shown in Figure 1.2. They cover an initial stellar mass range 0.1 to 300 $M_\odot$. For clarity, evolutionary phases after the tip of the red giant branch are omitted. The solid line corresponds to solar metallicity tracks, the dashed line belong to a lower value of [Z] $= -0.75$. In the reddish isochrone at a stellar age of 10 million years, we see the effect of pre-MS evolution. The most massive stars ($\gtrapprox$ 18 $M_\odot$) have already left the MS, when solar type stars ($\lessapprox$ 1.8 $M_\odot$) have not even arrived there yet.

1.5 Stellar Spectra

The detailed analysis of stellar light predates theories of stellar evolution by several decades. The first sophisticated classification scheme for stars by Anni Jump Cannon was established before it was even clear what stars are composed of (Sobel, 2016).
It is common knowledge among astrophysicists, that the overall shape of the spectral energy distribution can be approximated to zero order by a black body curve, reflecting their effective temperature $T_{\rm eff}$. However, upon closer inspection, the spectra reveal a series of narrow, dark absorption features at specific wavelengths. These absorption lines, superimposed on the continuum, became the key diagnostics for the physical conditions and composition of stellar photospheres and by extension stars themselves. Figure 1.3 shows the optical spectra of different main-sequence stars. The temperature, stellar mass and spectral classification is printed on the right, the image was reproduced by own means after Gray & Corbally (2009, Figure 2.1) with the spectra from the Indo-US library (Valdes et al., 2004). The hottest O-type stars show absorption lines of ionized helium and relatively scarce metal lines, while their hydrogen lines, though present, are weaker compared to cooler stars, despite hydrogen being the most abundant element in their photospheres. As temperatures decline into the B spectral class, neutral helium lines strengthen and hydrogen absorption grows more pronounced. A-type stars are distinguished by their intense hydrogen Balmer lines and subtle metal signatures, while F stars show a diminution in hydrogen strength paired with increasingly prominent ionized metal lines. Moving to cooler G stars, hydrogen lines further fade as neutral metal lines emerge and molecular bands begin to appear. Our sun is an example thereof. K stars feature dominant neutral metal absorption and strong molecular bands, with hydrogen lines becoming faint. Finally, the coolest M stars' spectra are largely defined by robust molecular band absorption, particularly TiO, with hydrogen lines typically absent (Rajpurohit et al., 2018). Proxima Centauri and Barnard's star are some of the most prominent class M dwarfs. Bochanski et al. (2010) found that 70% of the Galactic stellar population falls into this category.
It must be clear that the spectral type of a star is something which is easy to determine but can only capture its current state. Following a stars's evolutionary path on the HRD, their effective temperatures $T_{\rm eff}$, luminosities L, and surface gravities $\log g$ can change significantly during their life cycles, altering their spectral appearances. Hot supergiants of spectral types B and A exhibit significantly narrower Balmer lines compared to their main sequence counterparts (Gray & Corbally, 2009, chapter 2.2). Additionally, metal lines become significantly stronger in the evolved stages relative to main sequence stars

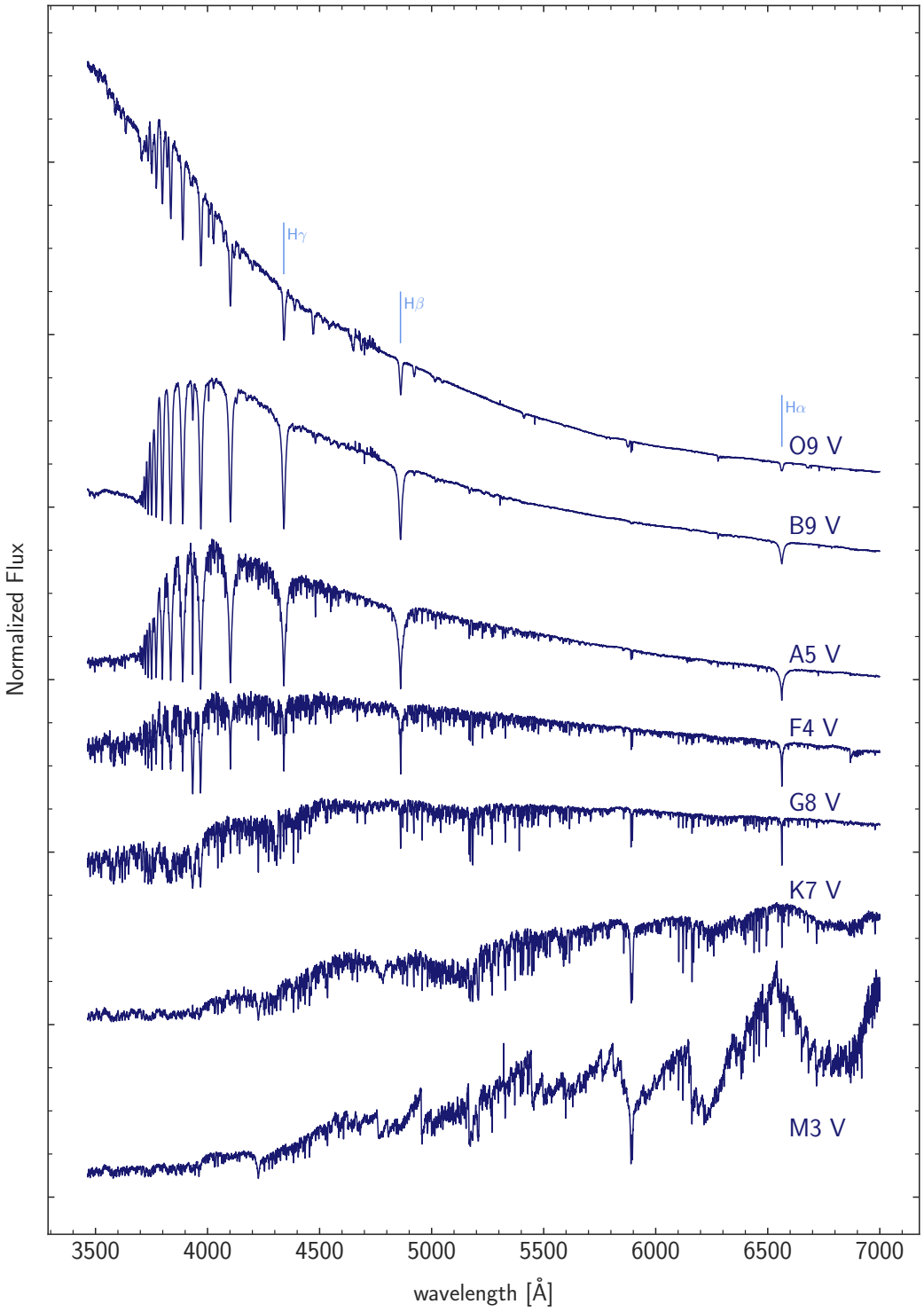

Figure 1.3: The OBAFGKM spectral sequence of main-sequence stars (luminosity class V). The spectra are normalized to unity at $5550 - 5550$ Å and then plotted with vertical offsets for better visibility. The spectra are taken from the Indo-US spectral library (Valdes et al., 2004). Star IDs (from top to bottom): `HD 149757, HD 149630, HD 11636, HD 87822, HD 10700, HD 237903, G 103-68`

for the same spectral types A, F, and G. However, metallicity can have a similar effect on spectra.
This similarity in spectral behavior shows that distinguishing between evolutionary (aging) effects and metallicity variations can be challenging. Worthey (1994) put it in a simple formula: Increasing the age by a factor of three is almost indistinguishable from increasing the metallicity by a factor of two on most spectral indices. In SPS, we will see that this age-metallicity degeneracy is to some extent native and can more or less only be ameliorated with higher S/N ratio. Suitable advanced mathematical tools like renormalization, our bootstrapping technique or adding Monte-Carlo noise can provide insights into the extend of the error in the obtained physical quantities through the degeneracy.

1.6 The Initial Mass Function of Stars

In the last chapter it became clear, that the initial mass of a star is the key predictor for its luminosity, lifetime, and final evolutionary stages. However, it is not a priori clear what the overall distribution of stellar masses will be. That is, how many stars form within a particular mass range [m,m+Δm]. This distribution is captured by the stellar Initial Mass Function (IMF) and crucial for the chemical enrichment of the galaxy and feedback processes within it. Although low-mass stars account for most of the total stellar mass, they have relatively little light output, have extraordinarily long lifespans, and represent the primary contributors to a galaxy's long-term stellar mass. In contrast, massive stars dominate the luminosity of a stellar population, produce energetic feedback via stellar winds and supernovae, and are key drivers of enrichment in the interstellar medium (ISM). In SPS, this has to be taken into account.
The form of the IMF was first characterized empirically by Salpeter (1955) as a power law:

$$dN = M^{-\alpha}\, dM \quad \text{with} \quad \alpha \approx 2.35$$

for stars between roughly 0.4 and 10 solar masses. Low-mass stars are progressively more numerous than high-mass stars. Modern work shows that at masses below about 0.5 solar masses the IMF flattens, indicating a relative excess of low-mass stars compared to the pure Salpeter power-law (Kroupa et al., 2026). We will mostly use the Chabrier-IMF (Chabrier, 2003) description in the subsequent analysis.
Precisely determining the IMF is challenging due to observational difficulties such as counting stars in young populations or corrections for unresolved binaries (Bastian et al., 2010). Despite these challenges, the IMF is often assumed to be roughly universal within the Milky Way and similar galaxies, although some evidence suggests it may vary in different environments or at earlier cosmic times. It has been debated, for example, that low-mass stars are less likely to form in metal-poor molecular clouds because the lack of metals leads to inefficient radiative cooling (Bromm & Larson, 2004). Our studies (section 2.7) show that the impact of the IMF on SPS is rather small (but also consider Martín-Navarro et al. 2024). We only probed low redshift ($z \leq 0.25$) galaxies, so this might have to be reconsidered in the high-redshift universe.

1.7 Extinction in Stellar Population Synthesis

As light from a stellar photosphere passes through the interstellar medium, dust grains primarily absorb and scatter photons. Unfortunately for astrophysical observations, more energetic (bluer) photons are scattered more efficiently than lower energy (redder) photons. As a result, the observed spectral energy distribution of the stars may be affected complicating the stellar analysis by a threefold age-metallicity-dust degeneracy of the SED. A young stellar population SED may look like the one of an older, more metal-poor population. This is a severe problem for all population studies based on SEDs or photometric color indices alone (Jones et al., 2025a; Roediger & Courteau, 2015). In our approach we break this degeneracy by using stellar absorption lines, whose strengths (equivalent width) is unaffected by dust absorption.

While the general impact of dust on spectra is largely intuitive, a detailed and rigorous quantitative description is not widely familiar among astrophysicists. The overall amount of extinction is described by the extinction curve A(λ), which expresses extinction as a function of wavelength. The shape and steepness of this curve provide insight into the composition, size distribution, and spatial arrangement of dust present in the medium. The steepness and features of this curve reveal details about the dust composition and grain sizes, and its shape can differ significantly from one galaxy to another (compare Fitzpatrick 1999 with O'Donnell 1994 or Calzetti et al. 2000). To measure the effect of extinction on stellar colors, the color excess E(B-V) is defined by

$$E(B-V) = A(B) - A(V) = (B-V) - (B-V)_0$$

with A(B) and A(V) as the extinctions in the B and V bands, respectively. In other words, the color excess quantifies the extent to which dust has made an object's color (i.e. B-V) appear redder than its intrinsic (unobscured) color $(B\text{-}V)_0$ (Irwin, 2007, chapter 3.5). Within stellar population synthesis with spatially resolved spectra, we are able to draw 2D maps of the colour excess as part of the fit result and can identify regions of excessive dust in the ISM. A related and fundamental quantity is the ratio of total to selective extinction, $R_V = A(V)/E(B-V)$. This parameter describes the relationship between absolute extinction in the V band and the wavelength-dependent change in extinction between B and V. R_V is directly influenced by the properties of the dust grains, such as their average size and composition (silicate cores, formation of ice mantles, see Shaw (2006, chapter 5.9)). In typical diffuse Milky Way regions, R_V is about 3.1, but it can range from ~ 2 in dense, grain-fragmenting environments to ~ 7 in the center of giant molecular clouds (Foster et al., 2013; Cikota et al., 2016; Urbaneja et al., 2017). Spatial variations in R_V and the observed extinction curve[5] can thus be used to probe the physical conditions and processes governing dust evolution in different astrophysical environments. We will try to

[5]In full spectral fitting, the 'reduction in light' we measure is actually due to attenuation rather than extinction. Extinction refers to the amount of light lost along a single line of sight as a result of absorption and scattering of photons out of that path by dust (Calzetti, 2013). It assumes a simple geometry where a background source is obscured by a dust screen and does not consider scattering back into the line of sight. Attenuation, however, denotes the overall decrease in light intensity when accounting for more complex

determine not only the amount of reddening $E(B-V)$, but also try to fit R_V values in our population synthesis approach.
One aspect, which should be kept in mind in this context, is that star formation occurs in dusty molecular clouds regions. This means that it might not be correct to assume that all stars in a certain spatial area are affected by the same kind of extinction law and the same reddening. It is therefore not unreasonable to assume that young stellar populations ($\leq 5-10$ Myr) are more obscured as they are still affiliated with their birth cloud (Charlot & Fall, 2000). It is therefore of interest to incorporate this effect into our fitting routines (see section 4.4.4).

1.8 Piecing it all together: Single Stellar Populations

The previous chapters introduced various aspects of stellar evolution, stellar spectra, IMF and dust treatment. The next logical step is to tie these elements together through single stellar populations (Tinsley, 1968). This is an idealized group of stars that formed at the same time (sometimes termed 'coeval'), share the same initial metallicity, but have a range of stellar masses fixed by an IMF. A real galaxy population can then, in a second step, be built from a combination of such SSPs.
To build a simple stellar population model, one starts with stellar evolution tracks. At any given age, these tracks specify each star's position in the Hertzsprung-Russell (HR) diagram, including parameters such as luminosity, effective temperature and surface gravity. These stellar properties are then linked to one or several spectra in a library (theoretical or empirical) to provide the star's observable spectral energy distribution based on its characteristics. The IMF determines the relative number of stars formed at each mass, which, combined with the lifetime of stars at each mass, allows calculation of the total contribution of all stars still present at the model's age. Finally, the resulting SED can be modified with an extinction law. Mathematically, this can be written in a compact way:

$$F_{\mathrm{SSP}}(t,Z) = \int_{m_1}^{m_2} \Phi(M)\, F_{\mathrm{star}}\Big(T_{\mathrm{eff}}(M), \log g(M); t, Z\Big)\, dM \tag{1.1}$$

Dust modifies the emergent SED via the following relation:

$$F_{obs}(t,Z,\lambda) = 10^{-0.4\,E(B-V)\,k(\lambda)}\, F_{\mathrm{SSP}}(t,Z,\lambda) \tag{1.2}$$

Hereby, $k(\lambda)$ is the reddening curve as a function of wavelength λ. Several numerical algorithms can be found in the literature on how to calculate 1.1. We will use the fortran-based code `'Flexible Stellar Population Synthesis' (FSPS)` by Conroy & Gunn (2010a). In Figure 1.4, we show different SSP-spectra (at [Z]=0.25) of different ages that were used among others in the following chapters. They were computed using `FSPS`, adopting a

geometries, such as multiple lines of sight, scattering of photons back into the observer's direction, and a mixture of sources and dust (Salim & Narayanan, 2020). This is typically what is observed in our spectra but is often not clearly distinguished in the literature. Here, we should rather refer to the attenuation curve instead of the observed extinction curve.

Chabrier-IMF (Chabrier, 2003), MIST isochrones (Dotter, 2016; Choi et al., 2016), and the empirical stellar catalog MILES as the primary stellar library (Sánchez-Blázquez et al., 2006). For additional details, refer for instance to section 6.4.3. All spectra are fixed to unity in the wavelength region around $4400-4450$ Å. What makes these spectra interesting is not only the rapidly changing slopes but also the evolving individual spectral features over time, despite the metallicity in the stellar photospheres remaining roughly constant over time.

1.9 Metallicity in the ISM: Problems, Methods, and Meaning

The term 'metallicity' was used already 19 times in this introductory sections. In astronomy, it is a measure of the amount of elements heavier than hydrogen (H) and helium (He). When imagining a group of stars, their mean metal content is simply the fraction of the mass of the metals divided by the total mass of the stars. In sections 5.2.2 and 6.4.2, we will work with this definition within the framework of SPS.

Even though the above definition is rather simple, the determination of metallicity in the extragalactic regime is not straight-forward. The gold standard, nearly unrivaled in the literature is the analysis of emission features of HII regions. This metallicity is conventionally expressed as the oxygen-to-hydrogen number fraction, commonly denoted as $12 + \log(\mathrm{O/H})$. Oxygen [O] is the most abundant element in the universe after H and He. Converting $\log(\mathrm{O/H})$ to full metallicity, an abundance pattern must be used. Using solar abundance (Asplund et al., 2009), we arrive at the first-order approximation $12 + \log(\mathrm{O/H}) - 8.69 \approx [Z]$.
HII regions consist of gas which is ionized through luminous massive stars and remain in a state of statistical equilibrium. Photoionization heating generated by ultraviolet photons from the central stars is balanced by radiative cooling, predominantly through collisionally excited forbidden-line emission from metal ions. While normal recombination of electrons with ions also occurs, the recombination photons tend to be reabsorbed locally within the nebula, rendering recombination ineffective as a cooling mechanism.
Also, since metals strongly enhance cooling efficiency, increasing the metallicity lowers the electron temperature (T_e) established in the nebula (Wiersma et al., 2009). In turn, a reduced T_e decreases the collisional excitation rates of forbidden transitions, which modifies the observed emission-line strengths. Additionally, the electron density (n_e) plays a critical role in the nebula. Higher electron densities inhibit cooling processes (by collisionally de-excitating the ions before a forbidden transition can occur) and thus can cause a slight increase in T_e. This in turn modifies the emission again.
These fundamental interlinked processes underpin the spectroscopic methods for determining gas-phase metallicity. The electron density n_e can be extracted for instance from [O II] $\lambda3729/\lambda3726$ or [S II] $\lambda6717/\lambda6731$ line ratios. The temperature can be extracted from so

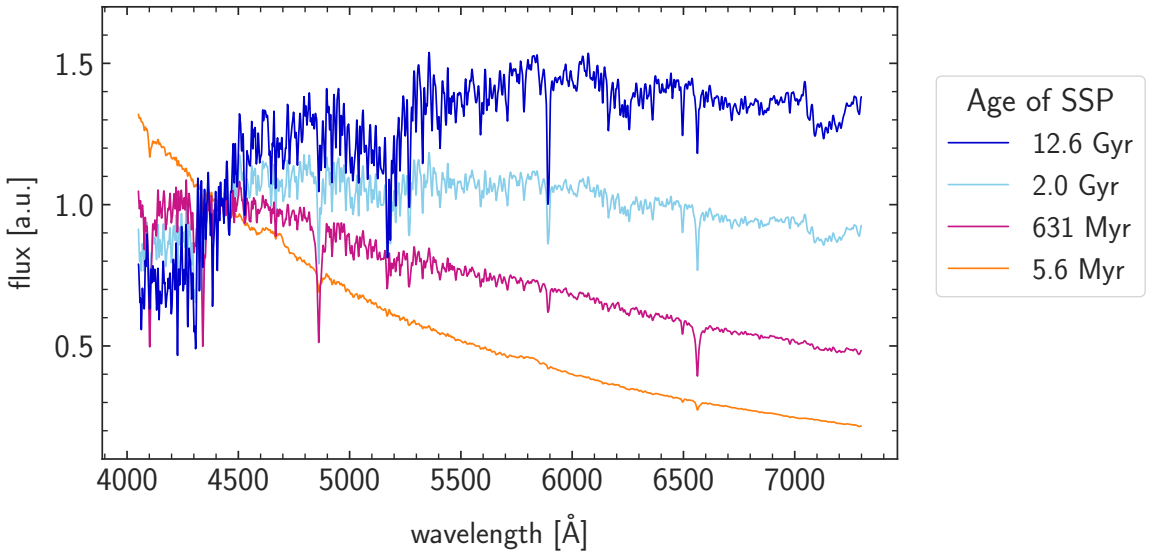

Figure 1.4: Example SSP spectra from our main template set. The ages of the corresponding SSP are indicated on the right. The metallicity is fixed to [Z]=0.25 and all spectra are normalized to unity in the range of $4400 - 4450$ Å. The overall flux is therefore in arbitrary units (a.u.).

called 'auroral' lines: [O III] λ4363, [S iii] λ6312 [N ii], λ5755 or $\lambda\lambda 7320, 7330$ (Berg et al., 2015). The approach that employs these temperature-sensitive diagnostics is known as the 'direct' or electron temperature (T_e) method. This method is widely regarded as the most physically grounded and least model-dependent means of obtaining gas-phase metallicities. Nevertheless, its application is limited primarily to nearby or low-metallicity H II regions because the auroral lines required for temperature determination are inherently faint and often simply undetectable (Andrews & Martini, 2013). When this is the case, metallicity must be derived using so-called strong-line methods, which rely solely on strong forbidden and recombination lines such as [O II] $\lambda\lambda 3726, 3729$, H$\beta$, [O III] λ5007, Hα, [N II] λ6584, and [S II] $\lambda\lambda 6717, 6731$. Although these lines do not directly provide electron temperature diagnostics, their ratios encode metallicity information because of the underlying physical relationship between metallicity, ionization, and excitation conditions (Pilyugin & Grebel, 2016).

Strong-line metallicity indicators can be classified into two broad categories: empirical calibrations and theoretical photoionization model-based calibrations. Empirical calibrations utilize samples of nearby H II regions with reliable metallicities obtained via the direct method to establish empirical relations between these strong emission-line ratios and oxygen abundance. Examples are the calibrations presented in Pettini & Pagel (2004) and Marino et al. (2013). The principal advantage of this approach lies in its observationally anchored nature without much modeling. However, it seems more and more questionable that the physical conditions of star-forming regions have remained comparable over cosmic times. In the high-z universe, systematically higher ISM pressures, ionization parameters, and harder ionizing radiation fields seem to persisted making the application of these calibrations somewhat troublesome (Shirazi et al., 2014). Theoretical calibrations address

these issues by employing detailed photoionization models that self-consistently simulate the physical conditions and resultant emission-line spectra across a broad parameter space in metallicity, ionization parameter, density, and stellar ionizing spectra. These models compute theoretical relations between strong-line ratios and metallicity from first principles (i.e. shown in Kewley & Dopita 2002; Pilyugin & Thuan 2005; Thomas et al. 2018). But their worth depends critically on the accuracy of the input atomic data, stellar fluxes, and completeness of physical processes. Also it is commonly assumed that the ionized region is homogeneous such that n_e and T_e remain approximately constant or vary only within ionization zones in the nebulae. This approximation does not seem to be correct (Méndez-Delgado et al., 2023; Rickards Vaught et al., 2024).

Overall, comparing different strong-line methods still leads to large uncertainties, extensively shown in Kewley & Ellison (2008); Teimoorinia et al. (2021). It is even shown that different strong line methods lead easily to different results for the metallicity gradients in star-forming galaxies (Bresolin et al., 2009a). Most importantly, the comparison of strong-line methods with accurate extragalactic spectroscopy of blue and red super-giant stars shows that they are highly uncertain (Kudritzki et al., 2012; Bresolin et al., 2016; Davies et al., 2017; Kudritzki et al., 2024).

Employing strong-line diagnostics is only allowed in HII regions, not for diffuse ISM emission (DIG) or star-forming emission contaminated by AGN (Kewley et al., 2019). Interesting regions are therefore missed. SPS estimates on young stars works in much larger galaxy regions, even in the Narrow-line Region (NLR) of AGNs. Careful attention is only needed when the AGN contributes to both line and continuum emission, as it occurs in an unobscured broad line region (BLR) (Hickox & Alexander, 2018, Figure 4). For obtaining a value for a young stellar population in SPS, we found that $> 10\% - 20\%$ of the light in a spectral pixel (spaxel) needs to come from this population for a reliable estimate.

Would one expect to find the same metallicity values in the gas-phase and the stellar component in a certain HII region? Generally, the answer is no. The gas-phase diagnostics above reflects only the metals that are present in the interstellar gas, whereas the "full" metallicity of the region can be higher. This discrepancy arises because a significant fraction is locked up in dust grains. In contrast, stars that form from the interstellar medium will inherit the total metallicity (gas + dust) from the ISM, providing a more complete abundance present at the time of their formation. Not surprisingly, dust depletion is found to be more pronounced in environments with overall higher metallicity (Rémy-Ruyer et al., 2014; Bresolin et al., 2025). SPS combined with spatially resolved spectra is a valuable tool that has the possibility to extend such research as well. It overcomes the weaknesses of HII-region emission line diagnostics and provides accurate stellar metallicities.

1.10 Main principle of full-spectral fitting

The main principle of full-spectral fitting is to model an observed spectrum by comparing it with combinations of reference models across the entire available wavelength range, not only using specific wavelength features. The templates or references models are the single stellar population spectra presented in chapter 1.8. From a mathematical perspective, the main principle of SPS can then be rephrased: We search a model spectrum $M_{\rm pred}(\lambda)$ which is constructed from a collection of SSPs (flux $f_{\lambda,i}$) with ages t_i and metallicities $[\mathrm{Z}]_i = \log(\mathrm{Z}_i/\mathrm{Z}_\odot)$ as

$$M_{\rm pred}(\lambda) = D_\lambda(R_V, E(B-V)) \left[\sum_{i=1}^{n_{SSP}} b_i f_{\lambda,i}(t_i, [Z]_i) \right]. \tag{1.3}$$

Here, $D_\lambda(R_V, E(B-V))$ represents the attenuation curve applied to account for the dust reddening described by the colour excess $E(B-V)$ and the total-to-selective extinction parameter R_V.
The ultimate aim of the fit is to find the coefficients b_i and the colour excess $E(B-V)$. Normally, the SSP spectra (as well as the observed spectra) are normalized to unity in a certain wavelength range without prominent emission or absorption features (mostly B or V-band). Because of this normalization, the sum of all b_i coefficients adds up to one, making each b_j the fractional contribution of its SSP to the integrated light (at the normalization wavelength).

All observed spectra inevitably contain noise, which is quantified by a wavelength-depended uncertainty $\sigma(\lambda)$. To now find the best-fitting model, the residuals between the observed flux $F_{\rm obs}(\lambda)$ and the predicted model spectrum $M_{\rm pred}(\lambda)$ are computed, and their weighted square differences are summed across the wavelength range to form the chi-squared statistic:

$$\chi^2 = \sum_\lambda \left(\frac{F_{\rm obs}(\lambda) - M_{\rm pred}(\lambda)}{\sigma(\lambda)} \right)^2 \tag{1.4}$$

Minimizing with respect to the coefficients b_i and colour excess $E(B-V)$ is done through an iterative algorithm and yields an optimal mix of stellar populations and the amount of reddening that reproduces the observed spectrum accurately.
The body of literature has extensively grown since the initial papers by Heavens et al. (2004); Cid Fernandes et al. (2005); Ocvirk et al. (2006), and many authors stated that such a simple χ^2-minimization in full-spectral fitting is not sufficient due to intrinsic degeneracies among model parameters. These degeneracies arise when two different combinations of b_i produce very similar integrated spectra, resulting in multiple model solutions $M_{\rm pred}(\lambda)$ with nearly indistinguishable χ^2-values. Therefore, more sophisticated fitting algorithms were proposed. Prime examples are the regularization approach in `pPXF` (Cappellari & Emsellem, 2004; Cappellari, 2017, 2023) and the iterative process controlled by the Bayesian Information Criterion in `FIREFLY` (Wilkinson et al., 2017, 2021). In the following chapters, we will make use of several different stellar fitting codes, including our own χ^2-minimization

routine, as well as `FIREFLY`, `pPXF` and `STARLIGHT` (Cid Fernandes et al., 2011a, 2013).

In practice, several additional complications arise during full-spectral fitting. One major issue is the presence of line emission from star-forming regions, especially prominent in the Balmer lines but also in certain oxygen, nitrogen and sulfur lines. These emission lines can interfere with the fitting of the underlying stellar populations, so these wavelength regions are typically masked during the fitting process. Interstellar absorption features also belong in this category. Although these different contaminated regions often hold valuable information about stellar age and other properties, the fitting still succeeds statistically by using thousands of other wavelength points in the spectrum.
Another important complication is the velocity dispersion and stellar rotation, which cause broadening and shifts in the spectra. These kinematic parameters are usually determined independently ahead of the spectral fitting or simultaneously modeled to avoid biases.

The final step involves calculating the mean stellar metallicity and age once the b_i coefficients have been determined. In full-spectrum fitting of stellar populations, these mean values are generally computed as light-weighted and mass-weighted averages.
The light-weighted mean age or metallicity places weight on the contribution of stellar populations proportional to their luminosity. This means younger, brighter stars have a stronger influence in the light-weighted values. As a result, the light-weighted age is more sensitive to recent star formation episodes and tends to be biased toward younger stellar ages. The mean light-weighted age would be calculated as the sum over the chosen ages $\log(t_i)$ of the SSPs:

$$\log(t)^{\mathrm{lw}} = \frac{1}{\sum_i b_i} \sum_i b_i \log(t_i) \tag{1.5}$$

The mass-weighted mean age or metallicity, on the other hand, weights each stellar population component according to its stellar mass contribution. This gives a measure more representative of the average epoch when the bulk of the stars formed, as it accounts for the mass locked in stars rather than their brightness. We have to convert the light-fractions b_i to mass-fractions $\tilde{b_i}$ in this case (MacArthur et al., 2009). This is done using the mass-to-light ratio γ_i, a piece of information normally tracked by the isochrones:

$$\tilde{b_i} = \frac{b_i \gamma_i}{\sum_i b_i \gamma_i}. \tag{1.6}$$

For the metal mass fraction of the whole stellar population, we then obtain

$$Z = \frac{M_Z}{M} = \sum_i \tilde{b_i} Z_i \tag{1.7}$$

In this context, Z_i represents the linear (not logarithmic) metallicity value from the corresponding SSP. We apply the logarithm only *after* computing the combined value Z. This differs from the conventional mass-weighted metallicity definition commonly used in the literature. To clarify this distinction, we will later refer to our approach as the *physical*

metallicity in chapter 6 but will already use it beforehand. Sections 6.4.2 as well as 5.2.2 will motivate this choice. Successful comparisons of our physical metallicity values with those derived from individual stellar probes in M83 will validate this approach. For this comparison to work, we will also employ an age split, which means we will mostly focus on 'the metallicity of the young (old) stellar population'. For example, in equation 1.7, the summation is then not carried out over all SSPs but only over a subset restricted to those below a specific age. The definition of 'young' varies by galaxy, ranging from less than 100 million years in M83 to about 1.6 billion years in NGC 1365. In general, in the first billion years, significant chemical evolution is not expected. This is discussed in section 2.2 in greater length.

Having established the main ideas of SPS, we will apply full-spectral fitting in various contexts across the next five chapters. The analysis will begin with stacked SDSS spectra (chapter 2), proceed to using SPS as a tool for testing a generative AI model (chapter 3), and then move on to spatially resolved spectra from multiple galaxies (chapter 4, 5, 6). As it is a cumulative thesis, each will start with the corresponding publication information, the author list as well as a more broader research context. After that, the abstract and the main body is reprinted. All references have been removed from the individual publications and consolidated at the end of the thesis. References that were originally arXiv preprints at the time of publication have been updated to their published journal versions. In the last chapter (chapter 7), we will give an outlook as well as an idea of an unified theory of star-forming nuclear rings in barred galaxies.

2

Mass Metallicity Relationship of SDSS Star Forming Galaxies: Population Synthesis Analysis and Effects of Star Burst Length, Extinction Law, Initial Mass Function and Star Formation Rate

Published in the Astrophysical Journal, **949**:60 (14pp), 2023 June 1

Authors: Eva Sextl, Rolf-Peter Kudritzki, H. Jabran Zahid, and I-Ting Ho

Research Context: In this first study, we use SPS to examine the mass–metallicity relationship (MZR), which plays a central role in tracing the chemical evolution of galaxies. The MZR is the product of the interplay between gas accretion, star formation efficiency, and subsequent feedback. By applying our own spectral fitting method, we confirm the 'downsizing' effect, meaning that more massive galaxies formed their stars earlier. Additionally, the dust properties of the galaxies are discussed. Though initially uncertain, we successfully separated the spectral light into young and old stellar components, which allows for a more precise study of chemical evolution over time. We maintain the approach of using a single robust age cut when moving to spatially resolved data later on, as finer subdivisions cannot be reliably achieved even with the high signal-to-noise stacked SDSS data. Unlike many previous studies, we also test how physical assumptions of burst duration and dust modeling influence our fitting results. From the perspective of stellar astrophysics, testing these factors is a natural and necessary step. We build upon these insights in our subsequent work.
Note: In this publication, the term 'single stellar bursts' (SSB) is used as an alternative expression for 'single stellar populations' (SSPs), as introduced in the early sections. Both terms refer to the same concept of a stellar population formed in a brief, uniform burst of star formation.

Abstract: We investigate the mass–metallicity relationship of star-forming galaxies by analyzing the absorption line spectra of $\sim 200,000$ galaxies in the Sloan Digital Sky Survey. The galaxy spectra are stacked in bins of stellar mass, and a population synthesis technique is applied yielding the metallicities, ages, and star formation history of the young and old stellar population together with interstellar reddening and extinction. We adopt different lengths of the initial starbursts and different initial mass functions for the calculation of model spectra of the single stellar populations contributing to the total integrated spectrum. We also allow for deviations of the ratio of extinction to reddening R_V from 3.1 and determine the value from the spectral fit. We find that burst length and R_V have a significant influence on the determination of metallicities, whereas the effect of the initial mass function is small. The R_V values are larger than 3.1. The metallicities of the young stellar population agree with extragalactic spectroscopic studies of individual massive supergiant stars and are significantly higher than those of the older stellar population. This confirms galaxy evolution models where metallicity depends on the ratio of gas to stellar mass and where this ratio decreases with time. Star formation history is found to depend on galaxy stellar mass. Massive galaxies are dominated by stars formed at early times.

2.1 Introduction

Star forming galaxies show a tight relationship between total stellar mass and average metallicity, the mass-metallicity relationship ('MZR', see for instance Lequeux et al. 1979; Tremonti et al. 2004; Kudritzki et al. 2016; Bresolin et al. 2022). This relationship while evolving and becoming steeper holds out to redshifts z larger than 3.3 (Vale Asari et al. 2009; Zahid et al. 2014; Genzel et al. 2015; Sanders et al. 2021). In view of the complicated interplay between complex processes such as gas accretion, star formation, nucleosynthesis and chemical evolution, stellar and galactic winds, dynamical evolution and merging the existence of a simple relationship such as the MZR seems to be a Rosetta stone to understand galaxy formation and evolution. As a consequence, a large variety of approaches has been developed to use the MZR as a constraint of galaxy formation and evolution, Davé et al. (2011), Yates et al. (2012), Dayal et al. (2013), Schaye et al. (2015), Peng et al. (2015), Spitoni et al. (2017a,b), Pantoni et al. (2019), Lapi et al. (2020), Spitoni et al. (2020), Trussler et al. (2020), Kudritzki et al. (2021a,b) to name only a few. However, there is an important problem. Many of the observational MZR results obtained are based on measurements of the strongest ionized interstellar medium (ISM) emission lines, which are then converted into oxygen abundances. These 'strong line methods' depend heavily on the calibration method used. Kewley & Ellison (2008) in an emission line analysis of $50,000$ star forming Sloan Digital Sky Survey (SDSS) galaxies demonstrated convincingly that the systematic uncertainties in oxygen abundances can be as large as 0.8 dex. As a result, the slope of the MZR can vary significantly for the same set of observed emission line data depending on the calibration applied.

An obvious alternative approach is the analysis of low resolution absorption line spectra of

individual stars. Blue and red supergiants (BSG and RSG) as the brightest stars at visual or infra-red light, respectively, are the ideal objects for this purpose. Galaxy metallicities obtained by this method have only small uncertainties of at most 0.1 dex (systematic and random, see Gazak et al. 2015) and have been used to construct a very reliable MZR, see Kudritzki et al. 2016; Davies et al. 2017; Bresolin et al. 2022, and references therein. Unfortunately, the method is limited with respect to galactic distance. The most distant objects studied so far are the Antennae galaxies and their super star clusters at 20 Mpc (Lardo et al., 2015).

In view of this limitation a third technique which has been well advanced over the last two decades has become truly important, the analysis of stellar absorption line spectra of the integrated stellar population through population synthesis techniques. The advantage of this technique is that it reaches out to much larger distances because of the relatively high surface brightnesses of galaxies. In addition, it can provide information about the young and old stellar population and the star formation history.

The general idea was pioneered by Tinsley (1968) and Spinrad & Taylor (1972). With significant further improvements of stellar evolution theory and stellar spectral modeling the concept was then advanced by many groups, see for instance Arimoto & Yoshii (1987), Bressan et al. (1996), Reichardt et al. (2001), Bruzual & Charlot (2003), Cardiel et al. (2003) and references therein. More recent work used the advantages of increased computer power and improved the method for applications on massive spectroscopic galaxy surveys, first focusing on spectra of the central regions of galaxies (Gallazzi et al. 2005; Cid Fernandes et al. 2005; Panter et al. 2008; Conroy et al. 2009; Koleva et al. 2009; Sánchez-Blázquez et al. 2011; Peng et al. 2015; Zahid et al. 2017) and later on spectra of spatially resolved regions of galaxies obtained with Integral Field Units (Yoachim et al. 2012; González Delgado et al. 2015; Schaefer et al. 2017; Parikh et al. 2021).

Given the enormous potential of this technique it is important to carefully assess the systematic effects arising from the large variety of assumptions which enter this approach. While this has been done already to a large extend in previous work, our work presented here is investigating a variety of additional important aspects, which have not been addressed so far in much detail. We study the effects of finite star formation burst lengths compared with instantaneous bursts, the effects of pre-main sequence evolution and initial mass function and we assess the influence of an interstellar reddening law characterized by a ratio R_V of extinction to reddening deviating from the standard value of 3.1. We will also investigate the influence of star formation rate (SFR) on MZR, extinction and ages. For this purpose we start from our previous work (Zahid et al., 2017) and apply an improved technique to analyse a sample of $200,000$ SDSS star forming galaxies with spectra stacked into bins of stellar mass. We compare the MZRs obtained in this way for the different assumptions with the MZR from supergiant spectroscopy, which we use as benchmark. We will also discuss stellar ages and star formation history.

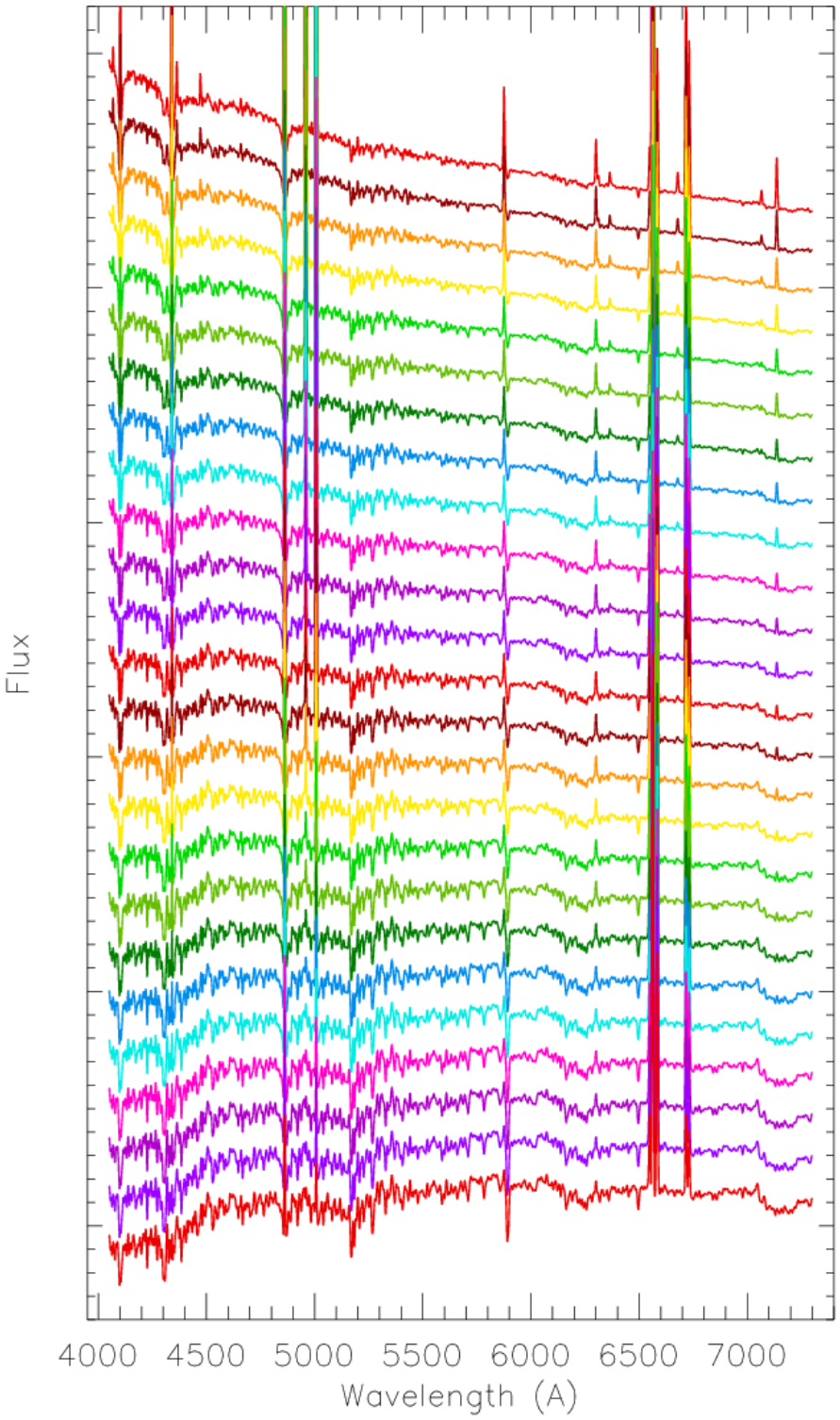

Figure 2.1: Fluxes (arbitrary units) of the stacked SDSS spectra in 25 mass bins from log $M_* = 8.55$ (top) to 10.95 (bottom). For clarity the spectra are shifted by 0.2 units from one mass bin to the next.

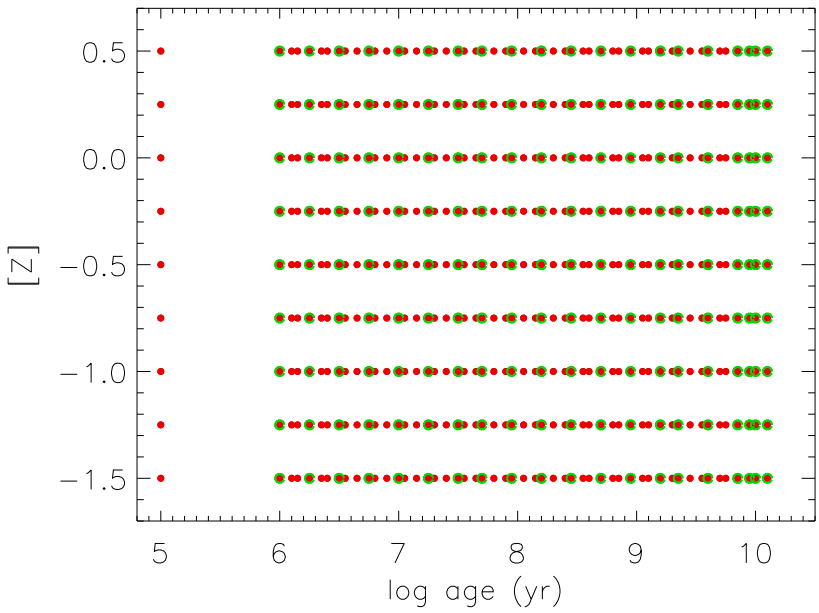

Figure 2.2: The grid of SSB metallicities [Z] and ages for the calculation of model spectra using eq. (1). Filled red circles: high age resolution grid, green circles: low resolution grid.

2.2 Observed Spectra and Analysis Technique

The same dataset as described in Zahid et al. (2017) is used. The observations consist of SDSS spectra of about 200,000 star forming galaxies in the redshift range $0.027 \leq z \leq 0.25$. The galaxies were selected according to the strengths of their interstellar medium (ISM) emission lines and the redshift range was chosen to ensure rest-frame wavelength coverage of the [OII] λ3727 and λ7330 emission lines. Since we are interested only in the average galaxy properties as a function of their stellar mass, we have stacked the spectra in 25 bins of stellar mass log M_* (measured in units of $M_\odot$) from 8.55 to 10.95 in steps of 0.1 dex. In this way the signal-to-noise is strongly enhanced for the analysis and ranges from 160 at the low mass end to 1300 at higher masses (see Table in Zahid et al. (2017)). To avoid systematic effects as a function of stellar mass caused by different line widths we have convolved all spectra to the line width FWHM = 330 km s^{-1} found for the bin with the highest stellar mass. In addition, the spectra are normalized by setting the mean flux between 4400 and 4450 Å equal to unity. Details of galaxy selection, stellar mass determination, stacking and convolution procedure are given in Zahid et al. (2017).

The spectra of the 25 mass bins are shown in Figure 2.1. Strikingly, the SED slope changes from low to high stellar mass and the stellar absorption lines become stronger. We will show that this is caused by systematic differences in interstellar extinction, average stellar age and metallicity.

The technique to analyse these spectra in order to extract information about stellar population metallicity and ages is a modification of the approach introduced by Zahid et al.

(2017). We model the spectrum of the integrated stellar population M_λ as a linear combination of the spectra of single stellar bursts (SSB) $f_{\lambda,i}(t_i, [Z]_i)$ with age t_i and logarithmic metallicity $[Z]_i = \log Z/Z_\odot$

$$M_\lambda = D_\lambda(R_V, E(B-V)) \sum_{i=1}^{n_{SSB}} b_i f_{\lambda,i}(t_i, [Z]_i). \quad (2.1)$$

The coefficients b_i describe the contribution of burst i with age t_i and metallicity $[Z]_i$. $D_\lambda(R_V, E(B-V))$ accounts for the absorption by interstellar dust, which depends on interstellar reddening E(B-V) and $R_V = A_V/E(B\text{-}V)$ the ratio of interstellar extinction to reddening in the V-band. The value of R_V characterizes the reddening law, at least to first order. As is well known from studies of stellar SEDs in star forming regions, R_V can cover a wide range from 2 to 6 (see, for instance, Urbaneja et al. 2017). We use the interstellar reddening law by O'Donnell (1994), which is a modification of Cardelli et al. (1989).

The SSB spectra are calculated using the Flexible Stellar Population Synthesis code (FSPS, version 3.2) (Conroy et al., 2009; Conroy & Gunn, 2010a) and adopting a Chabrier (2003) initial mass function, the MILES stellar spectral library (Sánchez-Blázquez et al., 2006) and the MESA stellar evolution isochrones (MIST, Choi et al. 2016; Dotter 2016). We also account for finite time lengths of the stellar bursts (0.1, 1.0, 10.0 Myr). This will be discussed in the next section. Finally, our model spectra are normalized in the same way as the observed spectra, convolved to the equal resolution and interpolated to the same integer values of wavelength points as the observed spectra.

The modelling of the spectra by eq. (1) does not account for the contribution of a potential HII-region nebular continuum, which can become important in cases of extremely high star formation rates with very strong nebular emission as shown by Cardoso et al. (2022). However, the strength of the hydrogen nebular emission lines relative to the stellar continuum allows us to estimate the effects of nebular continuum emission for our analysis. The H_β emission equivalent widths in our stacked spectra is $\lesssim 20$ Å and, thus, the nebular continuum contribution to the total spectrum is very small. We have verified this conclusion by estimating the nebular contribution from the measurement of H_β emission equivalent width and by subtracting a theoretical reddened nebular continuum. We have then repeated the analysis with modified spectrum and found only very small changes with respect to metallicity (≤ 0.01 dex) and age ($\leq 1\%$). In our analysis of the SFR dependence of the stellar MZRs in section 9 below we have encountered a very few cases in the highest SFR quintile with larger H_β equivalent widths. But even here the effects on metallicity were smaller than 0.05 dex.

For the selection of metallicities and ages of the SSB spectra we use two rectangular grids consisting of 9 [Z] values and 52 (high age resolution) and 20 (low age resolution) ages, respectively. The metallicities range from [Z] = -1.5 to 0.5 increasing in steps of 0.25 dex. The low resolution ages start at 1Myr and increase in logarithmic steps of Δ log t[Gyr] = 0.25 until 7.08 Gyr and then continue with 8.91, 10.0 and 12.59 Gyr. The high resolution age grid starts at 0.1 Myr with a step to 1.0 Myr and then continues with logarithmic steps Δ log t[Gyr] alternating between 0.05 and 0.1 until 12.59 Gyr are reached. This leads to a

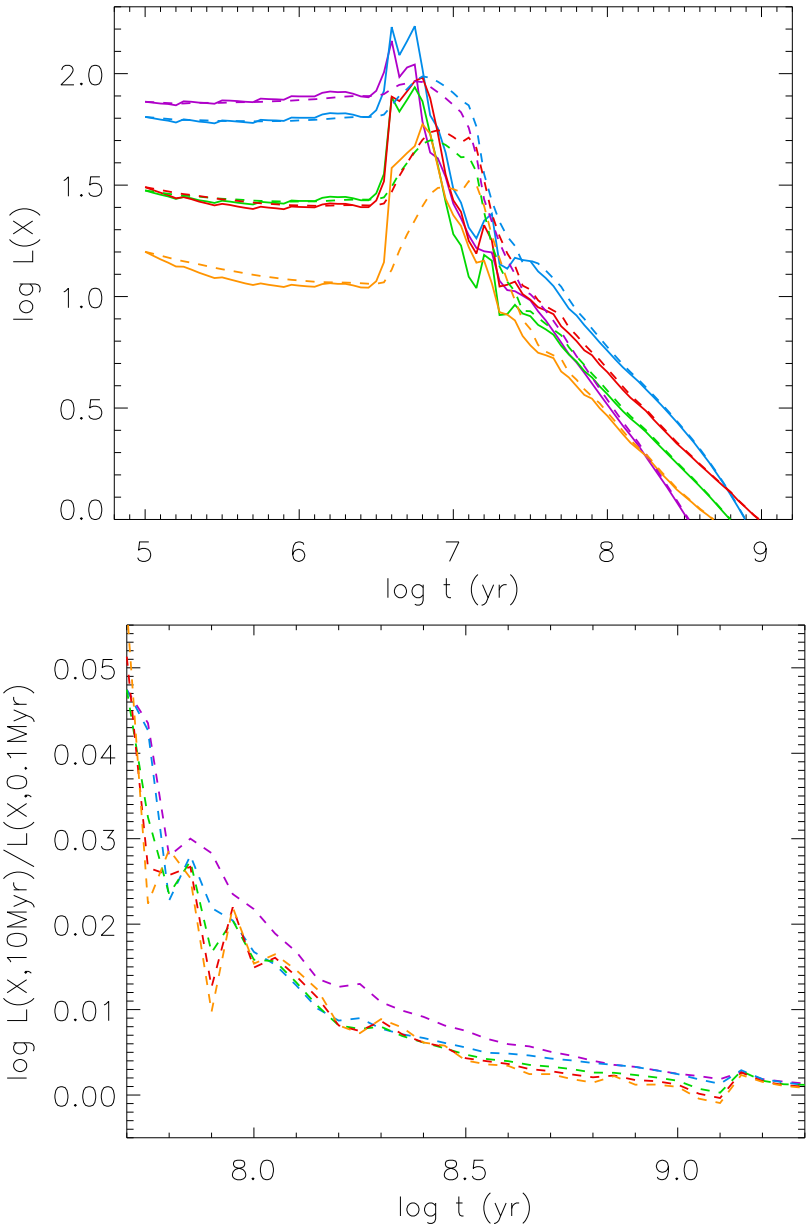

Figure 2.3: Luminosities of SSBs as a function of age (yrs) for different spectral passbands (pink: U, blue: B, green: V, red: R, orange: I). The solid curves correspond to a burst duration $t_b = 0.1$ Myr, the dashed curves to $t_b = 10$ Myr. The bottom figure shows the logarithm of the ratio of luminosities of 10 Myr to 0.1 Myr bursts at larger ages. A metallicity of [Z]=0 has been used for this example.

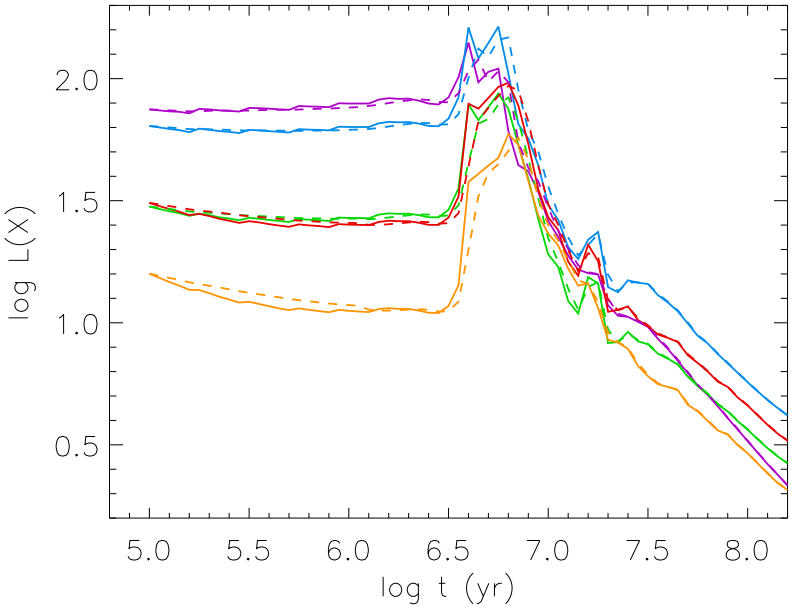

Figure 2.4: Same as Figure 2.3 (top) but the dashed curves correspond to $t_b = 1$ Myr.

total number of SSB $n_{SSB} = 468$ in the high age resolution and 180 in the low resolution case. Metallicities and ages are illustrated in Figure 2.2.
In the fit of the observed spectra with the model spectra we then adopt a grid of R_V and E(B-V) values. For each pair of R_V and E(B-V) we calculate the wavelength dependent dust attenuation factor $D_\lambda(R_V, E(B-V))$ and use the bonded-variables least squares (`BVLS`) algorithm by Stark & Parker (1995), translated to IDL by Michele Cappellari[1] to determine the coefficients b_i. With the b_i the comparison of the model spectrum with the observations leads to a χ^2 value for each R_V, E(B-V) pair and the minimum of χ^2 defines the best fit yielding final values for R_V and E(B-V) and average metallicity [Z] and age t_{av} defined as

$$[Z] = \sum_{i=1}^{n_{SSB}} b_i [Z]_i \tag{2.2}$$

and

$$t_{av} = \sum_{i=1}^{n_{SSB}} b_i t_i. \tag{2.3}$$

Introducing a young and old stellar population through $t_i \leq 1.6$ Gyr and $t_i \geq 1.6$ Gyr, respectively, we can calculate corresponding metallicities $[Z]_{young}$, $[Z]_{old}$ and ages t_{young}, t_{old} via

[1] `https://www-astro.physics.ox.ac.uk/~cappellari/idl/bvls.pro`

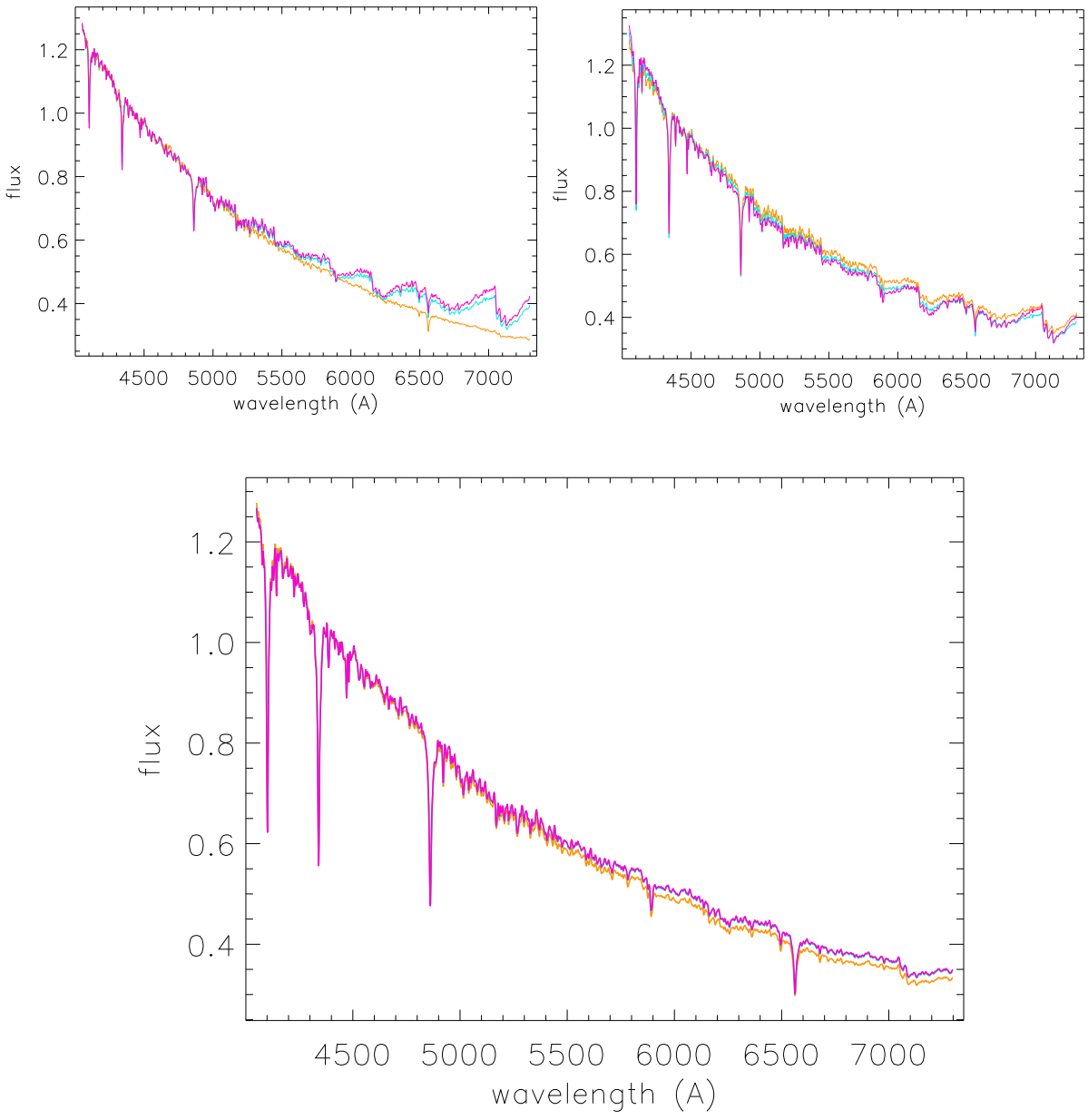

Figure 2.5: Spectra of SSBs at different ages for different burst lengths (pink: t_b = 0.1 Myr, cyan: 1 Myr, orange: 10 Myr). Top left: age = 10 Myr, top right: 19 Myrs, bottom: 45 Myrs)

$$b_{young} = \sum_{i_{young}} b_i, b_{old} = \sum_{i_{old}} b_i \tag{2.4}$$

and

$$[Z]_{young} = \frac{1}{b_{young}} \sum_{i_{young}} b_i [Z]_i \tag{2.5}$$

$$[Z]_{old} = \frac{1}{b_{old}} \sum_{i_{old}} b_i [Z]_i \tag{2.6}$$

$$t_{young} = \frac{1}{b_{young}} \sum_{i_{young}} b_i t_i \tag{2.7}$$

$$t_{old} = \frac{1}{b_{old}} \sum_{i_{old}} b_i t_i. \tag{2.8}$$

The choice of 1.6 Gyr for the definition of the young population is motivated by galaxy chemical evolution models which show only small changes (≤ 0.1 dex) of metallicity during the final 1 to 2 Gyrs of evolution (Spitoni et al., 2017a,b; Kudritzki et al., 2021a,b). Moreover, the molecular gas depletion time which defines star formation efficiency, is of the same order (1.9 Gyr, see Leroy et al. 2008). They young and old population fitting is insensitive to the selected value, for instance, chosing 2.5 instead of 1.6 Gyr does not change the results.
We note that due to the normalization of our spectra between 4400 and 4450 Å the [Z] and t-values obtained in this way are effectively B-band luminosity weighted metallicities and ages. This will become more evident further below.
The results for metallicities, ages, reddening and extinction obtained in this way will be discussed in the next sections.

2.3 The Effects of Star Formation Burst Length on SSB spectra

Most commonly, the spectra of star bursts are calculated by adopting the approximation of so-called 'instantaneous bursts', for which the stellar evolution isochrone at one singular time step is used. However, as is well known, star formation in star forming regions is not instantaneous but happens over finite time scales. For instance, as shown by Efremov & Elmegreen (1998), the star formation time t_b of a burst is correlated with the size of the star forming region and can cover a wide range from 0.1 to 10 Myr in regions where associations and star clusters form. More recent work on star formation in molecular clouds confirmed burst lengths of a few million years (Corbelli et al., 2017; Kim et al., 2021). It is, thus, important to investigate what influence t_b can have on the burst model spectra and the resulting analysis.

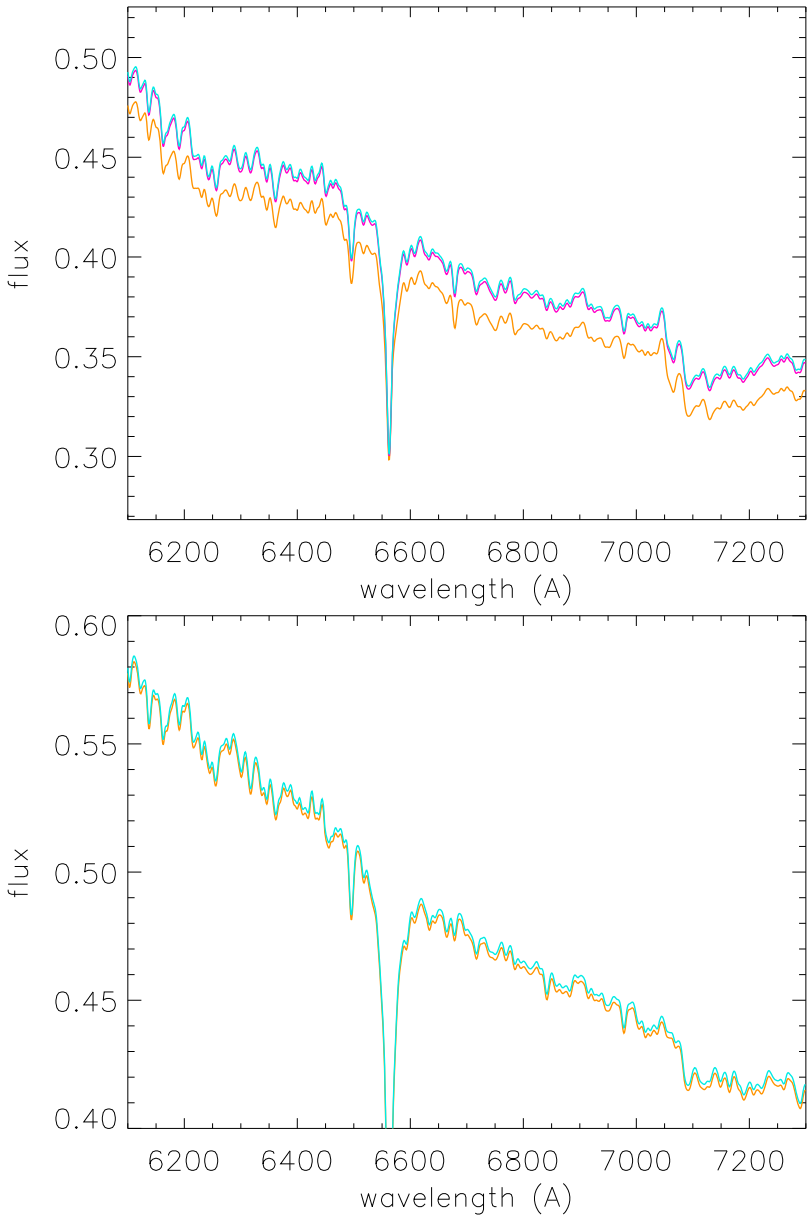

Figure 2.6: Same as Figure 2.5 but with a different wavelength range for ages of 45 Myr (top) and 501 Myr (bottom).

If $L_{iso}(\lambda, \tau)$ is the total luminosity per Angstroem at wavelength λ of an isochrone of age τ, then the luminosity L(λ,t,t_0,t_b) of a burst at time t, which started at t_0 is

$$L(\lambda, t, t_0, t_b) = \frac{1}{(t - t_0)} \int_{t_0}^{t} L_{iso}(\lambda, \tau) d\tau, \tag{2.9}$$

for $t_0 \leq t \leq t_b + t_0$ and

$$L(\lambda, t, t_0, t_b) = \frac{1}{t_b} \int_{t-t_0}^{t} L_{iso}(\lambda, \tau) d\tau \tag{2.10}$$

for $t \geq t_b + t_0$.

We adopted constant star formation rate during the burst and L(λ,t,t_0,t_b) is the luminosity averaged over the duration of the burst. Figures 2.3 and 2.4 show the effects of burst duration on the luminosities of SSBs as a function of age in different spectral bands. They are quite dramatic around the peak at ages of 5-10 Myrs (up to 0.3 dex) and then become weaker but continue to be noticeable ($\geq$ 0.005 dex) compared with the S/N of the spectra until values of $t_b/t \approx 0.02$ are reached (see Figures 2.3 bottom). This is a consequence of the power law behaviour $L_{iso}(X,t) \propto t^{-n}$ for larger values of t which leads to $L(X,t,t_0,t_b) = L_{iso}(X,t)(1+nt_b/(2t))$ for small values of t_b/t. X stands for the spectral passband (U, V, B, R, I). In the same way the spectra of SSBs show the effects of burst length. Examples are given in figures 2.5 and 2.6. The differences between the spectra of different burst length become small at ages much larger than the burst length as discussed above. We note that all luminosities are given in units of the solar luminosity $L_\odot$.
The influence of the adopted burst lengths on the analysis of the observed spectra will be investigated in the next section.

2.4 Analysis with Different Burst Lengths and Time Resolution

In this section we use SSBs calculated for different burst lengths and time resolution to analyse our stacked SDSS spectra. We note that we allow for variations of R_V in our spectral fits. As will be discussed in section 5, the R_V obtained are substantially higher than 3.1 (see Figure 2.13).
Figures 2.7 and 2.8 summarize the results with respect to the MZR. We show metallicities of the young and old population and average metallicities as a function of stellar mass obtained when using the different sets of SSBs and compare with with the MZR of massive supergiant stars, which has been obtained by quantitative spectroscopy of individual objects in 17 nearby galaxies (see Bresolin et al. 2022 and references therein). These metallicities are accurate to 0.1 dex and serve as a benchmark for the young stellar population. The metallicity uncertainties of the SDSS spectral fits as shown in Figures 2.7 and 2.8 are up

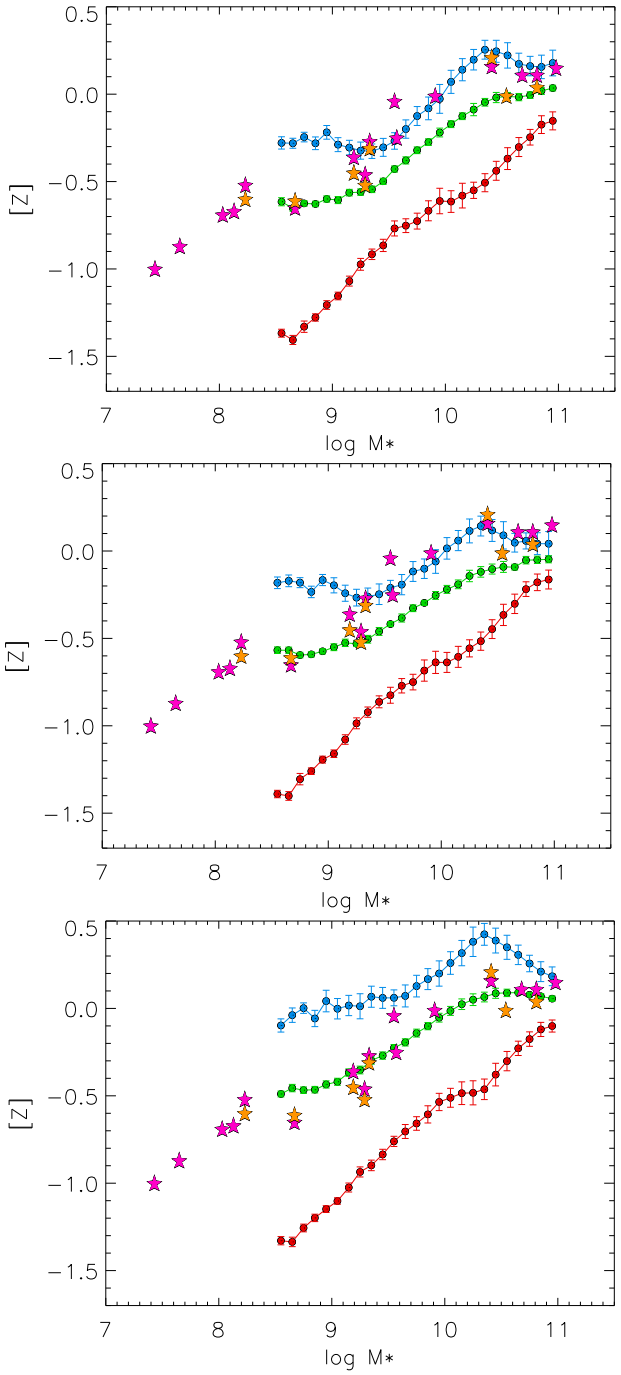

Figure 2.7: Analysis of SDSS star forming galaxies. Metallicities of the young (blue) and old (red) stellar population and average metallicities (green). The grid of SSB with high time resolution was used. Top: 0.1 Myr burst length, middle: 1 Myr Myr, bottom: 10 Myr. The MZR of blue and red supergiant stars (pink and orange stars) obtained from the analysis of individual stars in 17 galaxies is also shown as a benchmark for the young stellar population.

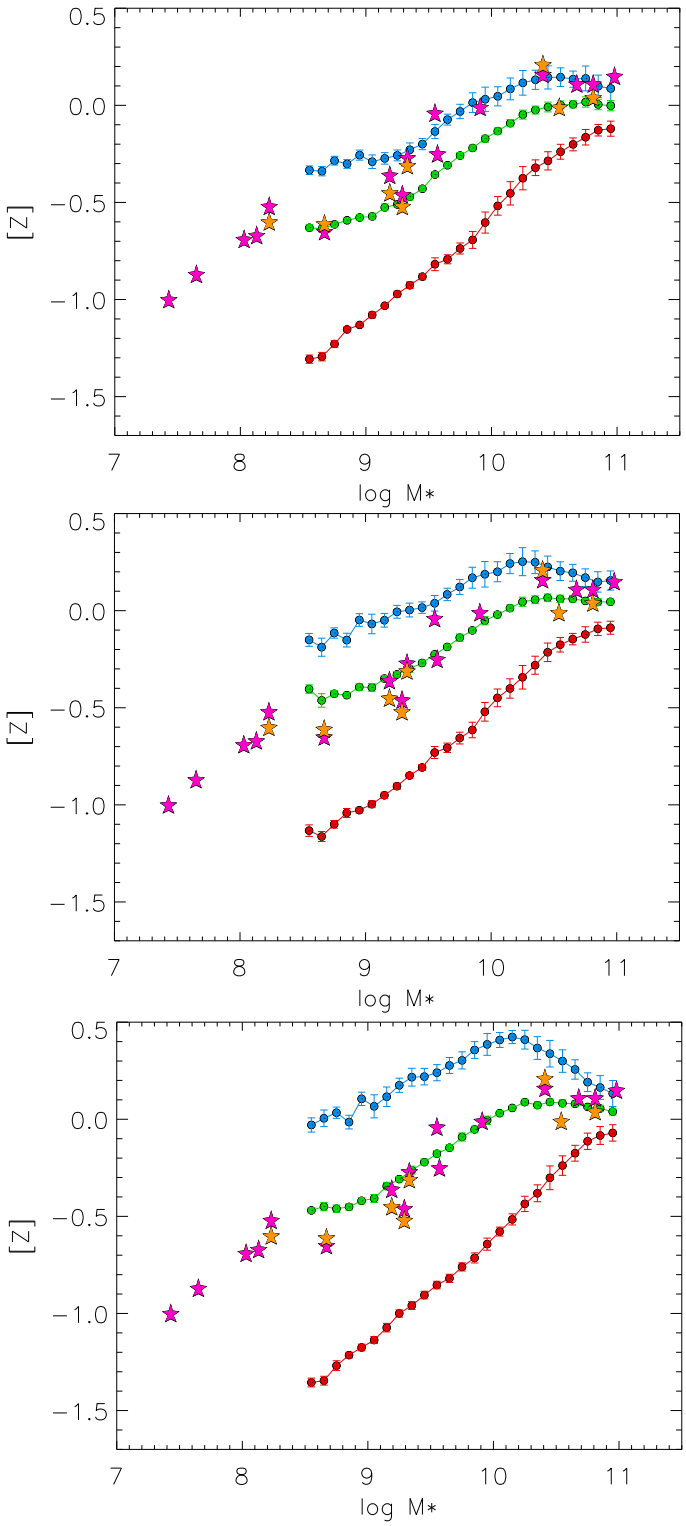

Figure 2.8: Same as Figure 2.7 but for the SSB grid with low time resolution.

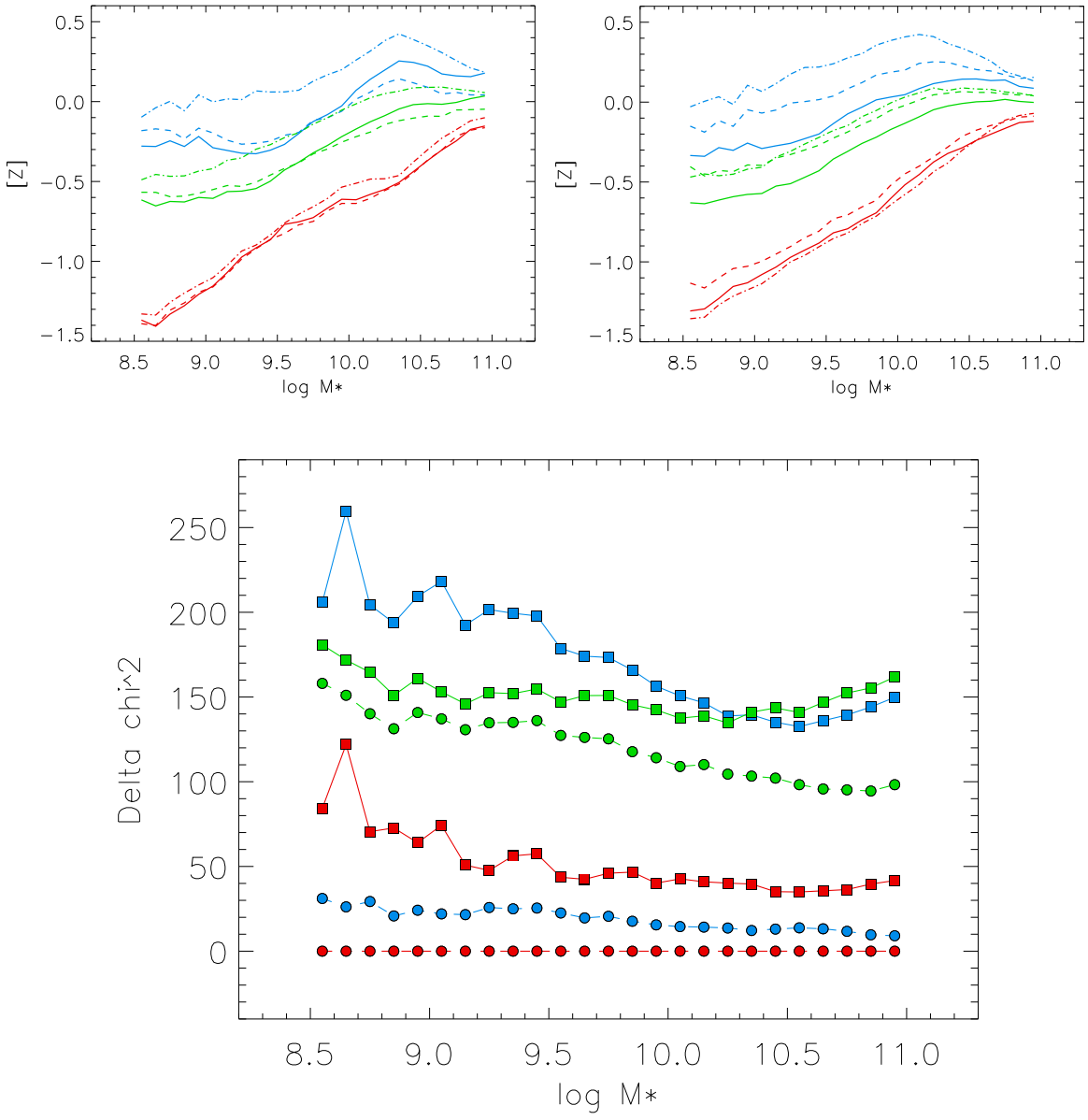

Figure 2.9: Top left: SDSS fit metallicities of Figure 2.7 (high time resolution) with all burst lengths overplotted (0.1 Myr: solid, 1 Myr: dashed, 10 Myr: dashed dotted). Top right: same as top but with metallicities of Figure 2.8 (low time resolution). Bottom: Assessement of the quality of the fits obtained with the different sets of SSB. Difference $\Delta\chi^2 = \chi^2_{min} - \chi^2_{min,0}$ for the different SSB spectral model fits as a function of galaxy stellar mass. $\chi^2_{min,0}$ is the value obtained with SSBs calculated with high time resolution and $t_b = 0.1$ Myr. Circles correspond to SSB with high time resolution, squares to low resolution, red color to 0.1 Myr bursts, blue color to 1.0 Myr and green to 10 Myr.

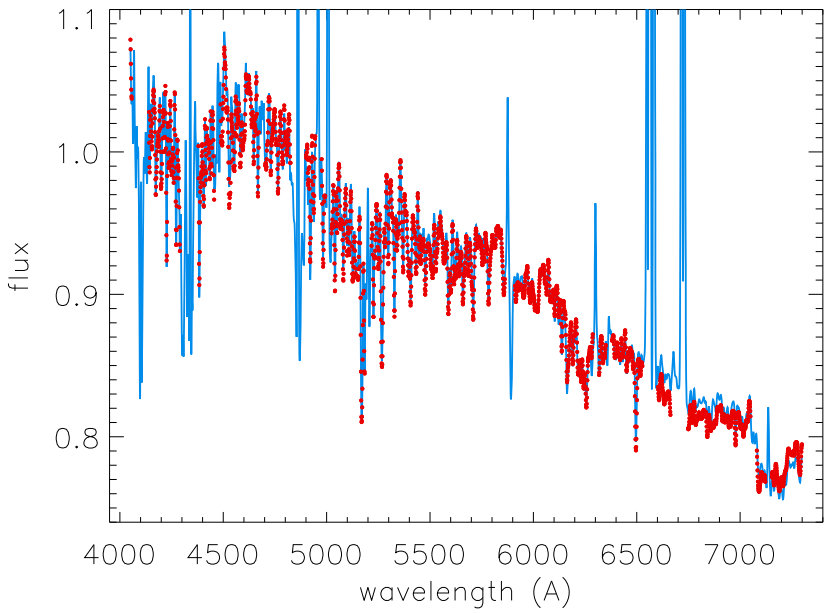

Figure 2.10: SSB spectral fit (red dots) of the observed spectrum (blue) for log $M_* = 9.75$. Note that for the fit we mask out regions contaminated by ISM emission or absorption lines. The fit spectrum is calculated with a burst length $t_b = 0.1$ Myr and high time resolution.

to 0.07 dex for the young and old population, respectively, and 0.03 dex for the average over all ages. They are obtained from Monte Carlo simulations with fits of the observed stacked spectra modified by adding Gaussian noise.

Figures 2.7 and 2.8 indicate that burst length and SSB time resolution have a significant effect of up to 0.4 dex on the determination $[Z]_{young}$, the metallicity of the young stellar population. The influence on the average metallicity [Z] is somewhat smaller (up to 0.2 dex) and the differences for the old population are below or about 0.1 dex and, thus, of the order of the fit uncertainties. A comparison of all metallicities obtained with different burst lengths is given in Figure 2.9.

The goodness of the fits is assessed in Figure 2.9 where we compare the χ^2-values obtained with the different sets of SSB for the fit of the observed SDSS spectra. (We note that number of wavelength points used for the calculation of χ^2 is $n_{pix} = 2523$). Figure 2.9 shows that the SSB models with the shortest burst length of 0.1 Myr and high time resolution provide the best fit, although the high time resolution fits with 1 Myr burst length come close. It is reassuring that for these two cases the SDSS young stellar population metallicities are in very good agreement with the metallicities of our supergiant benchmark sample (see Figure 2.7) . We take this as an indication that the population synthesis method is reliable.

Figure 2.10 shows the fit of the SDSS spectrum at log $M_* = 9.75$ as a typical example.

The metallicities obtained for the old stellar population $[Z]_{old}$ are significantly lower than $[Z]_{young}$. This reflects galactic chemical evolution and will be discussed below.

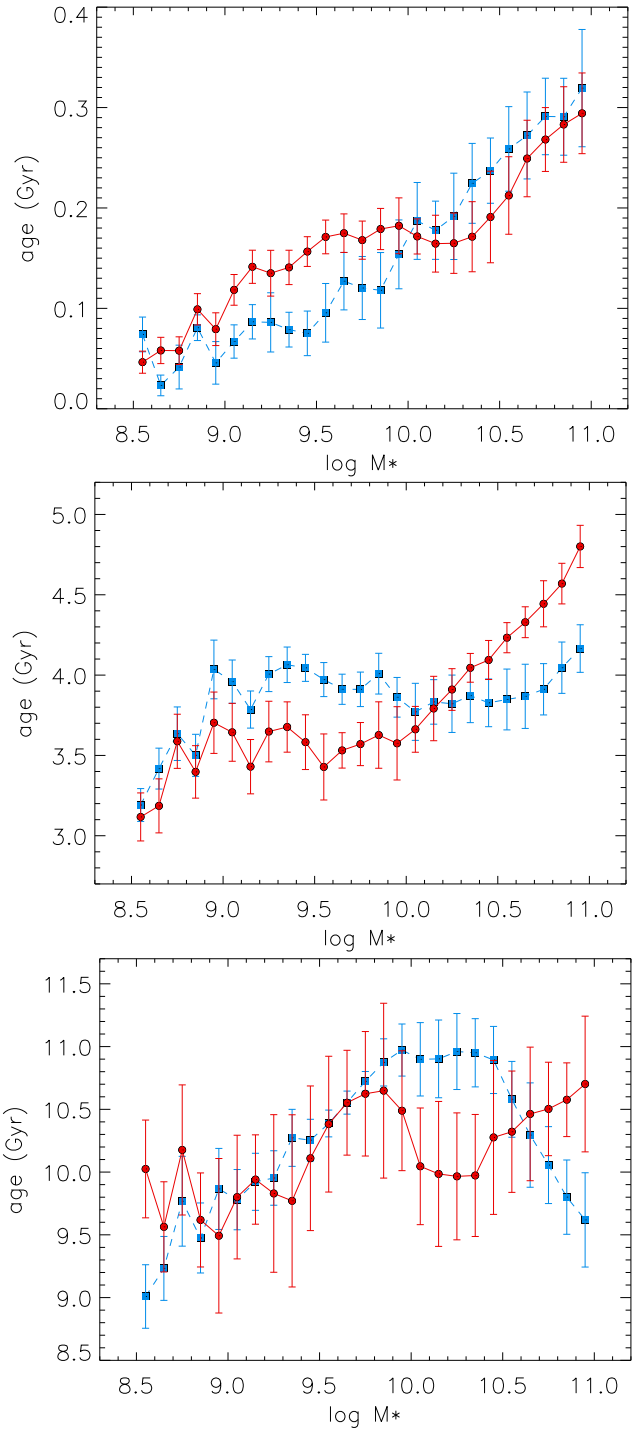

Figure 2.11: Ages t_{young} (top), t_{av} (middle) and t_{old} (bottom) as defined by equations (2.3), (2.7) and (2.8) as a function of galactic stellar mass obtained with spectral fits suing high time resolution and a burst length $t_b = 0.1$ Myr. Red values obtained with R_V fitted. Blue values with $R_V = 3.1$.

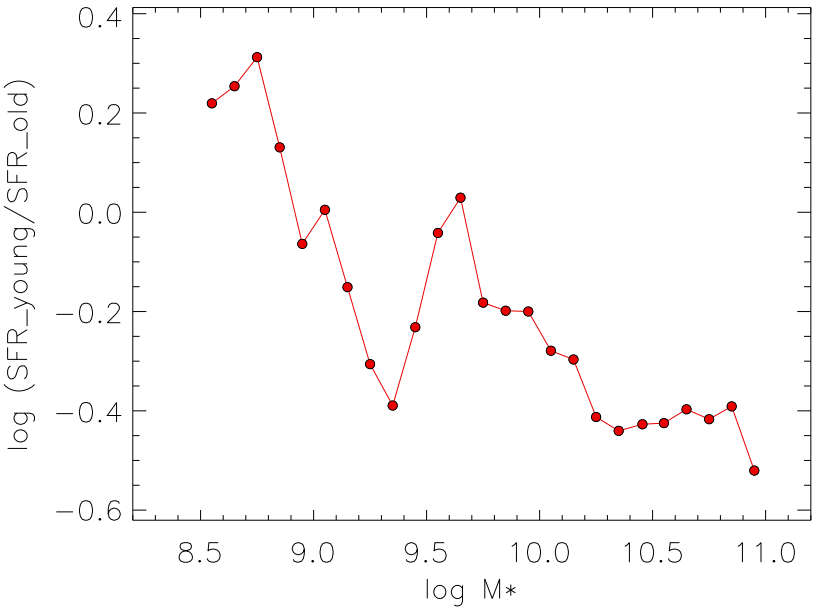

Figure 2.12: The ratio of star formation of young to the old stellar population as a function of galactic stellar mass. The fit of the observed spectra was carried out with $t_b = 0.1$ Myr and high time resolution.

We note that Zahid et al. (2017) in their work have used SSB with 10 Myr burst length and compared their average metallicities [Z] with the supergiant values finding good agreement. We confirm their result (see Figure 2.8), but we note that this comparison is misleading. Since supergiants have ages around 50 Myr, a comparison with $[Z]_{young}$ would have been more appropriate.

The average stellar ages t_{av} and the ages of the young and old population obtained with SSB of $t_b = 0.1$ Myr and the high age resolution grid are displayed in Figure 2.11 together with their error bars. The ages between 50 and 300 Myr of the young population confirm that a comparison with supergiant stars as a benchmark is appropriate. We notice a clear correlation of t_{young} with galactic stellar mass. No correlation is obtained for t_{av} and the age t_{old} of the old population.

The average redshift of our galaxy sample is z=0.08 corresponding to a cosmological look-back time of 1.05 Gyr (assuming a Hubble constant H_0=70.4 km s^{-1} Mpc^{-1} and a flat universe with Ω_Λ=0.728 and Ω_m=1-Ω_Λ). With $t_{old} \approx 10$ Gyr we then know that the stars of the old population have been formed on average at a lookback time of 11 Gyr equivalent to a redshift of $z \approx 2.5$. Thus, the metallicities obtained for the old stellar population in Figure 2.7 and 2.8 correspond to $z \approx 2.5$.

The fit of the observed spectrum yields the coefficients b_i in eq. (1) for the individual bursts, which can be related to the relative number contribution N_i of stars of isochrone i, for which the SSB model spectrum is calculated, via

$$b_i = N_i L_i(X). \tag{2.11}$$

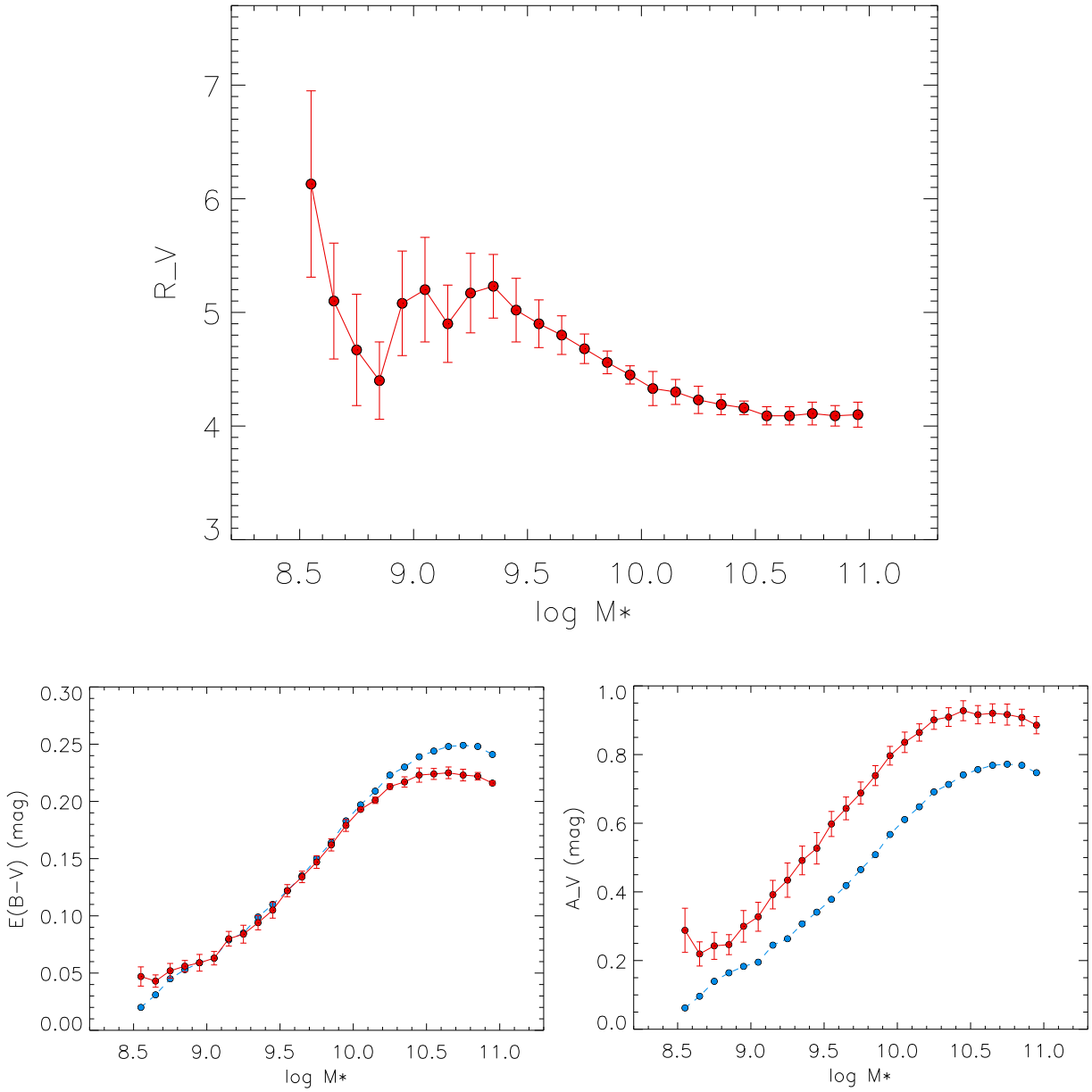

Figure 2.13: Top: The ratio of V-band extinction to reddening R_V as a function of stellar mass log M_*. Bottom left: Reddening E(B-V) as a function of stellar mass. Red: values obtained with R_V as a free parameter and determined as in the top figure. Blue: values obtained with $R_V = 3.1$. Bottom right: Interstellar V-band extinction A_V. Red and blue as in the middle figure. $t_b = 0.1$ Myr and high age resolution were used for the spectral fit.

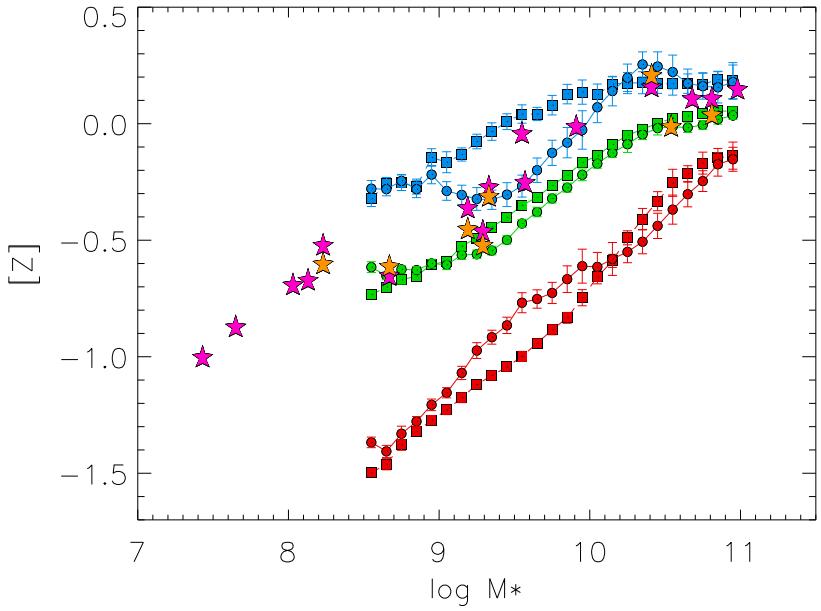

Figure 2.14: Same MZR as in Figure 2.7 (t_b = 0.1 Myr, high age resolution) but with the results of spectral fits with $R_V = 3.1$ additionally shown as squares.

$L_i(X)$ is the luminosity of the isochrone in passband X with an effective wavelength which corresponds to the wavelength at which the observed spectra and the SSB spectra are normalized. Since our normalization interval is 4400 to 4450 Å the B-band is the appropriate choice for X (examples for $L_i(X)$ as a function of isochrone age are given in Figures 2.3 and 2.4). Eq. (2.11) explains why the metallicities and ages of our spectral fits are B-band luminosity weighted quantities.
Since $N_i \propto \psi_i \Delta t_i$, where Δt_i is the time interval between isochrone i and the next older isochrone in our SSB grid, Eq. (2.11) can be used to estimate star formation rates ψ for the young and old population

$$\psi_{young} \propto \sum_{i_{young}} \frac{b_i}{\Delta t_i L_i}; \psi_{old} \propto \sum_{i_{old}} \frac{b_i}{\Delta t_i L_i}. \tag{2.12}$$

Figure 2.12 shows the ratio of star formation of the young to the old population as a function of galaxy stellar mass. We see the obvious trend that low mass galaxies are presently more active than high mass galaxies.

2.5 Reddening and the Effects of the Extinction Law

Since a long time there have been clear indications of deviations from the standard value $R_V = 3.1$ in star forming regions of the Milky Way (see, for example, Feinstein et al. 1973; Herbst 1976; The et al. 1980; Cardelli et al. 1989). Similar results have been found for

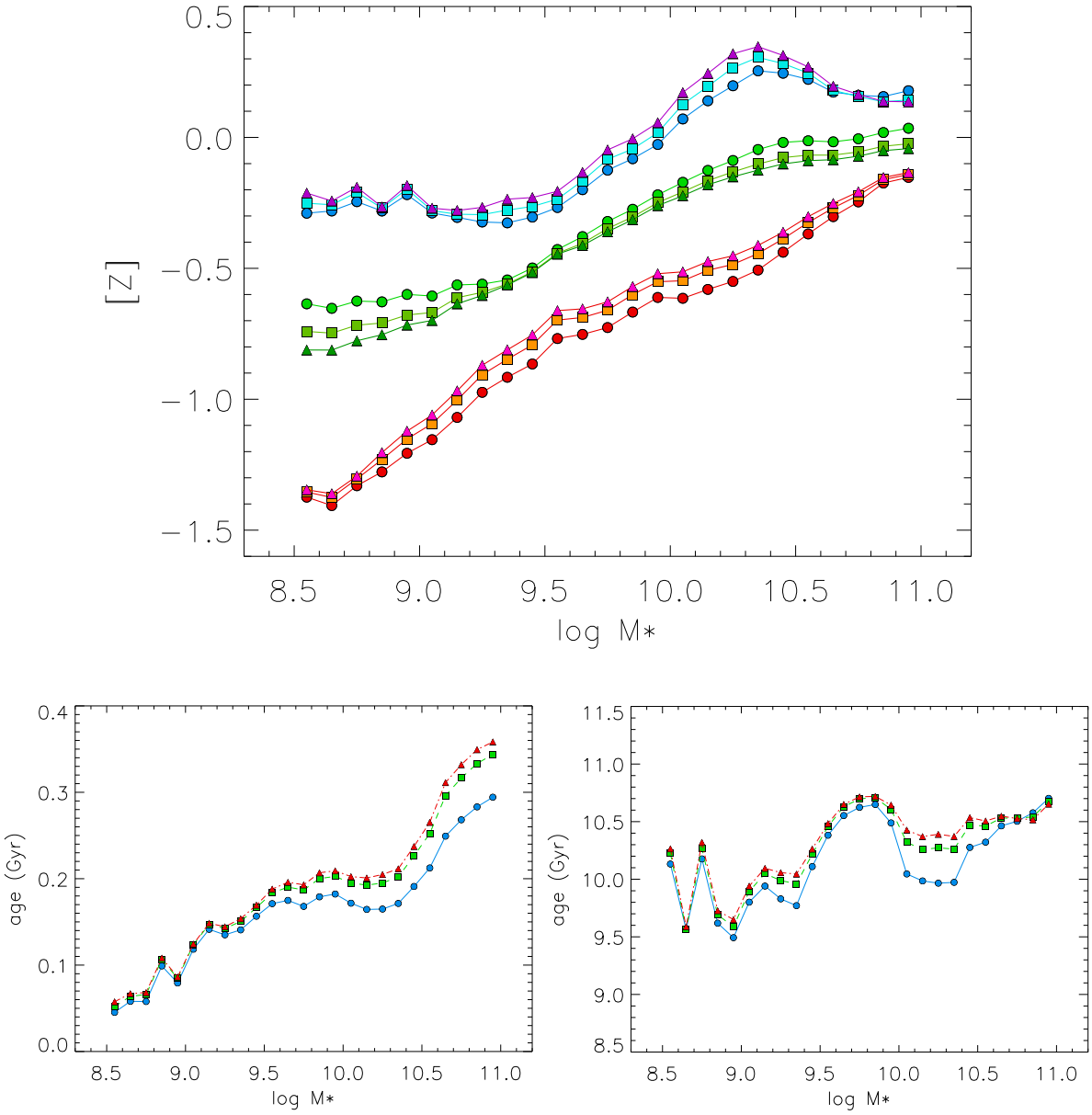

Figure 2.15: Top : Metallicities obtained with different normalization, where violet, cyan and blue belong to the young population, pink, orange and red to the old population and green colors show the average metallicities. Circles correspond to B-band normalization, squares to V-band, and triangles to R-band. Bottom left: Ages of the young population. Blue color: B-band normalization, green color: V-Band, red color: R-band. Bottom right: Same as the middle plot, but for the old population. Again $t_b = 0.1$ Myr and high age resolution were used for the spectra fit.

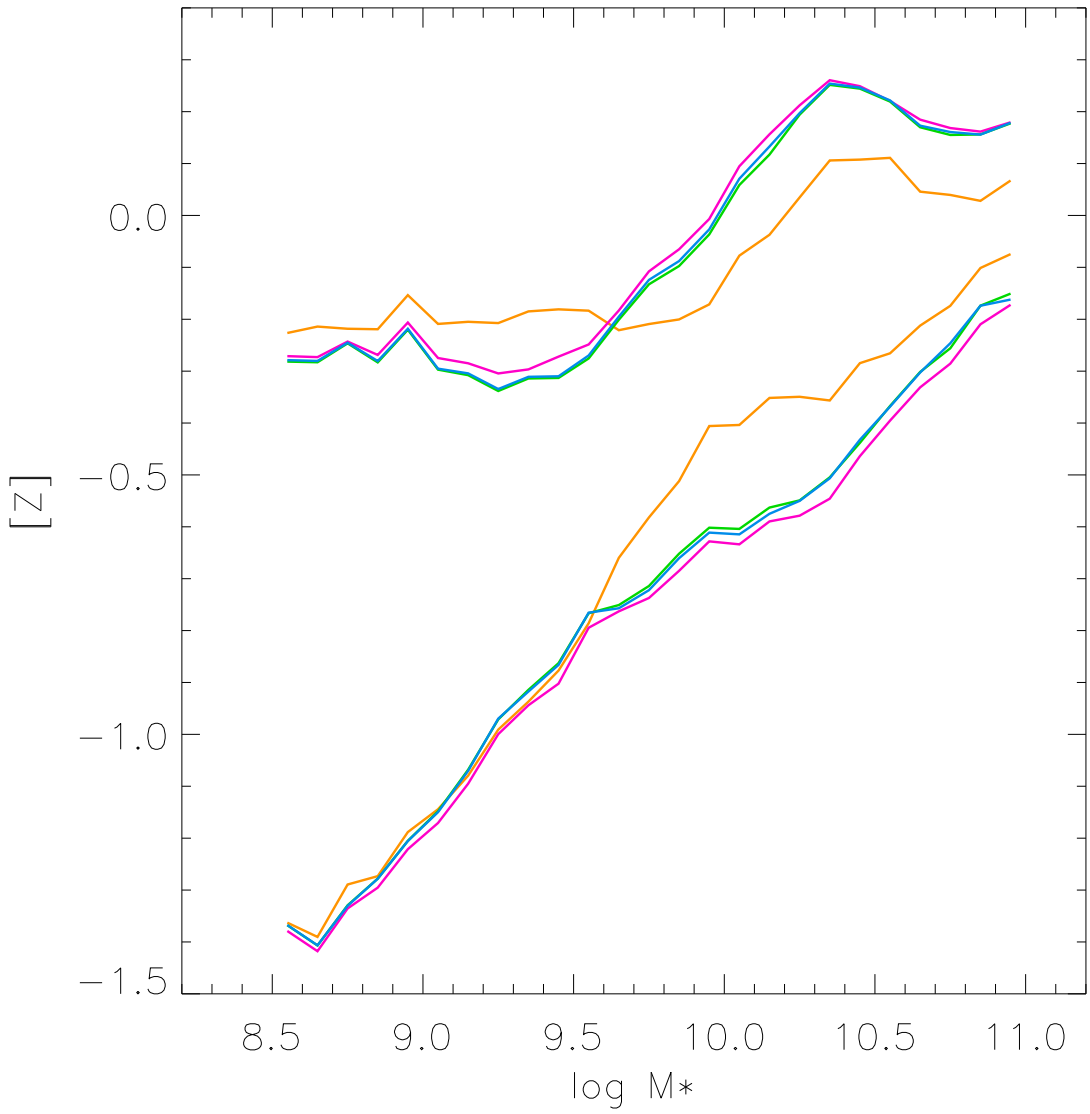

Figure 2.16: MZRs obtained by analysis with model spectra assuming different IMFs. Curves the in upper part of the figure correspond to the young population, curves in the lower part to the old population. Blue: Chabrier (2003), pink: Kroupa (2001), green: van Dokkum (2008), orange: Salpeter (1955).

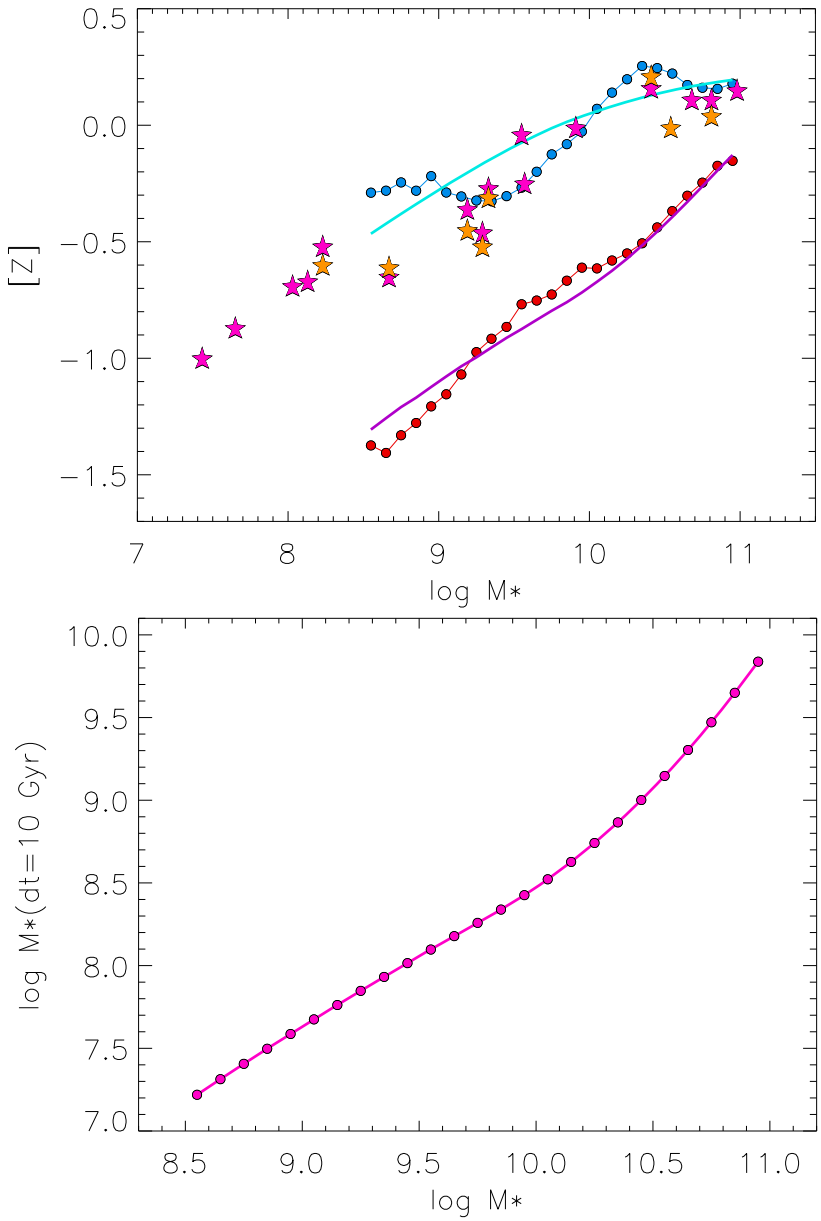

Figure 2.17: The chemical evolution of star forming SDSS galaxies. Top: Metallicities of the young and old stellar population (as in Figure 2.7 top) and of supergiant stars compared with B-band luminosity weighted metallicities predicted by galaxy evolution models (Kudritzki et al., 2021a,b) for very young stars (cyan) and stars 10 Gyr older (violet). Bottom: Mass of the galaxy evolution models at lookback time Δt = 10 Gyr as a function of galaxy final stellar mass.

the Large Magellanic Cloud, see Maíz Apellániz et al. (2017), Urbaneja et al. (2017) and Holwerda & Keel (2013) in their differential IFU SED study of two galaxy pairs conclude that the canonical extinction law with $R_V = 3.1$ does not fit their data. In consequence, it is important to keep R_V as free parameter for the SSB fits of the observed spectra as described in section 2.

Figure 2.13 (top) shows the R_V values obtained in our analysis for the case of $t_b = 0.1$ Myr and high age resolution. While the values at lower stellar masses have large uncertainties, we generally find values larger than 3.1 at all stellar masses. We believe the reason is that the SDSS observations sample the central regions of the star forming galaxies where still a lot of star formation in dense clouds is going on. These natal birthclouds act as an additional source of attenuation. In consequence, the contribution of the diffuse ISM with $R_V = 3.1$ is small. We speculate that the reason for the obvious correlation with stellar mass is that the young stellar population is younger at lower mass (see Figure 2.11) and that the density in the star forming regions is higher. The influence of varying density has been described by Witt & Gordon in a series of seminal papers (Witt & Gordon, 1996; Gordon et al., 1997; Witt & Gordon, 2000). As a rule of thumb, an increasing inhomogeneity with alternating high- and low-density regions in the ISM structure leads to flattened ('grayer') attenuation curves. In our case, using a CCM/O'Donnell extinction law, a shallower slope is equivalent to high values of R_V. See also Berlind et al. (1997) for an in depth discussion of this issue in case of the galaxy NGC 2207.

We note that the average value found for the LMC ($\log M_* = 9.2$) by Urbaneja et al. (2017), $R_V = 4.6$, is in good agreement with Figure 2.13. It is important to note that the difference from the standard reddening law in star forming galaxies at all masses has important consequences for other aspects of astrophysics. For instance, the estimate of galaxy luminosities and the corresponding mass to light ratios can be affected. Distance determinations based on stellar distance indicators and the resulting cosmological distance ladder might be influenced as well (see, for instance, Urbaneja et al. 2017; Falco et al. 1999).

Reddening E(B-V) and V-band extinction A_V are also shown in Figure 2.13 (middle and bottom, respectively). Again, there is a clear correlation with stellar mass. Such correlations have already been found in previous work (Brinchmann et al., 2004; Asari et al., 2007; Garn & Best, 2010; Zahid et al., 2013). We note, however, that the deviation of R_V from the standard value 3.1 leads to significantly higher extinction of about 0.2 magnitudes.

Ignoring a potential variation of R_V and restricting to values of 3.1 also affects the determination of metallicities and the MZR. This is demonstrated in Figure 2.14, where results obtained with $R_V = 3.1$ are over-plotted. With differences up to 0.4 dex the effects are significant for the young and old population, most importantly in the middle mass range.

The determination of ages t_{young}, t_{old}, and t_{av} is also affected, if a fixed value $R_V = 3.1$ is adopted (see Figure 2.11). The differences can be as large 50% and 10% for the young and population, respectively, and 15% for the average stellar age.

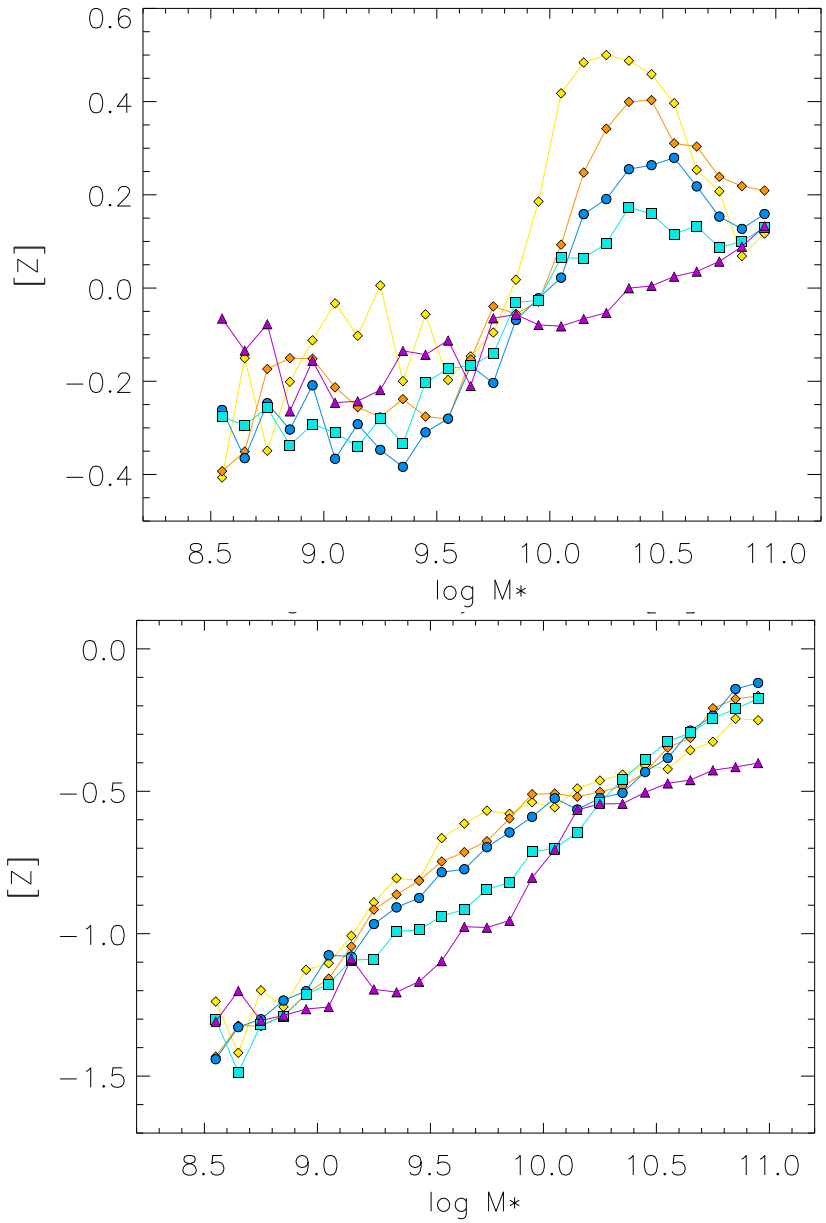

Figure 2.18: Metallicities of star forming SDSS galaxies stacked in quintiles of star formation rates at each stellar mass. Yellow, orange, blue, cyan, violet colors correspond to the different quintiles from lowest to highest SFR. Top: MZR of the young population, bottom: old population.

2.6 Spectral Normalization

The metallicities and ages obtained in the previous sections are B-band luminosity averages because we have normalized our spectra by setting the mean flux between 4400 and 4450 Å to unity. This is illustrated by eq. (11). It is, therefore, important to investigate how metallicities and ages change depending on the wavelength interval selected for normalization. For that purpose we have repeated the analysis with normalizations between 5500 and 5550 Å (V-band) and 6950 and 7000 Å (R-band). The comparison of the metallicities and ages obtained with the different normalizations are shown in Figure 2.15.
The differences between the different normalizations are small. The metallicities of the young and old population increase gradually with the normalization shifted towards the red, but the maximum difference is ~ 0.1 dex only slightly larger than the metallicity uncertainties discussed in section 2.4. Ages also increase by a small amount but the differences are comparable to the errors shown in Figure 2.16.
We note that R_V, E(B-V), A_V and the star formation histories (as displayed in Figure 2.12) remain unchanged and do not depend on the spectral normalization interval.

2.7 Initial Mass Function and Pre-Main Sequence Evolution

For our calculation of SSB model spectra we have adopted a Chabrier (2003) initial mass function (IMF). As discussed by Conroy et al. (2009), there are viable alternatives such as the IMFs by Kroupa (2001) and van Dokkum (2008). In order to investigate the influence of the choice of the IMF on our analysis we have additionally calculated model spectra with these two alternatives and then repeated the analysis. The resulting MZRs are shown in Figure 2.16 for high time resolution and $t_b = 0.1$ Myr. While the differences in metallicity arising from the choices of the different IMFs are noticeable, they are at most 0.05 dex and, thus, not a major source of systematic uncertainties. We have also included calculations with the original IMF suggested by Salpeter (1955), which is a simple power law without a modification at the low mass end. Here the differences are larger, 0.1 dex for the young and up to 0.2 dex for the old stellar population, respectively. Figure 2.16 confirms the results found in previous work (Cid Fernandes et al., 2005; Wilkinson et al., 2017).
The MESA stellar isochrones used in the calculation of our spectra include pre-main sequence evolution towards the zero-age mains sequence (ZAMS). As a consequence, young isochrones for which the more massive stars are leaving the main sequence have a contribution from stars with lower mass, which are still moving towards the main sequence and have luminosities significantly higher than the ZAMS at the same stellar mass (see Choi et al. 2016 and Dotter 2016). Because of the IMF these lower mass pre-main sequence objects could, thus, influence the integrated isochrone spectra and lead to differences when compared with isochrones just starting at the ZAMS. Since such isochrones have also been used in population synthesis diagnostic work, we have carried out an additional test with modified MESA isochrones, which start at the ZAMS. As it turns out, the MZRs obtained

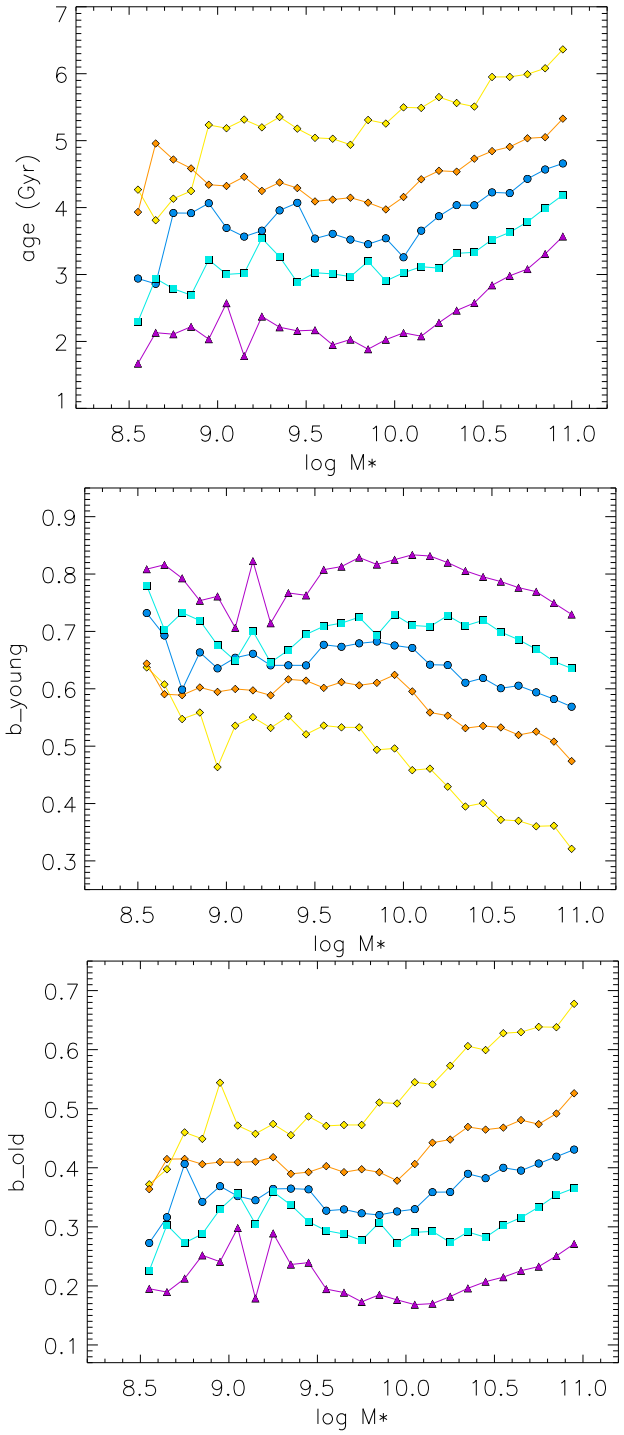

Figure 2.19: Top: average age t_{av} (top figure) of the stellar population as a function of stellar mass in different bins of star formation rate. Middle and bottom: weight contributions of the young and old population b_{young} and b_{old}. The color code is the same as in Figure 2.18.

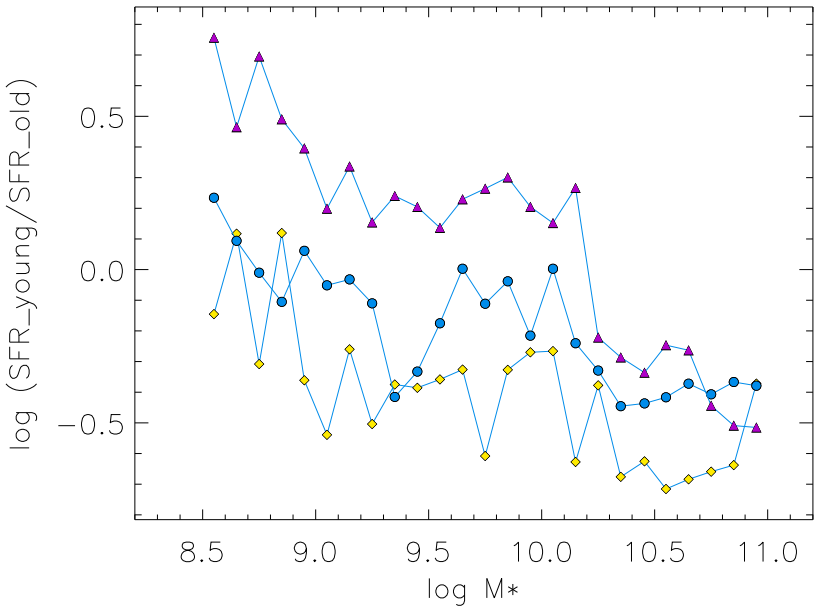

Figure 2.20: The ratio of star formation rate of young to the old stellar population as a function of stellar mass for the galaxies in different bins of star formation rate. The color code is the same as in Figure 2.18 but only three bins are shown for the sake of clarity.

with model spectra calculated in this way are very similar to the ones where pre-main sequence evolution is included. The reason is the high luminosity of the more massive star on the main sequence or moving away, which have a dominating influence on the total spectrum. The inclusion of the pre-main sequence phase is obviously of minor importance for the results of our spectral diagnostics.

2.8 A Comparison with Lookback Galaxy Evolution Models

Figure 2.7 and 2.8 indicate a strong evolution of stellar metallicities as a function of age. The metallicities of the old population which is about 10 Gyr older are significantly lower and the difference is anti-correlated with galaxy stellar mass. This can be understood with the help of galaxy evolution models using the standard framework of chemical evolution. Kudritzki et al. (2021a,b) have introduced 'lookback' models where the competing processes of gas infall from the cosmic web and the circumgalactic medium, galactic winds and star formation are assumed to lead to a redshift dependent power law relationship between galactic gas mass and stellar mass, $M_g = A(z)M_*^{\beta}$ and stars are formed along the observed star formation main sequences with star formation rates $\psi = \psi_0(z)M^{\delta}$. With these assumptions and the usual chemical evolution equation metallicity [Z] becomes a simple analytical function of the ratio of stellar to gas mass M_*/M_g and decreases when this

ratio becomes smaller. This is very similar to the classical closed box model of chemical evolution (Searle & Sargent, 1972) but quantitatively the result is substantially different because of the power law dependence between gas and stellar mass.
Figure 2.17 (top) shows the metallicities of the lookback evolution model for each galaxy with different stellar mass for the young stars and stars 10 Gyr older overplotted to the result of our SDSS spectral analysis and the individual supergiants stars in galaxies. We note that these metallicities are luminosity weighted in the B-band. Details of the model are described in Kudritzki et al. (2021a,b). We note that $\beta = 0.5$ is adopted and ψ_0(z) has been increased by a factor of three to be in better agreement with the star formation rates of the SDSS galaxies at redshift z=0.08. The relative redshift dependence ψ(z) remains the same.
The agreement of the lookback models with the observations is good. The model reproduces the shape of the young stellar population MZR well and also the difference of the metallicities between the young stars and the old stars. We note that the galaxy stellar masses at lookback time Δt = 10 Gyr are significantly smaller than the final stellar masses. This is shown in the bottom part of Figure 2.17. The difference in stellar mass together with dependence of metallicity on M_*/M_g is the reason why the decline of the metallicity of the old population with decreasing stellar mass is steeper than for the younger population. Because of this mass difference the red curve in Figure 2.17 (top) does not represent a mass metallicity relationship at high redshift (z $\approx$ 2.5), but instead, describes the chemical evolution of these galaxies.

2.9 Star Formation Rate Dependence of Metallicity and Ages

From the study of HII region emission lines it has been found that MZRs contain a dependence on star formation rates as a third parameter (Mannucci et al., 2010; Yates et al., 2012; Sanders et al., 2021). Galaxies with higher star formation rates tend to have lower metallicities. Our analysis of stellar spectra provides the opportunity to investigate this effect with respect to stellar populations. For that purpose we follow the approach by Zahid et al. (2017) and divide the sample of our 200,000 SDSS spectra in quintiles of star formation rate. We then stack the spectra of these quintiles at each stellar mass and run our analysis on the stacked spectra of the quintiles. Since the spectra in the highest SFR quintile show strong HII emission lines for the lowest galaxy stellar masses, we include the effects of nebular continuum emission in our analysis as described in section 2. We use SSB with high age resolution and a short burst length t_b = 0.1 Myr for the analysis.
The resulting MZRs for the young and old population are given in Figure 2.18. We see a clear correlation with SFR for both the young population at high masses and the old population at intermediate masses. The metallicity errors are of the same order as shown in Figure 2.7 and described in section 2.4.
We have also determined population ages t_{young}, t_{old}, and t_{av}. While t_{young} and t_{old} seem

independent of star formation rate, the average age of the total population t_{av} as shown in Figure 2.19 reveals a very clear dependence. The average population in galaxies with a lower star formation rate is significantly older. Obviously, at the lower star formation rates it takes the galaxies much longer to build up their stellar population. In consequence, the contribution by the old stellar population b_{old} to the spectral fit is much higher, as is also shown in Figure 2.19. (Note that $t_{av} = b_{young}t_{young} + b_{old}t_{old}$ and that the second term dominates).
The stronger contribution of the older population is also reflected in the star formation history expressed by the ratio $\psi_{young}/\ \psi_{old}$ of star formation rates of the young to the old population. As Figure 2.20 demonstrates, this ratio is significantly smaller for galaxies with presently lower star formation rates.

2.10 Summary and Conclusions

In this section we summarize and discuss the major results of this work. In a first step we have investigated the influence of star formation burst lengths t_b on the results of the population synthesis analysis. As observations show (see section 3), t_b depends on the size of the star forming region and can range from a fraction of a Myr to many Myr. We find that the assumption of burst length influences the spectra of stellar isochrones significantly depending, of course, on isochrone age t and t_b. For ages t with $t_b/t \leq 0.02$ the signatures of burst length are clearly visible in the spectra. This affects the results of the population synthesis analysis, in particular, the metallicities of the young stellar population. Judging the quality of the spectral fits by means of their minimum χ^2 value we find that burst spectra calculated with $t_b = 0.1$ and 1.0 Myr give the best fit. Fits with 10 Myr bursts are worse.
Since we model the spectrum of the integrated stellar population as a sequence of bursts with different ages, the time resolution of this sequence is important. We have, therefore, tested the influence of the time resolution using two grids with different resolution of isochrone age steps. We find that the higher time resolution leads to lower χ^2 values of the spectral fits.

The analysis of the galaxy spectra with respect to metallicity and age requires a determination of interstellar reddening and extinction. Since it is well know that in the star forming regions of galaxies reddening laws deviate from the standard law of the diffuse ISM characterized by the $R_V = 3.1$, we determine R_V as an independent additional parameter. We find values clearly larger than 3.1 indicating a strong contribution of dense star forming regions to the reddening. The R_V values are largest for low mass galaxies. For these galaxies the average age of the young population is lowest. In consequence, the contribution by stars originating from compact regions of star formation might be strongest. Allowing for deviations of R_V from 3.1 has a significant influence on the determination of metallicity (up to 0.4 dex), population ages (10 to 50% and, of course, interstellar extinction (0.2 magnitudes). We note that this striking general difference from the standard reddening

law in star forming galaxies has important consequences for other aspects of astrophysics such as, for instance, distance determinations and the cosmological distance ladder or the estimate of galaxy luminosities.

The metallicity of the young population of our star forming SDSS galaxies is in good agreement with massive supergiant stars where the metallicities are obtained through accurate spectral analysis of a large sample of galaxies in the local universe. We take this as a crucial confirmation that our population synthesis analysis technique is reliable. The average age we derive for the young population is between 50 and 300 Myrs increasing with galactic stellar mass. It is, thus, in the same range as the supergiant ages and, consequently, we expect the metallicities to be similar.

We also determine the average metallicities and ages of the old population. The metallicities are significantly smaller than for the young population. The age difference to the young population is about 10 Gyr. Thus, we are seeing the results of chemical evolution over 10 Gyr. We compare these results with galaxy evolution look back models and find good agreement. Both, the mass-metallicity relationship of the young population and the metallicities of the old population are well reproduced. This supports a galaxy evolution model where metallicity depends on the ratio of gas mass to stellar mass and where this ratio decreases with time.

For this comparison we calculated B-band luminosity weighted metallicities of our models because our observed and model spectra are normalized to unity between 4400 to 4450 Å and our analysis effectively provides B-band luminosity weighted metallicities and ages. However, we have checked the effects of normalization by introducing normalizations between 5500 and 5550 and 6950 and 7000 Å and found that they are small. Changes due to the different normalizations are comparable to the fit uncertainties.

From the weight contributions to the total spectrum of isochrones at different ages we can also estimate star formation rates. We calculate the ratio of star formation rate of the young and old population and find an anti-correlation with galaxy stellar mass. Low mass galaxies show a much higher star formation contribution of the younger population. On the other hand, more massive galaxies are dominated by stars that formed at early times. This is in agreement with the observations of 'galaxy downsizing' as originally detected by Cowie et al. (1996) and followed up in comprehensive galaxy survey work (see, for instance, Pilyugin & Thuan 2011; Thomas et al. 2019 and references therein).

For the calculation of our model spectra we have assumed a Chabrier (2003) initial mass function. In order to test the influence of this assumption we repeat the analysis using the IMFs by Kroupa (2001), van Dokkum (2008) and Salpeter (1955). The differences with respect to metallicity are very small (≤ 0.05 dex) for the first three IMFs, but are larger for the Salpeter IMF (0.1 dex and 0.2 dex for the young and old population, respectively).

Finally, we investigate the dependence of metallicity and ages on star formation rate. We stack the spectra of the $200,000$ SDSS galaxies in quintiles of SFR at each stellar mass and repeat the analysis for each quintile. We find a correlation of metallicity with SFR for higher and intermediate stellar masses for the young and old population. In addition, the average age of the total stellar population shows a clear dependence on SFR. The population in galaxies with lower SFR is significantly older and the contribution of the old

population to the integrated spectrum is much larger. In the same way, the ratio of SFR of the young to the old population is smaller for galaxies with smaller SFR.
In summary, the results provide important implications for galaxy evolution and underline the power of spectroscopic population synthesis analysis techniques.

3

Galaxy spectroscopy without spectra: Galaxy properties from photometric images with conditional diffusion models

Published in the Astrophysical Journal, **977**:131 (22pp), 2024 December 10

Authors: Lars Doorenbos, Eva Sextl (shared first-authorship), Kevin Heng, Stefano Cavuoti, Massimo Brescia, Olena Torbaniuk, Giuseppe Longo, Raphael Sznitman, and Pablo Márquez-Neila

Research Context: At a time when artificial intelligence has become a transformative force across all areas of research, its integration into astrophysics has opened new possibilities for addressing long-standing observational challenges. Modern wide-field surveys capture billions of galaxies in unprecedented detail, yet spectroscopic follow-up remains limited by both telescope time and instrument constraints. This widening gap between photometric and spectroscopic coverage has motivated researchers to seek data-driven solutions capable of bridging it.

It was within this context that Prof. Kevin Heng introduced my supervisor and me to two computer scientists, Lars Doorenbos and Pablo Márquez-Neila, whose expertise in generative modeling offered a novel way forward. Their proposal was simple yet challening: can the full optical spectrum of a galaxy be inferred directly from its imaging data? By combining astrophysical insights with advances in machine learning, we began exploring this question. The result is a method capable of artificially generating realistic galaxy spectra from photometric inputs alone, enabling the estimation of metallicity, stellar ages, and other spectroscopic indices without prior observations. The success of this approach, recognized the AI-HUB@LMU Prize 2024 for the Most Innovative AI-based Research Project, underscores the potential of AI not merely as a computational convenience but as a tool for scientific discovery.

Abstract: Modern spectroscopic surveys can only target a small fraction of the vast amount of photometrically cataloged sources in photometric surveys. Here, we report the development of a generative artificial intelligence (AI) method capable of predicting optical galaxy spectra from photometric broadband images alone. This method draws from the latest advances in diffusion models in combination with contrastive networks. We pass multiband galaxy images into the architecture to obtain optical spectra. From these, robust values for galaxy properties can be derived with any methods in the spectroscopic toolbox, such as standard population synthesis techniques and Lick indices. When trained and tested on 64×64 pixel images from the Sloan Digital Sky Survey, the global bimodality of star-forming and quiescent galaxies in photometric space is recovered, as well as a mass–metallicity relation of star-forming galaxies. The comparison between the observed and the artificially created spectra shows good agreement in overall metallicity, age, Dn4000, stellar velocity dispersion, and $E(B-V)$ values. Photometric redshift estimates of our generative algorithm can compete with other current, specialized deep learning techniques. Moreover, this work is the first attempt in the literature to infer velocity dispersion from photometric images. Additionally, we can predict the presence of an active galactic nucleus up to an accuracy of 82%. With our method, scientifically interesting galaxy properties, normally requiring spectroscopic inputs, can be obtained in future data sets from large-scale photometric surveys alone. The spectra prediction via AI can further assist in creating realistic mock catalogs.

3.1 Introduction

Astrophysics, like many other sciences, is currently undergoing a significant transformation due to the avalanche of high-quality data from various sky surveys (Borne, 2010; Bell et al., 2009). Merely forty years ago, astronomical image data sets were measured in kilo- or megabytes. Twenty years ago, by the beginning of the 21st century, data releases for the first large-scale survey, the Sloan Digital Sky Survey (SDSS), started. Other well-known surveys such as Pan-STARRS (Kaiser et al., 2002), DESI (DESI Collaboration et al., 2016a,b), and Euclid (Racca et al., 2016) followed. DESI alone now has captured more galaxies than 10 years of SDSS (Setton et al., 2023). The currently built Vera C. Rubin Observatory in Chile is designed to collect 20 terabytes per night over the time span of 10 years (Ivezić et al., 2019). Yet, most objects are only captured via photometry or photometric imaging. Spectra are only available for a small portion of the captured galaxies due to the extended duration needed for exposure and the limited capacity of spectroscopic instruments to handle multiple measurements simultaneously (Kremer et al., 2017). Furthermore, the magnitude limits for spectroscopy are much brighter, thus preventing spectroscopic observations of faint galaxies. For instance, Legacy Survey of Space and Time (LSST) investigations will likely acquire spectra for less than 1% of the galaxies involved (Matheson et al., 2013).

Greatly simplified, the overall goal of photometry is to map observed colors to galaxy

properties. When only apparent magnitudes in several broad-band filters are available for a galaxy, performing a panchromatic SED fitting (from UV to IR) has become a popular approach. The best suitable spectral energy distribution is chosen from a large sample of pre-computed templates, which assume, among others, different star formation and metal enrichment histories (Mitchell et al., 2013; Yuan et al., 2020). The use of state-of-the-art publicly available codes is discussed in Lower et al. (2020); van Mierlo et al. (2023). The SED fitting method allows for the evaluation of critical characteristics like the star formation rate (SFR) and stellar mass of a galaxy, which are crucial for comprehending their formation and evolution. Normally, these methods use solely color information, not images with morphological features (i.e., the brightness distribution across the galaxy). With such reconstructed SEDs, it is not possible to make trustworthy and accurate age or metallicity claims, as was recently shown in Nersesian et al. (2024). Even the use of additional narrow-band filters to given broad-bands does not seem to improve the recovery of galaxy parameters beyond stellar mass and SFR (Csizi et al., 2024). Determining stellar age, stellar metallicity, and dust properties with photometry alone seem rather hopeless.
With the increasing integration of Artificial Intelligence (AI) in astronomy, new avenues have opened up for deriving parameters from photometric data with machine learning techniques. Wu et al. (2023) predicted stellar atmospheric parameters like effective temperature from stellar photometric images, and Chen et al. (2021); Doorenbos et al. (2022) succeeded in recognizing active galactic nuclei (AGN) with a deep neural network that takes photometric magnitudes as input. Several classification tasks of celestial objects, which would traditionally require spectroscopic data, will soon be fully automated using only photometric bands (Zeraatgari et al., 2024). In this paper, we combine our proposed generative AI (GenAI) system with large quantities of photometric images to go a step further toward an all-embracing use of the upcoming full-sky surveys.
We present a pilot study of predicting optical spectra directly from photometric broad-band images in the SDSS survey. We show that their spectral resolution and overall quality are sufficient to analyze them with common spectroscopic tools. In doing so, we can recover interesting physical parameters such as the population age or mean metallicity. This could be a classical absorption feature analysis (i.e. Lick indices) or a full-spectral fitting code as part of stellar population synthesis.
Unlike previous attempts in the literature, we choose to make a detour over the generation of optical spectra and *not* predict the physical quantities directly from the images. Therefore, we can detach ourselves from answering unsolved questions such as which full-spectral fitting code performs best (Woo et al., 2024). Once the spectrum is created from the generative AI, the choice of the spectroscopic analysis method is left to the user. It must only be ensured that the quality and the information content of the predicted spectra are similar to the real, observed ones. We believe that this freedom in subsequent research questions is worth the higher computational cost for a generative AI. In section 3.2, we describe the utilized SDSS data and introduce our machine learning pipeline and implementation in section 3.3. We use a diverse tool set to evaluate the predicted spectra, for which we explain the details in section 3.4. Major results are presented in section 3.5. A final summary with an outlook is found in 3.6. Further technical comments on the algorithms are given

in the appendix 3.7. Additional thoughts on the test set are also found there.

3.2 Data

The significance of data in machine learning cannot be overstated. The type and quantity of data provided to an algorithm play a crucial role in its ability to extract information and generate accurate results. Creating artificial spectra in a spectral resolution suitable for follow-up analysis likely requires a large dataset with hundreds of thousands of entries. The natural first choice for this is the Sloan Digital Sky Survey. In its third phase in 2014, it encompassed more than one-third of the entire celestial sphere and is freely accessible[1]. Numerous research groups have already applied a variety of machine learning techniques to SDSS in order to answer scientific questions about galaxies, quasars, and various other celestial objects (Hoyle et al. 2015; Si et al. 2021; Curti et al. 2022; Miller et al. 2015; Brescia et al. 2015 to name a few). We aim to build further upon this work.

3.2.1 Multiband images

We utilize pre-processed broadband images from the dataset made available[2] by Pasquet et al. (2019) for their work on photometric redshift estimation with a deep convolutional neural network. For each broadband in SDSS, the galaxy's brightness is captured in an image. Their total dataset contains 659 857 galaxies of the 12th Data Release (DR12) of the Sloan Digital Sky Survey (Alam et al., 2015) in a redshift range of $0 < z < 0.7$. For each galaxy, astrometrically calibrated imaging data in u, g, r, i, and z filters with $0.396''$/pixel sampling is avaiflable through the automated data-pipeline of SDSS (Padmanabhan et al., 2008; Stoughton et al., 2002). Further re-sampling and stacking of the obtainable broadband images by Pasquet et al. (2019) leads to a final $64 \times 64 \times 5$ data cube centered on each spectroscopic target. For our purposes, a further cut in redshift is made later on.
Example images can be found in figure 3.1. It should be emphasized that images with adjacent objects (in either the forefront or background) are not removed from the sample. As a result, together with the size, morphology, and surface brightness, information about the environment is also fed into the generative model (Dey et al., 2022). Thus, more information is available to break various degeneracies.

3.2.2 Galaxy spectra

After obtaining the images, the corresponding optical galaxy spectra and their labels were extracted from the SDSS database. For such large queries, the most efficient way is using CasJobs (Li & Thakar, 2008), a flexible, advanced SQL-based interface. We obtain galaxy spectra in the spectroscopic redshift range of $0.05 < z \leq 0.15$, which show no problematic

[1] `https://live-sdss4org-dr12.pantheonsite.io/scope/`
[2] `https://deepdip.iap.fr/#item/60ef1e05be2b8ebb048d951d`

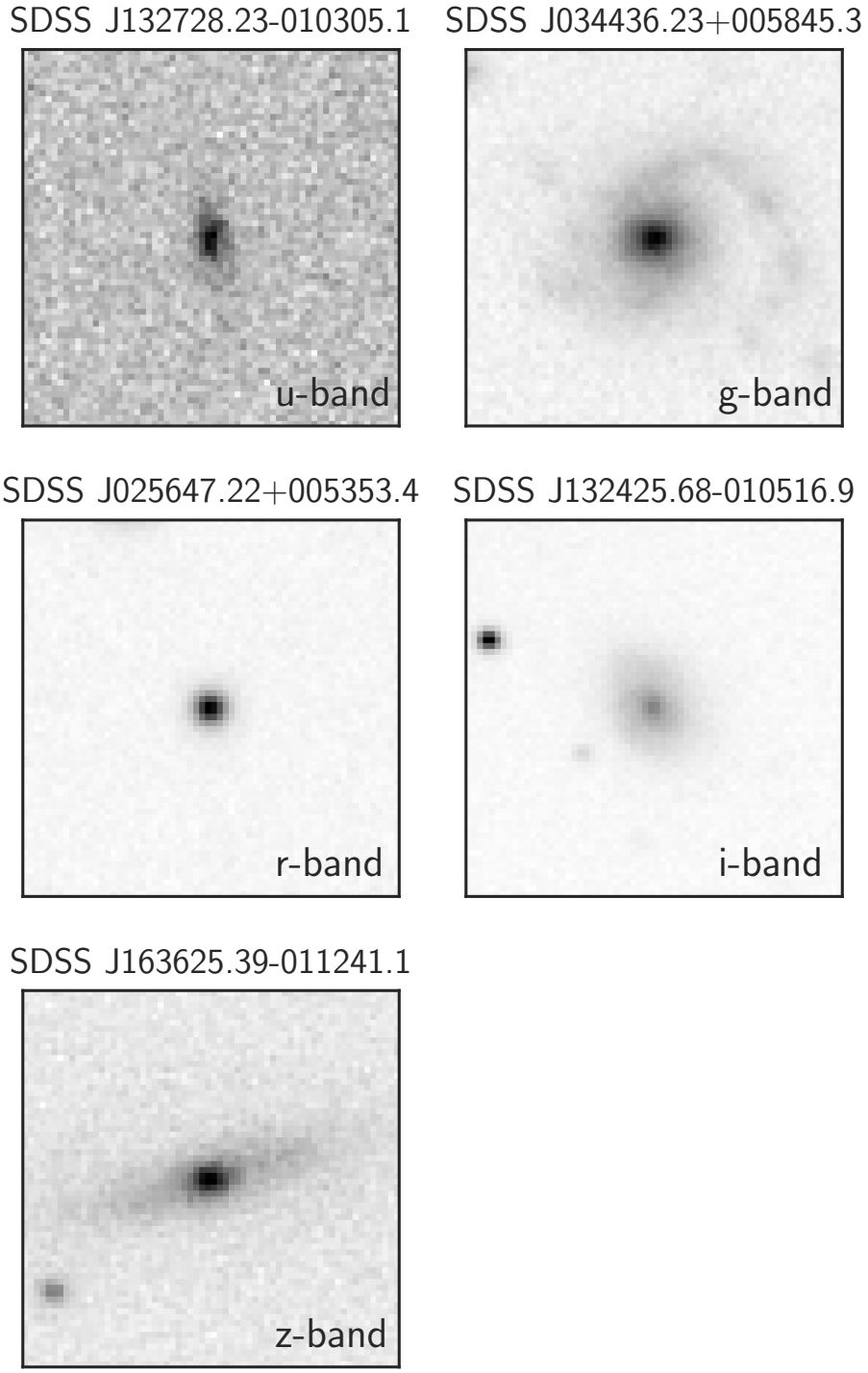

Figure 3.1: Visualization of photometric images of *different* galaxies in the training set, which serves as the input for the machine learning algorithm. The corresponding galaxy name can be found at the top of the image and the depicted band is written on each image. We chose to visualize diverse objects to better emphasize the variety of galaxy images in the training set.

flags[3] and reasonable Petrosian radii and de Vaucouleurs/exponential surface brightness fits. The complete query code is shown in Appendix 3.10. This final sample contains 270 621 image-spectra pairs spanning a wide range of morphology classes, such as spiral galaxies with bulge and/or bar components, ellipticals, and irregular galaxies at low redshift with their distinct spectral features. To minimize errors caused by aperture effects, more than 20% of the total light emitted by each galaxy should be captured by the fibres. This fraction is guaranteed by implementing the lower redshift cut of 0.05 in our sample selection (Kewley et al., 2005). Yet, the derivation of SFRs would still be heavily affected by the aperture in this redshift bracket (Duarte Puertas et al., 2017), so we refrain from obtaining them.

A further word of caution needs to be said in this regard. The aperture effect inherently found in the SDSS data itself can technically also lead to false classifications. For instance, a galaxy might be erroneously categorized as retired based on its central spectrum, when in reality, it harbors active star formation in its outer regions not captured by the SDSS fiber. This discrepancy highlights a fundamental mismatch between the photometric and spectroscopic data in SDSS which is hard to come by: while photometric images capture the entire visible extent of galaxies, the spectra used for training are limited to the fiber-covered regions. While the bias is expected to be relatively consistent across the sample within our chosen redshift regime, the model probably cannot be reliably applied to predict spectra of galaxies outside this range. It is beyond the scope of this paper to mitigate this effect.

We split the data into 268 603 samples for training the algorithm, 512 for validation/fine-tuning the model's performance, and 1 506 as the test set. We set apart these fractions of the data for the validation and test sets due to the large overall size of the dataset and the large number of computationally involved analyses of the generated spectra we performed. Nonetheless, a test set with over 1 500 objects allows us to draw robust conclusions in the following sections, and small ratios for testing and validation are standard practice in deep learning when dealing with big datasets and/or computationally involved evaluations (Amari et al., 1997; Ng, 2017). Moreover, in absolute terms, our validation and test sizes match those used in deep learning practice, for instance, in semantic segmentation (Cordts et al., 2016). The test dataset was never used in training; instead, it is used to assess the model's performance on unseen data. Figure 3.2 shows some artificial spectra from the test set compared to their observed counterparts.

The morphological categories 'elliptical', 'spiral', and 'uncertain' for each galaxy in the test set, which are used later on, are determined by the citizen science project Galaxy Zoo (Lintott et al., 2008, 2011). Galaxies were labeled as 'uncertain' if their images were not clearly voted on as spiral or elliptical. These galaxies are most likely composite bulge-disk systems in which neither the bulge nor disk overshadows the other according to Schawinski et al. (2014). In this context, it should also be mentioned that a clear identification of merger systems via images is difficult as galaxies can appear to be isolated galaxies in the image (lacking visual features like tidal features) but appear to have undergone a recent

[3] `https://live-sdss4org-dr16.pantheonsite.io/tutorials/flags`

merger when further investigated (Nevin et al., 2019). Therefore, analysis of the galaxies with respect to the categories merger/no merger was omitted. We reduced the resolution of the spectra from the original $R \sim 2000$ to $R \sim 1500$ at 5000 Å due to the high computing capacity needed. Nonetheless, this is still larger than comparable studies (Holwerda et al., 2021; Wu & Peek, 2020). These smoothed spectra are used during training; therefore, the predicted spectra also show this reduced spectral resolution. As final preparatory work, the spectra are interpolated and tailored to 1 Angstrom steps in the range of $4000 - 8499$ Å. Each spectrum is then normalized to a value of 1 between $6900 - 6950$ Å (R-band) rest-frame wavelength. This region does not contain prominent absorption or emission features and is, therefore, suited for the task, as we want the overall continuum to be scaled. Other possible wavelength regions would be $4400 - 4450$ Å (B-band) or $5500 - 5550$ Å (V-band). This does not change the results of the upcoming analysis, especially not those of the full-spectral fitting (Sextl et al., 2023). For the spectral fits in section 3.4.1, the spectrum to be fitted and the model templates always receive such a scaling for numerical stability.
Now-and-then occurring skylines in the training data are not removed, and the spectra are *not* shifted in the rest-frame. We also decided against removing galactic extinction in the images and the spectra since the overall reddening is rather small: 85% of our sample has E(B-V) values lower than 0.05 (Pasquet et al., 2019).

3.3 Procedure

We frame the problem of predicting galaxy spectra from photometry as modeling the conditional distribution of spectra given an image[4]. Specifically, we want to approximate the empirical distribution

$$p(\text{spectrum} \mid \text{image}), \tag{3.1}$$

which is defined by the training data, using a neural network. However, directly learning this distribution over high-resolution spectra is both challenging and computationally expensive.
Instead, we follow recent works on high-resolution image synthesis e.g., Blattmann et al. (2023); Ho et al. (2022); Saharia et al. (2022) and decompose the problem into two parts. First, we learn the simpler distribution of low-resolution spectra conditioned on images,

$$p(\text{low-res spectrum} \mid \text{image}) \equiv p_{lr}. \tag{3.2}$$

Second, we learn the image-conditional distribution over full-resolution spectra, with an additional condition on the corresponding low-resolution spectrum,

$$p(\text{spectrum} \mid \text{image, low-res spectrum}) \equiv p_{sr}. \tag{3.3}$$

By combining the two, we can generate a spectrum for a given image by drawing a sample from p_{lr} and then using it as the condition for p_{sr}. This effectively upsamples the low-resolution spectrum to the original resolution, which is fit for analysis. In practice, we

[4]Parts of this section are based on Doorenbos et al. (2022), presented at the NeurIPS 2022 workshop on Machine Learning and the Physical Sciences.

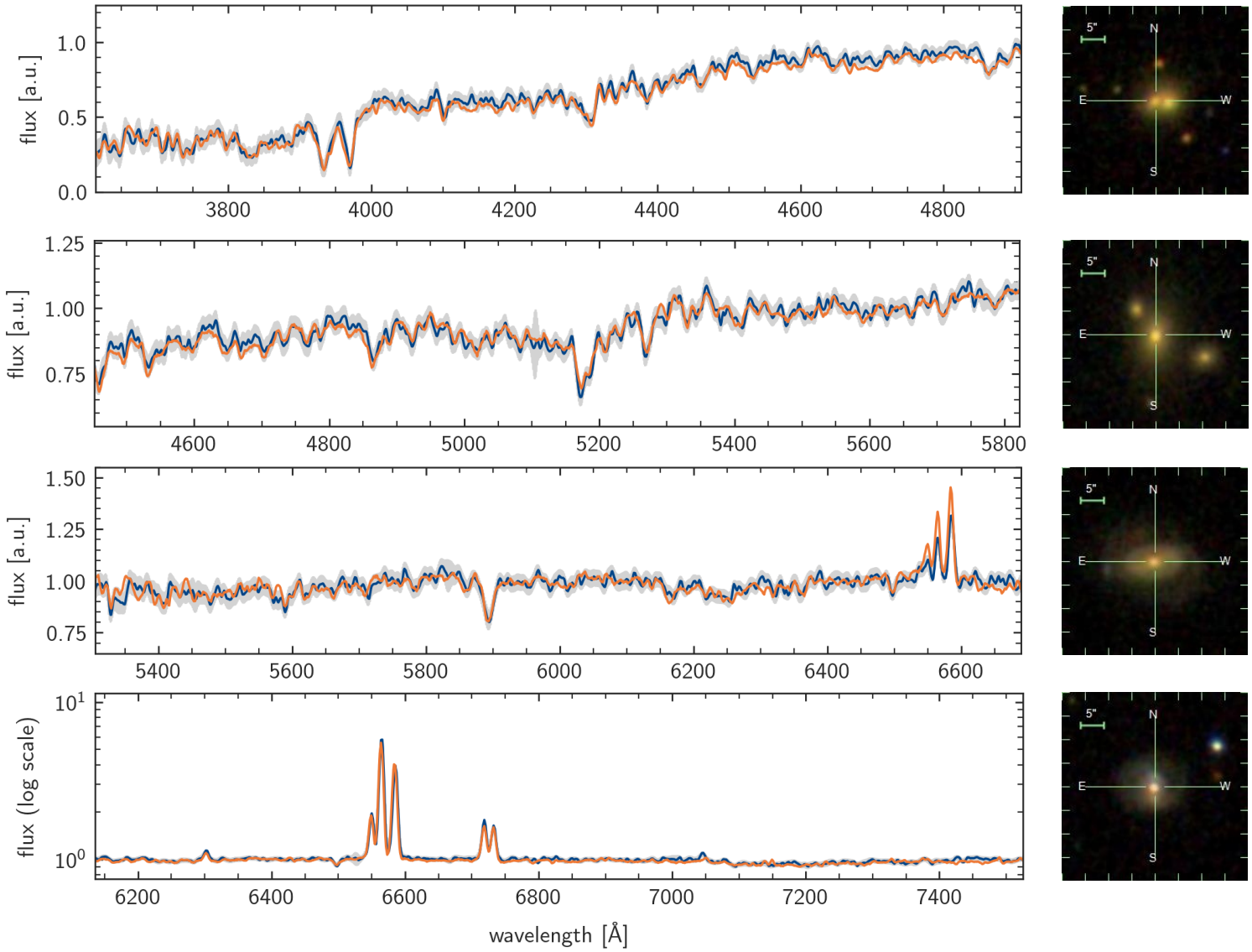

Figure 3.2: An overview of different predicted spectra (orange) and their associated smoothed observed spectra (blue) in the rest-frame from the test set. Grey-shaded areas depict the corresponding $1-\sigma$ error bars of the smoothed observed spectra. The galaxies show different morphologies (according to the Galaxy Zoo classification: uncertain, elliptical, uncertain, spiral) as visible in the corresponding SDSS tri-color images from the inner three bands on the right. These jpeg images are available on the Skyserver and only serve as an illustration for the reader; the algorithm uses 5-band images. The first example is a possible merger; the third example is classified as LINER by Brinchmann et al. (2004), and the galaxy at the bottom is best described as star bursting. The galaxy names read (from top to bottom): SDSS J205600.32-053137.8, SDSS J150109.86+472039.6, SDSS J105728.22+065954.4, SDSS J025019.52-070223.4

learn both distributions with a conditional diffusion model (CDM), which is the current state-of-the-art in generative modeling (Ho et al., 2020; Rombach et al., 2022). Generative models are a class of data-driven algorithms that model the probability distribution of observed data and generate new samples resembling the training data. These models have found success in various domains by offering the ability to easily generate new data instances that closely mirror the characteristics of the training set (Baranchuk et al., 2022; de Melo et al., 2022; Zhang et al., 2021).
While CDMs can generate realistic samples that closely mirror the characteristics of the training set, they do not allow for density estimation. Consequently, sampling from the CDMs results in multiple possible spectra for a given object without information on their likelihood. Nonetheless, we need to select one of the spectra for our subsequent analyses. To decide which spectrum we select for follow-up evaluation, we use multimodal contrastive learning (Chen et al., 2020) as a heuristic to find high-likelihood samples of the learned distribution, which has proven to work well in practice (Ramesh et al., 2021). Multimodal contrastive learning is a representation learning algorithm that learns informative features from a dataset without having access to any labels.
Specifically, multimodal contrastive learning learns to map images and spectra into a shared representation space, where images and spectra with similar representations are likely to belong to the same object. We rank the generated spectra based on the similarities between their representations and that of the original image, then select the best-matching samples. Our full method for predicting spectra from photometry begins by sampling several 563-dimensional spectra for an image with the low-resolution CDM. We select the three best synthetic spectra according to the low-resolution contrastive network. Then, we generate five full-resolution spectra for each of the selected low-resolution spectra. Finally, we select the best-matching spectrum with the full-resolution contrastive network, giving us the final synthetic spectrum for the object.
A visualization of our pipeline is provided in Figure 3.3. We provide further technical details in Appendix 3.9.

3.3.1 Implementation details

We train all networks using Adam (Kingma & Ba, 2015) with a learning rate of 10^{-4}, with the contrastive networks using a weight decay of 10^{-3}. We use a batch size of 512 for the low-resolution experiments and 224/340 for the full-resolution CDM and contrastive network, respectively. The CDM uses 250 timesteps with a cosine variance schedule, exponential moving average with $\alpha = 0.9999$, a ResNet-18 (He et al., 2016) for the image encoder τ_θ and a 1D U-net (Ronneberger et al., 2015) for the denoising autoencoder. The contrastive networks use a ResNet-50 (He et al., 2016) for the image encoder and a 1D ResNet encoder for the spectra, both with a latent dimensionality of 128.
We standardize the images by channel and predict the logarithm of the spectra so that the ranges of values better match the Gaussian noise used by the CDM. We apply data augmentation to the images to artificially increase the size of the training dataset and improve the generalizability of the algorithm, as, for instance, flipping the image of an

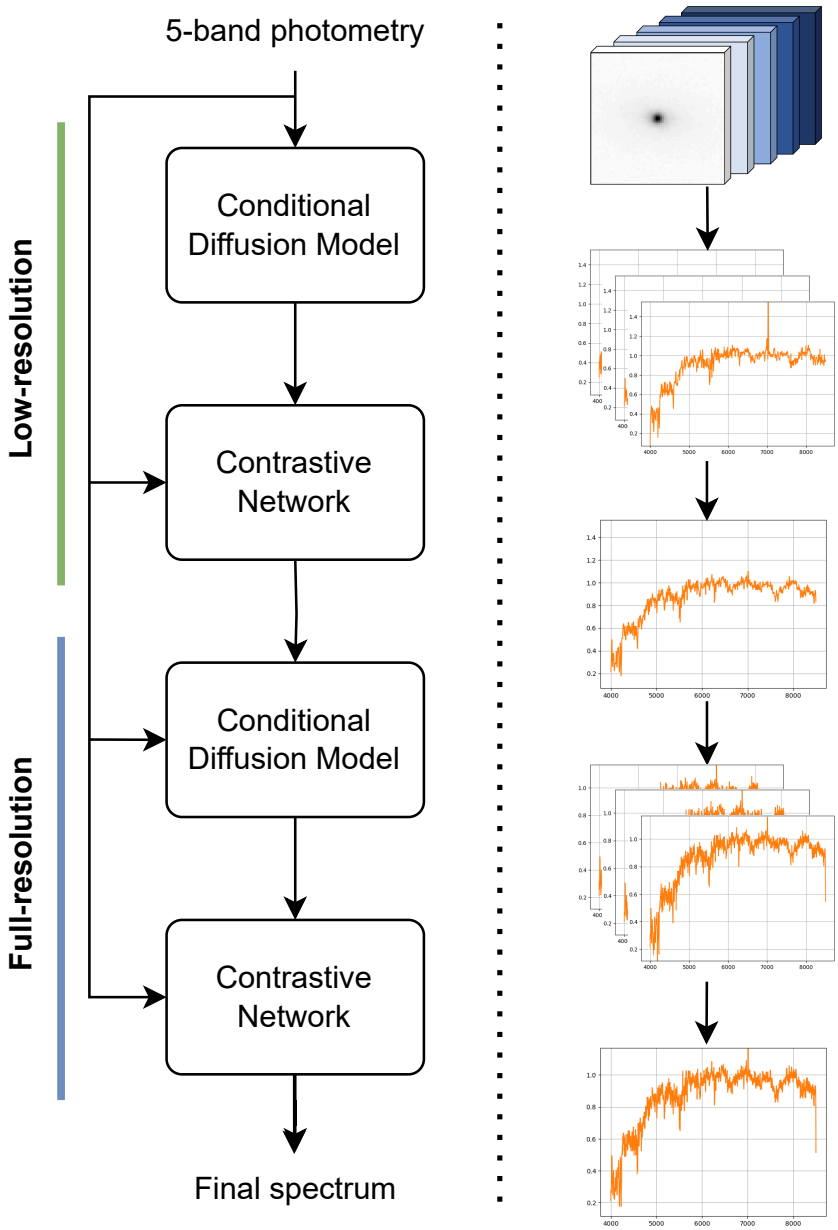

Figure 3.3: Visualization of our pipeline. We use a conditional diffusion model to generate candidate low-resolution spectra for the given image and select the best matching candidates with a contrastive network. Then, we use a conditional diffusion model to upsample the candidate spectra to full-resolution candidates and select the final predicted spectrum with the second contrastive network.

object should not affect its spectrum. Specifically, we flip images horizontally and vertically with a probability of 0.5 and apply random cropping. We do not apply data augmentation to the spectra. We do not apply any data augmentation to the test samples used for evaluation in the following sections.
All models are trained with 2 NVIDIA GeForce RTX 3090s until convergence of the Mean Squared Error (MSE) between generated and ground-truth samples on the validation set. We make our code publicly available (Doorenbos & Sextl, 2024).

3.4 Evaluation Methods

In this section, we present the tools used to evaluate the information content of our artificial spectra. A successful generative model should not only produce galaxy spectra with similar shapes and matching overall features (*i.e.*, a low MSE) compared to their observed counterparts. More importantly, the extracted stellar population properties from the artificial spectra should coincide with those imprinted in the observed spectra. The spectroscopic toolbox we utilize for this contains two stellar population fitting codes (subsection 3.4.1) capable of recovering the mean age, metallicity, extinction, and stellar mass of a galaxy from its spectrum. It also encompasses measurements of the strength of prominent emission and absorption lines (Lick Indices) and band-head features (such as Dn4000). A detailed explanation and the corresponding definitions are found in subsection 3.4.2. Finally, we assess whether the generative model has learned to link typical AGN emission to photometric features and evaluate it through popular performance metrics in machine learning (subsection 3.4.3).

Table 3.1: Spectral Indices

Index	Blue Side band [Å]	Line [Å]	Red side band [Å]	Reference	Frame
Dn4000	3850.000 – 3950.000		4000.000 – 4100.000	Balogh et al. (1999)	air
Mg b	5142.625 – 5161.375	5160.125 – 5192.625	5191.375 – 5206.375	Trager et al. (1998)	air
Fe5270	5233.150 – 5248.150	5245.650 – 5285.650	5285.650 – 5318.150	Trager et al. (1998)	air
Fe5335	5304.625 – 5315.875	5312.125 – 5352.125	5353.375 – 5363.375	Trager et al. (1998)	air
Hβ	4827.875 – 4847.875	4847.875 – 4876.625	4876.625 – 4891.625	Trager et al. (1998)	air

SDSS spectra are provided in vacuum wavelengths, but many indices are measured in air. If so, the SDSS wavelengths are converted using Morton (1991). Yet, the resulting error would be negligible. It should also be mentioned that Dn4000 as a spectral index is measured using the flux per unit frequency (F_ν), not flux per unit wavelength (F_λ) as the others.

3.4.1 Full spectral fitting

A possible way of evaluating the quality of artificially generated spectra is to run full-spectral fitting codes on them. As the name states, these techniques work on the complete wavelength range available, not only on distinct spectral features such as the Balmer lines. Today, they are a standard procedure to determine galaxy properties, including age, stellar

metallicity, stellar mass, and dust extinction of composite or spatially-resolved stellar populations. In this work, we used `FIREFLY` (Wilkinson et al., 2015, 2017) and `pPXF` (Cappellari & Emsellem, 2004; Cappellari, 2017, 2023), two well-known non-parametric population synthesis codes available from the astrophysical community. They do not assume a star formation history a priori but try to recover it, along with other properties, from the spectrum and are, therefore, quite general (i.e., concerning merger events). The user should nevertheless not blindly trust the complete star-formation history (SFH); a reduction to a robust young and old population can sometimes be the only way to statistically sound statements (Cid Fernandes et al., 2005).

`pPXF` applies a penalized maximum likelihood approach to fit single-burst stellar population models (SSPs) on spectra. By imposing a penalty on pixels that are not well characterized by the templates, it works to minimize template mismatch. One of the advantages of the code is the possibility of simultaneous fitting of gas emission lines along with stellar kinematics (velocity dispersion) and stellar population. With this software, we are using the included model templates from (Vazdekis et al., 2016). We realigned our work to Jupyter Notebook examples[5] available online, which show the use of an additional bootstrapping method (Davidson & Flachaire, 2008) with `pPXF` during the fit. As a first step in this procedure, a regularization (smoothing of template weights with `regul`=10) was applied. The emerging residuals are stored and then used to bootstrap the spectrum 50 times. This leads to robust average galaxy properties (mean age, mean metallicity, ...) and an estimate for their uncertainties (see also Kacharov et al. 2018 for more details).

When replicating the examples, we strongly recommend using the newer `.dust-function` for the extinction, not the now obsolete `.reddening/ .gas-reddening` keywords which are used in the examples.

`FIREFLY` is a chi-squared minimization fitting code that fits combinations of SSPs to spectroscopic data, following an iterative best-fitting process controlled by the Bayesian information criterion. This approach has been designed to be a good way to recover galaxy properties, especially in low S/N-regimes, where accurately deriving properties from spectral fits becomes more and more challenging (Goddard et al., 2017). Extinction due to dust is not fitted in a conventional way: A High-Pass Filter (HPF) is used to rectify the continuum before fitting, allowing for the removal of large-scale modes of the spectrum associated with dust and/or poor flux calibration. Regions with nebular emission lines are masked out during the process.

The `FIREFLY` package is supplied with the pre-calculated stellar population models of Maraston & Strömbäck 2011 (MILES Falcón-Barroso et al. 2011 as the stellar library combined with a Kroupa IMF Kroupa 2001 in a fuel-consumption approach). We also ran tests with the models used in (Sextl et al., 2024) derived with FSPS v3.2 (Conroy et al., 2009) and a combination of several stellar catalogs (MILES in combination with additional templates from Post-AGB, WR-stars etc) with a Chabrier IMF (Chabrier, 2003) and MIST isochrones (Dotter, 2016; Choi et al., 2016; Paxton et al., 2011). This leads to substantially longer run times of the code but not to improved results in the evaluation

[5] `https://github.com/micappe/ppxf_examples`

metrics presented in this section. The lack of hot stars ($T > 9000$ K) in the MILES library (Martins & Coelho, 2007) does not seem to play a crucial role in the setup here. We, therefore, remain with the Maraston & Strömbäck SSPs. The corresponding age grid covers SSPs between 6.5 Myr and the Age of the universe, while the sampled metallicities read $[Z] = -1.3, -0.3, 0.0$, and 0.3. Regions with emission lines or absorption features polluted with emission are masked for a functioning fit. As an extinction law, Calzetti (2001) is chosen. For the observed spectra, the velocity dispersion (σ_*) retrieved from `pPXF` was used in the input file. These values are in agreement with the error bars with the values for σ_* deposited in the SDSS archive. The artificial spectra tend to show similar velocity dispersions as their real counterparts (see figure 3.8).
As an additional asset, we also integrate the bootstrapping method from above into the `FIREFLY` Python routines. Due to longer calculation times, the spectra are only bootstrapped 10 times. Yet, `FIREFLY` is a code already designed to work in a low S/N regime, and we will see that the artificial spectra perform equally well with both codes.

A key distinction between the codes lies in the treatment of dust: While `pPXF` assumes a dust reddening law and dust is treated as an adjustable fit parameter, `FIREFLY` determines the effect of dust prior to the main fitting by comparing the large modes of data and models (Wilkinson et al., 2017). We emphasize that the focus of this work does not lie in the comparison between the different codes or SSPs but in the performance of the predicted spectra in contrast to the true observed spectra. Absolute values from full spectral fitting are always affected by systematic differences in the technique itself and underlying stellar population models and their ingredients (Baldwin et al., 2018; Oyarzún et al., 2019; Chen et al., 2010; Ge et al., 2019). Figure 3.4 shows four full-spectral fit examples for `FIREFLY` and `pPXF` on selected galaxies in the test set.

3.4.2 Spectral Features

Before the widespread use of full-spectral fitting techniques as described above, a limited number of prominent stellar absorption features were examined. Their strength or equivalent width is not sensitive to flux calibration and is available even at modest resolution and low S/N optical spectra. Extensive research in the 1980/1990s by Burstein et al. (1984); Worthey et al. (1994); Worthey & Ottaviani (1997); Trager et al. (1998) led to the Lick index system, a set of 25 optical absorption-line indices, the most commonly used in absorption-line analyses of old stellar populations. Each index in this system is defined by a central "feature bandpass" and two adjacent windows, blue- and rewards, for defining so-called "pseudo-continua" acting as baselines. Some indices are known to be more age-sensitive (e.g., Hydrogen Balmer lines) or metallicity-sensitive (e.g., Fe, Mg features). The well-known additional dependence on α-enhancement (α/Fe) complicates the picture, and efforts went into constructing combined metallicity indices with a weak α-dependence (see below).
In our work, we measure prominent Lick indices (equivalent widths compared to two sidebands) and also Dn4000 as a "bandhead" index (difference of two passbands) based on

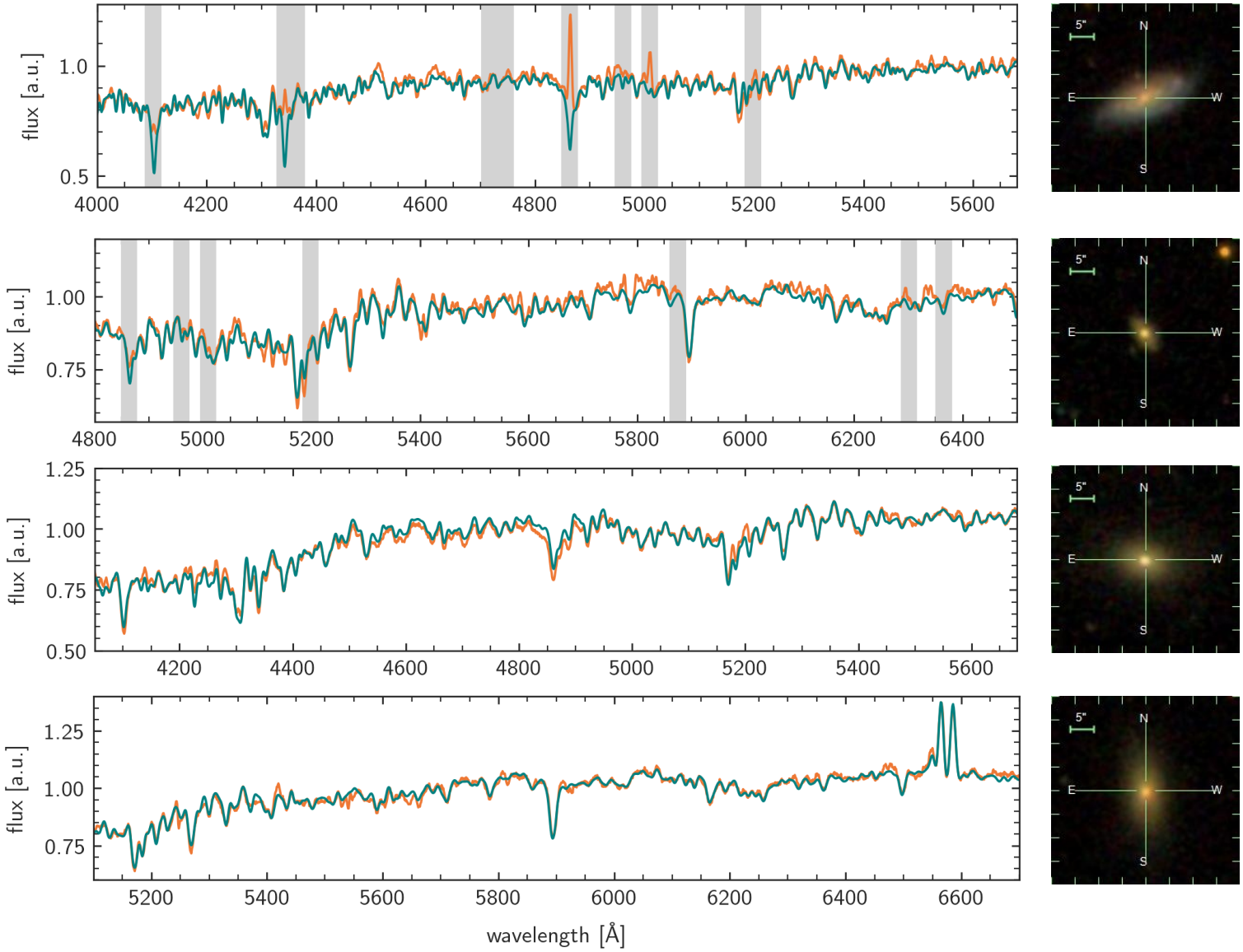

Figure 3.4: Another four predicted created spectra (orange) and their corresponding full-spectrum fits with a population synthesis code. A `FIREFLY` result is shown in the first two rows. Regions with potential emission lines (not necessarily visible in each spectrum) are masked out for the fit and displayed here on a gray background. The third and fourth spectra are fitted with `pPXF` with emission and absorption fitted in parallel. The images on the right show again the corresponding SDSS tri-color images for illustration; the algorithm uses 5-band images.

the recipes in the Mapping Nearby Galaxies at Apache Point Observatory (MaNGA) data pipeline (Westfall et al., 2019) with the program `PYPHOT` (Fouesneau, 2022). This package does not take into account uncertainties in the flux. SDSS galaxies also do not show strong wavelength-dependent noise, which would distort the measured Lick values (Nersesian et al., 2024). Table 3.1 shows the utilized indices and their pseudo-continua wavelength ranges. As a robust metallicity indicator independent of α-enhancement, the averaged Lick index [MgFe]$'$ from Thomas et al. (2003) is computed from our measurements:

$$[\mathrm{MgFe}]' = \sqrt{\mathrm{Mg\ b} \cdot (0.72 \cdot \mathrm{Fe5270} + 0.28 \cdot \mathrm{Fe5335})} \tag{3.4}$$

We do deteriorate the spectral resolution to reach the original wavelength-dependent Lick resolution (FWHM[4000 Å]=11.5 Å, FWHM[6000 Å]=8.9 Å).
Lick Indices were originally mainly used for quiescent galaxies without visible emission lines, but star-forming galaxies in our test sample can have strong Hβ-emission. Even the vanishing star formation rates of ellipticals can trigger this emission (Whitaker et al., 2013). In order to prevent contamination in this line index, we measure this index not from the original spectra but from the model fits obtained from `FIREFLY`. The fit only contains stellar light and no emission from gas. Other spectral features are not affected by this issue.
Velocity dispersion broadening has another non-negligible effect on absorption index measurements and has to be accounted for. Many artificial spectra show similar velocity dispersions as the real observations (figure 3.8 top right), yet some deviate strongly. We apply the method presented in Zheng et al. (2019) to remove the effect of the velocity dispersion altogether, keeping in mind that single SDSS galaxies can show values of $\sigma_* \approx 400\,\mathrm{km/s}$. The authors assume a simple polynomial relation between spectral indices with and without velocity dispersion broadening and provide suitable coefficients for our used indices:

$$x_0 = p_0 + p_1 x^{p_2} + p_3 \sigma^{p_4} + p_5 x^{p_6} \sigma^{p_7} \tag{3.5}$$

σ is the velocity dispersion measured in km/s and x, x_0 are spectral index values before/after correction. The values for the coefficients p_0 to p_7 for each index can be found in Zheng et al. (2019) table 2. The uncertainties traced through this method are usually below 5%. In order to use equation 3.5, robust velocity dispersions of our artificial and observed spectra are needed. We measure them with `pPXF` (see 3.4.1).

3.4.3 Performance on AGN recognition

For a typical binary classification task in machine learning, various performance metrics are used to evaluate how accurate the predictions are. In subsection 3.5.7, we will ask the question of whether a galaxy harbors an AGN or not according to its position in the Baldwin-Phillips-Terlevich (BPT) diagram (Baldwin et al., 1981). For this, the real observed spectra or the artificial spectra are used as a starting point. If both spectra (the true and the predicted one) lead to the same classification as AGN, we speak of a true positive (TP). If the emission lines in both spectra point towards a pure star-forming

galaxy, it is a true negative (TN). FN (False negative) denotes the number of AGNs not showing up in the artificial spectra. The three metrics used in our work are:

$$\text{Accuracy} = \frac{\text{TP} + \text{TN}}{\text{Total}} \tag{3.6}$$

$$\text{Precision} = \text{Purity} = \frac{\text{TP}}{\text{TP} + \text{FP}} \tag{3.7}$$

$$\text{Recall} = \text{Sensitivity} = \frac{\text{TP}}{\text{TP} + \text{FN}} \tag{3.8}$$

An evaluation based on accuracy should only be used in approximately equally sized groups, as unbalanced sizes lead to largely overestimated accuracy scores.

3.5 Results

3.5.1 Quality assessment

First, we mathematically assess the performance of our generative model before discussing the spectroscopic quality of the predicted spectra. One possible way to evaluate the difference between the predicted and observed spectra is by comparing them at each wavelength point. To do this, we shift the anticipated redshift of the artificial spectra to match the true redshift of the observed spectra. Figure 3.5 shows the quality indicator $\overline{\Delta}$ for the whole test set of 1506 galaxies split into different morphological groups defined by the galaxy zoo. It is defined as

$$\overline{\Delta} = \frac{1}{N} \sum_{\lambda} \frac{|O_\lambda - F_\lambda|}{O_\lambda} \tag{3.9}$$

with the number of wavelength points N, O_λ and F_λ represent the observed and the predicted spectra respectively. As such, $\overline{\Delta}$ can be interpreted as a measure of the mean relative deviation between the true and artificial galaxy spectrum (after Cid Fernandes et al. 2013). The median $\overline{\Delta}$ in the test set is 5.5%, and 90% of all spectra have values less than 10%. The inspection of the worst matches ($\overline{\Delta} > 30$) reveals that the generative model heavily under- or overestimated the strength of the Balmer emission lines in these cases. The strong discrepancy in a few wavelength points affected the overall sum in equation (3.9); the same holds true for the MSE error. A further inspection indicates that these poorly forecasted galaxies are mostly noisy low-mass starburst galaxies (EW $H\alpha >$ 35Å) categorized as "spiral" and "uncertain" in roughly equal parts. When calculating $\chi^2 = \sum \frac{|O_\lambda - F_\lambda|^2}{\sigma_\lambda^2}$ which incorporates the uncertainty of the observed spectra σ_λ, all three morphological groups perform equally well. This is surprising since emission lines are usually narrow in comparison to the width of the broad-band filter, and photons from the continuum, not from the emission line, account for most of the signal. Such a performance can only be achieved by relating emission line fluxes not only to the averaged colors of

the galaxy but also to the distribution of colors/magnitudes in the images. How well the generative model recovers line ratios is discussed in section 3.5.7. We do not have error bars for the predicted spectra available as we focused on obtaining a single best estimate for the spectrum of an object. However, while CDMs do not allow us to access the learned distribution directly, one can, in principle, sample multiple candidate spectra per image. In future work, we plan to explore how to use these to provide uncertainty estimates for our predicted spectra.

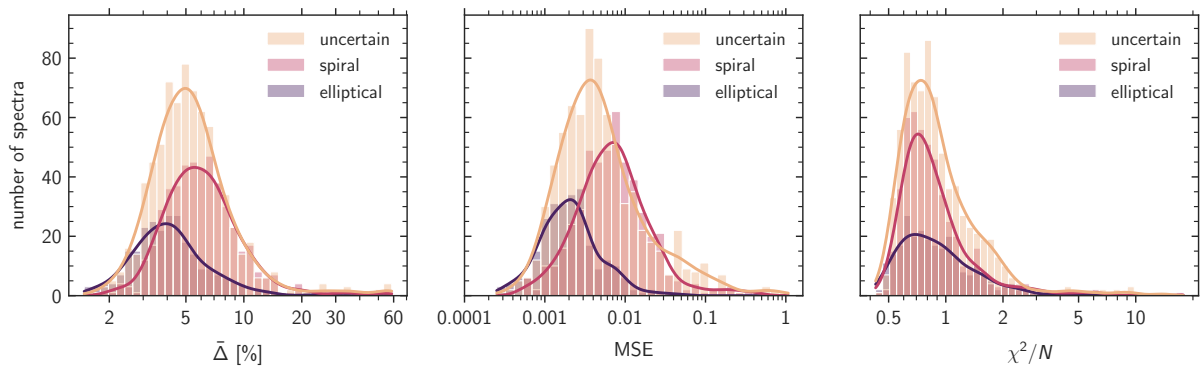

Figure 3.5: Histogram of $\overline{\Delta}$, Mean Square Error (MSE) and χ^2/N (with N the number of flux-points) of all galaxies in the test set split into different morphologies. When taking into account the uncertainty of the observed spectra, all three groups perform equally well. The morphological categories "elliptical", "spiral", and "uncertain" were determined by the citizen science project Galaxy Zoo Lintott et al. (2008, 2011)). Galaxies were labeled as "uncertain" if their images were not clearly voted on as spiral or elliptical. Note that this does not say much about their spectral classification as, for instance, a post-merger starburst galaxy could belong to this group.

3.5.2 Redshift estimate

Since we do not remove the redshift in our galaxy sample, the generative model also predicts not only the spectrum itself but also an accompanying redshift. We measure this "photo-z" in the artificial spectra and compare it to the true spectral redshift (z_{spec}). This term is slightly odd as we measure the redshift in a spectrum, but this underlying artificial spectrum is a prediction on photometric images alone. As there are no suitable words to describe this situation, we refer to these redshift estimates as "predict-z". Often used statistics concerning redshifts are:

- $\Delta z = (z_{pred}\text{-}z_{spec})/(1+z_{spec})$
- $\sigma_{MAD} = 1.4826 \cdot |\Delta z - \text{median}(\Delta z)|$

The MAD value (for Median Absolute Deviation) is a common tool for comparing the quality of the predicted redshifts. It is a general measure of dispersion similar to the standard deviation but more robust to outliers. Pasquet et al. (2019), whose training set

we are using, achieved a $\sigma_{MAD} = 0.00912$, significantly lower than other machine learning techniques on the same samples. Later work with various ML architectures expanded this work, e.g., Henghes et al. (2022); Schuldt et al. (2021); Lima et al. (2022). On our rather limited redshift sample ($0.05 < z < 0.15$) we achieve values of $\sigma_{MAD} = 0.01177$ and obtain 2 from 1 506 outliers with $\Delta z > 0.05$, see Figure 3.6. Unlike other methods, this competitive result is only a byproduct of our generative AI, which is not limited to predicting redshift alone. However, we tested here only on a relatively narrow redshift range. The cited literature mostly focuses on redshifts up to $z \sim 1$ or beyond.
Predicting redshift from images, in general, offers a significant advantage over traditional methods that rely on limited and biased information (i.e., only colors and magnitudes) taken from pre-processed catalogs (D'Isanto & Polsterer, 2018). The user is simply not biased in selecting measured properties obtained from the galaxy image beforehand. The question of which features are most important does not present itself when using images as basically all features imaginable are present Hoyle (2016). While supervised convolutional neural networks are the natural choice for redshift prediction with photometric images (Brescia et al., 2021), we show that conditional diffusion models are also successful - when a small detour over spectra is taken. Improving photometric redshift estimates is one of the most pressing needs in the next generation of photometric surveys to unlock their full potential (Newman & Gruen, 2022). Further work will show whether our approach can help in this regard.

3.5.3 Spectral Indices

In the previous section, we showed that the observed and predicted spectra agree quantitatively to a high degree. To further quantify the ML output, we measure spectral indices at several key absorption features in all galaxies in the test set. These can be sensitive to metallicity (Fe5270, Fe5335, Mg b, [MgFe]′), age (Hβ) or both (Dn4000, Paulino-Afonso et al. 2020). For proper measurement of the correct spectral regions, all spectra are shifted into the rest frame beforehand. Figure 3.7 shows the velocity dispersion corrected indices for the predicted and the observed spectra of the uncertain & elliptical morphological group.
For [MgFe]′ and Dn4000, we see a strong correlation between observed and predicted values, which also translates into high Pearson correlation coefficients ($\rho = 0.71$ and $\rho = 0.91$). For Mg b, the values correlate well, $\rho = 0.60$, yet the correlation is improved heavily up to $\rho = 0.78$ if only the subset of ellipticals is used. Buzzoni (2015) argue that the forbidden [N I] line emission at 5199 Å can add to the red Mg b pseudo-continuum and enlarge the index value (and lead to higher metallicities). Since [N I] is generally correlated with [O III] emission, Mg b values in star-forming galaxies are generally unreliable. A wrong prediction of [N I] from our generative model might, therefore, negatively influence the comparison to the observed spectra.
For the two iron indices, a one-to-one relation is no longer clearly identifiable. The correlation coefficients are below 0.5 for all indices; Fe5335 is as low as $\rho = 0.2$. These two neighboring features are generally less prominent in the galaxy spectra. Fe5270, in par-

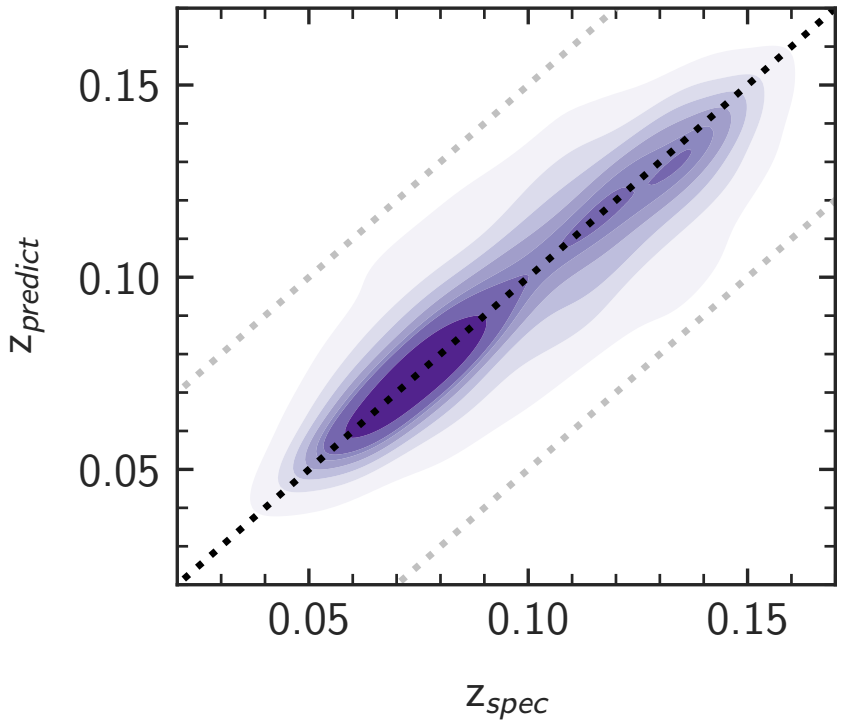

Figure 3.6: Comparison between the spectroscopic redshift from the observed spectra (z_{spec}) and the prediction from our generative AI for the galaxies ($z_{predict}$) in the test set. Instead of single data points, the overall kernel density estimate is shown for a clearer point of view. The grey dotted lines mark the regions with catastrophic outliers with $|\Delta z/(1+z_{spec})| > 0.05$. The black dotted line shows the one-to-one relation.

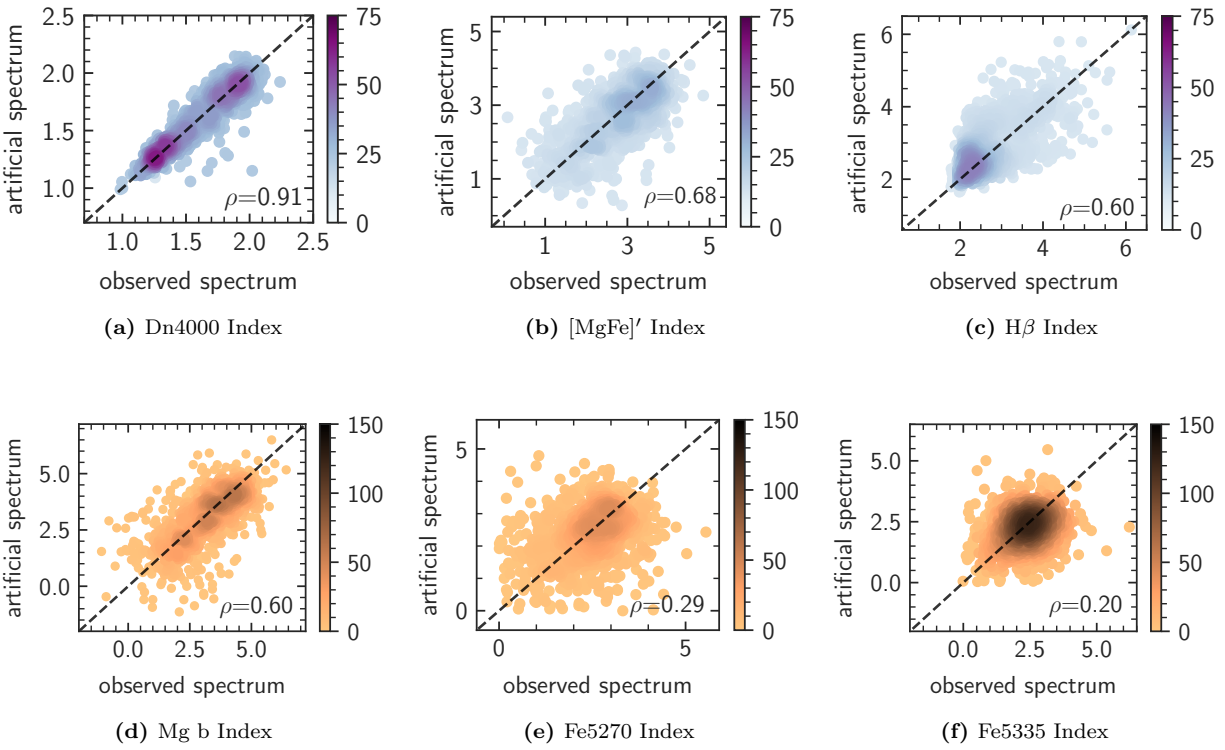

(a) Dn4000 Index **(b)** [MgFe]′ Index **(c)** Hβ Index

(d) Mg b Index **(e)** Fe5270 Index **(f)** Fe5335 Index

Figure 3.7: Comparison of Lick Indices measured using the observed spectra and the predicted spectra. Spiral galaxies were excluded. The color coding of the density plots indicates how many galaxies reside at a specific (x,y)-position and is kept frozen in each row for comparability. Pearson correlation coefficients ρ are printed in each subfigure.

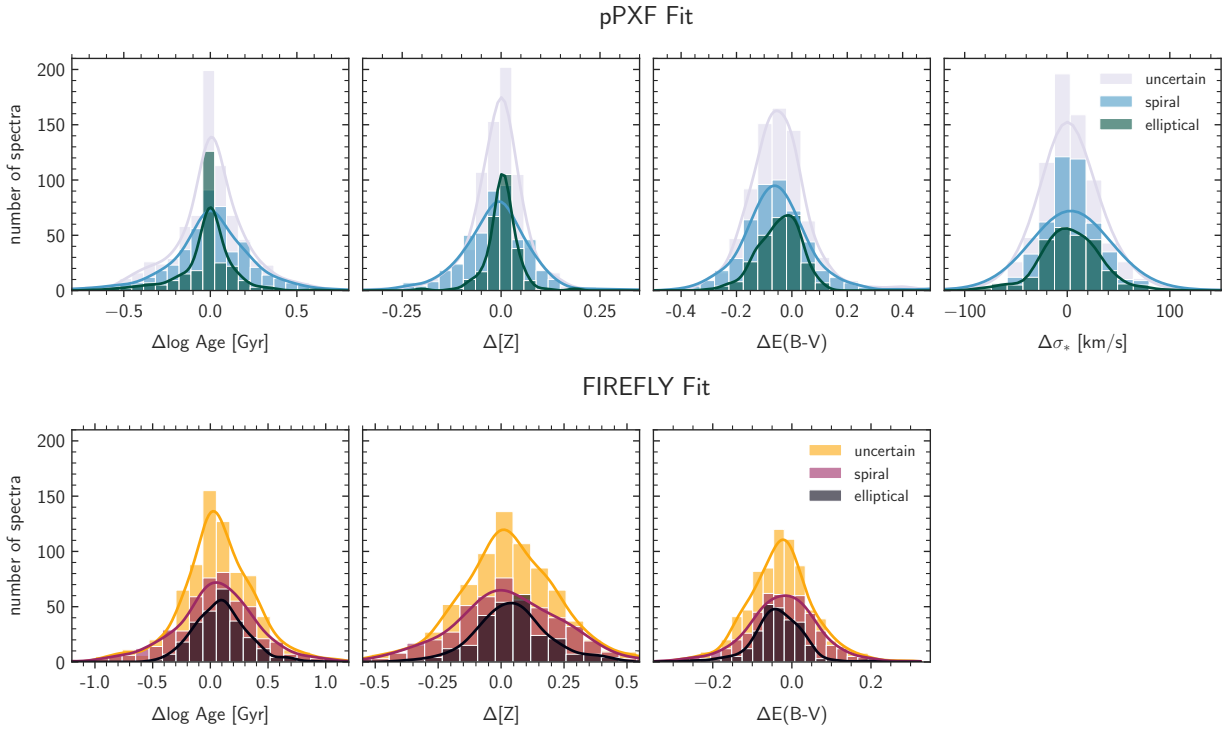

Figure 3.8: Distribution of differences (observed minus predicted) in the derived physical quantities for the used fitting codes. Each histogram shows the difference in inferred quantities (age, metallicity, E(B-V), σ_*) between the real and predicted spectra. The first row in green colors shows the results for the fitting code `pPXF`, and the second row shows the results for FIREFLY. Different morphological categories as marked before.

ticular, testifies of cool main sequence stars (around 4500 K) and MK III giants (Buzzoni et al., 2009). The fraction of light from such stars in our spectra is small in comparison to the contribution of luminous main-sequence or supergiant stars.

3.5.4 Full-spectral fitting results

The metallicity of stars in galaxies is an important indicator of the chemical evolution of a galaxy. Yet, measuring gas or stellar metallicity from photometric data alone presents challenges due to the age-metallicity-dust degeneracy. This means that a galaxy can appear red for various reasons, including the cessation of star formation, high metallicity, or strong attenuation. Additional information like morphological features can help to lift these problems. In the second column of figure 3.8, the differences between metallicity derived for the observed spectra are compared with the values determined by the predicted spectra. The first row shows `pPXF` results, the second row shows the FIREFLY fits.
Concerning `pPXF`, 86% of all predicted spectra coincide in metallicity within 0.10 dex. Taking into account the obtained error bars from the bootstrapping procedure, which are of the order of 0.07 dex in the median, 95% of metallicity values derived from the predicted

spectra coincide with their real counterparts. As expected, the elliptical galaxies show narrower distributions than spirals as they have an overall narrower range of metallicities (see for instance Li et al. 2018, figure 5) and easier star-formation histories. For `FIREFLY`, the scatter is larger. 44% of all galaxies coincide within 0.10 dex and 70% within 0.2 dex. Higher uncertainties in the `FIREFLY` metallicity (0.11 dex in the median) due to the lower number of bootstrapping cycles do not counterbalance this. The values of the flux-weighted age show similar results. For `pPXF`, the scatter is 0.23 dex in the median, and for `FIREFLY`, 0.33 dex. For that, the deviations in reddening are notably smaller for FIREFLY independent of the morphological group (0.08 dex vs 0.13 dex in `pPXF`). This most likely has to do with the different fitting algorithms themselves, which are further explored in the next subsection. The mean of ΔE(B-V) is not exactly at zero, but at ~ -0.05 which means that the GenAI predicts dust extinction values slightly too high. This effect is consistently found in all galaxy types as well as fitting codes, also in the larger test set found in the appendix 3.8.

The velocity dispersion in the spectra cannot be fitted with `FIREFLY` (see section 3.4.1); this is only implemented in `pPXF`. The shown distribution in the top right of figure 3.8 has an overall mean of -1.4 km/s and a standard deviation of 40 km/s. The distribution is visibly smaller for ellipticals (in dark green), with a standard deviation of 29 km/s. Whether these numbers are good enough for a scientific application depends on the task in mind. But one should not forget that precise measurement of stellar velocity dispersion provides additional insights into the gravitational potential well that encompasses the stars. Since this potential is primarily influenced by dark matter, the velocity dispersion also indirectly indicates the characteristics of the dark matter halo (Zahid et al., 2016). Even though this quantity is of prime scientific importance, the authors are unaware of attempts in the literature to predict the stellar velocity dispersion from photometry.

In the closing of this chapter, the absolute values of the metallicity can be considered. In figure 3.9, the overall mass-metallicity relationship is shown for the predicted spectra (top with `FIREFLY`, bottom with `ppXF`). These coincide overall with the lookback evolution models by Kudritzki et al. (2021a). Assuming a redshift-dependent relationship between gas mass and stellar mass enabled them to derive numerical models of chemical evolution that are easy to calculate. The all-in-all scatter in the mass-metallicity relation is expected as it also depends on SFR as a third parameter (Mannucci et al., 2010). Galaxies with lower SFR tend to have higher metallicities at the same stellar mass and vice versa. There is a slight discrepancy between the values derived from the two different codes and SSPs. Metallicities with `pPXF` tend to be systematically lower by $\sim$ 0.1 dex. This was also observed in Oyarzún et al. (2019) fitting spatially resolved passive early-type galaxies from the MaNGA survey. One possible origin might be the spacing of the metallicity grid of the SSPs or the overall spectral library.

3.5.5 Degeneracies Between Age, Metallicity and Reddening

It has been long recognized that optical spectra exhibit degeneracies in terms of age, metallicity, and dust properties. This means that different stellar populations with varying

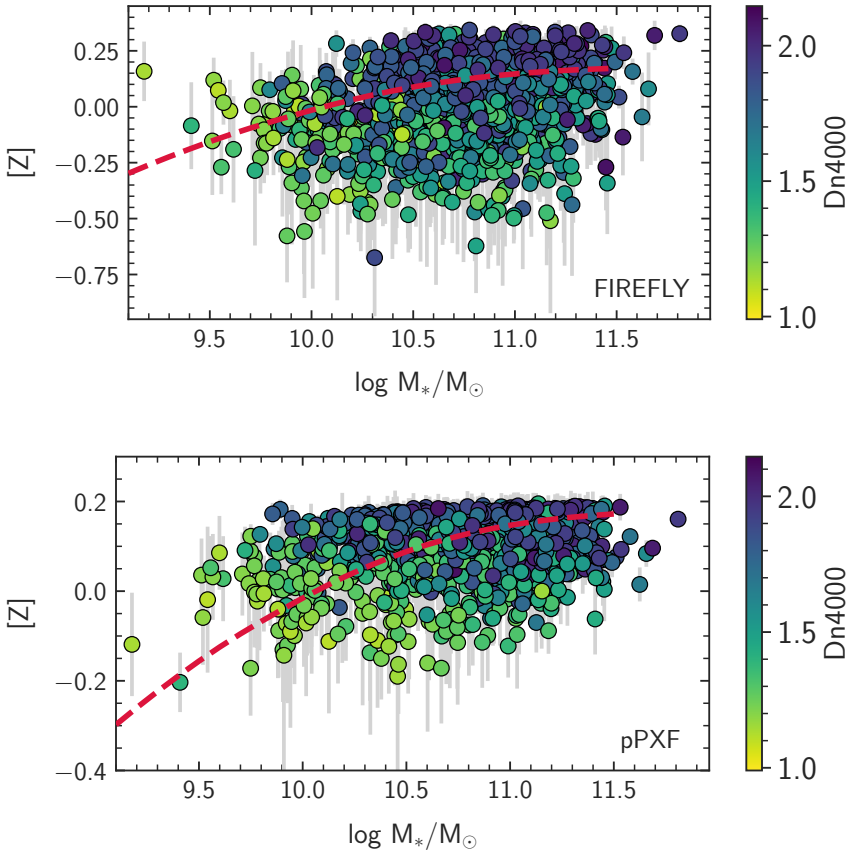

Figure 3.9: The final mass-metallicity relationship for the predicted SDSS spectra. The result for `FIREFLY` can be found in the upper panel, and for `pPXF` in the lower one. Error bars in the metallicity indicate the 1-sigma uncertainty derived by the corresponding bootstrapping procedure. The stellar mass estimates come from the SDSS photometry alone (Maraston et al., 2009). The dashed red lines show the galaxy lookback evolution models from Kudritzki et al. (2021a,b). The colors indicate the value of Dn4000 for each galaxy. Low values (in yellow) point toward young galaxies, and high values (dark blue) towards older stellar populations. SDSS galaxies mostly occupy the space of old and metal-rich populations at low redshift; we also find this in the test set.

ages, metallicities, and dust properties can have nearly identical optical spectra, making it challenging to distinguish between them based solely on their observations (Worthey et al., 1994). With the advent of full-spectral fitting, this problem has become more pressing. The breakdown of the integrated spectrum into a combination of different building blocks (the simple stellar populations) does not necessarily lead to a unique solution, meaning that a different set of SSPs can also create the same flux output. Also, slight fluctuations due to noise can impact the fitting result obtained. There exist intrinsic limitations to the precision to which age and metallicity can be determined without reformulating the problem (i.e., by having a larger wavelength coverage López Fernández et al. 2016, or using higher S/N data).
Fitting the rather low S/N SDSS galaxy spectra is also expected to be plagued by this problem. We, therefore, use `pPXF`, which uses a regularization procedure that is said to be a suitable mathematical tool for such an ill-posed problem. Additionally, we implemented a bootstrapping procedure that tackles the impact of noise in the spectra. Yet, both codes still show degeneracies in age, metallicity, and reddening, which is not surprising. Figure 3.10 shows the difference of metallicity between the predicted and observed metallicity on the x-axis and the deviation in log age on the y-axis. The overall color coding marks the discrepancy in the color excess E(B-V), i.e., reddening. `FIREFLY` (bottom panel) shows a preferred degeneracy in age and metallicity, whereas, for `pPXF`, a degeneracy between age and color excess emerges. This is identical to what Woo et al. (2024) found using mock-spectra from the magnetohydrodynamical simulation IllustrisTNG[6]. Yet, we discourage a direct comparison of both codes as they do not use identical SSPs in our case. Nevertheless, the generative AI's predicted spectra can be used with both codes without problems despite incorporating completely different fitting procedures and templates. Also, it seems that a not negligible part of the deviation in the physical quantities between the predicted and observed spectra seen in the histograms of Figure 3.8 do not necessarily come from a different information content of the observed/predicted spectral pair but from the overall degeneracies which plague full-spectral fitting overall in this S/N regime. As a result, even better predictions of the generative AI might not inevitably lead to better conformity as the limiting factor is the reconstruction of physical quantities from spectra, not the spectra themselves.

3.5.6 Bimodality of Galaxies

A further testing ground for the predicted galaxy spectra is the bimodality of galaxies. For decades, a separation of the galaxy population into two distinct groups has been observed in various physical quantities, including color, mass, age, and spectral indices such as Dn4000. This bimodality suggests that galaxies can be broadly classified into two categories: one population dominated by older, more massive, and redder galaxies with lower star formation rates ('the red sequence') and another population consisting of younger, less massive, bluer galaxies with higher star formation rates ('blue cloud')

[6]https://www.tng-project.org/

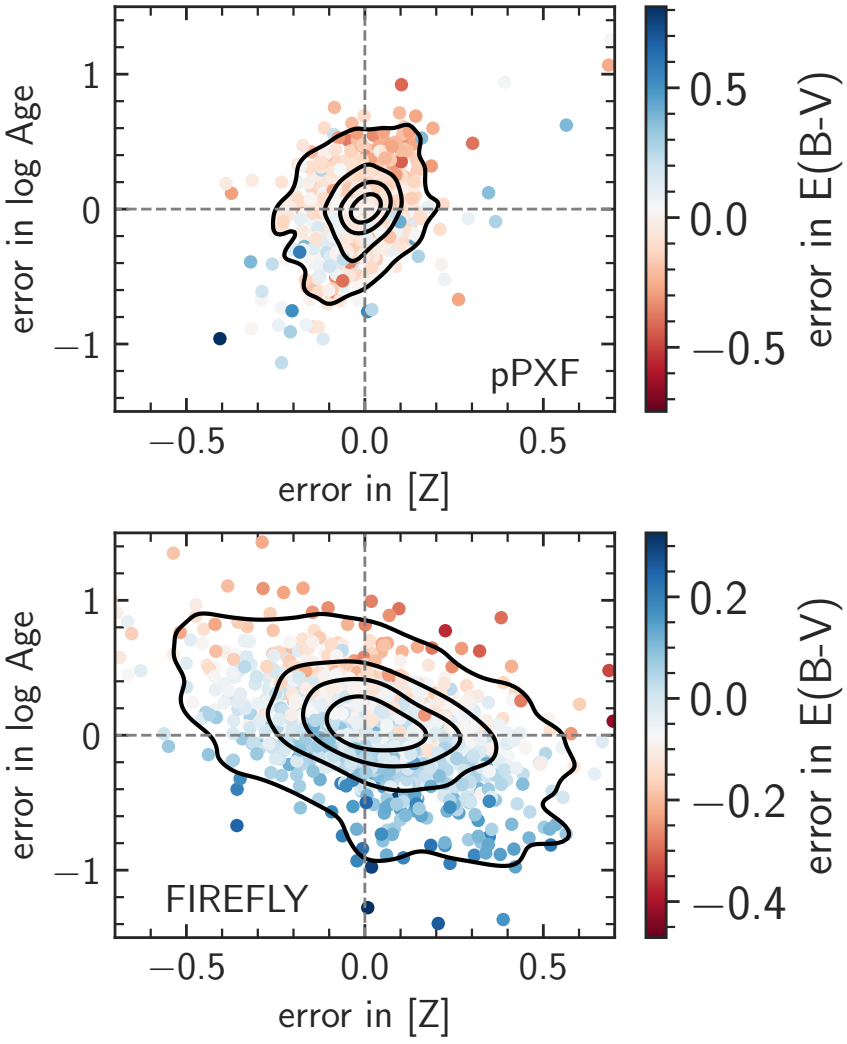

Figure 3.10: Visualization of the degeneracy for both codes. The x-axis (y-axis) depicts the difference between the metallicity (log Age) from the observed and predicted spectrum. In other words, error in $[Z]$ means $[Z]_{obs} - [Z]_{pred}$. The color-coding shows the error in the reddening. Contours are again drawn with a kernel estimate representing a 2D histogram analog. Whereas `FIREFLY` incorporates an expected age-metallicity degeneracy, `pPXF` shifted the problem more towards a blurring in age-reddening.

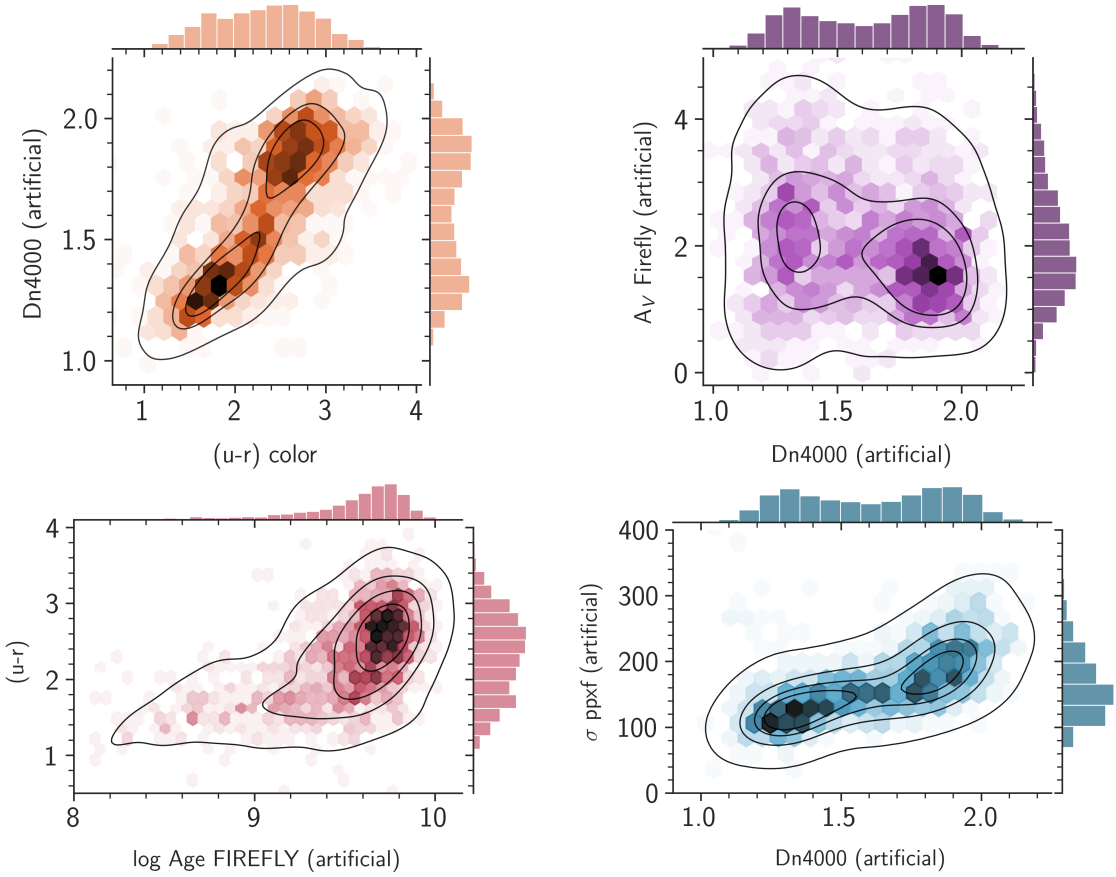

Figure 3.11: Bimodality of the galaxy population in the test sample. All shown quantities are retrieved exclusively with artificial spectra and photometry. No observed SDSS spectra from the test set were used. The color coding in each subplot indicates again how many galaxies reside at a specific (x,y)-position; darker means more galaxies. Additionally, kernel density estimates (KDE) are overdrawn to highlight the bimodal behavior in mean stellar age, extinction, velocity dispersion, extinction, and color.

(Holmberg, 1958; Roberts & Haynes, 1994; Strateva et al., 2001). The analysis of the predicted spectra is able to reproduce this two-fold distribution. Figure 3.11 shows the relation of physical quantities (reddening, stellar age, σ_*, Dn4000, u-r) in relation to each other. All of these data points were solely derived from the artificial spectra and (u-r) color from photometry. As most of these relations are already seen partially in photometric colors itself (Baldry et al., 2004), our machine learning algorithm is supposed to pick them up, and this subsection can therefore be seen as a consistency check.

The relations in the upper panels and the lower left in Figure 3.11 were shown in an identical manner for SDSS galaxies in the work of Mateus et al. (2006) using the full-spectral fitting code `STARLIGHT` (Cid Fernandes et al., 2005, 2007). Their analysis also goes into detail about why one can expect these relations. On this occasion, it should be noted that the depicted log Age (mean stellar age), is actually the mean flux-weighted stellar age, i.e.

a quantity biased towards the age of stars that produce most of the flux in a spectrum. These are mostly very young, high-mass stars formed in recent star formation episodes, which die off quickly (on the scale of less than several hundred million years). Dn4000 and colors are also heavily affected by the flux of these types of stars, which drives some of the observed bimodal behavior seen in Figure 3.11.
Yet, Mateus et al. (2006) used the original available SDSS spectra for their analysis at that time (DR2). We derived the same relations from purely AI-predicted spectra. This reinforces the idea that the generative AI not only produces spectra that have an overall suitable shape but also captures the nature of the galaxies. Morphology, size, and colors of the galaxy are interlinked with the properties of the stellar populations through complicated relations (Skibba et al., 2009; Darg et al., 2010). Our method is capable of taking full advantage of this.
The most interesting relation not mentioned yet is the relation in the lower right panel of Figure 3.11. With `pPXF`, we are able to retrieve values for the velocity dispersion σ_* of the predicted spectra. So, at the end of the day, our generative AI predicts σ_* from photometric broad-band images alone. In the literature, σ_* is commonly measured with the help of spectra or indirect with the help of scaling relations (Bezanson et al., 2012). In practice this can mean for instance that the stellar mass of early-type galaxies (ETGs) is measured photometrically and in a second step σ_* is inferred from its correlation to stellar mass. Here, we derive the values through the utilization of `pPXF` on the artificial spectra, but other template-fitting techniques are also possible. When taking the complete test set (no split in different groups), the measurements of σ_* of the observed and the predicted spectra agree with a negligible median offset of 0.5% with a dispersion of 20%. There seem to be no other attempts (machine-learning or traditional) on the prediction of σ_* in the literature from photometric images. As the colors of a galaxy are not affected by a different velocity dispersion given a spectrum (Tortorelli et al., 2024), the 2D information seems to be the deciding factor here. The generative AI seems to pick up the fundamental plane of elliptical galaxies (relation between the effective radius, average surface brightness, and central velocity dispersion) and is therefore able to predict σ_* values for the corresponding galaxies. For late-type galaxies (LTGs) the situation is less clear, but even there relations between σ_* and other physical properties can be found (Napolitano et al., 2020). But this also explains why the generative AI is doing a better prediction task for elliptical galaxies (see again Figure 3.8 top right).

3.5.7 AGN classification

As a final quality test, we focus on AGN recognition in emission-line galaxies. As the generative model predicts the complete spectrum of the galaxy, not only stellar light, it suggests itself to make use of the predicted emission lines. We make use of the classic BPT diagnostic diagram (Baldwin et al., 1981), which compares the relative strength of collision lines of metals to recombination lines of hydrogen. The primary diagram assesses the line ratio [O III]λ5007/ Hβ to [N II] λ6584/ Hα. Due to the pairs of wavelengths being close together, these ratios are not affected by differential extinction. We measure

		predicted			
		passive	pure SF	AGN	
	passive	359	33	72	464
actual	pure SF	23	448	68	539
	AGN	45	88	370	503
		427	569	510	1506

Table 3.2: Confusion matrix of the test set: The whole test set contains 1 506 galaxies. Each row of the table indicates the actual class and each column represents the predicted class label. A value in the cell is a count of the number of predictions made for a class that are actually for a given class. The diagonal elements count correct predictions, whereas the off-diagonal elements count the galaxies where the emission line ratios of the predicted spectra suggest a wrong class.

the lines after subtracting the fit of the stellar population from `FIREFLY`. Figure 3.12 top shows the BPT diagram for the observed spectra. The galaxies tend to lie in two well-defined sequences in the BPT diagram, leading to a characteristic "seagull" shape. The left-wing sequence in dark blue is associated with star-forming galaxies, while the right-wing sequence in red is associated (partially) with other ionization mechanisms (mostly AGN). The solid line represents the classification curve from (Kewley et al., 2001) defining the upper limit for finding pure SF galaxies. Galaxies were labeled as passive when the equivalent widths (EW) of Hα were smaller than 1 Å or when a visual examination showed no spectra left after the subtraction of the continuum. This threshold has the advantage of being independent of any S/N ratio, which is not available in predicted spectra in the first place. Cid Fernandes et al. (2011b) argue that this criterion is independent of data quality and has a better astrophysical meaning. We measure the EW of Hα with the python package `specutils`. More problematic is the case when one of the four prominent emission lines used in the classical BPT diagram is missing, as this galaxy cannot be placed in Figure 3.12. Our simple solution is then the assignment as a passive galaxy even though this is not physically correct: The center of this galaxy can simply be (partially) dust-obscured. Ratios between obscured and un-obscured AGN can even be as large as ~ 3 (Ballantyne et al., 2011). As this is a general problem of the optical bands we cannot solve, wavelength regimes in the IR provide useful alternatives with less extinction and open up a realm for new line diagnostics (Calabrò et al., 2023).

The BPT diagram of artificial spectra is shown in the right panel of Figure 3.12. From the 1 506 synthetic spectra, 1 079 also showed measurable emission according to the criteria from above. Table 3.2 shows the 3×3 confusion matrix, with rows corresponding to actually being AGN, SF, and passive and columns corresponding to the predicted classification from the artificial spectra. In other words, each row of the matrix represents the objects in the actual class (passive, pure SF, AGN), while each column represents the galaxies in the predicted class from the artificial spectra. From these values, the evaluation metrics can be calculated. The accuracy of predicting a possible AGN is 82%; the precision resides at 73%. The recall is on the same level with 74%. Usually, precision (everything flagged AGN should indeed be an AGN) and recall (not missing any AGNs) are in tension; tuning

machine learning on one of these quantities usually diminishes the other, and the optimal trade-off depends on the task at hand. As this paper acts as a feasibility study, the obtained performance metrics already show encouraging results, especially as these AGN predictions come for free from the generated spectra. No specific algorithm solely used for this purpose had to be trained. For instance, Cavuoti et al. (2014) tried to answer the same question (distinguishing AGN and non-AGN with photometry) using various machine-learning methods applied specifically for this task. Instead of images, they used dereddened SDSS colors, the dereddened magnitude in the r band, the fiber magnitude in the r band, and the photometric redshift. A support vector machine (SVM) achieved the best result with an accuracy of 76% with a test set size of 25466 objects.
For a proper analysis, the uncertainty in the measurements has to be taken into account. The classifications for our observed spectra will certainly not be completely correct and contain some errors. We follow Richardson et al. (2016) in estimating the error budget: Hβ and [O III] λ5007 are free from overlaps with other prominent emission lines and, therefore, rather easy to fit with a Gaussian. Uncertainties arise through noise in the flux and mainly systematic calibration errors, with an estimate of 15%. Contrarily, Hα is partially blended with [N II] $\lambda\lambda 6548, 6584$, which leads to higher errors around 20% for Hα and 30% of [N II] λ6584. Measuring the equivalent width of Hα was multiplied with a Gaussian error with a standard deviation of 1 to incorporate uncertainty. Some measured EWs are slightly lower than 1 Å, and the corresponding galaxy is labeled as passive; with the error budget, they can now find their way in the diagram. All of these errors can be propagated and give a rough probability for the label of the galaxy from the observed spectra (i.e., 95% probability of being an AGN). The same analysis can be done for the artificial galaxy spectra. Now, random number draws can be drawn where each label (true and predicted) is flipped according to the assigned probability (Adebayo et al., 2023). Galaxies in the upper right corner of the BPT diagram have low changes of classification other than AGN (the BPT diagram is in log-scale), whereas pure star-forming galaxies in the vicinity of the Kauffmann line can swap more easily towards AGN candidates. We run 5000 experiments with a simple random number generator in Python and obtain the following uncertainties for the evaluation metrics (see subsection 3.4.3 again for their definitions) from the slightly changed labels:

- Recall = Completeness = 0.736 ± 0.018
- Precision = 0.725 ± 0.016
- Accuracy = 0.818 ± 0.011

As the BPT diagram is on a log scale, uncertainties in the evaluation metrics turn out to be quite small in the end. We still show them here for completeness. More interesting is the reason why the generative AI can predict correct emission lines in the first place. This is at first puzzling since most of the photons in a given broad-band filter come from the stellar continuum and not from an emission line except in extreme cases. Only the broadband photometry of infant massive star clusters is known to be heavily affected by nebular

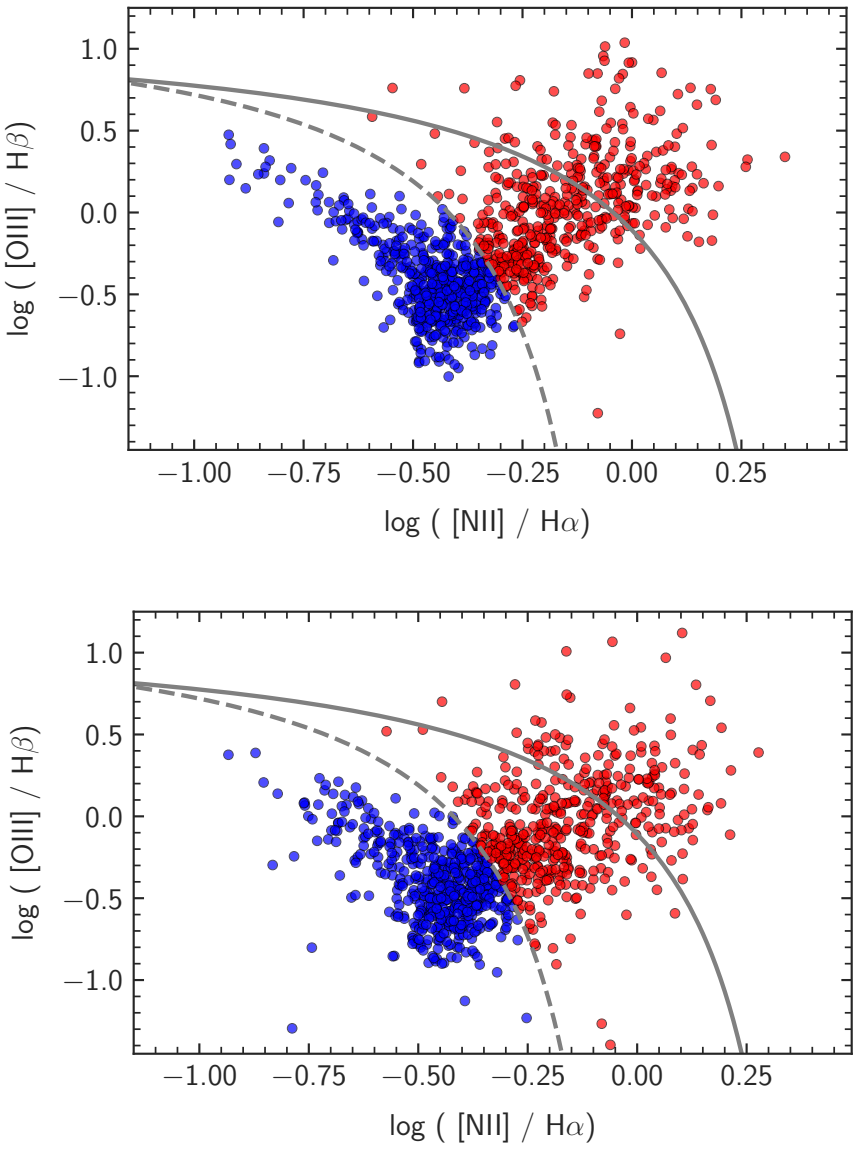

Figure 3.12: BPT diagram for the real spectra (top) and the predicted spectra (bottom). Pure star-forming and possible AGNs are split in both cases by the empirical relation found by Kauffmann et al. (2003) (dashed grey). The additional solid grey line from (Kewley et al., 2001) is drawn as an additional guideline. Galaxies in the region between the two lines (often labeled as composites) probably contain AGN but are still likely to be dominated by the contribution of star formation.

emission, both in lines and continuum (Reines et al., 2010). Yet, our algorithm produces the correct AGN-emission line features only having the photometric images at hand. On second thought, AGNs do not occur at random. A large-scale bar, easily identifiable in photometric images, can, for instance, fuel infalling gas into the central regions of a galaxy (if gas is available in the first place) and trigger both central star formation and the activation of AGNs. Also, star formation activity is stronger in galaxies with large bars (Oh et al., 2012). Work on spatially-resolved spectra in the CALIFA survey by Lacerda et al. (2020) showed further links between AGNs and their hosts. AGNs seem to be concentrated in the high-mass, high-metallicity regime. Their ages are between those of pure blue cloud and red sequence galaxies, and some morphological types are preferred (Sab-Sb types). Additionally, galaxy color and morphology can be affected by the presence of an AGN (Pierce et al., 2010). All of these relations, some of them stronger than others, help relate the optical emission lines with the photometric images. Therefore, it is no surprise that photometric colors (solely colors) correlate with the equivalent widths of emission lines (Abdalla et al., 2008). Yet these authors also found a certain degree of degeneracy between the colors of many passive galaxies and SF ones. The spatial 2D information of colors we provide seems to break this as the distinction between SF and AGN is solid in Table 3.2. Another hint on the feasibility of our approach can be found in Khederlarian et al. (2024), who used a neural network to predict the equivalent width of bright optical emission lines from the continuum, having the creation of mock catalogs in mind. That such approaches proved to be a success (also earlier work from Beck et al. 2016 with PCA) is not a surprise if one considers how emission lines are produced in the first place. Nebular line emission is created when recombination occurs or when collisionally excited states in atoms or ions decay. This, on the other hand, depends on both the ionizing radiation field (ionization parameter, properties of the stars ionizing the gas) and the metallicity of the gas (metals act as coolants in a nebula) (Kewley et al., 2019). Photoionization codes in combination with stellar population synthesis like in Byler et al. (2017) were therefore capable of showing how emission line intensities correlate with the stellar population properties (age, metallicity). The latter also heavily affects the continuum shape and the broad-band photometry.

3.5.8 Disentangling color and spatial information

Our generative AI learns the distribution of spectra conditioned on 5-band images with a resolution of 64x64, containing spatially resolved information (morphology) and pure color/magnitude information. The question arises: which of both is more important in successfully generating synthetic spectra? To explore this, we train multiple CDMs with the same overall architecture as before but different input images by degrading their resolution and color information. Instead of the 64x64 images, stepwise coarser ones with 32x32, 16x16, 8x8, 4x4, 2x2 and finally 1x1 pixels are used. The overall area covered by the image (the FoV) remains the same, as well as the assignment of objects in the training, validation, and test set. Additionally, cases were considered where not all five bands were used; in the most extreme case, only the g-band alone was given to the generative AI. After training for each case, the spectra of the test set are predicted.

Resolution	Bands	MSE ($\times 10^{-3}$)
64x64	5 (ugriz)	10.7
32x32	5 (ugriz)	10.8
16x16	5 (ugriz)	11.5
8x8	5 (ugriz)	12.4
4x4	5 (ugriz)	14.3
2x2	5 (ugriz)	20.0
1x1	5 (ugriz)	24.7
32x32	3 (gri)	11.6
16x16	3 (gri)	12.2
1x1	1 (mean of ugriz)	65.3
1x1	1 (g)	54.0

Table 3.3: Mean MSE over 256 test objects with various image resolutions and bands (lower is better). All spectra are shifted to the rest-frame beforehand, and the fixed region of $4000 - 7000$Å was used for this analysis. The numbers show that high-resolution, multi-band images give the best results.

Not surprisingly, we find that by reducing the image resolution and thus gradually destroying the spatial information but keeping five bands, the mean squared error (MSE) of the generated spectra increases as listed in the first part of table 3.3. This means that predicted spectra now differ more strongly from the observed ones. Also, having more bands available improves the performance of our method (second part of the table). Figure 3.13 illustrates the differences in the generated spectra, showing results for different spatial resolutions and a different number of bands. We show an example of what the images look like after reducing resolution in Figure 3.14.
Our experiment shows that both spatial information and magnitudes are important for the successful generation of spectra, although which is more important is inconclusive. Removing the two outermost bands has approximately the same effect as quartering the number of pixels in an image (one step coarser spatial resolution). Incorporating additional bands, especially small-band filters, will likely improve the results even further. Additional higher spatial resolution might not have such an impact.
Finally, using only one band is not sufficient enough to provide a usable spectrum, as the SEDs and emission lines strongly deviate from the real observations.

3.5.9 Impact of the number of galaxies in the images

The training set is built in such a way that the spectroscopic target galaxy is always in the center of each image. However, in a substantial fraction ($\sim$22%) of images, additional galaxies are visible near the borders. Can such a contamination lead to problems in redshift estimates or other physical properties? Or is it useful information?
To inspect this further, a reliable way of counting galaxies in the broad-band images is needed. We achieve this by using the tricolor g,r,i jpeg-images of each SDSS galaxy available on the SDSS website and working on them with the python `opencv` package. The

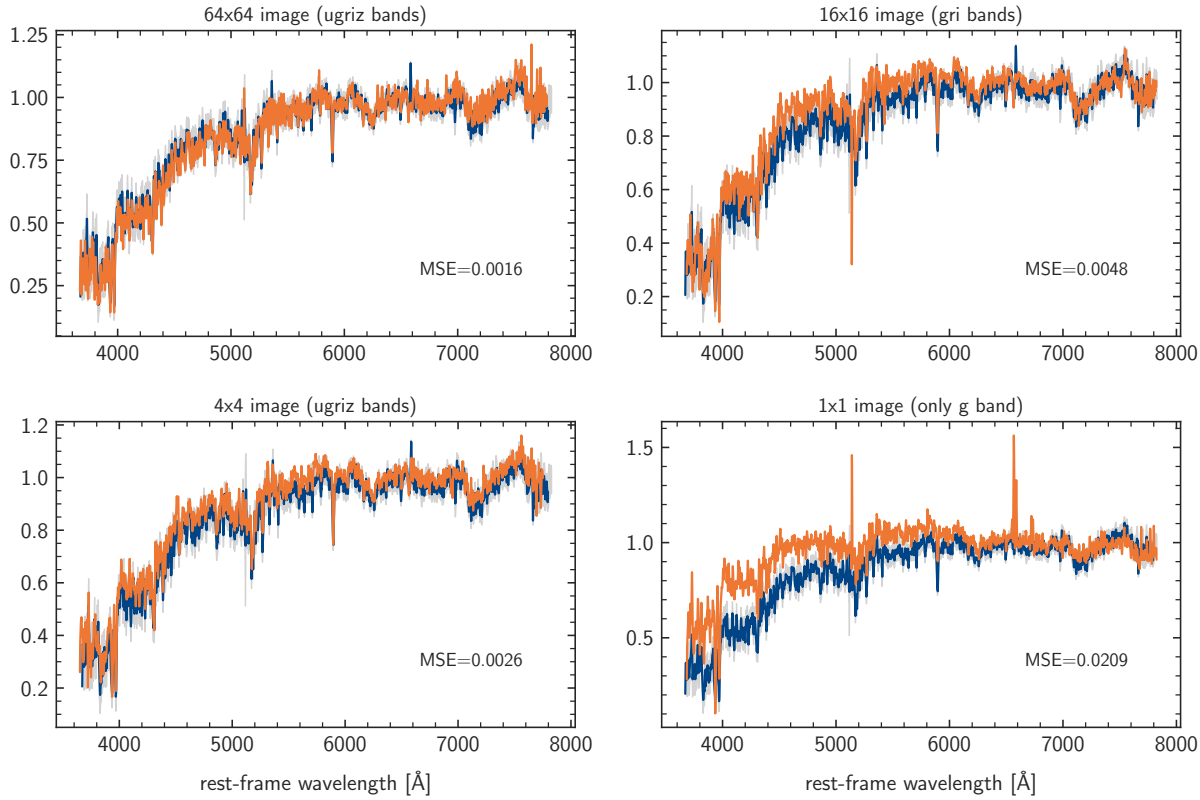

Figure 3.13: Generated spectra (in orange) for the object SDSS J091940.30+144450.4 based on input images with a resolution of 64x64 (in 5 bands), 16x16 (in 3 bands), 4x4 (in 5 bands), 1x1 (in 1 band only). The smoothed observed spectrum is drawn in each subplot in dark blue, and the 1-sigma error bars in grey. All spectra are shifted to the rest frame, and the MSE is written in each sub-figure for a better overview. Results are visibly better with higher-resolution images and more color information available. Given only the information in the g-band causes the generative AI to spuriously predict overall wrong shapes (wrong SEDs) and often strong emission lines.

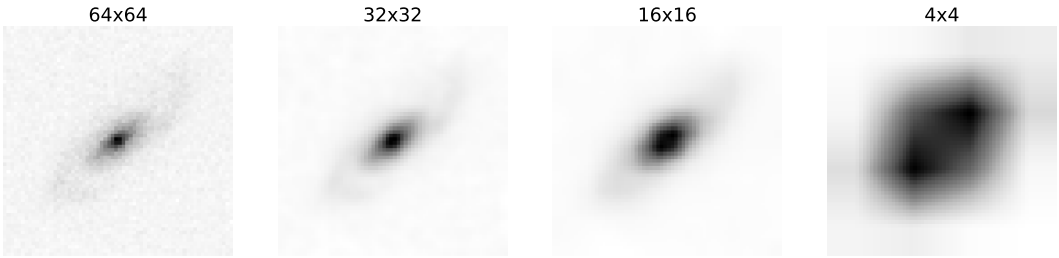

Figure 3.14: Illustration of the r-band of the spiral galaxy SDSS J143419.97-011332.1 using varying resolutions. This galaxy is part of the training set.

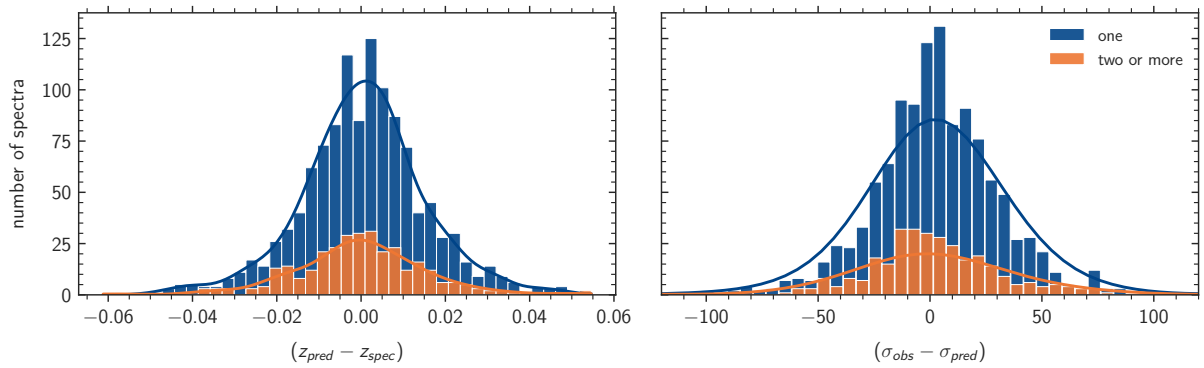

Figure 3.15: Distribution of the differences between the physical quantity derived from the observed and the predicted spectrum. Left: redshift prediction, right: velocity dispersion. The dark blue color means that only one galaxy is visible in the image, and the orange distribution means that two or more galaxies are clearly visible.

process begins with converting each image to grayscale and applying subtle Gaussian blurs. Next, we utilize `opencv`'s built-in threshold function to transform the original image into a binary or segmented format using a predetermined threshold value. This step effectively distinguishes the galaxies (foreground) from the dark background. The final stage involves drawing and tallying contours, which provides the total galaxy count in each image. By adjusting and testing parameters at each processing step, we were able to develop a reliable method for determining the number of additional galaxies in various scenarios. To validate this approach, we manually counted several hundred galaxies as a cross-check.
It is after this step that it is possible to check whether the redshift information we obtain from the predicted spectra gets worse for multiple objects in the image. In Figure 3.15 (left part), we separated the test set into two different groups, depending on the number of overall visible objects in the images: only one galaxy or additional 'contamination' galaxies. The distributions for the various cases appear quite similar and lead to the same σ_{MAD} values as calculated in the sections before.
A further research question might be whether other quantities might be affected by the contamination of additional galaxies. We checked all of them and only found no significant offset in any of the discussed quantities. Shown in Figure 3.15 (right part) is the velocity dispersion where one might expect a small effect given the distribution. In the median, the discrepancy is less than 3 km/s, negligible compared to the error estimate (around 8 km/s) from the bootstrapping procedure. Where it was possible, we also tested our results in the larger test set discussed in the appendix and came to the same conclusions.

3.6 Summary

In this work, we have explored the possibility of generating complete galaxy spectra from photometric broadband images alone. We applied a versatile spectroscopic toolkit to evaluate the quality and information content of our 'artificial' or 'predicted' spectra, leading

us to the following conclusions:

- The mean relative deviation between the observed and predicted galaxy spectra showed the largest discrepancies in low-mass star bursting spirals due to wrong predictions of the extensive emission lines. A refined analysis incorporating the uncertainties of the observed flux at these data points showed that the galaxy spectra from different morphological groups were predicted equally well.

- A comparison between spectral indices measured in predicted and observed spectra showed excellent agreement in Dn4000 and good agreement in the prominent spectral features [MgFe]′, Hbeta, and Mg b. Difficulties for the generative AI arise only in weaker Lick indices such as Fe5270 and Fe5335.

- The predicted and observed spectra were evaluated with two stellar population fitting codes (`pPXF` & `FIREFLY`). The mean metallicity of the galaxy was recovered from the artificial spectrum; 86% of all predicted spectra coincide in metallicity within 0.10 dex with `pPXF`. `FIREFLY` performed worse with 70% agreement within 0.2 dex. Overall, the use of `Firefly` delivered metallicities approximately 0.1 dex higher than those of `pPXF`. This is consistent with earlier findings from the literature comparing the performance of these two fitting codes. Values of the mean age of the stellar population and extinction showed good agreement: 0.3 dex scatter in log age and 0.1 dex scatter in E(B-V) as an overall rule of thumb.

- With our procedure generating artificial spectra, it becomes possible to predict the central velocity dispersions from photometric images alone. To our knowledge, this is the first attempt in the literature to do so. On our test set, we obtain values that are consistent with values from the observed spectra within 20%.

- The presented machine learning algorithm recovers the famous bimodality of galaxy populations in colors, Dn4000, mean stellar age, extinction, and velocity dispersion using solely artificial spectra. It links colors and their 2D distribution (including morphological features) in the photometric images with physical quantities retrievable from spectra.

- It is possible to identify AGN candidates from the photometric images with an accuracy of 82%. For this, emission line ratios of the artificial spectra were evaluated in the BPT diagram.

In short, our approach can successfully predict various galaxy properties without explicitly training to do so. We show reasonable estimates for quantities such as age, metallicity, dust reddening, and velocity dispersion from photometric images alone by making a detour over artificial spectra, and more properties can easily be derived. The use of different fitting codes, different spectral templates, or the calculation of other physical quantities not mentioned here can be realized with the predicted spectra at free will - even years after the original generation of the spectra with the GenAI. This freedom in research justifies

the computational costs. We believe the most promising applications of our method are in upcoming all-sky surveys such as Euclid and LSST, which will only have spectroscopic information on a small subset of the objects for which photometric images will be taken. By generating artificial spectra, we can, for instance, determine objects that are likely to be interesting and perform more targeted spectroscopic follow-ups.

3.7 Appendix

3.8 On the size of the test set

The size of a test set in machine learning is a crucial factor that can significantly influence model evaluation and performance assessment. In this paper, we worked with a relatively small test set of 1506 objects (0.5% split). The bottlenecks of the whole analysis of the test set are the full-spectral fitting codes, which take of the order of minutes for one spectrum (including bootstrapping procedure). Using machine-learning techniques for the spectral evaluation seems promising, as recently demonstrated in Hunt et al. (2024). However, analyzing the performance of a black box ML algorithm with another new ML algorithm is too extreme and cannot be managed in one step. We believe it makes more sense to evaluate the predicted spectra in a traditional and well-founded manner.
To keep the computation times manageable, the presented test set was chosen quite small, but this always carries the danger of not having entirely representative performance estimates. In the following, we show that our results are nevertheless reliable by additionally evaluating the GenAI results on a test sample consisting of 14000 objects ($\sim 5\%$) solely with `ppxf`. We chose the exact same settings as in the main part of the paper and recreated the Figures 3.5, 3.6, and 3.8 now with this larger test set. Concerning the redshift estimates, we obtained a new value of $\sigma_{MAD} = 0.01178$ compared to $\sigma_{MAD} = 0.01177$ from the small test set. The obtained distributions look nearly identical compared to the ones of the smaller test set. We, therefore, conclude that it is unlikely that the smaller statistic hurts the results in the main body of the paper.

3.9 Technical details

In this section, we provide a more detailed description of our method, including technical aspects of diffusion models and contrastive learning, following the workflow in Figure 3.3. In the first step, we learn the conditional distribution over low-resolution spectra $p(\text{low-res spectrum} \mid \text{image})$ with a conditional diffusion model. **Diffusion models** are generative models that model the probability distribution of observed data and can generate new samples that closely mirror the characteristics of the training set. Diffusion models are trained using a combination of two Markov chains of length T, known as the *forward* and *backward* processes (Ho et al., 2020).

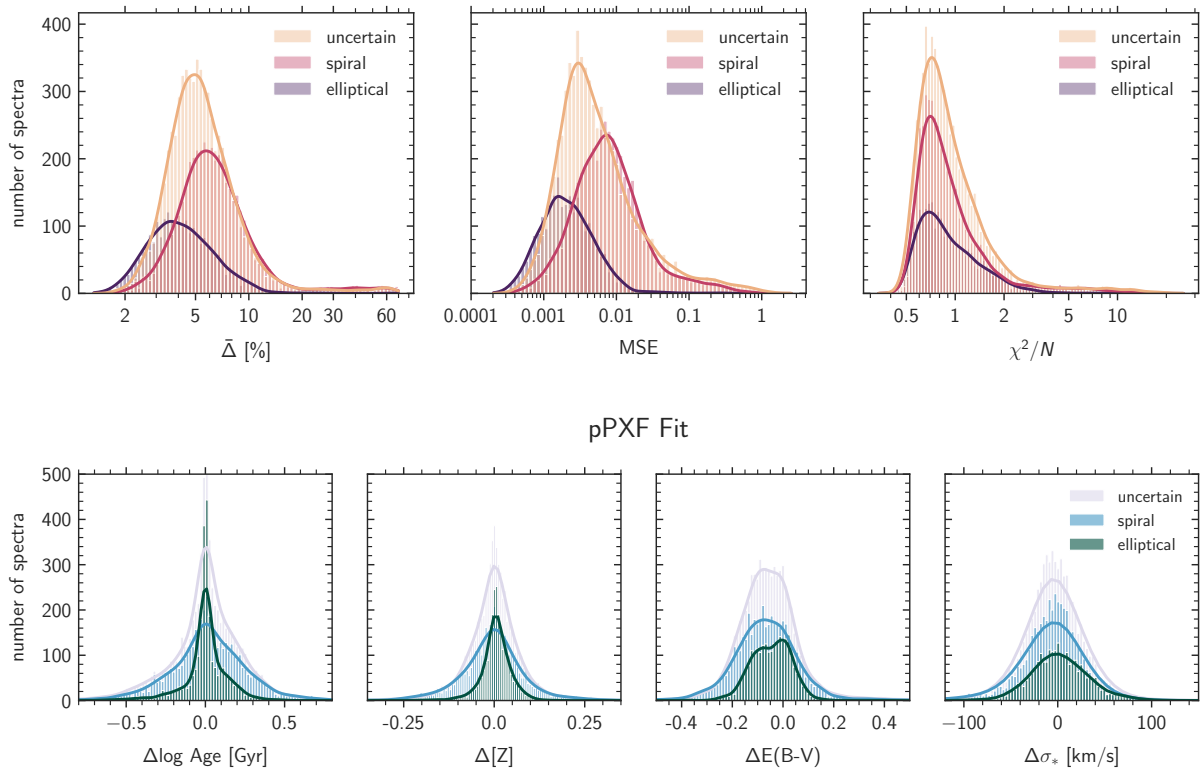

Figure 3.16: Updated version of Figure 3.5 and 3.8 with the larger test set. Top: Histograms of $\overline{\Delta}$, Mean Square Error (MSE), and χ^2/N (with N the number of flux-points) of the 14000 galaxies split into the different morphologies. Bottom: Distribution of differences in the derived physical quantities for pPXF between the real and predicted spectra.

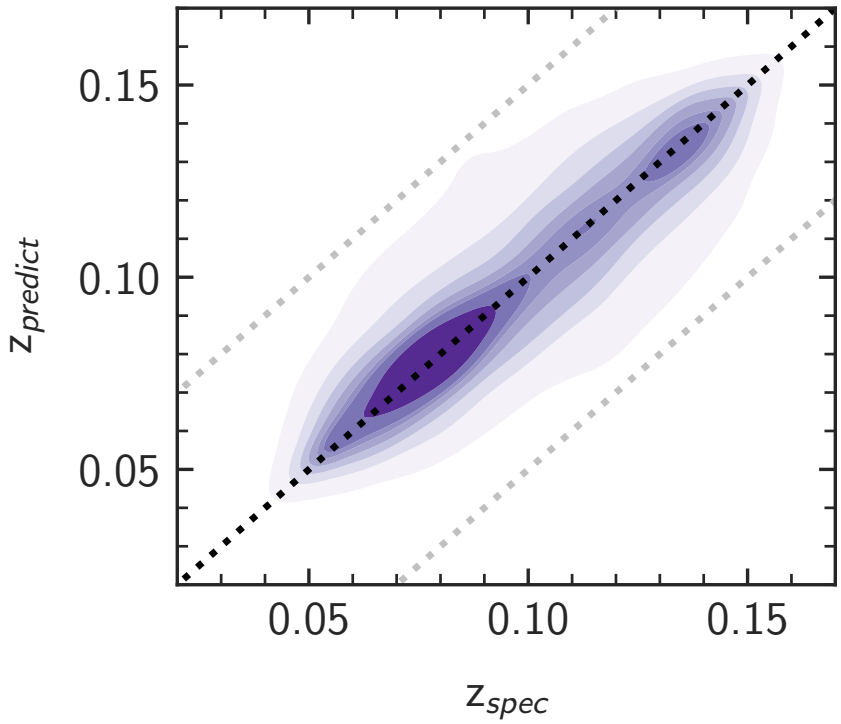

Figure 3.17: Updated version of of Figure 3.6 with the larger test set. It shows the comparison between the spectroscopic redshift from the observed spectra (z_{spec}) and the prediction from our generative AI for the galaxies ($z_{predict}$). Instead of single data points, the overall kernel density estimate is shown for a clearer point of view. The grey dotted lines mark the regions with catastrophic outliers with $|\Delta z/(1+z_{spec})| > 0.05$. The black dotted line shows the one-to-one relation.

The forward process gradually adds Gaussian noise to a sample x_0 with a fixed variance schedule $\beta_1, ..., \beta_T$ depending on the time step $t \in [1, T]$. This process transforms the original sample x_0 into Gaussian noise at x_T. The backward denoising process aims to reverse the forward process by learning to predict the denoised version x_0 from x_t with an autoencoder neural network ϵ_θ. In practice, ϵ_θ learns to predict the noise (Ho et al., 2020; Rombach et al., 2022), with the simplified objective

$$L_{DM} = \mathbb{E}_{x_0,t,\epsilon\sim\mathcal{N}(0,\mathbf{I})} \left(\| \epsilon - \epsilon_\theta(x_t, t) \|^2 \right). \tag{3.10}$$

After training is complete, the backward process describes the data distribution. With it, diffusion models can generate new samples by sampling from an isotropic Gaussian distribution and using the backward process to iteratively denoise it for T timesteps.
Vanilla diffusion models generate *unconditional* samples. In our case, these will be spectra that are similar to the spectra in the training dataset, but they are not related to a specific image. Instead, in order to generate spectra for a specific object, we condition the noise prediction network ϵ_θ on the input image. This allows us to sample from a *conditional* distribution of spectra given an image. These models are known as conditional diffusion models (CDM). Specifically, the CDM projects the condition image y to a latent space using a learnable mapping τ_θ and introduces it into the network with cross-attention at multiple layers of the autoencoder (Rombach et al., 2022). This gives the conditional loss function for a sample x,

$$L_{CDM} = \mathbb{E}_{x_0,y,t,\epsilon\sim\mathcal{N}(0,\mathbf{I})} \left(\| \epsilon - \epsilon_\theta(x_t, t, \tau_\theta(y)) \|^2 \right), \tag{3.11}$$

i.e., it learns to denoise a spectrum given the corresponding image.
Thus, the first step of our method is sampling multiple possible spectra for an object from the low-resolution CDM, $\mathrm{CDM_{lr}}$, given its image. However, as described in the main text, CDMs do not allow for density estimation and sampling from the CDMs results in multiple possible spectra for a given object without information on their likelihood. To select the most promising spectra for follow-up evaluation, we use multimodal contrastive learning (Chen et al., 2020) as a heuristic to find high-likelihood samples of the learned distribution.
Contrastive learning is a method for self-supervised learning. Unlike traditional supervised learning, which relies on manual annotations, in self-supervised learning, the supervision is automatically generated from unlabelled input data. For contrastive learning, the underlying idea is that two *views* of a sample, such as two pictures of an object taken at different angles, should have a similar representation.
Formally, contrastive learning optimizes a neural network to minimize the distance between the features of two views of the same object while maximizing the distances to the features of other samples. This contrastive loss for a batch of size N is given by (Chen et al., 2020)

$$\ell_{i,j} = -\log \frac{\exp(\mathrm{sim}(\boldsymbol{z}_i, \boldsymbol{z}_j)/\tau)}{\sum_{k=1}^{2N} \mathbf{1}_{[k\neq i]} \exp(\mathrm{sim}(\boldsymbol{z}_i, \boldsymbol{z}_k)/\tau)}, \tag{3.12}$$

for views i and j of an object, where $\boldsymbol{z}$ represents their feature representation, τ the temperature, and $\text{sim}(\cdot, \cdot)$ a similarity measure, typically the cosine similarity.
In our case, the two views of an object are given by its image and spectrum. When the different views come from different modalities, this technique is called multimodal contrastive learning. In our case, we learn to map images and spectra into a shared representation space, where images and spectra with similar representations are likely to belong to the same object.
The second step of our algorithm involves using the contrastive network trained on the low-resolution spectra and corresponding images to rank the generated spectra by CDM_{lr} based on the similarities between their representations and that of the original image. We then select the best-matching samples to continue with the next steps. At this point, we have generated a handful of high-likelihood but low-resolution spectra for an object.
For step three, we train a second CDM to generate full-resolution spectra using the same process as in step one, with the only difference being an extra condition on the corresponding low-resolution spectrum. We do this by stacking the low-resolution spectrum with the original one channel-wise into x_t^{comb}, which is then used to train the full-resolution CDM:

$$L_{CDM_{sr}} = \mathbb{E}_{x_0,y,t,\epsilon\sim\mathcal{N}(0,\mathbf{I})} \left(\| \epsilon - \epsilon_\theta(x_t^{comb}, t, \tau_\theta(y)) \|^2 \right). \tag{3.13}$$

In short, this model learns to denoise a full-resolution spectrum, given the corresponding low-resolution spectrum and image, and is used to generate full-resolution versions of the most artificial spectra from step two.
The fourth step uses a second contrastive network to find the best matching full-resolution spectrum for an image. This contrastive network is trained as in step two, with the only difference being that it uses full-resolution instead of low-resolution images.
In summary, our full method samples several 563-dimensional spectra for an image with CDM_{lr}. We select the three best synthetic spectra according to the low-resolution contrastive network. Then, we generate five full-resolution spectra for each of the selected low-resolution spectra. Finally, we select the best-matching spectrum with the full-resolution contrastive network, giving us the final synthetic spectrum for the object.

3.10 SQL Query

```
    SELECT
--/ Ids
 S.specObjID, SP.objID, P.ra, P.dec,
  --/ Needed for spectra retrieving
 S.firstrelease, S.programname, S.instrument, S.run2d,
 --/ Redshift and velocity dispersion
 S.z,  S.zerr, S.velDisp, S.velDispErr,
 --/ Petrosian radius
 P.petroRad_u, P.petroRad_g, P.petroRad_r, P.petroRad_i, P.petroRad_z,
  --/ Radius containing 90% of Petrosian flux
 P.petroR90_u, P.petroR90_g, P.petroR90_r, P.petroR90_i, P.petroR90_z,
 --/ Magnitude in 3 arcsec diameter fiber radius
 P.fiberMag_u, P.fiberMag_g, P.fiberMag_r, P.fiberMag_i, P.fiberMag_z,
 --/ r-band extinction
 P.extinction_r,
```

```
--/ Overall signal-to-noise-squared measure for plate
 S.plateSN2,
--/ surface brightness fit (exponential and de Vaucouleurs)
 P.modelMag_u, P.modelMag_g, P.modelMag_r, P.modelMag_i, P.modelMag_z,
 P.cmodelMag_u, P.cmodelMag_g, P.cmodelMag_r, P.cmodelMag_i, P.cmodelMag_z,
 --/ from galaxy zoo
 z.p_mg, z.p_el_debiased, z.p_cs_debiased, z.spiral, z.elliptical, z.uncertain,
 --/ photometric mass estimates
 M.logMass as logMass_Maraston09, CD.logMass as logMass_ConroyDust, CND.logMass as logMass_ConroyNoDust

INTO
 mydb.spectraGeneration

FROM
 MyDB.MyTable_2 as SP
 JOIN SpecObj as S ON SP.specObjID=S.specObjID
 JOIN PhotoObjAll as P ON SP.objID=P.objID
 JOIN zooSpec as Z ON SP.specObjID=Z.specObjID
 JOIN stellarMassFSPSGranWideDust as CD  ON SP.specObjID=CD.specObjID
 JOIN stellarMassFSPSGranWideNoDust as CND ON SP.specObjID=CND.specObjID
 JOIN stellarMassPassivePort as M  ON SP.specObjID=M.specObjID
WHERE

 S.class = 'GALAXY' --/ select only galaxies (spectroscopically)
 AND P.mode = 1 --/ includes only objects which are "primary" in the survey
 AND S.z >= 0.05 --/ minimum redshift
 AND S.z<=0.15 --/ maximum redshift
 AND S.instrument = 'SDSS' --/ spectra from only one instrument

 --/ Removing Objects with Deblending Problems

 AND (flags_r & 0x20) = 0 --/ not PEAKCENTER
 AND (flags_r & 0x80000) = 0 --/ not NOTCHECKED
 AND ((flags_r & 0x400000000000) = 0 OR P.psfmagerr_r <= 0.2)
 --/ high S/N or not DEBLEND_NOPEAK this is suggested by SDSS

 --/ Removing Objects with Interpolation Problems

 AND (flags_r & 0x800000000000) = 0 --/ not PSF_FLUX_INTERP
 AND (flags_r & 0x10000000000) = 0 --/ not BAD_COUNTS_ERROR
 AND ((flags_r & 0x100000000000) = 0 OR (flags_r & 0x1000) = 0)
 --/ not both INTERP_CENTER AND CR

 --/ Removing Suspicious Detections
    --/ For stars AND galaxies (with type = 6 or 3), the "clean" flag checks
    --/ that the object has pixels detected in the first pass (BINNED1),
    --/ that it isn't saturated (SATURATED), AND that it has a valid radial
    --/ profile (NOPROFILE).

 AND (flags_r & 0x10000000) != 0 --/ BINNED1
 AND (flags_r & 0x40000) = 0 --/ not SATURATED
 AND (flags_r & 0x80) = 0 --/ not NOPROFILE

  --/ Remove Meaningless Values

 AND P.petroRad_u>0
 AND P.petroRad_g>0
 AND P.petroRad_r>0
 AND P.petroRad_i>0
 AND P.petroRad_z>0

 AND P.petroR90_u>0
 AND P.petroR90_g>0
 AND P.petroR90_r>0
 AND P.petroR90_i>0
```

```
AND P.petroR90_z>0

AND P.petroRad_u<20
AND P.petroRad_g<20
AND P.petroRad_r<20
AND P.petroRad_i<20
AND P.petroRad_z<20

AND P.petroR90_u<20
AND P.petroR90_g<20
AND P.petroR90_r<20
AND P.petroR90_i<20
AND P.petroR90_z<20

AND P.fiberMag_u>0
AND P.fiberMag_g>0
AND P.fiberMag_r>0
AND P.fiberMag_i>0
AND P.fiberMag_z>0

AND P.modelMag_u>0
AND P.modelMag_g>0
AND P.modelMag_r>0
AND P.modelMag_i>0
AND P.modelMag_z>0

AND P.cmodelMag_u>0
AND P.cmodelMag_g>0
AND P.cmodelMag_r>0
AND P.cmodelMag_i>0
AND P.cmodelMag_z>0
```

4

The TYPHOON stellar population synthesis survey: I. The young stellar population of the Great Barred Spiral NGC 1365

Published in the Astrophysical Journal, **960**:83 (12pp), 2024 January 1

Authors: Eva Sextl, Rolf-Peter Kudritzki, Andreas Burkert, I-Ting Ho, H. Jabran Zahid, Mark Seibert, Andrew J. Battisti, Barry F. Madore, and Jeffrey A. Rich

Research Context: We start to apply SPS on spatially resolved spectra of the TYPHOON integral-field spectroscopic survey. The observations which took place at the 2.5m du Pont Telescope at the Las Campanas Observatory in Chile, provide pseudo-IFS data of 44 nearby, large angular-sized (> 3') galaxies in the southern sky. Unlike traditional integral-field units (IFUs) that capture the entire field of view at once, TYPHOON uses the Progressive Integral Step Method (PrISM), also referred to as the 'step-and-stare' technique. This method moves a long slit across the galaxies, enabling nearly complete coverage of the optical disk in a more efficient and cost-effective manner for galaxies with high surface brightness that span large areas of the night sky. The spectrograph also has a rare wavelength regime starting already at 3650 Å, which offers best opportunities to study young stellar populations in detail. A key finding from our analysis is an unusual behavior observed in the young stellar population (< 100 Myr) within the central kiloparsec of this galaxy. Although we later identified such behavior in other galaxies, the signal in NGC 1365 is exceptionally clear. See also section 5.6 in this context, which provides a detailed view of the inner region of NGC 1365 using the newer definition of metallicity, termed 'physical metallicity' introduced in 1.10.

Abstract: We analyze TYPHOON long slit absorption line spectra of the starburst barred spiral galaxy NGC 1365 obtained with the Progressive Integral Step Method covering an area of 15 square kpc. Applying a population synthesis technique, we determine the spatial distribution of ages and metallicity of the young and old stellar population together with star formation rates, reddening, extinction and the ratio R_V of extinction to reddening. We detect a clear indication of inside-out growth of the stellar disk beyond 3 kpc characterized by an outward increasing luminosity fraction of the young stellar population, a decreasing average age and a history of mass growth, which was finished 2 Gyrs later in the outermost disk. The metallicity of the young stellar population is clearly super solar but decreases towards larger galactocentric radii with a gradient of -0.02 dex/kpc. On the other hand, the metal content of the old population does not show a gradient and stays constant at a level roughly 0.4 dex lower than that of the young population. In the center of NGC 1365 we find a confined region where the metallicity of the young population drops dramatically and becomes lower than that of the old population. We attribute this to infall of metal poor gas and, additionally, to interrupted chemical evolution where star formation is stopped by AGN and supernova feedback and then after several Gyrs resumes with gas ejected by stellar winds from earlier generations of stars. We provide a simple model calculation as support for the latter.

4.1 Introduction

Spectroscopic studies of galaxies with integral field units (IFU) have become an important tool to investigate the evolution of galaxies. Spatially resolved maps of their chemical composition, stellar ages, star formation rates and gas properties provide unique information about the complex physical processes affecting galaxy evolution (see, for instance, Bittner et al. (2020), Carrillo et al. (2020), Parikh et al. (2021), Emsellem et al. (2022), Pessa et al. (2023), Westmoquette et al. (2011), Sánchez-Blázquez et al. (2014), Thainá-Batista et al. (2023)). Usually, because of the relatively small field of view of the available IFUs (of the order of one arcminute) this work has been mostly concentrated on galaxies with small angular size or only central regions. Therefore, given the enormous potential of these spectroscopic stellar population studies, we have started a project with the goal to extend this work to cover large parts of galactic disks together with their central regions. The TYPHOON survey which uses stepwise combined long slit spectra of galaxies seems ideal for this purpose. For the population synthesis analysis of the integrated stellar population absorption line spectra we will use the technique developed and described in Sextl et al. (2023).

We start the project with the population synthesis analysis with the starbursting type 2 Seyfert barred-spiral NGC 1365 in the Fornax cluster. With an isophotal radius of R_{25} = 5.61 arcmin or 29.55 kpc at a distance of 18.1 Mpc (Ho et al., 2017) NGC 1365 is a galaxy of huge dimensions and ideally suited for a long-slit IFU-like investigation. It is well studied with respect to the dynamics of its gas and stellar content (Lindblad (1999),

Zánmar Sánchez et al. (2008), Jałocha et al. (2010)). It is an almost face-on galaxy, which avoids line of sight confusion complications and minimizes effects of interstellar extinction. The central region shows extensive star formation and the presence of a low luminosity AGN with two conical outflows (see Venturi et al. (2018) and references therein). In addition, the chemical composition of its ionized ISM has been carefully investigated (Ho et al., 2017; Chen et al., 2023) and first long slit star formation studies have already been carried out (Sánchez-Blázquez et al., 2011). Since the galaxy is characterized by strong star formation activity, the blue sensitivity of TYPHOON is an advantage and allows for a good characterization of the properties of its young stellar population. This will provide important information extending the work and the results obtained recently within the comprehensive ESO VLT PHANGS-MUSE survey (Emsellem et al., 2022; Pessa et al., 2023).
We describe the observations in section 4.2 and the population synthesis analysis technique in section 4.3. The results are presented in sections 4.4 followed by a discussion in 4.5.

4.2 Observations

The TYPHOON survey (P.I. B. Madore) uses the Las Campanas du Pont 2.5m telescope Wide Field CCD imaging spectrograph with a custom long-slit of 18 arcmin length and 1.65 arcsec width which progressively scans across the galaxies (Progressive Integral Step Method, PrISM) to construct 3D data cubes of 1.65 times 1.65 arcsec^2 spaxels. At a distance of 18.1 Mpc (Jang et al., 2018) 1.65 arcsec are equivalent to 145 pc. The spectral resolution corresponds to a FWHM of 8.2 Å. In the case of NGC 1365 the slit was placed along the north-south direction. More details of the observations are described in Ho et al. (2017) and Chen et al. (2023). Figure 4.1 provides a BVR color composite image constructed from the TYPHOON data cube. The figure has already been shown in Ho et al. (2017) but is repeated here for illustration. NGC 1365 is a massive galaxy with a stellar mass of log $M_* = 10.95$ (in solar units, Muñoz-Mateos et al. 2013, Leroy et al. 2019), an isophotal radius of 5.61 arcmin (de Vaucouleurs, 1991), inclination angle of 35.7 degrees and a position angle of 49.5 degrees based on 2MASS photometry (Jarrett et al. 2003, see Ho et al. 2017 Table 1).
For our population synthesis analysis we use the spectral range from 4000 to 7070 Å where the flux calibrated spectra have the best signal. Compared to the range from 4800 to 7000 Å used in the PHANGS-MUSE study by Pessa et al. (2023) this is an important blueward extension which enables a more accurate characterization of the young stellar population. If needed, we combine the spectra of neighboring individual spaxels by Voronoi binning using Cappellari & Copin (2003) to obtain a minimum signal-to-noise ratio of 30 in the stellar continuum at 5000 Å. However, in order to avoid averaging over too large spatial dimensions we exclude bins consisting of more than 400 TYPHOON spaxel. We also remove bins containing the contribution of bright foreground stars. This leaves us with spectra of 359 bins distributed over the galaxy. As an example, Figure 4.2 shows the spectra of two bins and the corresponding stellar population fits. Figures 4.3 and 4.5 give an impression

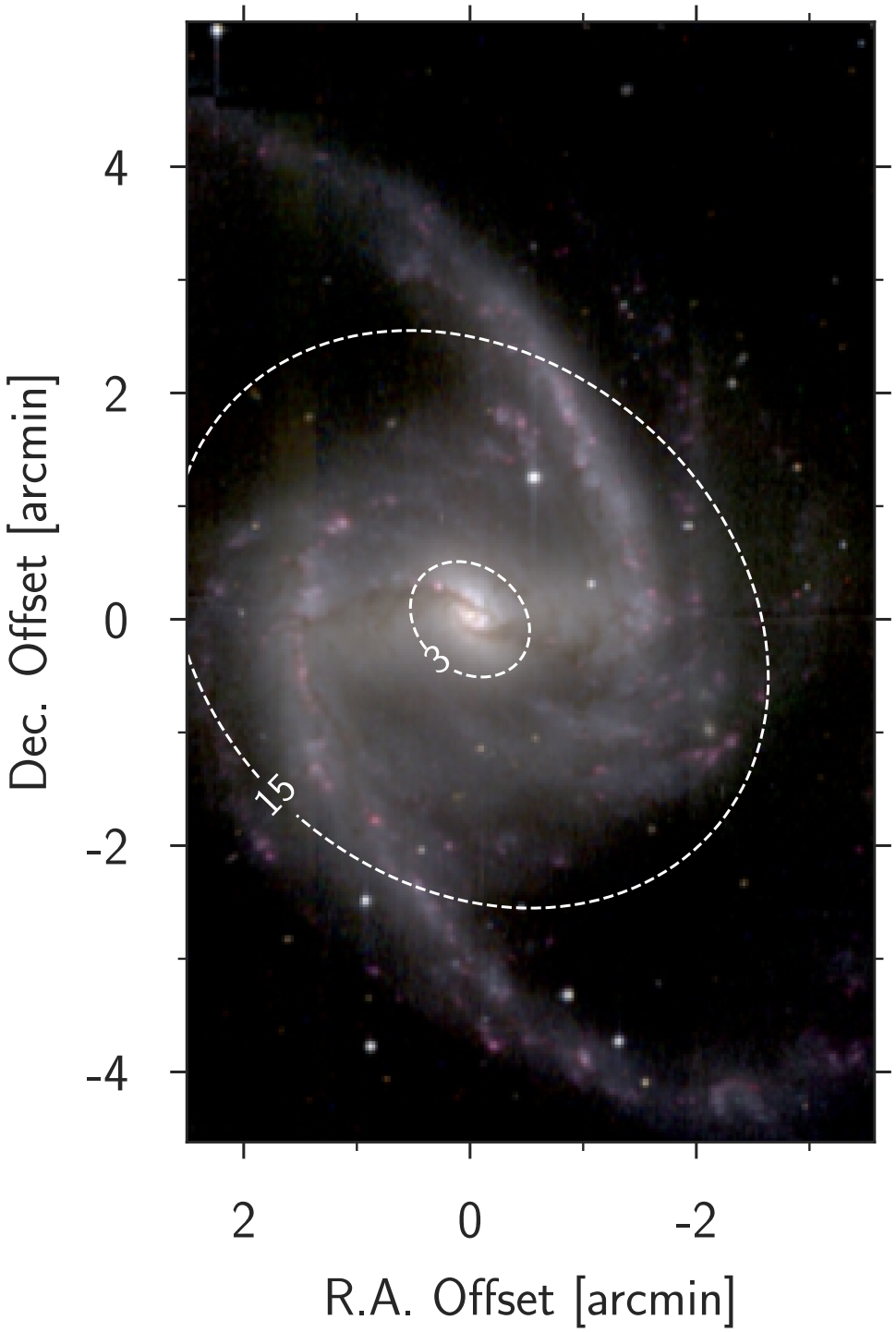

Figure 4.1: TYPHOON BVI color composite image of NGC 1365. The position of the central AGN is indicated by a small green cross. The bar extends roughly 200" on the sky (Lindblad, 1999) corresponding to ∼17.6 kpc projected length. The two dashed ellipses indicate galactocentric distances of 3 and 15 kpc, respectively. East is towards the left and north towards the top.

of the spatial distribution of the bins analyzed.

4.3 Analysis Method

Our population synthesis method is described in detail in Sextl et al. (2023). We fit the SED and absorption line spectra of the integrated stellar population with a linear combination of the spectra of single stellar populations (SSP) of different ages and metallicities. This allows us to constrain the average metallicity and age of the population together with reddening E(B-V), extinction A_V and the ratio $R_V = A_V/E(B\text{-}V)$, which characterizes the steepness of the reddening law. The observed and SSP template spectra are normalized in the range between 5500 to 5550 Å. Therefore, the metallicities and ages obtained in this way are V-band luminosity weighted averages (see Sextl et al. 2023).
The model spectrum of the integrated stellar population M_λ combines the spectra of single stellar populations (SSPs) $f_{\lambda,i}(t_i, [Z]_i)$ with age t_i and logarithmic metallicity $[Z]_i = \log Z/Z_\odot$

$$M_\lambda = D_\lambda(R_V, E(B-V)) \left[\sum_{i=1}^{n_{SSP}} b_i f_{\lambda,i}(t_i, [Z]_i) + b_a f_\lambda^a \right] \tag{4.1}$$

where the coefficients b_i describe the contribution of burst i with age t_i and metallicity $[Z]_i$ and $D_\lambda(R_V, E(B-V))$ accounts for the absorption by interstellar dust. b_a accounts for the contribution of a featureless AGN continuum f_λ^a with wavelength slope $\lambda^{-0.5}$ (as in Cardoso et al. (2017)). This additional template is only utilized in the fitting process of bins near the center which show broad-line region (BLR) features in their spectra.
We apply the Flexible Stellar Population Synthesis code (FSPS, version 3.2) (Conroy et al., 2009; Conroy & Gunn, 2010a) for the calculation of the individual SSP spectra together with the MILES library (Sánchez-Blázquez et al., 2006) and MESA stellar evolution isochrones (Choi et al., 2016; Dotter, 2016) and a Chabrier (2003) initial mass function are adopted. It is important to note that FSPS utilizes not only one main stellar library option, but adds supplementary stellar spectra from complementary evolutionary phases. Thus, the limited number of stars with T > 9000 K in the empirical MILES library (as can be seen in Martins & Coelho (2007)), is enlarged by hot star spectra from Eldridge et al. (2017) and Wolf-Rayet spectra from Smith et al. (2002). Spectra of AGB-, post-AGB- and carbon stars are added (Lançon & Wood, 2000; Rauch, 2003; Aringer et al., 2009). The final set of our SSP spectra is then adjusted to the TYPHOON spectral resolution. Because of the low TYPHOON spectral resolution we do not consider the line broadening effects of stellar velocity dispersion, which has been measured, for instance, by Bittner et al. (2020) or Pessa et al. (2023).
As in Sextl et al. (2023) we account for finite time lengths of the stellar bursts of 0.1, 1.0 and 10.0 Myr but we find that SSP spectra with the shortest burst length result in the best spectral fits with lowest residual χ^2 value. To account for the effects of interstellar dust, we apply the attenuation law by Calzetti et al. (2000) with variable R_V (deviating from the Calzetti standard value R_V=4.05), derived empirically in local starburst galaxies.

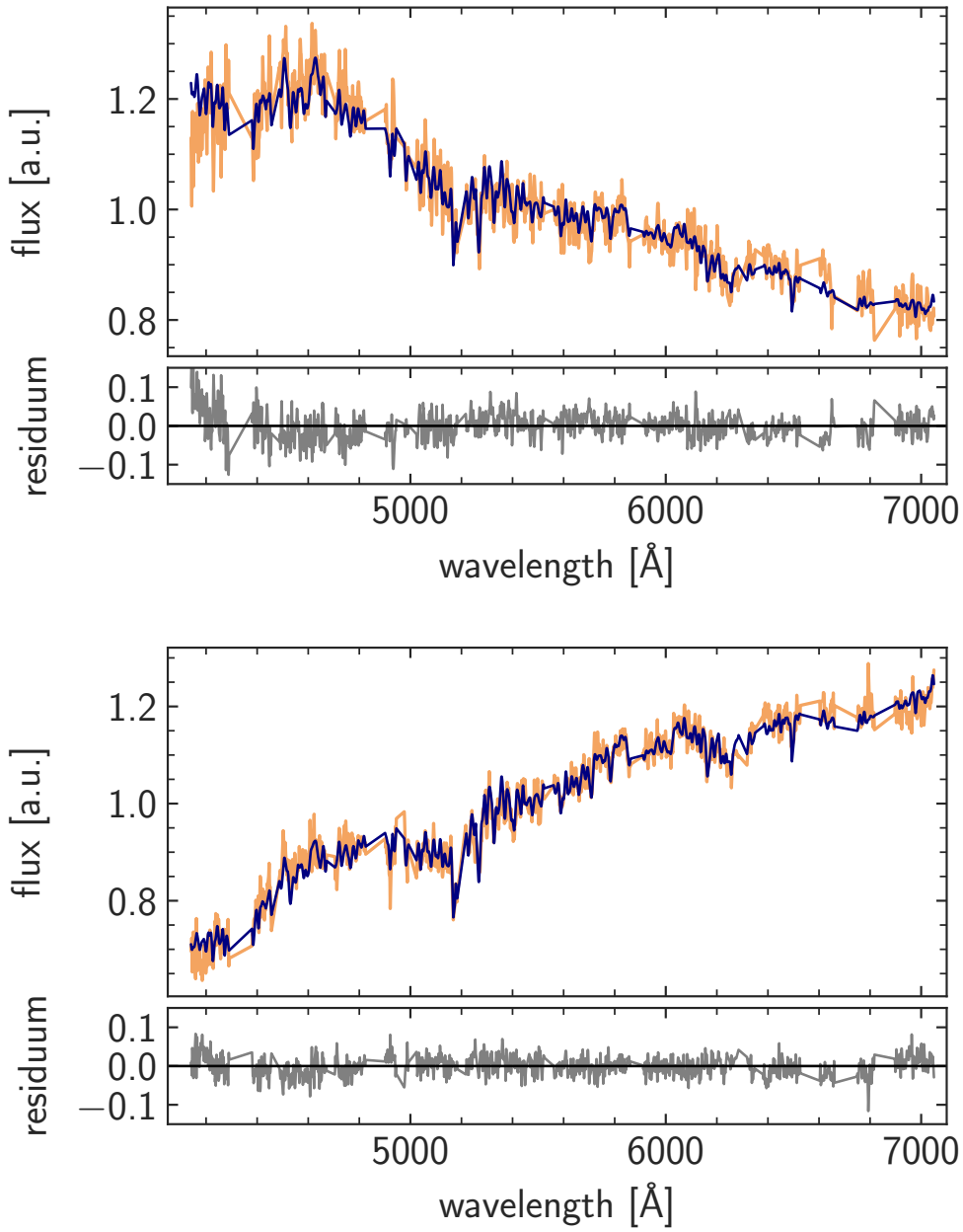

Figure 4.2: TYPHOON spectrum (orange) and the corresponding stellar population fit (dark blue). Note that for the fit ISM emission and absorption lines and broad stellar Balmer lines are masked out. The resulting gaps are shown as straight lines. The top spectrum corresponds to bin 16 at $\Delta\alpha = -1.073$ arcmin and $\Delta\delta = 1.292$ arcmin (northern spiral arm) and the bottom spectrum to bin 153 at $\Delta\alpha = -0.192$ arcmin and $\Delta\delta = -0.11$ arcmin (on the southern dust lane in the center). The different physical properties of the stellar populations are discussed in section 4.4.

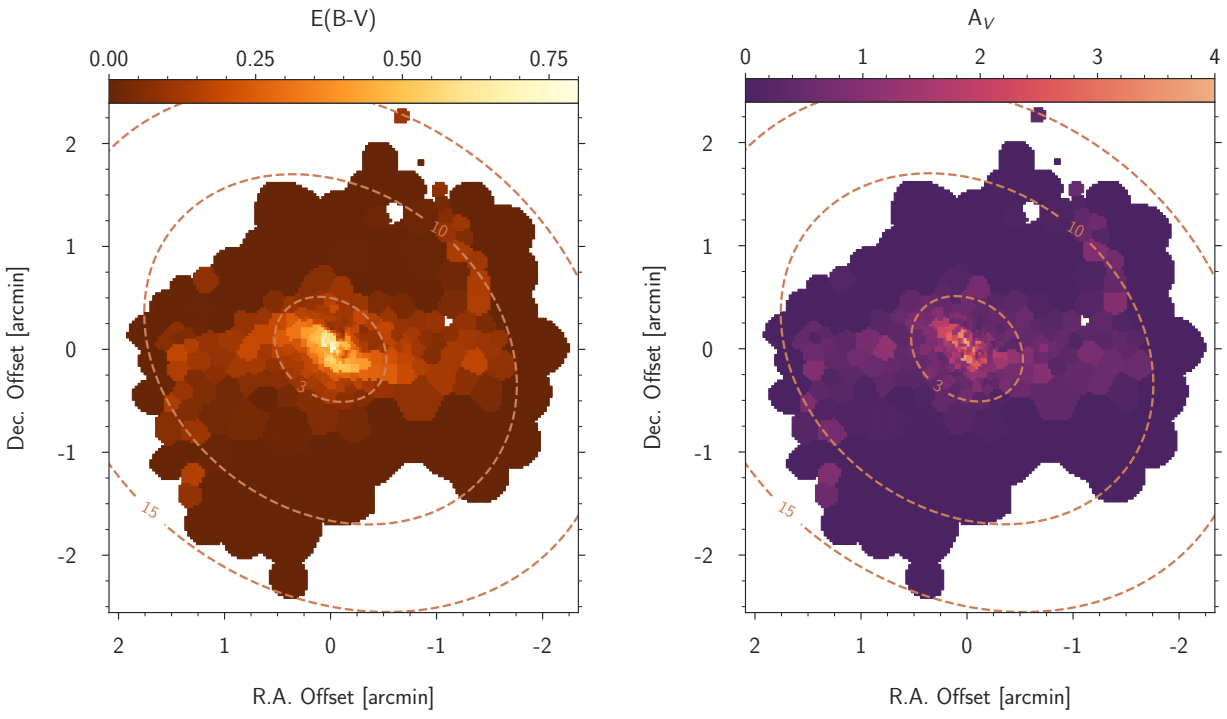

(a) Reddening map

(b) Extinction map

Figure 4.3: Reddening (a) and extinction (b) maps of NGC 1365 obtained with our population synthesis fit. The central region is indicated by the green cross. The ellipses indicate galactocentric distances of 3, 10, and 15 kpc.

For the choice of SSPs we use the high resolution age described in Sextl et al. (2023), which starts at 0.1 Myr with a step to 1.0 Myr and then continues with logarithmic steps Δlog t (in Gyr) alternating between 0.05 and 0.1 dex until 12.59 Gyr. The metallicities start at [Z] = -1.5 and increases in steps of 0.25 dex until [Z] = 0.5 as the highest value of the grid. We have, thus, a grid with $n_a = 52$ ages and $n_z = 9$ metallicities and a total number of $n_{SSP} = 468$ SSPs.

In our fitting procedure we correct for the radial velocity shifts of the observed spectra. We also measure the equivalent widths of the ISM nebular emission lines of hydrogen H_β to account for nebular emission continuum if needed (see Sextl et al. 2023). The equivalent width is used to estimate the contribution of the nebular continuum at the wavelength of H_β and the wavelength dependence is calculated by accounting for nebular hydrogen and helium bound-free, free-free and 2-photon emission. The (generally weak) nebular continuum contribution is then subtracted from the observed spectra. In addition, as in Sextl et al. (2023) spectral regions contaminated by ISM emission or absorption lines are not included in the spectral fit of the stellar population.

After these steps, the coefficients b_i and b_a are then determined by adopting a grid of R_V and E(B-V) values. For each pair of these quantities we calculate $D_\lambda(R_V, E(B-V))$, use a least square algorithm to directly solve for the coefficients b, calculate the model spectrum

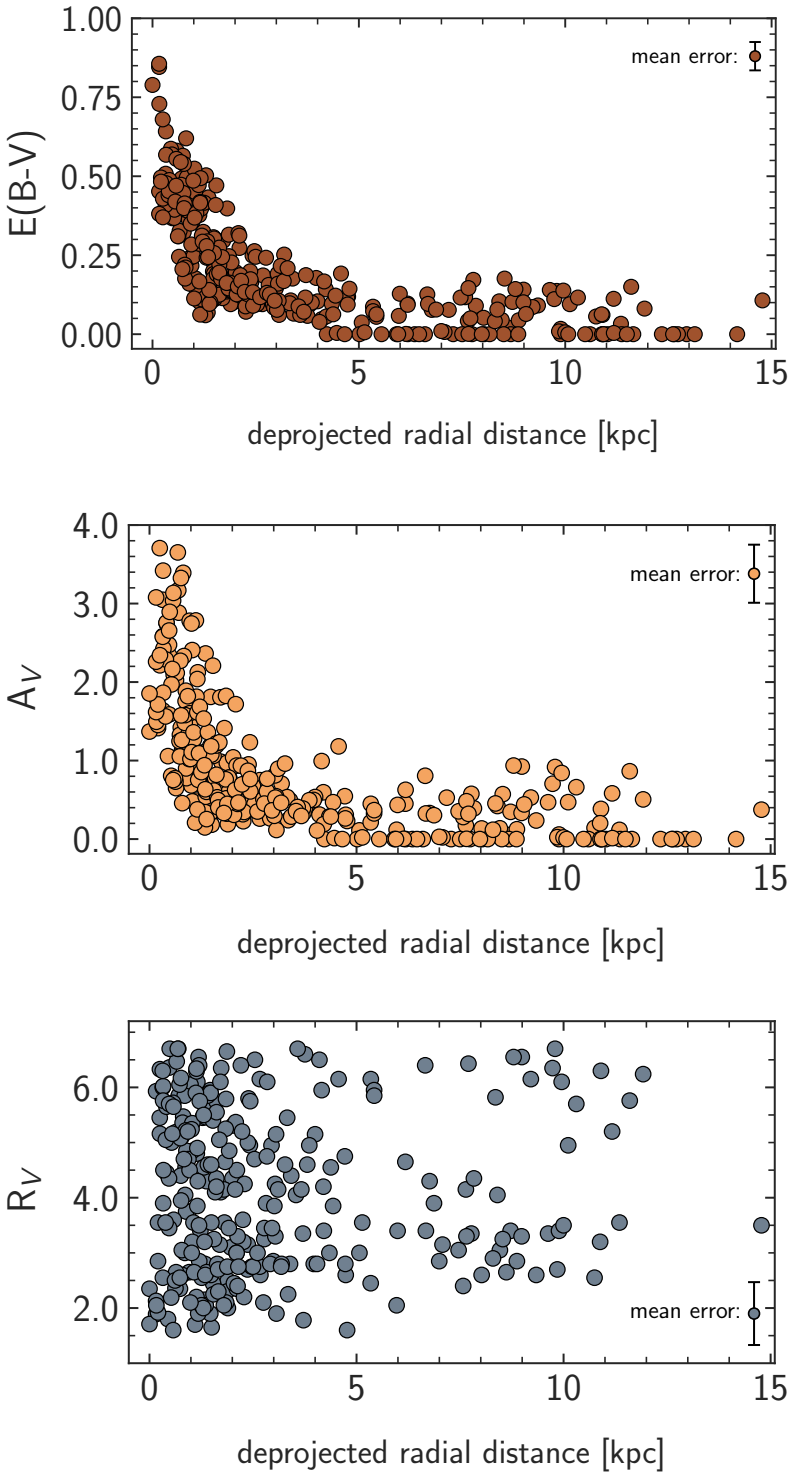

Figure 4.4: Radial distribution as a function of deprojected galactocentric distance of reddening E(B-V) (top), extinction A_V (middle) and R_V (bottom).

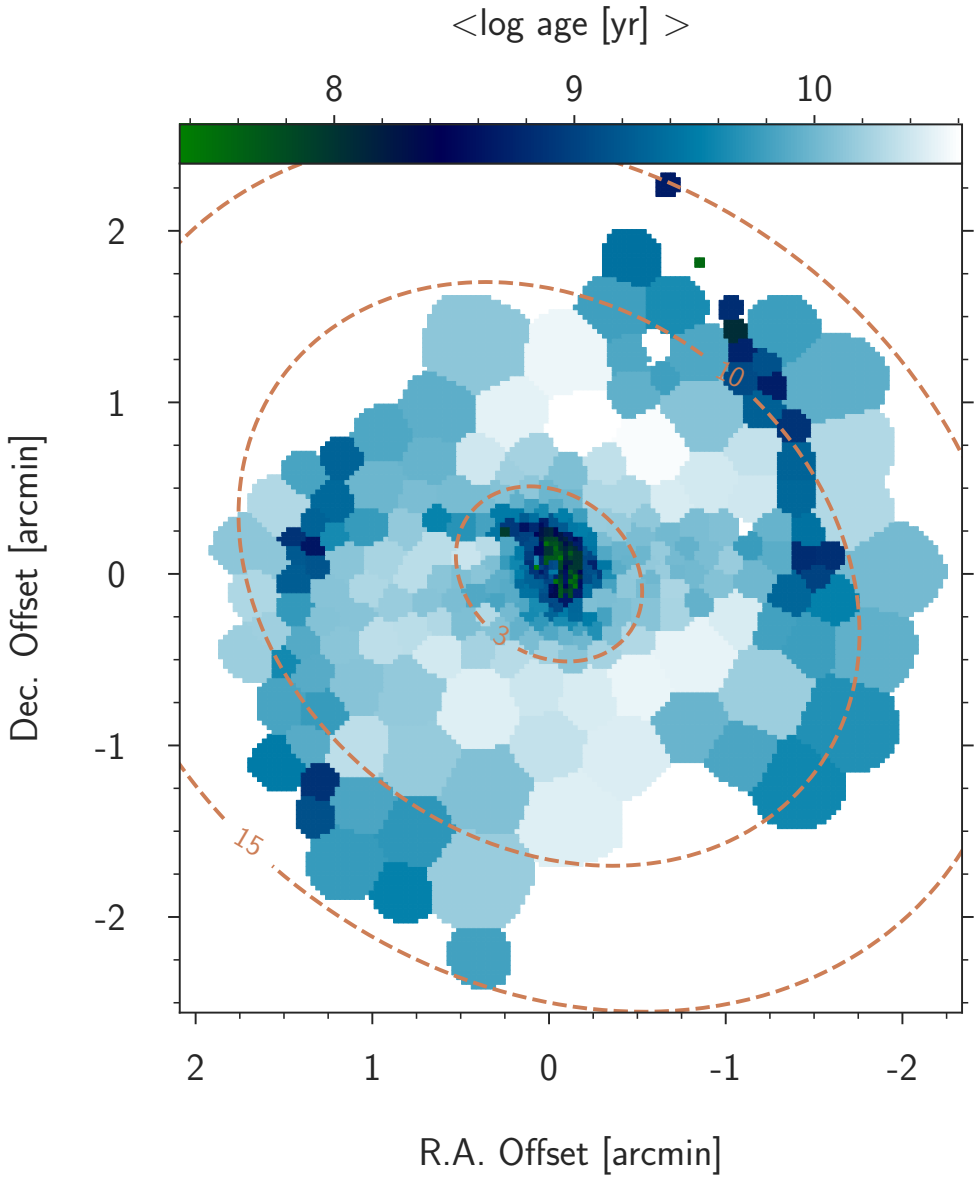

Figure 4.5: Map of average population age. The dashed ellipses indicate galactocentric distances of 3, 10, and 15 kpc, respectively.

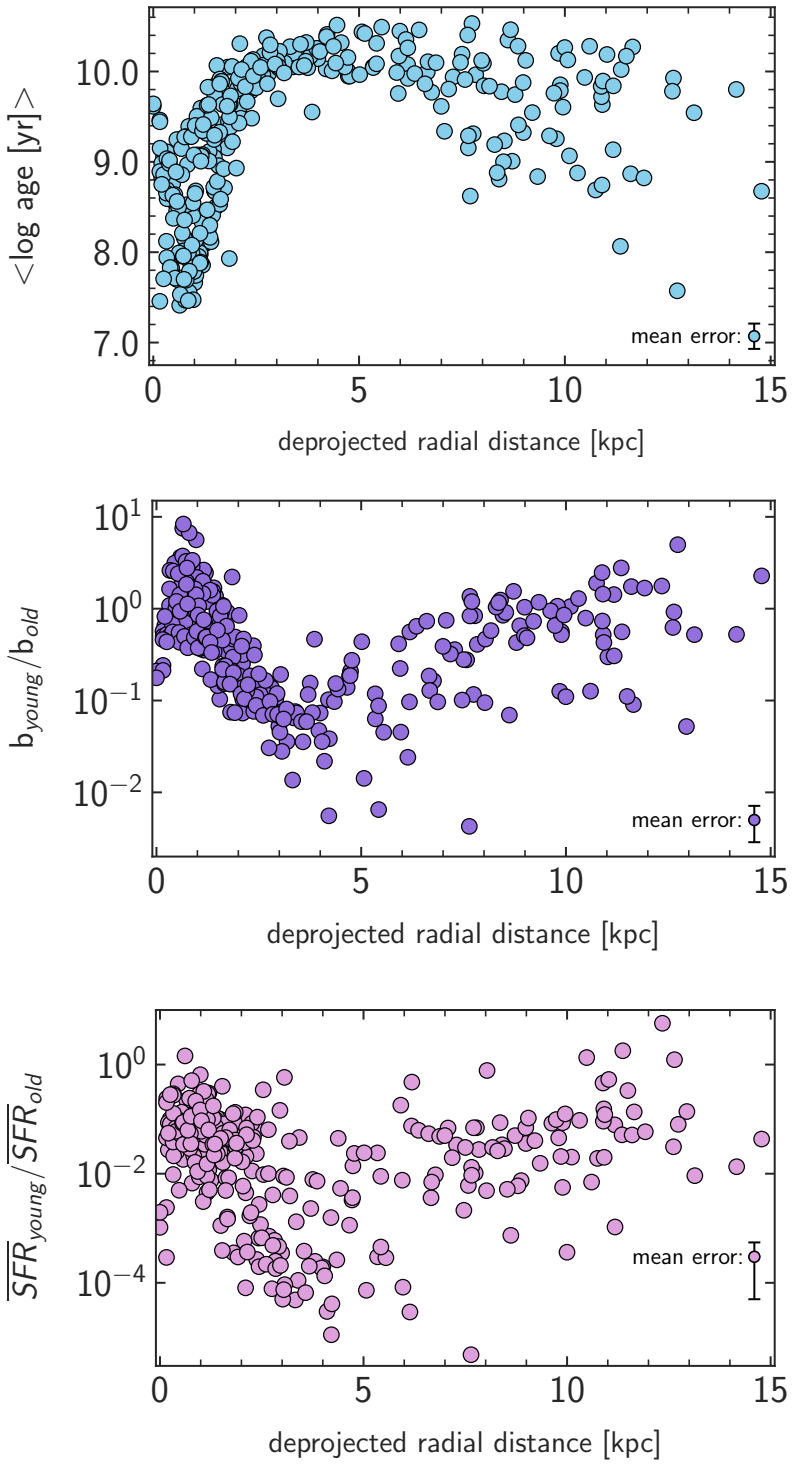

Figure 4.6: Radial distribution of average population age (top), the ratio b_{young}/b_{old} (middle), which is ratio of the contribution of the young and old population to the total observed population spectrum, and the ratio of average star formation rates of the young to the old population.

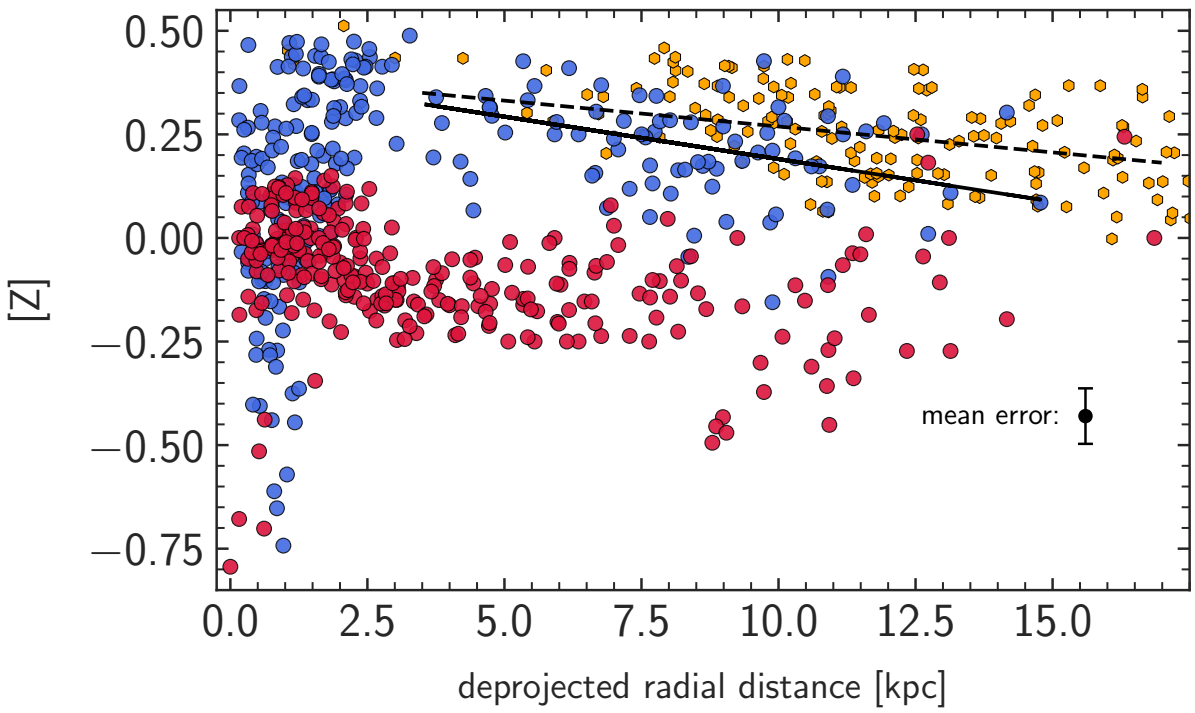

Figure 4.7: Radial distribution of the logarithm of metallicity relative to the sun. The young and old population are plotted in blue and red, respectively. HII-region metallicities based on oxygen abundances (Ho et al., 2017) are shown in yellow. We also show regressions for the young stellar population (solid) and the HII-regions (dashed) calculated for galactocentric distances larger than 3.5 kpc.

and a χ^2 value by comparing with the observed spectrum. The minimum of χ^2 defines the best fit. Errors are estimated by fitting the observed spectra modified by adding Monte Carlo Gaussian noise with zero mean and a standard deviation corresponding to the flux error at each wavelength point. The uncertainties of the stellar population parameters are then calculated as the standard deviation of their distributions produced by 20 such Monte Carlo realizations.
Following the arguments in Sextl et al. (2023) we use a characteristic age limit of 1.6 Gyr to distinguish between the young and old population and determine average ages and metallicities of these two populations separately. Through $t_i \leq 1.6$ Gyr and $t_i \geq 1.6$ Gyr, respectively, we introduce the young and old population and define the corresponding metallicities $[Z]_y$, $[Z]_o$ and ages $\log(t_y)$, $\log(t_o)$ via

$$b_y = \sum_{i_y} b_i, b_o = \sum_{i_o} b_i \tag{4.2}$$

and

$$[Z]_y = \frac{1}{b_y} \sum_{i_y} b_i [Z]_i \tag{4.3}$$

$$[Z]_o = \frac{1}{b_o} \sum_{i_o} b_i [Z]_i \tag{4.4}$$

$$log(t_y) = \frac{1}{b_y} \sum_{i_{young}} b_i log(t_i) \tag{4.5}$$

$$log(t_o) = \frac{1}{b_o} \sum_{i_{old}} b_i log(t_i). \tag{4.6}$$

The average values of the total population, young and old, are then calculated as

$$[Z] = b_y[Z]_y + b_o[Z]_o, log(t) = b_y log(t_y) + b_o log(t_o) \tag{4.7}$$

As explained in Sextl et al. (2023) metallicities and ages obtained in this way are luminosity weighted averages. The results of our analysis are presented in the next section.

4.4 Results

In the following subsections we present the results of our stellar population fits. We start with the maps of interstellar extinction. We then discuss the distribution of ages and metallicity of the young and old stellar population in the outer disk and the central region of the galaxy.

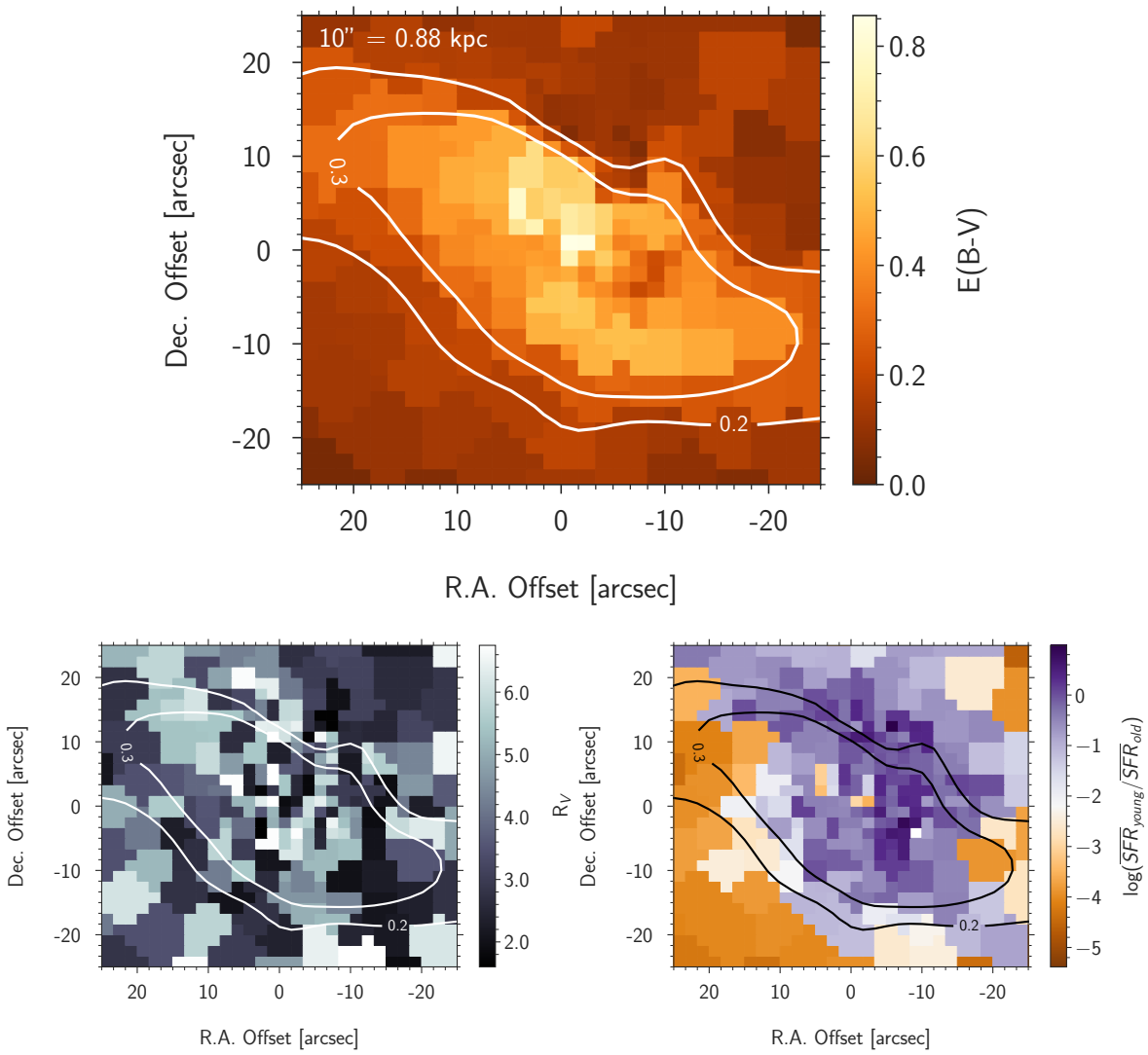

Figure 4.8: The central region of NGC 1365. Maps of the color excess E(B-V) (top), R_V (bottom left), and the ratio of the average star formation rate of the young and old population (bottom right). Isocontours of interstellar reddening E(B-V) are overplotted for E(B-V) = 0.2 and 0.3 mag.

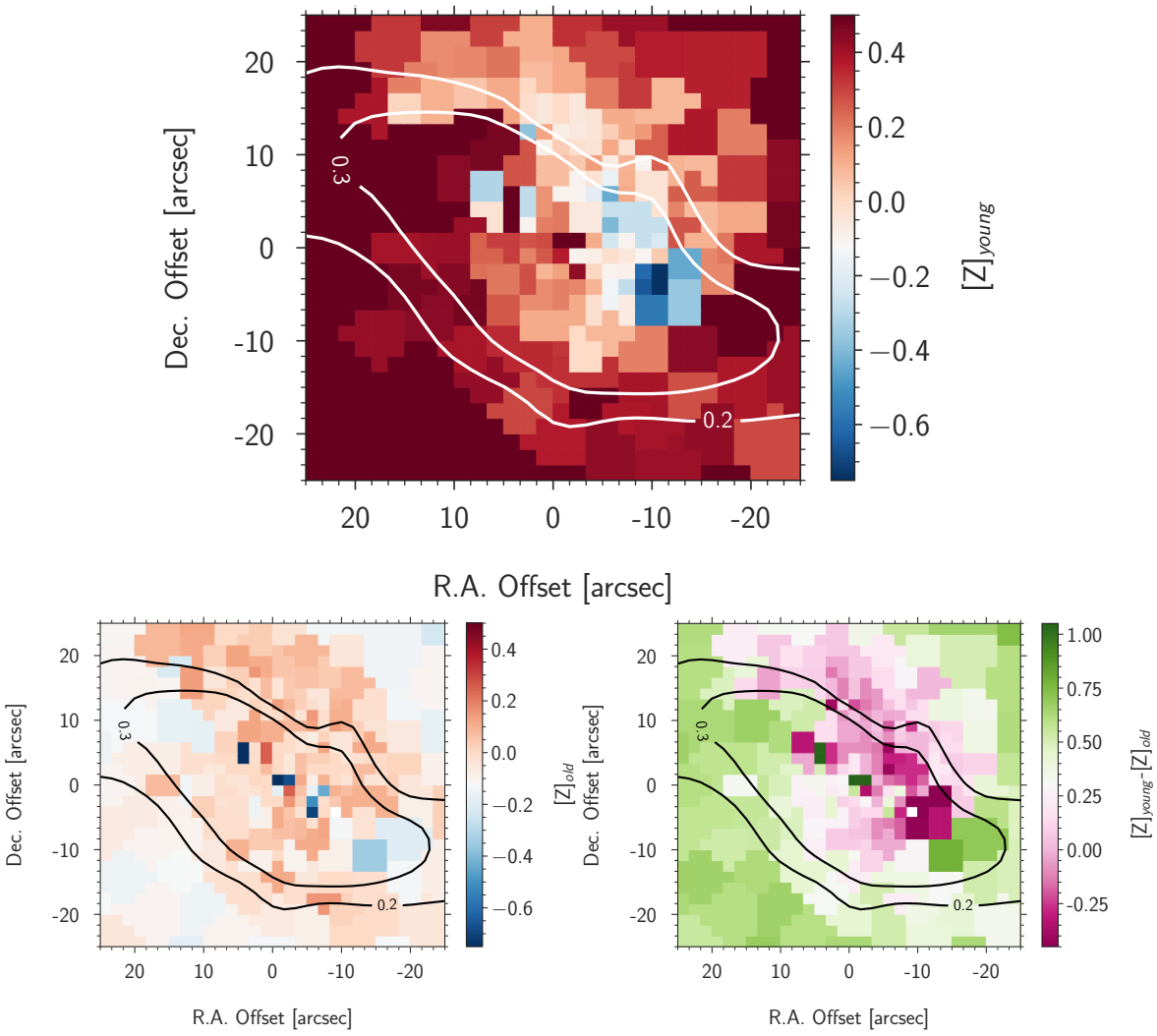

Figure 4.9: Central maps of stellar metallicity $[Z]_y$ and $[Z]_o$ of the young (top) and old (bottom left) population with the same axis range. The bottom right figure shows the difference Δ [Z] = $[Z]_y$ - $[Z]_o$. Negative differences are marked in pink tones. Isocontours of interstellar reddening E(B-V) are overplotted as in Figure 4.8. The mean errors of $[Z]_y$ and $[Z]_o$ in the FoV are ∼0.12 dex and ∼0.10 dex, respectively.

4.4.1 Reddening and extinction

The spatial distribution of reddening E(B-V) and extinction A_V by interstellar dust is shown in Figure 4.3. We find very strong effects in the center and bar and a moderate enhancement along the spiral arms. For the outer disk outside the spiral arms reddening is low and close to the Milky Way foreground reddening of $E(B\text{-}V)_{MW} = 0.018$ mag (Schlafly & Finkbeiner, 2011). We provide additional information in Figure 4.4, which shows the radial distributions as a function of galactocentric distance together with the fit uncertainties. We note again that in our spectral fit of interstellar dust we have included the determination of R_V which is allowed to deviate from the 'standard' values such as 3.1 for the diffuse Milky Way ISM or 4.05 for the Calzetti-law in starburst galaxies. Such deviations are common in star forming galaxies (see discussion and references in Sextl et al. 2023). The bottom of Figure 4.4 shows the radial distribution of the R_V values which we encounter together with their errors. Bins with E(B-V) values < 0.005 have been removed since the slope of the attenuation curve cannot be quantified in this case. We find a mean value around 4.0 but with a wide scatter between 1.5 and 6.7. As comprehensively discussed in Salim & Narayanan (2020), extinction is not the same as attenuation due to the additional geometric and scattering components in the latter case. This also implies that one should be cautious here with the common interpretation of large values in R_V implying larger grain sizes (Battisti et al., 2017; Calzetti et al., 2000). It can nevertheless be used as an indicator for obscuration (Calzetti, 2001). A more detailed discussion of the central region will be given below.

4.4.2 Population ages and inside-out growth

Figure 4.5 displays the spatial map of the average population ages across the surface of NGC 1365 and Figure 4.6 (top) provides the corresponding radial distribution. We find a maximum of populations ages around a galactocentric distance of 5 kpc and lower ages towards the center and the outer edge. The decrease of age beyond 5 kpc is a clear indication that the outer disk is more and more dominated by the young stellar population. This is confirmed by the radial dependence of the ratio b_y/b_o, which represents the ratio of the luminosity contribution of the young and old population to the total observed population spectrum and which is also given in Figure 4.6. The contribution of the young population gradually increases when going beyond 3 kpc towards larger galactocentric distances.
As shown in Sextl et al. (2023) (equations 11 and 12 and text at the end of section 4) the SSP fit coefficients b_i can also be used to estimate the ratio of star formation rates of the young and old population. This ratio is also shown at the bottom of Figure 4.6. The outer disk shows a gradual increase of this ratio from 3 kpc outwards. We note that the average age of the young population in the different spatial bins of this region is between 0.1 and 1.0 Gyr with a very few exceptions of a very young population only 5 Myr old. The average ages of the old population are between 10 and 12.6 Gyr.
The decrease of average ages and the increased contribution to luminosity and star formation by the young population towards the outer radii is a clear indication of inside-out

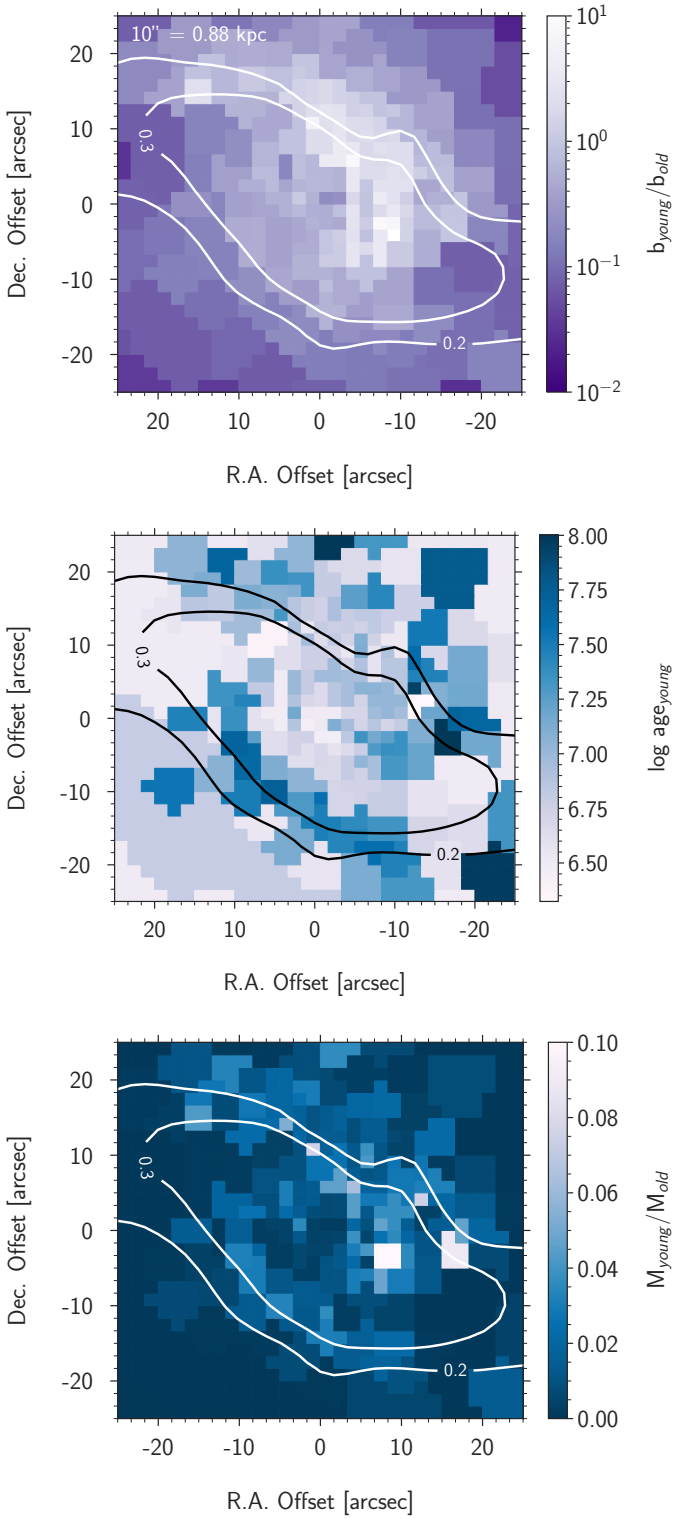

Figure 4.10: Central maps of the ratio b_y/b_o (top), the ages t_y of the young stellar population (middle), and the stellar mass ratio of the young and old population (bottom). Isocontours of interstellar reddening E(B-V) are overplotted as in Figure 4.8.

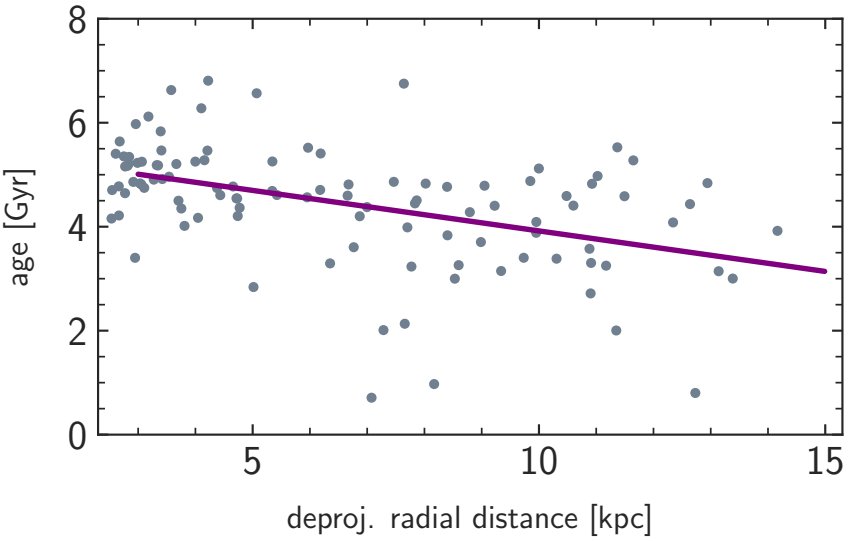

Figure 4.11: Age of the stellar population in each spectral bin at the time when 80 % of the stellar population has formed as a function of galactocentric radius in kpc. A linear regression curve is also shown. For details see text.

growth of the stellar disk of NGC 1365. This will be further discussed in Section 4.5.
From 3 kpc inwards the trend with galactocentric distance reverses. Average ages decrease and the contribution of the young population becomes stronger again. We will discuss this in the subsections below.

4.4.3 The metallicity of the young and old population of the outer disk

The radial distribution of metallicities (defined as [Z] = log $Z/Z_{\odot}$) for the young and old stellar population is plotted in Figure 4.7. We also add the metallicities of HII-regions obtained by Ho et al. (2017). They are based on oxygen abundances as a proxy for metallicity and the Baysian strong line calibration developed by Ho et al. The Asplund et al. 2009 value of log N(O)/N(H) + 12 = 8.69 has been adopted for the solar oxygen abundance.
In the outer disk beyond 3.5 kpc we find a negative metallicity gradient of the young population of -0.0207 ± 0.0028 dex/kpc in line with the expectations for a stellar disk which has formed inside-out. The stellar gradient is slightly steeper than the one obtained from HII-region emission lines and the value of metallicity is somewhat lower but these differences can be attributed to uncertainties of the HII-region strong line calibrations (see discussion in Ho et al. 2017; Bresolin et al. 2016). For the outer old population we note that the low metallicity bins with $[Z] \leq -0.35$ at a distance of 8-11 kpc are all located within the leading arm of the southern spiral right outside the bar. Apart from this anomaly there is no clear indication of an outer radial gradient of the old population. This is a

striking result and will be discussed in section 4.5. The global difference of ≈ 0.4 dex in [Z] between the young and old population agrees very well with the difference found for the massive star forming SDSS galaxies studied by Sextl et al. (2023) and with the prediction of chemical evolution models (see, for instance, Kudritzki et al. 2021a,b).
In addition to the outer negative gradient of $[Z]_y$ Figure 4.7 reveals a steep drop to low stellar metallicities of the young population towards the center of the galaxy. The metallicity of the old population, on the other hand, increases on average. This will addressed in the next subsection where we discuss the central region of the galaxy.

4.4.4 Central region

As already indicated in Figures 4.4 and 4.6 the central region of NGC 1365 is characterized by high interstellar extinction and a strong contribution of the young stellar population to the observed luminosity. This is demonstrated in more detail by Figures 4.8 and 4.10 which provide zoomed maps of the central region of reddening E(B-V), R_V, average star formation rate ratio, the luminosity contributions ratio of the young and old population, mass ratios, and the age of the young population. However, there is an obvious asymmetry in the sense that the increased luminosity contribution and star formation activity of the young population is confined mostly to the northern area with E(B-V) $\sim$ 0.2 to 0.3 mag and less is found in the corresponding south-east region. This has been discussed most recently by Schinnerer et al. (2023) in their analysis of JWST mid-IR imaging and ALMA CO observations. They concluded that the asymmetric gas infall along the bar has already initiated the intense star formation in the northern bar lane whereas in the dense molecular clouds in the south star formation has yet to come but will start very soon. This is in accordance with the rather similar gas properties in both regions.
We note that while luminosity contribution of the young population is very high in the central region, the ratio of masses of the populations is M_y/M_o is small with a mean value of 0.03 (see Figure 4.10 bottom). The reason for this significant difference to b_y/b_o is the higher luminosity of younger (and more massive) stars. Details of the computation of the mass ratio are described in Section 4.5.
The central map of R_V (Figure 4.8 middle) does not indicate any kind of spatial correlation. It appears that the R_V values are randomly distributed depending on how different gas clouds contribute to the attenuation (see Salim & Narayanan 2020; Battisti et al. 2017).
Most strikingly, as shown in Figure 4.9, the metallicity $[Z]_y$ of the young population formed in this central region is very low, sometimes even lower than the metallicity of the old population. Obviously, the surface bins with low metallicity in Figure 4.7 are all confined to a coherent area in the very center. This population has been formed most recently, as can be seen from Figure 4.10. This is in accordance with Whitmore et al. (2023) who identified several young star clusters with ages < 10 Myr in the central regions of NGC 1365. Since our spectral analysis contemplates all stars in a spaxel, not only the massive clusters, we expect slightly higher ages in our analysis. In general, it seems to be of prime importance to provide SSP templates with sufficient young ages for the fit to capture bins with such young clusters accordingly.

We note that central stellar metallicities of NGC 1365 have already been studied within two surveys using the ESO VLT integral field unit MUSE, the TIMER (Gadotti et al., 2019, 2020; Bittner et al., 2020) and the PHANGS (Emsellem et al., 2022) survey. Both surveys do not distinguish between metallicities of the young and old population and provide only an average over the total population but also indicate a drop of total metallicity towards the center (Pessa et al., 2023; Bittner, 2021). From our result we learn that this drop is caused by a strong burst of the formation of a very young population of low metallicity.
It is important to check whether the low metallicities encountered are an artifact of the fitting procedure or are caused by numerical uncertainty. As a first step, we have compared the minimum fit χ^2 values as a function of the metallicity obtained. We did not find any hint of a systematic difference. Fits at low metallicity have the same quality as high metallicity ones. In addition, we have applied an independent population synthesis algorithm and repeated the analysis for all TYPHOON bins by using the `STARLIGHT` package (Cid Fernandes et al., 2005; Asari et al., 2007) for all TYPHOON bins. Very similar results were found including the low metallicity bins in the center. We also note that keeping R_V fixed to the Calzetti standard value of 4.05 or assuming a Milky Way reddening law with constant $R_V = 3.1$ (Cardelli et al., 1989) produces a similar peculiar region of low metallicity.
We also experimented with differential interstellar extinction between the young and old population. Following Lo Faro et al. (2017) and Yuan et al. (2018) we introduced a factor f_{att}, which increases the reddening of the very young stars ($t \leq 10$ Myr) relative to the older stars by adopting E(B-V)($t \leq$ 10Myr) = E(B-V)/f_{att}. Applying a value of $f_{att} = 0.5$ we did not encounter substantial changes in the derived stellar properties larger than the fit uncertainties in the outer parts of the galaxy. However, in the central region, where the extinction is highest, the effect of inversion of metallicity between the young and old stellar population is increased. Fits with differential extinction tend to lower the metallicity for the young population even further by on average ~ 0.15 dex whereas $[Z]_o$ remains the same. Since f_{att} as an additional free parameter is poorly constrained, we refrain from a detailed follow up at this point but note that differential extinction tends to make the situation in the center more extreme.
Finally, we have checked how well the metal line absorption features are reproduced by our low metallity SSP fits. In Figure 4.13 we repeat the fit of bin 153 (already displayed in Figure 4.2) but now show the detailed fit of the metal absorption line features in two selected spectral regions. According to our fit the metallicity of the young population in this bin is $[Z]_y$ = -0.36. We conclude that given the quality of the spectra the metal lines are on average reproduced well. We take all this as a confirmation of our results.
An obvious question is whether there are HII regions in this confined region of low stellar metallicity and what their metallicities are. Very unfortunately, the most recent PHANGS-MUSE (Groves et al., 2023) and TYPHOON (Chen et al. 2023) HII-region and ISM emission line studies do not provide sufficient information allowing for conclusions about the ISM metallicity in this specific region. This is mostly caused by the strong contribution of the central AGN to the ISM ionizing radiation field.
One should also keep in mind that in the TYPHOON observation of NGC 1365 one spaxel

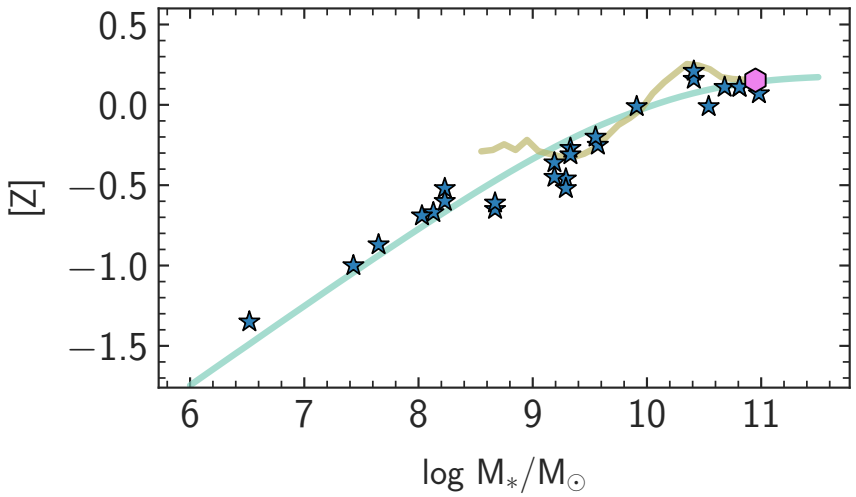

Figure 4.12: The mass metallicity relationship of star forming galaxies. Results from spectroscopy of individual red and blue supergiant stars are shown as stars (Bresolin et al. 2022, Urbaneja et al., 2023). These [Z] values refer to galactocentric distances of 0.4 R_{25} for galaxies with a metallicity gradient and to mean values for low mass irregular galaxies without a gradient. The value for NGC 1365 is given by the pink hexagon (see text). The population synthesis results by Sextl et al. (2023) for the average metallicity of the young stellar population of SDSS galaxies are plotted as khaki lines. The green curve is a prediction from galaxy evolution lookback models by Kudritzki et al. (2021a,b)

.

corresponds to 145 pc, so the whole low-metallicity region covers approx. a circle of 2 kpc in diameter. In kpc-resolution surveys at higher redshifts such relatively small regions would have been overlooked easily or would be dismissed as faulty spaxels. This makes the local TYPHOON sample especially valuable.
The physical nature of the low metallicity of the central young stellar population is discussed in the next section.

4.5 Discussion

As concluded in section 4.4.2 and Figures 4.5 and 4.6, the decrease of ages averaged over the total population and the increase of the ratio b_y/b_o is indicative of inside-out growth of the outer stellar disk of NGC 1365. An alternative way to investigate this is to look at the radial dependence of stellar mass growth. As described in Sextl et al. (2023) the fit coefficients b_i in Equation (1) of the spectral fit of an observed spectral bin can be related to the relative number contribution N_i of stars of isochrone i, for which the SSP model spectrum is calculated, and the V-band luminosity $L_i(V)$ of the isochrone via

$$b_i = N_i L_i. \tag{4.8}$$

With $N_i = b_i/L_i$ and the mass M_i of each isochrone the function

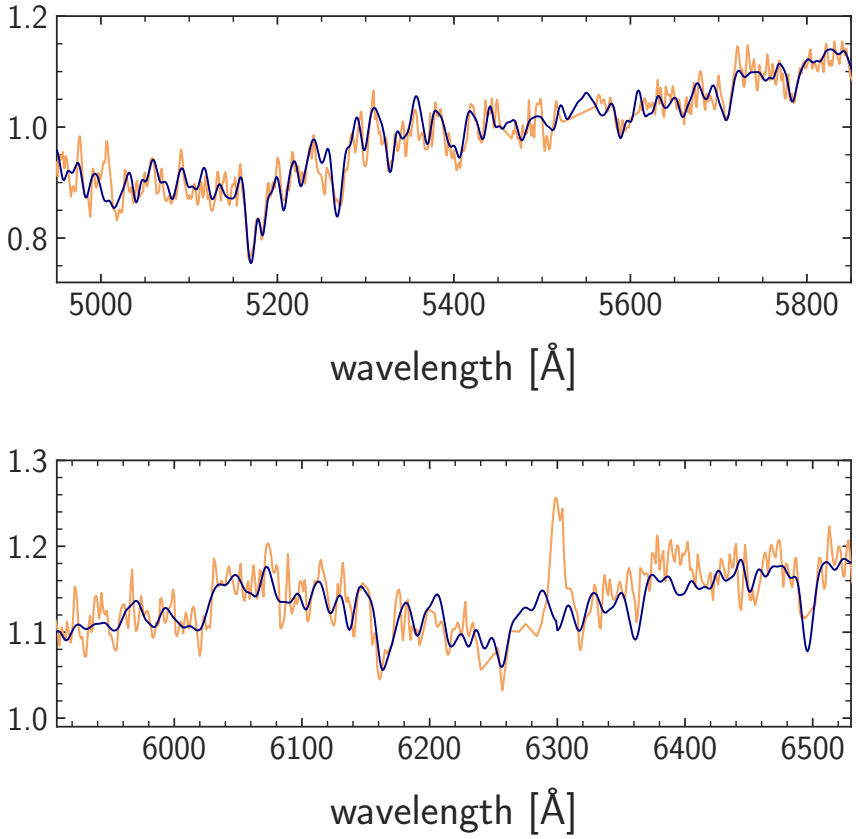

Figure 4.13: Spectral fit (black) of the absorption line features of bin 153. The metallicity of the young population is $[Z]_y$ = -0.36. Note that the TYPHOON spectrum has a gap from 5524 to 5561Å. The spectral regions at 5007 and 6300 Å are not included in the χ^2 spectral fit due to the contamination by ISM emission.

$$g(\log(t_i)) = \frac{\sum_{i_1=1}^{i} \sum_{i_2=1}^{n_z} N_{i_1,i_2} M_{i_1,i_2}}{\sum_{i_1=1}^{n_a} \sum_{i_2=1}^{n_z} N_{i_1,i_2} M_{i_1,i_2}} \tag{4.9}$$

describes the accumulative mass growth in the surface area of each spectral bin as a function of time. Note that in Equation (9) the inner sums in the nominator and denominator add up the contributions by different metallicities at the same age, whereas the outer sums accumulate the contribution of different ages.

Applying Equation (9) we can calculate the age (or lookback time) for each spectral bin, when 80 % of the stellar mass has formed. The corresponding radial distribution of ages is shown in Figure 4.11. We see a clear indication of inside-out growth beyond 2.5 kpc. At the outermost parts of the disk the mass growth was accomplished about 2 Gyr later than in the inner parts. We note that a similar result has been obtained by Pessa et al. (2023). According to standard chemical evolution models including galactic winds and gas infall (see, for instance, Hou et al. 2000; Chiappini et al. 2001; Kudritzki et al. 2015; Weinberg et al. 2017; Kang et al. 2021) the inside-out growth of the disk is the physical reason for the negative metallicity gradient of the young stellar population and the ISM in star forming disk spiral galaxies, which we also encounter in NGC 1365. The value of -0.02 dex/kpc determined in our work seems very small but NGC 1365 is a huge galaxy and renormalizing with respect to the isophotal radius leads to -0.59 dex/R_{25}. This value is in good agreement with gradients found from the quantitative spectroscopy of individual supergiant stars in nearby galaxies (see, for example, Kudritzki et al. 2012; Bresolin et al. 2022; Liu et al. 2022 and references therein) and comprehensive studies of metallicity gradients obtained from HII-regions such as Ho et al. (2015).

The average outer metallicity of the young population represented by the value $[Z]_y = 0.15$ at 0.4 R_{25} = 11.82 kpc is in good agreement with the mass-metallicity relationship (MZR) of star forming galaxies. Figure 4.12 shows a MZR comparison with the results obtained by the analysis of individual supergiant stars (Bresolin et al. 2022, Urbaneja et al., submitted to ApJ) and the SDSS population synthesis study of the young population by Sextl et al. (2023).

As already mentioned above, the average difference between the metallicity of the old and the young population of about 0.4 dex agrees with the result obtained by Sextl et al. (2023) in their investigation of the integrated spectra of 250000 SDSS galaxies. As for the metallicity gradients, the fact that we do not encounter a gradient for the outer old population is very interesting. When comparing gradients as a function of population age galaxy chemical evolution models yield different results depending on the assumptions made. Hou et al. (2000) find that gradients of the older population are steeper, whereas Chiappini et al. (2001) find the opposite. Roškar et al. (2008) point out that stellar migration will tend to flatten abundance gradients with time and predict younger populations to have a steeper gradient. It seems that population synthesis analysis might provide a powerful tool to investigate this issue and to provide additional constraints on galaxy evolution in this way. This will be an important part of our continued TYPHOON population synthesis survey.

A striking result is the low metallicity of the young population in a very confined region in the center (Figure 4.9). A straightforward first explanation is strong inflow of metal poor gas which has influenced the most recent star formation. This would be in line with the most recent work by Schinnerer et al. (2023) and the results by Zánmar Sánchez et al. (2008) who detected gas infall along the bar. Tabatabaei et al. (2013) gauged a relatively short timescale of only 300 Myrs in their submilimeter analysis on which gas from the bar looses angular momentum and flows into the center. However, it is not clear whether this infalling gas is metal poor and whether the amount of gas accumulated has been sufficient to form a new metal poor population. In principle, galaxy evolution models with infall and outflow can produce a younger population with a metallicity lower than the older population (Spitoni, 2015) but the differences are not as extreme as we encounter in NGC 1365. A crucial test would be a metallicity measurement of the infalling gas.

We propose an additional scenario as an explanation for the low metallicity of the central young stellar population, namely interrupted chemical evolution. In this scenario chemical evolution in the central region started in the usual way with heavy star formation and building up metals. Then, at a time when ISM metallicity had already reached high values of above solar, feedback from the central AGN together with stellar feedback from supernovae and winds created a strong central galactic wind and ejected the central gas so that star formation stopped for a long time. For a massive galaxy such as NGC 1365 an AGN can stay intermittently active for 1-5 Gyr and inhibit star formation on a scale of 1 Gyr (Stasińska et al., 2015).

In the meantime, the most massive stars which have already formed, continue to recycle metal enriched gas to the ISM through supernovae and winds but due to the energetic AGN and stellar activity this matter continues to be expelled. Then, after several Gyr this activity drops and a new reservoir of metal poorer ISM gas is built up again from stellar winds and mass-loss of stars of low mass of the older population, which formed earlier. This central reservoir eventually becomes dense enough to start formation again and the newly formed stars show the low metallicity composition of the older population.

Figure 4.14 shows the result of a simple Monte Carlo simulation, where we apply a closed-box chemical evolution model. We assume that stars form out of pristine gas with zero metallicity in an intense star formation process following a standard initial mass function (Kroupa, 2001). Metal enriched gas is recycled to the ISM through supernovae and stellar winds. We distinguish between stars with masses higher or lower than $9M_{\odot}$. For the former, all matter except a remnant of $3M_{\odot}$ is returned to the ISM and the mass of the convective core (Maeder, 1987; Ekström et al., 2012) is converted into metals by core-collapse supernovae. For the latter, we adopt a white dwarf mass using an initial-final mass relationship (Cummings et al., 2018) and recycle the remaining matter. For the metals produced by these objects we follow Kobayashi & Nomoto (2009) and assume that 7 percent of the stars in the mass range between 3 to 9 $M_{\odot}$ increase the mass of the final WD through binary accretion until the Chandrasekhar limit. A subsequent Supernova type Ia explosion returns the white dwarf mass as metals. For the stellar life times of both groups we use the main sequence fit values given by Ekström et al. (2012). In the case of SNIa explosions we do not account for the accretion time, which is short compared with

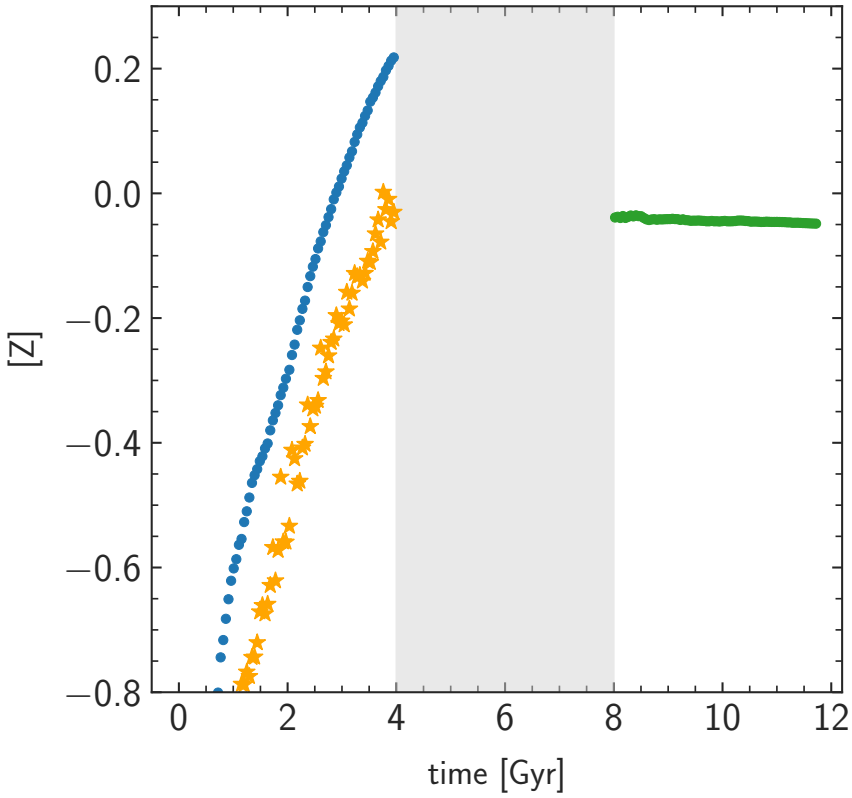

Figure 4.14: A simple chemical evolution model as example for the central region of NGC 1365. The metallicity of the ISM present in the center before the end of star formation at 4 Gyr is given in blue and the V-band luminosity averaged metallicity of the stars in orange. The abscissa is the evolution time in Gyr. The gray shaded area marks the time when the central ISM gas is ejected and star formation is quenched. The green symbols show the gas metallicity provided by stellar winds and supernovae of the old population after the central activity ejecting gas has stopped. For more details see text.

the stellar life time (Kobayashi & Nomoto, 2009).
As a result of our calculation, ISM metallicity (shown in blue) is increasing quickly. Young, newly formed stars will resemble the ISM metallicity but the metallicity of older stars will be lower. We show the V-band luminosity averaged metallicities of the stars in orange. (As mentioned above the metallicities and ages we derive in our population synthesis approach are luminosity weighted quantities).
After 4 Gyr star formation comes to a hold because of the energetic processes in the center, which eject all star forming gas, and the evolution stops. After all the ISM gas is quickly expelled from the center, the existing massive stars still recycle gas to the ISM. However, because of the AGN activity the new ISM gas still continues to be expelled and the central region remains gas free. Then, 8 Gyr after the whole chemical evolution started, the central activity stops and a new reservoir of ISM gas forms because of stellar winds and mass-loss from the existing low mass stars of different ages and low metallicity. The ISM metallicity of this new reservoir of gas is shown in green. It is slightly lower than the luminosity weighted metallicities of the old stars, which agrees qualitatively with Figure 4.9. Young stars forming out of this gas will resemble this metallicity. This explains how the formation of a lower metallicity young stellar population in the center is possible without invoking the infall of metal poor gas from outside.
An obvious question is whether the dying stars of the old population can provide enough gas for a new young population. As a very simple estimate we consider stars born at 3 Gyr in Figure 4.14. In our scenario the gas provided by stars with a main sequence lifetime shorter than 5 Gyr (or more massive than 1.18 $M_{\odot}$) is expelled by the central AGN activity. However, the gas recycled by stars less massive than 1.18 $M_{\odot}$ but with a higher mass than 0.958 $M_{\odot}$ (corresponding to a main sequence lifetime of 9 Gyr) can settle into the central region, because AGN activity has now stopped (we adopt $\tau_{MS} = 8(M/M_{\odot})^{-2.8}$ Gyr for the low mass main sequence lifetime). Using the IMF we calculate the mass of these dying stars in relation to the mass of all remaining stars with masses lower than 0.958 $M_{\odot}$ and obtain a ratio of 0.124. Assuming that half of this mass fraction is recycled as gas we obtain a ratio of gas mass to the mass of old stars of 0.06, which is a factor of two higher than the observed average mass ratio of the young to the old population (see Figure 4.10 bottom). A starburst of very high star formation efficiency (Fisher et al., 2022) could, thus, explain the observations within the framework of our model.
The goal of this simplified calculation is only to demonstrate that such an additional scenario can work. A better match of the observations could certainly be obtained by modifying parameters such as star formation rates, evolution and yields etc. and, most importantly, by including infall of metal poor gas, but that is beyond the scope of this paper. We note that the idea of recycled gas accumulating from an aging stellar population is not new, see for instance in Ciotti & Ostriker (2007).
The situation in the center of NGC 1365 is not unique as it seems. The Milky Way shows a metallicity of the young stellar population which increases from [Z] $\sim$ -0.35 at 15 kpc galactocentric distance to $\sim$ +0.3 at 4 kpc (Genovali et al., 2014; da Silva et al., 2022) but suddenly drops to solar or even subsolar towards the galactic center (Najarro et al., 2004, 2009; Davies et al., 2009a,b; Martins et al., 2008; Origlia et al., 2013; Do et al., 2015).

Figure 5 in Genovali et al. (2014) gives an excellent impression of the very similar situation in the Milky Way. Additionally, recent ESO VLT observations revealed an intense star formation period in the galactic center $\sim$ 0.6-1 Gyr ago after a long quiescent phase of approximately 6 Gyrs (Nogueras-Lara et al., 2020).
In summary, we conclude that detailed spatially resolved population synthesis studies of young and old populations in star forming galaxies are an extremely powerful tool to investigate the evolution of galaxies. We will continue this work within the framework of our TYPHOON survey.

5

The TYPHOON Stellar Population Synthesis Survey. II. The Nearby Grand Design Barred Spiral M83 - Central and Azimuthal Inhomogeneities of the Young Stellar Population

Published in the Astrophysical Journal, **987**:138 (19pp), 2025 July 10

Authors: Eva Sextl, Rolf-Peter Kudritzki, Fabio Bresolin, Kathryn Grasha, Hye-Jin Park, Qian-Hui Chen, Andrew J. Battisti, Mark Seibert, Barry F. Madore, and Jeffrey A. Rich

Research Context: In forth publication, we again apply SPS on spatially resolved spectra of the TYPHOON integral-field spectroscopic survey. This time on starburst barred spiral galaxy M83 (NGC 5236), the highest signal-to-noise galaxy in the currently reduced sample. At only a distance of $\sim$ 4.8 Mpc, this galaxy offers a unique opportunity to compare our findings of the metallicity of the young stellar population with that from individual young stellar probes (blue supergiant stars, young massive clusters, super star clusters). The literature does not include any previous studies that have performed such a direct, in-place (in situ) comparison in a star-forming galaxy. Instead, only simulated or mock experiments have been documented. If M83 were closer to Earth, SPS analyses might suffer from contamination by individual point sources, making its current distance an ideal 'sweet spot' for this study.
The center of M83 is known to be peculiar. Its optical nucleus, the center of stellar rotation and the possible AGN do not align. Its vigorous central star formation is believed to be influenced by interactions with nearby galaxies, possibly including the dwarf and low-metallicity irregular galaxy NGC 5253. We will show that the metallicity of the young population is also unexpectedly low in certain central regions. A substantial amount of literature already exists on this galaxy, complemented by further IFU observations from MUSE, which is recognized as one of the world's best IFU spectrographs. This allows for comparing our results on the same spatial regions with two different telescopes and spectrographs (see section 6.11).

Abstract We apply population synthesis techniques to analyze TYPHOON long slit spectra of the starburst barred spiral galaxy M83. The analysis covers a central square of 5 arcmin side length. We determine the spatial distribution of dust through the analysis of reddening and extinction, together with star formation rates, ages, and metallicities of young and old stellar populations. For the first time, a spatial one-to-one comparison of metallicities derived from full-spectral fitting techniques with those obtained from individual young stellar probes has been carried out. The comparison with blue supergiant stars, young massive star clusters, and super star clusters shows a high degree of concordance when wavelength coverage in the B-band is available. The metallicity of the young population is supersolar and does not show a radial metallicity gradient along the investigated part of the disk, in agreement with our chemical evolution model. However, a notable decrease in metallicity is observed in a tightly confined region at the galaxy center, coinciding with circumnuclear orbits. We attribute this to matter infall either from the circumgalactic medium or a dwarf galaxy interloper or, alternatively, to AGN-interrupted chemical evolution. We confirm the presence of a dust cavity with a diameter of 260 pc close to the galaxy center. Dust absorption and molecular CO emission are spatially well correlated. We find an anticorrelation between R_V, the ratio of dust attenuation to reddening, and the emission strength of molecular species present in photo-dissociation regions. We confirm our results by using alternative fitting algorithms and stellar libraries.

5.1 Introduction

The spatial distribution of gaseous and stellar metallicity provides unique information on the evolution of galaxies. For instance, negative metallicity gradients in the disks of massive star-forming galaxies, i.e. the linear decline of the logarithm of metallicity with galactocentric distance, are commonly used to constrain galaxy growth rates, star formation efficiency, and the effects of galactic winds and matter infall (see, for example, Kang et al. 2021, 2023; Kudritzki et al. 2015; Mollá et al. 2017). Although it seems that these gradients are universal when normalized to a characteristic scale length (Sánchez et al., 2014; Ho et al., 2015), there has been growing evidence that the concept of negative gradients is too simple. Extensive studies of H II region metal abundances have shown clear deviations from single gradients and revealed a flattening of the spatial metallicity distribution in the central and also in the outer parts of galaxy disks (Bresolin et al., 2009b, 2012; Goddard et al., 2011; Sánchez-Menguiano et al., 2016, 2018; Franchetto et al., 2021; Groves et al., 2023; Chen et al., 2023). Positive metallicity gradients were encountered at higher redshifts and may indicate the influence of galaxy interaction and very strong infall (Tissera et al., 2022; Vallini et al., 2024). In addition, deviations from the azimuthal homogeneity of metallicity, sometimes associated with spiral arms, have been observed (Ho et al., 2017, 2018; Kreckel et al., 2019; Sánchez-Menguiano et al., 2020), indicating

the importance of localized enrichment through strong star formation activity or metal dilution through matter infall. Theoretical chemical evolution models indicate that spiral density waves may indeed introduce metallicity inhomogeneities (Ho et al., 2017; Spitoni et al., 2019; Mollá et al., 2019).

Given the relevance of these intriguing results, it is important to carry out an independent investigation using metallicity information obtained from the quantitative spectroscopy of the young stellar population in galaxies. Indeed, spectroscopy of individual blue and red supergiant stars has resulted in accurate measurements of massive star metallicities and metallicity gradients and revealed that H II region abundance measurements are frequently affected by systematic uncertainties (Kudritzki et al., 2008, 2012, 2016; Bresolin et al., 2009a, 2016, 2022; Gazak et al., 2015; Davies et al., 2017; Lardo et al., 2015; Liu et al., 2022). At the same time, these observations did not allow one to investigate deviations from azimuthal homogeneity because of the small number of individual stellar targets distributed over the galaxy surface.

A very promising alternative is the use of integral field units (IFU) and the population synthesis analysis of the spectra of the integrated stellar populations. To be precise, we apply techniques for full-spectral fitting. It compares combinations of single-burst stellar population models (SSPs) to observed spectra in order to extract physical properties of the stellar populations, such as age, metallicity, and star formation history, either for entire galaxies or spatially resolved regions. The power of this method has been demonstrated in a large number of publications (see, for instance, Bittner et al. 2020, Carrillo et al. 2020, Parikh et al. 2021, Emsellem et al. 2022, Pessa et al. 2023, Westmoquette et al. 2011, Sánchez-Blázquez et al. 2014, Thainá-Batista et al. 2023), which provided unique information about the distribution of ages and metallicities averaged over all populations, old and young, in the galaxies investigated. However, for our purpose, which focuses on the properties of the young stellar population, it is important to use observations and a methodology that are capable of disentangling the contributions of young and old stars over a large spatial area of the galaxies.

The TYPHOON survey (see Section 5.2 for more details), which uses stepwise combined long-slit spectra of galaxies, is ideal for this purpose. It is based on observations covering a large field of view across a wide wavelength range, including the blue to near-UV parts of the stellar spectral energy distributions (SEDs), which are absolutely crucial to constrain the properties of the young stars from the spectra of the integrated populations. We started a project to systematically investigate the disentangled properties of the young and old stellar populations in nearby star-forming galaxies. In a first step, we have studied the barred spiral NGC 1365 and have obtained crucial information about the distribution of dust, star formation rates, metallicities, and ages (Sextl et al. 2024, hereafter Paper I). Most intriguingly, we found a significant drop in the metallicity of the young population in a closely confined region in the center of the galaxy, which we interpreted as the result of infall of metal-poor gas along the bar or AGN interrupted chemical evolution, or both. Now in the next step, we turn to M83.

M83 (= NGC 5236) is the nearest face-on, grand-design barred spiral galaxy showing evidence of intense recent star formation activity and ongoing star formation bursts in its

center and two spiral arms over at least the last 10 Myr (Dopita et al., 2010). A schematic illustration of M83's most prominent (gas) structures can be found in Koda et al. (2023).

This galaxy has experienced six supernovae in the last century as a result of its high star-forming activity. Detailed optical spectroscopy of blue supergiant stars (BSGs, Bresolin et al. 2016), together with the study of UV and optical integrated spectra of young massive clusters (YMCs, Hernandez et al. 2018, 2019), the NIR spectroscopic analysis of the red supergiant-dominated super star clusters (SSCs, Davies et al. 2017), and the exploration of metal emission and absorption lines from the interstellar medium (ISM, Bresolin et al. 2005, 2016; Hernandez et al. 2021; Grasha et al. 2022) indicate high metallicity, clearly higher than the metallicity in the sun and the young stars and the ISM of the solar neighborhood Asplund et al. (2009). However, these investigations disagree with regard to the metallicity gradient in the inner part of the galactic disk, located within two-thirds of the isophotal radius. The SSCs indicate a flat metallicity distribution without any gradient, the ISM emission and absorption lines point to a very weak gradient, whereas the YMCs and BSGs provide evidence for a stronger gradient. The low number of objects and their sparse distribution is possibly affecting the conclusions about the metallicity distribution. A more complete spatial coverage of the young stellar population over the galaxy might provide a clearer picture. In addition, comparing metallicities obtained from individual stellar sources (BSGs, YMCs, SSCs) and cospatial population synthesis will allow for a crucial test of the accuracy of our population synthesis technique. Other substantial tests on full-stellar fitting itself are difficult and often limited to mock observations (Wilkinson et al., 2015) or simpler systems of globular clusters (Koleva et al., 2008; Cezario et al., 2013; Gonçalves et al., 2020). In a rare opportunity, we will compare the metallicities of the young stellar population (age $\leq$ 100 Myr) with those of the stellar probes at their specific positions in the galaxy. For this, a substantial part of M83 has to be observed in an IFU-like manner with a large spectral coverage, especially in the blue part of the optical spectrum. This approach will also enable us to investigate the properties and distribution of dust, as well as to look for potential correlations with the ISM molecular gas. In addition, we will also study the star formation properties of our target galaxy.

We describe the observations in Section 5.2. Here we also summarize the global properties of M83 and give a brief overview of the population synthesis analysis technique that we applied. The main results are presented in two sections. Section 5.3 analyzes the complex galactic distribution of interstellar dust, star formation rates and stellar ages, making a comparison with the distribution of molecular and cold atomic gas. Section 5.4 discusses the spatial distribution of stellar metallicity and compares with that inferred from the spectroscopy of individual supergiant stars and stellar clusters. In addition, Section 5.5 provides a test of the population synthesis method by comparing with an alternative fitting algorithm and single stellar population spectra, and Section 5.6 illustrates the potential problems deriving from the use of simple luminosity-weighted averages of stellar metallicity. Section 5.7 investigates the importance of the wavelength range of the analyzed stellar spectra, and, finally, Section 5.8 concludes the paper with a summary and discussion.

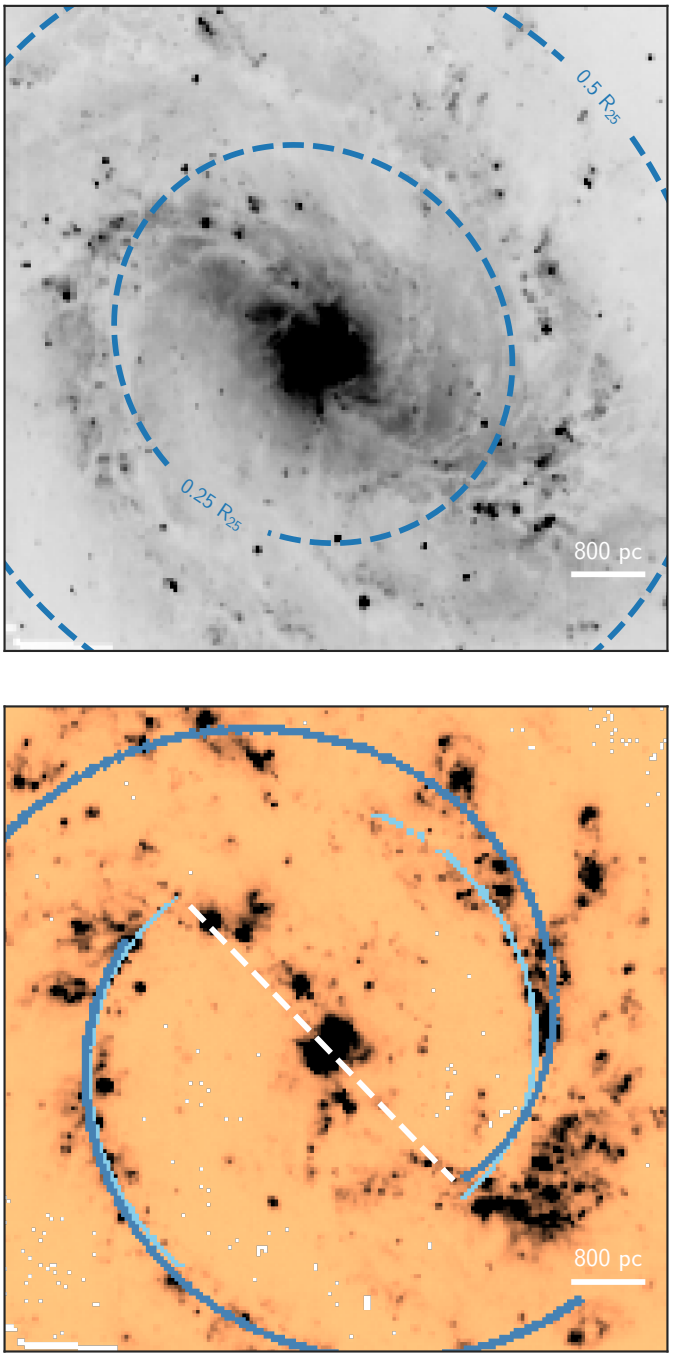

Figure 5.1: V-band image (top) and Hα line flux (bottom) of the inner disk of M83 created from the TYPHOON data cube. Top: The two dashed ellipses indicate galactocentric distances of 2.25 and 4.51 kpc, corresponding to isophotal radii of 0.25 and 0.50 R_{25}, respectively. Bottom: Two spiral arms using Hα are fitted with a logarithmic spiral (light-blue). In addition, similar fits of ALMA - CO(2-1) observations are over-plotted in dark blue. A schematic presentation of the bar is shown as white dashed line. East is towards the left and north towards the top in both panels.

5.2 Global Properties of M83, Observations and Analysis Method

M83 is a moderately massive galaxy with a stellar mass of $\log(M_*/M_\odot) = 10.41 \pm 0.10$ (Leroy et al. 2019; see also Bresolin et al. 2022), an isophotal radius of 6.44 ± 0.05 arcmin (de Vaucouleurs 1991, 9.01 kpc at the adopted distance), an inclination angle of 24 degrees and a position angle of 45 ± 5 degrees (Comte, 1981). Callanan et al. (2021) report, based on a review of existing data, a mean SFR of $0.8\,M_\odot\,\mathrm{yr}^{-1}$ for the central ~ 500 pc of M83. The distance to M83 of $\mathrm{d} = 4.81 \pm 0.2$ Mpc has been determined from blue supergiant stars (Bresolin et al. 2016, with the revision in Sextl et al. 2021 and Bresolin et al. 2022). This value is in agreement with those derived by other methods, such as the tip of the red giant branch (EDD data base, Tully et al. 2009) or the Planetary Nebulae luminosity function (Herrmann et al., 2008).

5.2.1 Observations

The TYPHOON survey observations (P.I. B. Madore) utilize the Las Campanas du Pont 2.5m telescope and the Wide Field CCD imaging spectrograph with a custom slit of 18 arcmin in length and 1.65 arcsec in width on the sky. To construct 3D data cubes with 1.65×1.65 arcsec^2 spaxels the slit scans progressively across the galaxies (Progressive Integral Step Method, PrISM) with the slit orientation typically in the north-south direction. At the distance of M83, 1.65 arcsec is equivalent to 38.5 pc. The final datacubes contain spectra in the wavelength range of 3650 to 8150 Å. Their spectral resolution is relatively low and corresponds to a FWHM of 8.2 Å. It does not allow us to constrain the line-broadening effects of stellar velocity dispersion. More details of the observational method are described in Grasha (2023) and Chen et al. (2023).

Figure 5.1 (top) provides a V-band continuum image constructed from parts of the TYPHOON data cube. We restrict our study to this high surface brightness part of the disk, within ~ 4 kpc from the center, because we need a minimum signal-to-noise ratio of our spectra for the analysis, as specified below. Additionally, the Hα line flux measured from each spaxel is shown in Figure 5.1 (bottom). The darker the pixel, the higher the line flux obtained with the LZIFU fitting tool (Ho et al., 2016). The values saturate at $1.2 \cdot 10^{-14}$ erg/s/cm^2 for better visibility of the morphological structures. M83 is a barred spiral galaxy. In visible wavelengths, including Hα, the spiral arms and clumpy star-forming regions dominate the view, making the bar less apparent. However, when observed in the infrared, the bar stands out clearly as a distinct structure of older stars and dust, cutting through the center of the galaxy (Frick et al., 2016; Gallais et al., 1991).

It should be emphasized that the transition regions, extending from the bar toward the beginning of the spiral arm, host prominent complexes of H II regions. We note that the ionizing flux in the northeast edge of the bar is slightly less pronounced than in the equivalent area in the southwest. However, ALMA observations of both areas examined in Koda et al. (2023) revealed that these filamentary structures harbor similarly huge amounts of

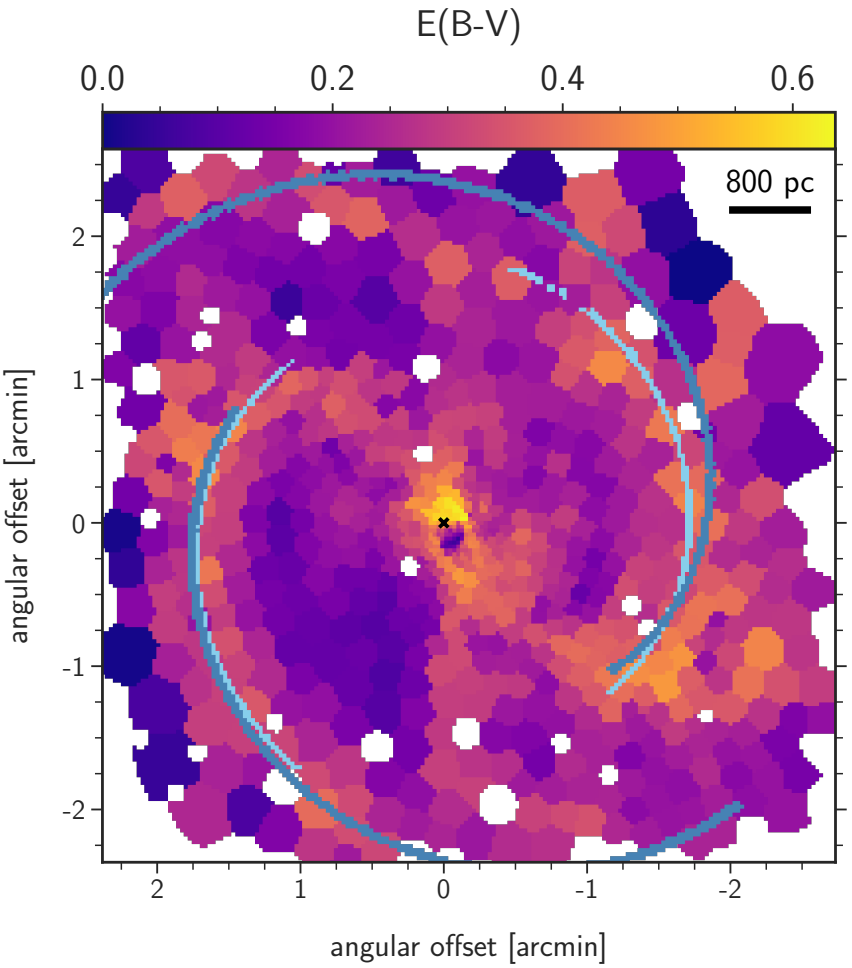

Figure 5.2: E(B-V) reddening map of M83 obtained from our TYPHOON population synthesis fit. The galaxy center defined by the peak of visible continuum surface brightness is at RA(J2000) = $13^h\,37^m\,00.95^s$ and DEC(J2000) = $-29^o\,51'\,55.50$ (Díaz et al., 2006) and indicated by a black cross. The spiral arms of Figure 5.1 are also indicated. Some areas are masked out as they are dominated by strong point sources and would therefore potentially lead to problematic fits (see text).

molecular gas and are probably caused by the overall galactic dynamics.
For our spectral analysis we use the spectral range from 4000 Å to 7070 Å. Here, the flux-calibrated spectra of the data cube have the highest signal-to-noise ratio. We stress that compared to the range 4800 Å to 7000 Å, typically used in studies carried out with the extremely powerful MUSE IFU attached to the ESO VLT, this is a crucial extension towards the blue which enables a more accurate characterization of the young stellar population. We will investigate this in more detail in Section 5.7.

5.2.2 Population synthesis method

Our population synthesis method has been described in detail in Sextl et al. (2023) and in Paper I. We repeat the basic aspects and also introduce a few changes relative to our previous work. The model spectrum M_λ of the integrated stellar population of a galaxy surface element is calculated as a linear combination of spectra of single stellar populations (SSPs) of different ages and metallicities $f_{\lambda,i}(t_i, [Z]_i)$ with age t_i and logarithmic metallicity $[Z]_i = \log Z_i/Z_\odot$ (Z_i is the metal mass fraction)

$$M_\lambda = D_\lambda(R_V, E(B-V)) \left[\sum_{i=1}^{n_{SSP}} b_i f_{\lambda,i}(t_i, [Z]_i) + b_a f_\lambda^a \right]. \tag{5.1}$$

The linear combination coefficients b_i describe the contribution to the total spectrum of a burst with age t_i and metallicity $[Z]_i$. n_{SSP} is the number of SSPs used. We note that the observed and SSP template spectra are normalized to an average value of unity in the range of 5500 to 5550 Å. Consequently, the sum over all b_i is also equal to unity. The function $D_\lambda(R_V, E(B-V))$ accounts for the absorption by interstellar dust. We use the dust attenuation law by Calzetti et al. (2000) with variable total to selective extinction R_V. An introductory paragraph about the quantity R_V is given in Sect. 5.3.1. We also account for the Milky Way foreground reddening adopting $E(B\text{-}V)_{MW} = 0.059$ (Schlafly & Finkbeiner, 2011) and the Cardelli et al. (1989) foreground reddening law with $R_V = 3.1$.
Our SSP fitting-templates are calculated from the Flexible Stellar Population Synthesis package (`FSPS`; version 3.2) (Conroy et al., 2009; Conroy & Gunn, 2010a) using the MILES empirical library of stellar spectra (Sánchez-Blázquez et al., 2006) augmented with a comprehensive set of spectra for young massive stars (see Paper I for details). They are identical to the SSPs in Sextl et al. (2023). In total, we use a grid with 52 age and 9 metallicity values (468 SSPs in total). The age grid is in logarithmic steps, roughly one-third of the models are 20 Myr and younger, with the two youngest models corresponding to ages of 0.1 and 1.0 Myr (for a detailed description of the ages, see Sextl et al. 2023). The lowest metallicity value of the grid is -1.5 dex.
We note that M83 is extensively star-forming; it is therefore important to use a set of spectral templates that include very young populations (in the realm of several Myr) and stellar libraries with hot, massive stars.
The coefficient b_a accounts for a featureless AGN continuum with wavelength dependence $\lambda^{-0.5}$ (Cardoso et al., 2017), but its contribution is negligible. An AGN characteristic broad-line region is not identifiable in any of the centrally located spectra.

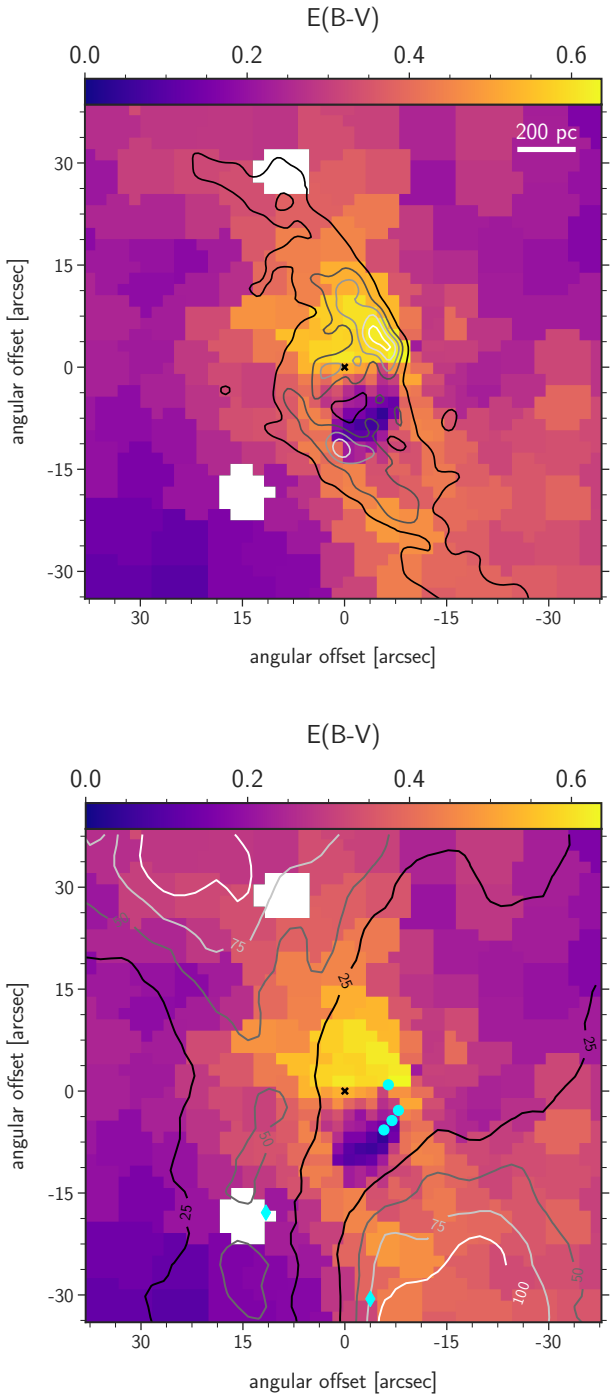

Figure 5.3: Enlarged reddening map of the central region of M83. The positions of six COS (HST) pointings of the YMCs studied by Hernandez et al. (2021) are indicated as cyan symbols. Circles correspond to clusters with very low H I column densities and diamonds refer to somewhat higher column densities (see text). ALMA CO(2-1) emission line isocontours are overplotted in the top figure in five regular steps of 200 K · km s^{-1} starting at 100 K · km s^{-1}. The bottom figures shows H I 21 cm isocontours in four equal steps from 25 to 100 Jy · beam^{-1} · m s^{-1}.

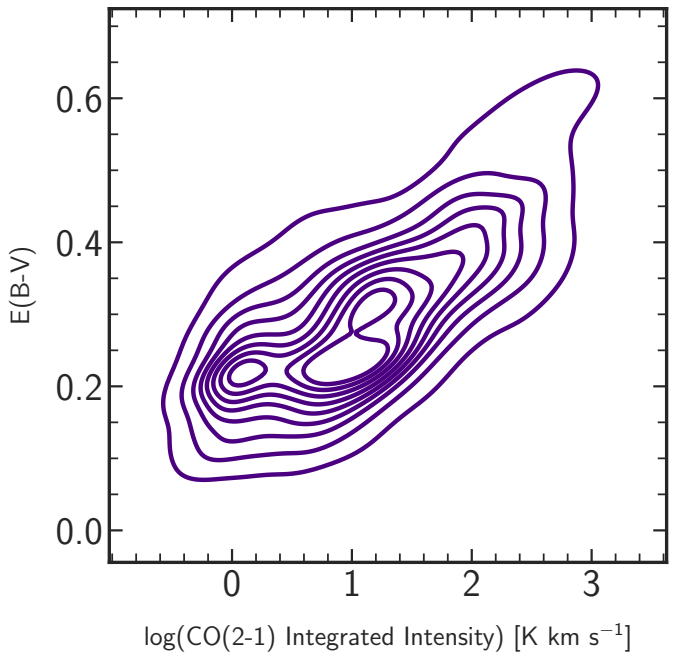

Figure 5.4: Isocontours showing the correlation between E(B-V) and CO(2-1) intensity in the central region of M83 shown in Fig. 5.3.

As explained in Sextl et al. (2023) the b_i are luminosity weighted fit coefficients. They can be expressed as

$$b_i = N_i L_i(V). \tag{5.2}$$

$L_i(V)$ is the luminosity in the V band of SSP isochrone i before spectral normalization and N_i is the number of stars represented by this SSP. We note that the N_i are the actual number of stars multiplied by a common factor to account for the normalization.
The metal content of the stellar population is obtained as follows. We use the current stellar mass of each SSP isochrone M_i, the metal mass fraction $Z_i = M_{Z,i}/M_i$ and the mass-to-light ratio $\gamma_i = M_i/L_i(V)$ and then calculate M_Z, the mass of metals contained by the stellar population

$$M_Z = \sum_i N_i M_i Z_i = \sum_i b_i \gamma_i Z_i \tag{5.3}$$

and the total stellar mass

$$M = \sum N_i M_i = \sum_i b_i \gamma_i. \tag{5.4}$$

For the metal mass fraction of the whole stellar population, we obtain

$$Z = \frac{M_Z}{M} = \sum_i \tilde{b}_i Z_i \tag{5.5}$$

with

$$\tilde{b_i} = \frac{b_i \gamma_i}{\sum_i b_i \gamma_i}. \tag{5.6}$$

Finally, using Eq. (5) and (6) the logarithmic stellar metallicity is then given by

$$[Z] = log(Z/Z_{\odot}). \tag{5.7}$$

We note that by using Eq. 5.5 to 5.7 we deviate from our earlier work in Sextl et al. (2023) and Paper I, where we have used luminosity-weighted means of $[Z]_i$ to calculate [Z]. We prefer the new approach because it provides a direct measurement of the metal content of the stellar population considered (the consequences of this new approach for the metallicities obtained in Paper I are discussed in Section 5.6).
The logarithmic age of the total population is calculated by

$$\log(t) = \sum_i \tilde{b_i} \log(t_i). \tag{5.8}$$

As mentioned above, M83 is a heavily star-forming galaxy. Thus, in order to investigate present star formation and chemical evolution and also to compare with independent spectroscopic observations of young stellar probes such as BSGs, SSCs and YMCs, as well as H II regions, it is important to extract the properties of the very young stellar population from the population synthesis fit. This is done by introducing an SSP age limit t^y_{lim} and separating the contribution of young stars through the condition $t_i \leq t^y_{lim}$.
The contribution of the young stars to the spectral fit is then

$$b_y = \sum_{i_y} b_i, t_i \leq t^y_{lim}. \tag{5.9}$$

The average metallicity $[Z]_y$ and the age $\log(t_y)$ of the young population are calculated in a similar way as in the equations above, but with sums restricted to the age bin defined by t^y_{lim}.
The star formation rate of the young population is

$$\psi_y = \frac{M_{iso} \cdot L(V)}{t^y_{lim}} \sum_{i_y} \frac{b_i}{L_i} \tag{5.10}$$

where M_{iso} is the original stellar mass of each SSP isochrone, when all its stars were formed. M_{iso} is the same for each SSP. L(V) is the observed V band luminosity of the TYPHOON Voronoi bin.
We will use $t^y_{lim} = 0.1$ Gyr to determine the ages and metallicities of the young stellar population. For the calculation of star formation rates we will adopt 20 and 5 Myr, respectively (see Section 5.3.3). To distinguish between these two cases, we introduce the star formation rates ψ^{20}_y and ψ^5_y accordingly.
In a similar way as for the young stars, we can also define the old stellar population. We introduce an SSP age limit t^o_{lim} and consider the contributions of old stars through the

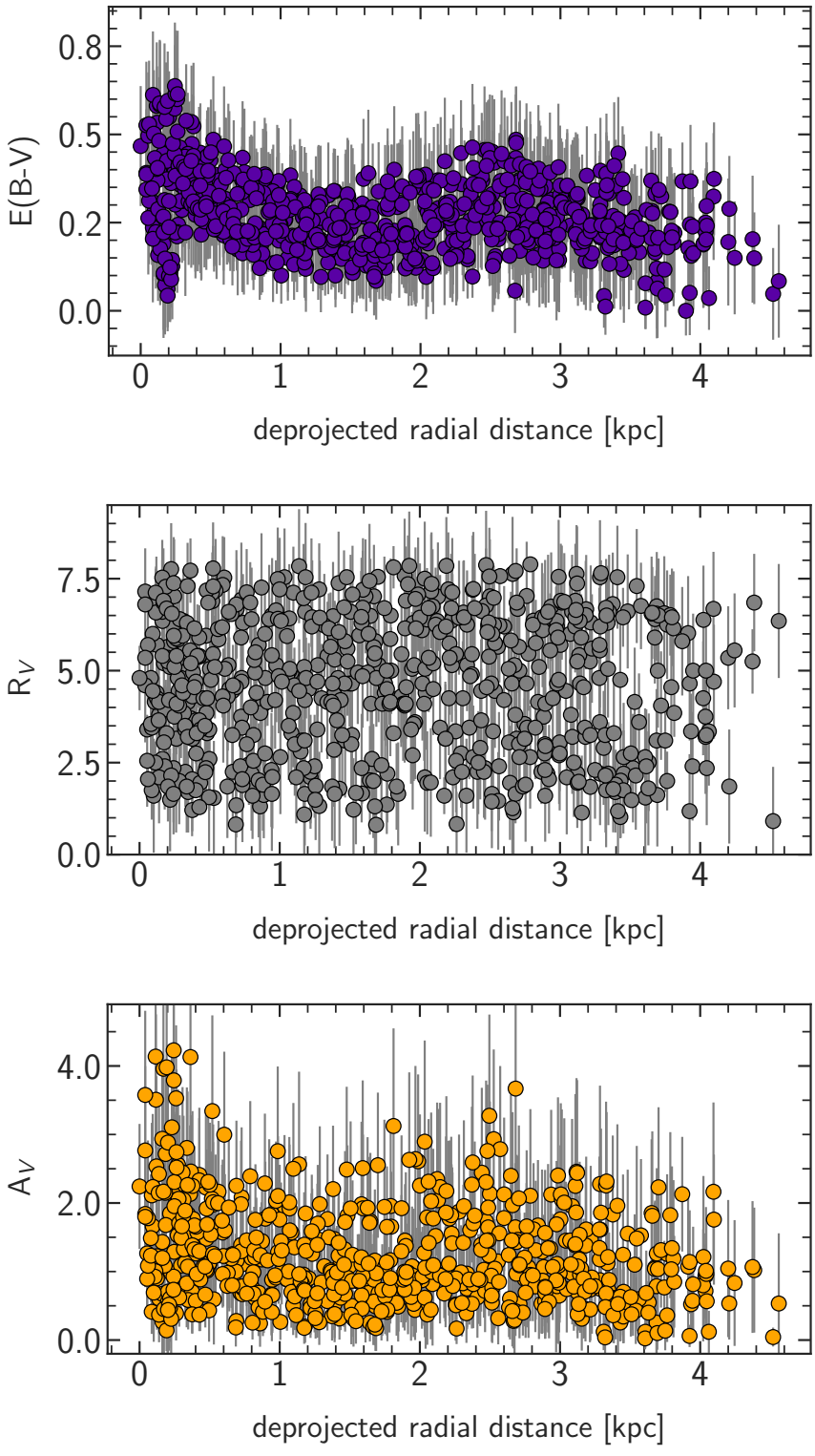

Figure 5.5: Radial distribution of E(B-V) (top), R_V (middle) and A_V (bottom).

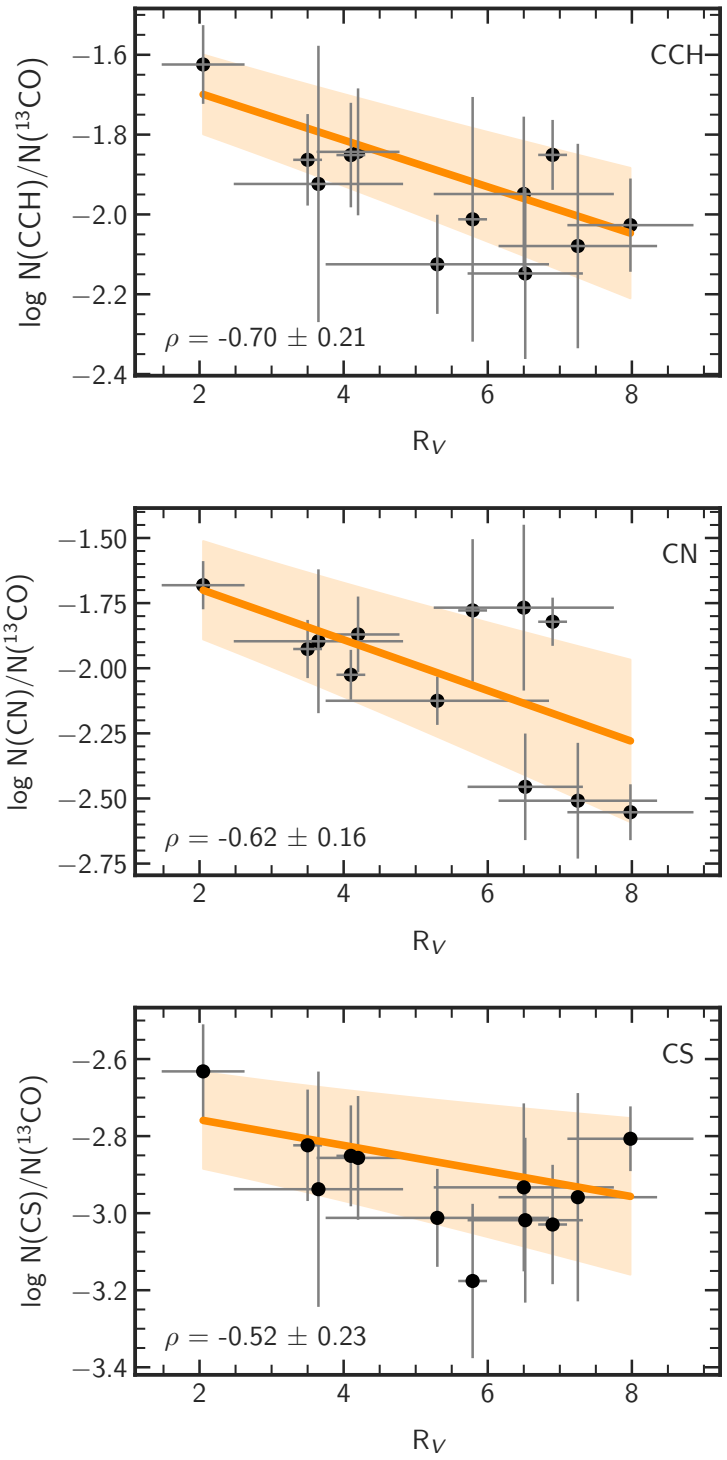

Figure 5.6: Correlation of R_V with column density ratios of three molecular species, CCH (ethynyl radical, top), CN (cyano radical, middle), and CS(carbon monosulfide, bottom), at selected positions in the central region of M83. A linear regression fit is shown in orange colors. The Pearson correlation coefficient ρ is printed at the left bottom of each plot and uncertainties of each data point are shown.

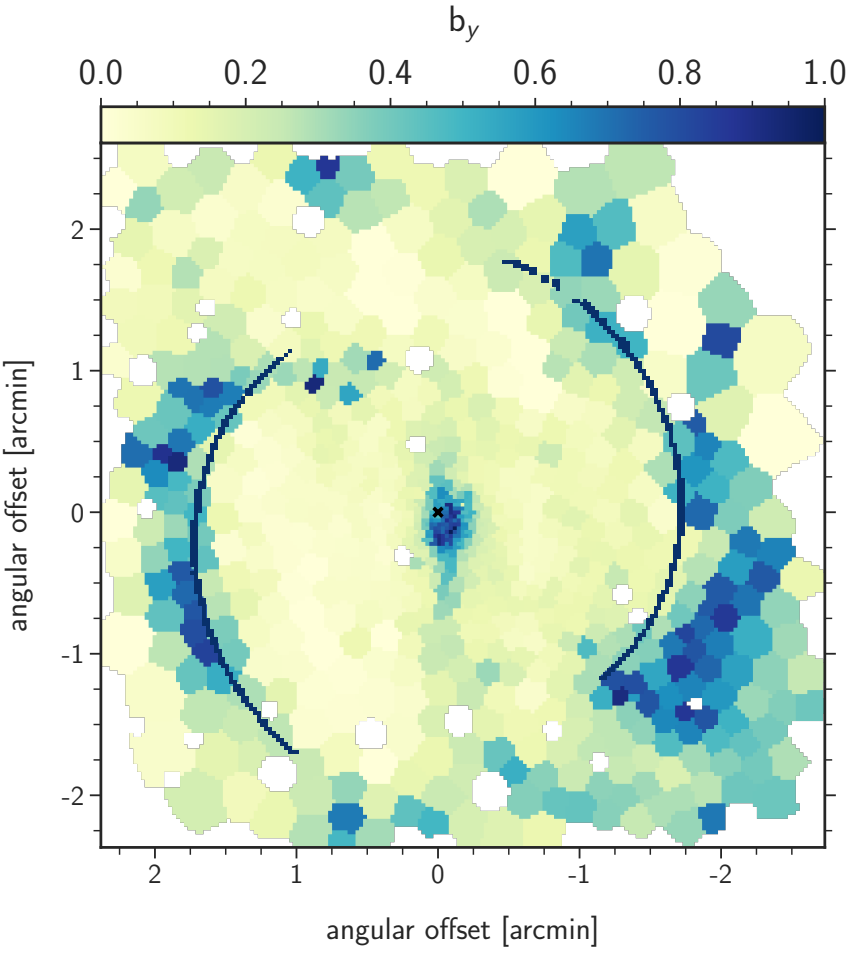

Figure 5.7: Spatial maps of the fit contribution coefficients b_y for the young stellar population. The plot indicates which fraction of the measured flux at 5500 Å comes from stars younger than 0.1 Gyr. The location of the CO spiral arm fit is shown in dark blue.

condition $t_i \geq t^o_{lim}$. This allows us to calculate the fit contributions b_o, metallicities $[Z]_o$, and ages $\log(t_o)$ as in Eq. (9) to (12), but with sums over SSP that satisfy the age criterion for the old population. As a typical value for t^o_{lim}, we will use 1.6 Gyr (see Paper I and Sextl et al. 2023).

The analysis requires a certain minimum signal-to-noise ratio for the observed spectra. Depending on the galaxy surface brightness we may need to combine spectra of adjacent individual spaxels to obtain this level. We accomplish this by Voronoi binning using Cappellari & Copin (2003) until we obtain a minimum signal-to-noise ratio of 60 in the stellar continuum at 5000 Å. The binning is performed over the FOV shown in Figure 5.1, and this spatial scale is maintained in the subsequent 2D maps, except for the zoomed-in view of the center. Because of the small distance of M83 and the high surface brightness, most of our Voronoi bins are relatively small and allow us to trace spatial variations such as spiral arms, except in the very outer galaxy regions where we start averaging over too large spatial dimensions. In those outer regions we exclude bins consisting of more than 330 TYPHOON spaxels. This leaves us with spectra of 737 bins distributed throughout the galaxy. Figure 5.2 gives an impression of the spatial distribution of the bins. With a distance of 4.81 Mpc, M83 is rather close and bright point sources could possibly interfere with the fitting procedure of unresolved stellar populations. We remove those areas following the foreground star removal algorithm outlined in Clark et al. (2018), utilizing the Python package PTS-7/8 [1] (a python toolkit for the SKIRT radiative transfer code presented in Camps & Baes (2015, 2020)). The procedure operates in our case on a CTIO 1.5m *R*-band image of M83 and starts by retrieving relevant entries from the 2MASS All-Sky Catalog of Point Sources (Cutri et al., 2003) using the Astroquery Python library[2]. For each cataloged position, the algorithm examines a small image patch, subtracting the estimated background and searching for a local peak using the Photutils Python package[3]. The process ignores positions where no reasonable signal-to-noise (SN>5) peak is found within a few pixels' radius. To prevent removal of compact sources within target galaxies (such as H II regions and massive clusters), the procedure only considers peaks that show no deviations from being true point sources, except for potential saturation in the brightest stars. We find that for TYPHOON IFU data with an FWHM of 2 arcsec for the point spread function (D'Agostino et al., 2018) and a low spatial resolution of 1.65 arcsec, this approach is good enough.

We apply a radial velocity correction to the observed spectra and then focus on the analysis of their stellar contribution by masking out spectral regions contaminated by ISM emission or absorption lines. However, we account for the nebular continuum emission potentially underlying the stellar spectra. The strength of this continuum is determined from the strength of observed Hα or Hβ emission. For details, we refer to Sextl et al. (2023).

After these preparative steps, the coefficients b_i and b_a are determined by adopting a grid of R_V and E(B-V) value. For each pair of these quantities we redden the model spectra

[1] https://github.com/SKIRT/PTS

[2] https://github.com/astropy/astroquery

[3] https://github.com/astropy/photutils

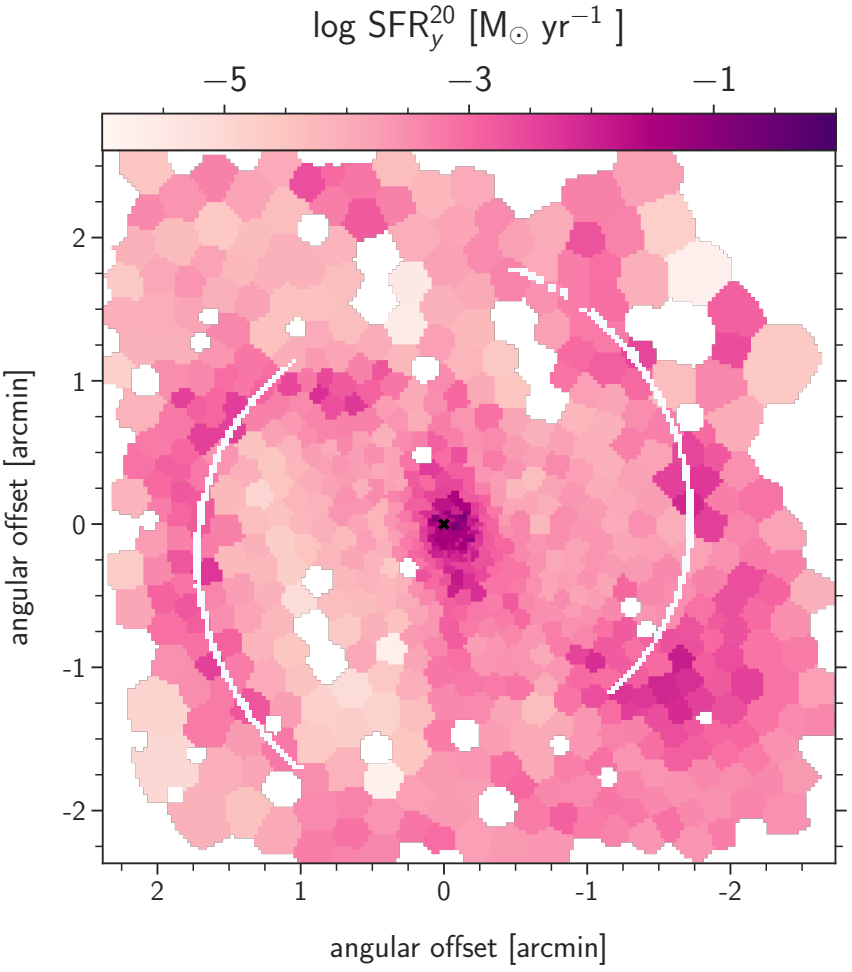

Figure 5.8: Spatial map of the star formation rate of the young stellar population ψ_y^{20} over the last 20 Myr.

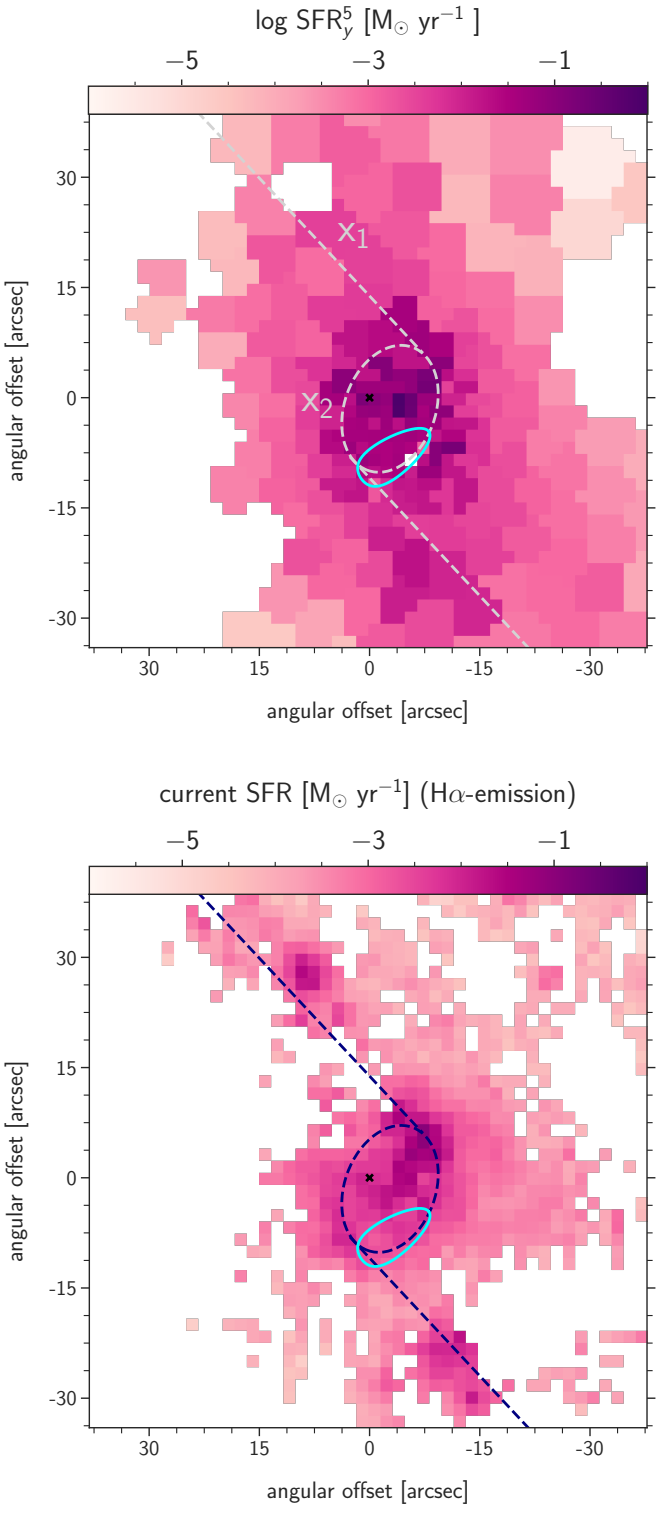

Figure 5.9: Top: Central map of most recent star formation ψ^5_y encountered over the last 5 Myr as obtained from our population synthesis analysis. Bottom: Central map of the star formation rate derived from Hα emission. The position of the dust cavity (in aqua) and the gas flow along potential x_1 & x_2 orbits are also shown (see text).

with $D_\lambda(R_V, E(B-V))$ and apply the bounded variable least-squares algorithm (`BVLS`, Stark & Parker 1995, see also Sextl et al. 2023) to directly solve for the coefficients b. We then use the resulting model spectrum and calculate a χ^2 value by comparing with the observed spectrum. The minimum of χ^2 defines the best fit with respect to R_V and E(B-V). We estimate errors by fitting again the observed spectra but this time modified by adding Monte Carlo Gaussian noise with zero mean and a standard deviation corresponding to the flux error at each wavelength point. The uncertainties of the stellar population parameters are then calculated as the standard deviation of their distributions produced by 50 such Monte Carlo realizations.
In the following sections, we present the results of our M83 population synthesis analysis.

5.3 Results: Reddening, star formation, ages, and inside-out growth

In the subsections following below we present the results with respect to reddening, extinction, star formation, average ages, and inside-out growth of the galactic disk.

5.3.1 Reddening and extinction: a dust cavity in the center and correlations with molecular gas

Figure 5.2 shows the reddening map of M83 obtained with our population synthesis approach. The contribution of Milky Way foreground reddening is subtracted as described above. Generally, we find enhanced reddening close to the spiral arms and the bar, which coincides with an increased emission from atomic and ionized H, cold molecular CO gas and cold and warm dust (see, for instance, Frick et al. 2016). For the northern spiral arm, where we have encountered a difference between the Hα and CO logarithmic fit, the maximum of the dust absorption follows the molecular gas.
Figure 5.3 provides an enlarged reddening map of the central region of the galaxy and reveals a complex structure of the dust distribution. Reddening is enhanced in a confined area north of the center, whereas southwest of the center we find a region of low extinction corresponding to a dust cavity. Its estimated size, with a diameter of 11 arcseconds, corresponds to approximately 260 parsecs. This dimension is comparable to the Local Bubble observed in the Milky Way (Zucker et al., 2022), hinting at a similar origin related to past enhanced star formation with supernovae. As we shall see later, the cavity is almost void of molecular and atomic ISM gas. Della Bruna et al. (2022) also highlight a significant dip in velocity dispersion within this area ($\sigma < 60$ km/s).
The dust cavity is also strikingly apparent in the multicolor optical images obtained with the Hubble Space Telescope. Figure 1 in Harris et al. (2001) very clearly reveals a bright elongated region south of the center that exactly coincides with our cavity. Very obviously, a hole in the dust distribution allows us to peek into a region containing bright massive clusters and stars. Measurements of the Balmer decrement through Hα and Hβ imaging

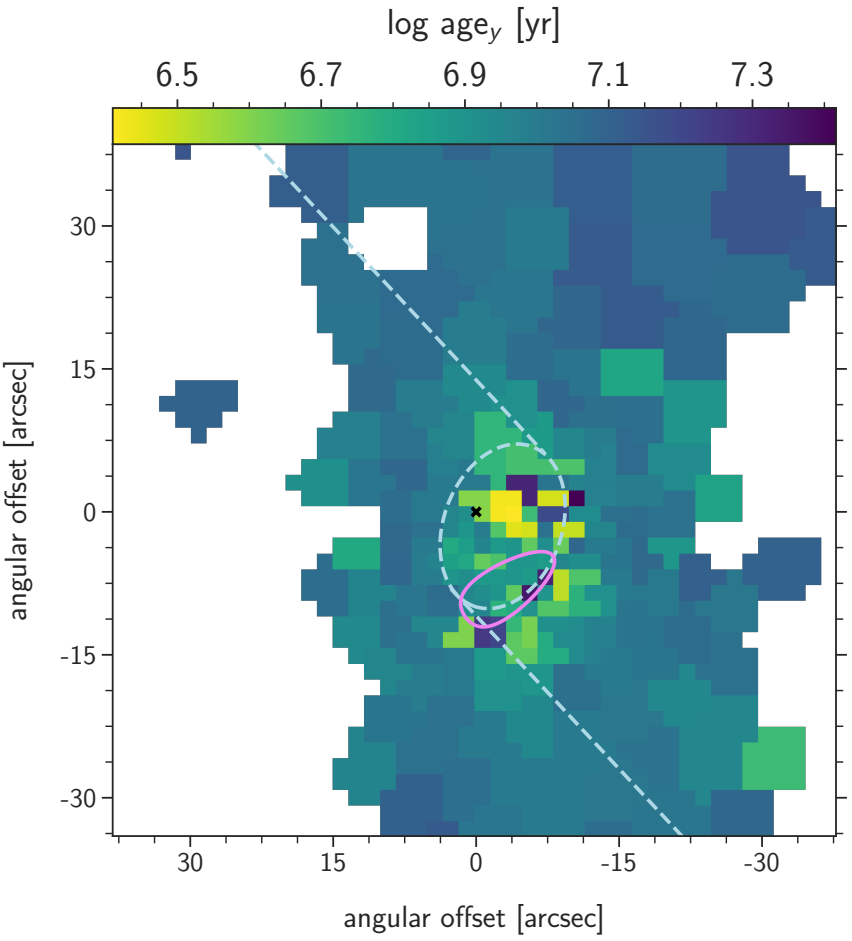

Figure 5.10: Central map of the average age (in years) of the young stellar population. x_1 & x_2 orbits (light blue) and the dust cavity (pink) are again overlaid.

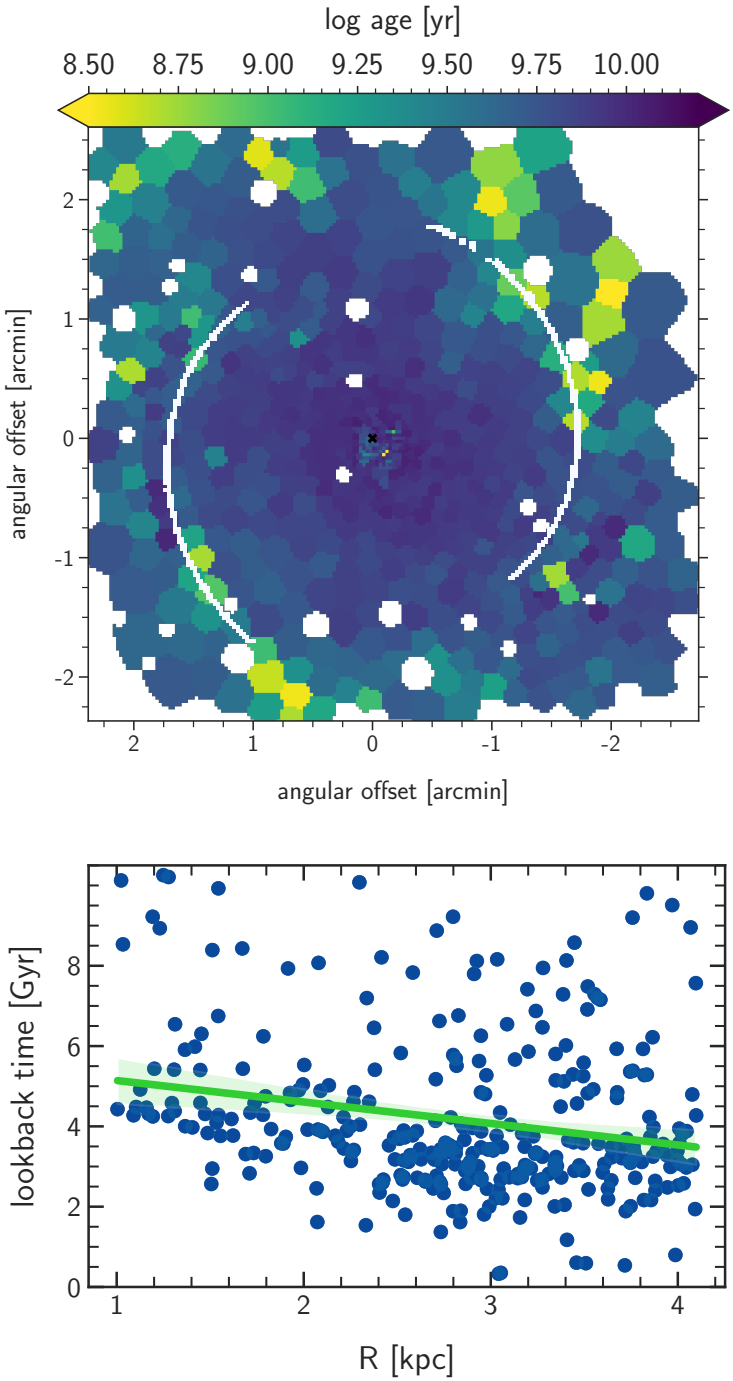

Figure 5.11: Top: Map of the average stellar population age. CO spiral arm fits are over-plotted for orientation. Bottom: Lookback time when 85 percent of the mass of the total stellar population has formed as a function of galactocentric radius in kiloparsec. A linear regression curve (in green) is also shown. A trend decreasing with radius indicates inside-out growth.

(Figure 4 in Harris et al. 2001) indicate very low reddening in our cavity region. We take this as confirmation that full-spectral fitting is a very powerful tool for investigating the distribution of reddening and interstellar dust.

We note that the complex pattern in the center of M83 with an extinction cavity surrounded by large extinction is not unique. Figure 3 of the TYPHOON study by Sextl et al. (2023) reveals a similar structure for the barred spiral NGC 1365. Because of the significantly larger distance of this galaxy (18 Mpc) the spatial resolution is worse and the effect appears to be less striking, but it is definitely there.

As the comparison with the ALMA CO (J = 2-1) isocontours shown in the upper part of Figure 5.3 indicates, the distribution of molecular gas roughly coincides with the distribution of dust. The peak of CO emission correlates with the northern region of strong reddening, and the dust cavity shows a low level of CO emission. Figure 5.4 documents the overall correlation between dust and CO in the center. This supports a scenario where the molecular gas forms out of the atomic gas in regions of enhanced dust density with dust grain surfaces acting as a catalyst. The ALMA observations used in the figures are described in Hirota et al. (2018) and were downloaded from the PHANGS archive[4].

Comparing with the H I 21 cm isocontours of the THINGS survey (Walter et al., 2008), we indeed find that the regions with the maximum concentration of E(B-V) and CO coincide with very low neutral hydrogen gas concentration (Figure 5.3, bottom part). This seems to agree with the transformation of atomic to molecular gas in the presence of dust. On the other hand, our dust cavity with low CO emission is still located in an area of very low H I column densities. This is further confirmed by the work of Hernandez et al. (2021), who carefully studied H I column densities in the central region by analyzing the strength of Lyα absorption lines superimposed on the UV spectra of the integrated light of YMCs. The location of these YMCs is also shown in Figure 5.3. The four objects of low absorption column densities ($\log[N(HI)/cm^2] \leq 20$) are located close to or inside the dust cavity. This points to an overall decrease of ISM matter density of all components, neutral and cold molecular gas and dust, in this part of the center. This is corroborated by Hernandez et al. (2023) in their JWST mid-IR investigation of the center of M83 detecting molecular emission of cold and warm H_2 gas.

The radial distribution of E(B-V), R_V, and A_V is shown in Figure 5.5. The radial plot of E(B-V) reflects the complex structure in the center and a reddening decline towards an outer average level of E(B-V) $\approx$ 0.2 mag. The small increase around 2.5 kpc is caused by the contribution of spiral arms and the large areas of related star formation. As in our study of NGC 1365, we find a wide range of R_V values, while A_V roughly follows the reddening distribution. No covariances between E(B-V) and R_V were encountered.

In general, the R_V parameter plays a significant role in characterizing the shape of the extinction or attenuation curves and can potentially provide information on the nature of dust grains. For a typical extinction situation with individual bright stellar point sources such as supergiant stars shining through a dust screen, sight lines that include larger dust particles create an extinction curve with a high value of R_V and produce flatter or 'greyer'

[4] `https://sites.google.com/view/phangs/home/data`

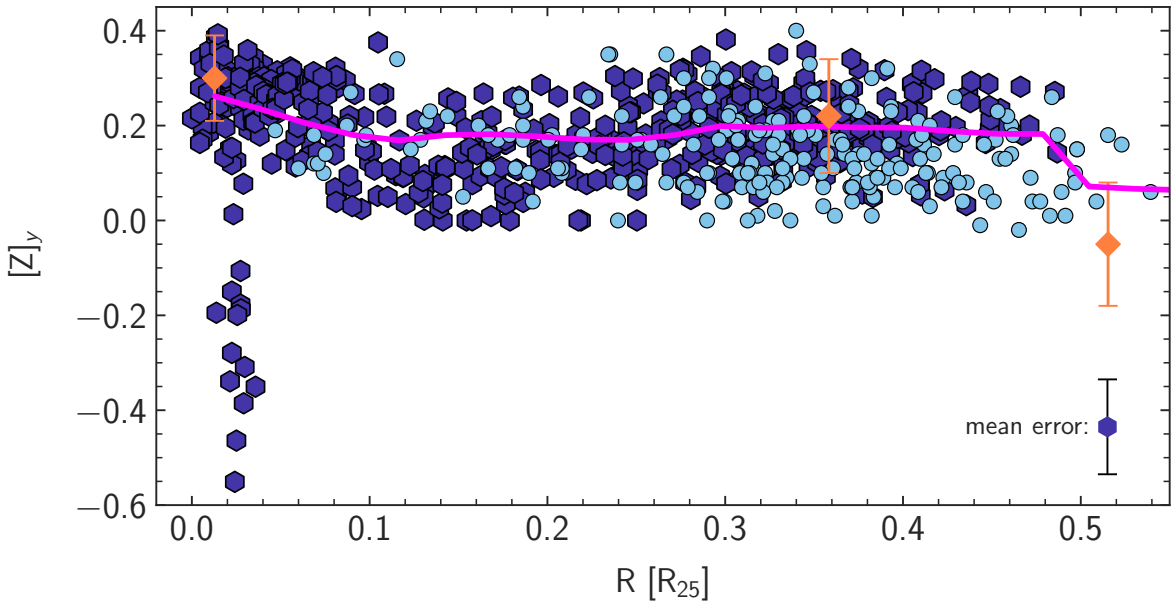

Figure 5.12: The radial gradients of the young population metallicities (in dark blue hexagons) from full-spectral fitting compared with results from individual H II regions. The H II region strong-line abundances (in light blue) were determined from the same TYPHOON data cube (Grasha et al. 2022, see text). In addition, H II region abundances obtained with the direct method by Bresolin et al. (2005, 2016) are shown in orange. Errorbars of individual Voronoi bins and TYPHOON H II regions are omitted for better visibility. They have average values of 0.1 dex as indicated. The prediction of the chemical evolution model presented in Bresolin et al. (2016) is shown in pink. For discussion see text.

extinction curves (Cardelli et al., 1989; Fitzpatrick & Massa, 2007). This means that the extinction is more uniform across different wavelengths, resulting in less wavelength-dependent reddening. A large variety of R_V values is observed in the literature, for instance, $R_V \sim 5$ in selected molecular clouds, $R_V \sim 1-3$ for supernovae type Ia and $R_V \sim 2-7$ for massive blue supergiant stars (Mandel et al., 2011; Dwek, 2005; Urbaneja et al., 2017; Kudritzki et al., 2024).

Unfortunately, for our population synthesis analysis with stellar sources distributed within the dusty ISM the interpretation is more complicated because we are dealing with attenuation curves (Calzetti, 2013). Still, with our comprehensive information on the spatial distribution of R_V it is particularly interesting to correlate its values with other properties in M83. In the radial plot (Figure 5.5, middle), the values appear to be arbitrarily distributed. We also find no correlation with metallicities, stellar ages, or the obtained color excess values in the associated bins. However, in the special case of M83, we also have the unique opportunity to compare with the results of an astrochemical ISM study.

Harada et al. (2019) analyzed ALMA data in the center of M83 and obtained the column densities of different molecular ISM species. This was done at 12 selected pointings in and around the circumnuclear ring (see their Figure 1). As the authors give the coordinates of these positions, we were able to obtain the corresponding R_V values from our fit. The main results are shown in Figure 5.6. We find an indication of an anti-correlation between our R_V and their fractional abundances of CCH (ethynyl radical) and somewhat weaker dependencies with CN (cyano radical) and CS (carbon monosulfide). A regression fit with uncertainty bands and the corresponding Pearson correlation coefficients with error estimates resulting from Monte Carlo bootstrapping are also plotted.

In other words, the molecular species CCH (and, to a lesser extent, CN and CS) might be preferentially abundant in regions where smaller dust grains dominate the dust size distribution. Of course, this interpretation of the observed correlations assumes that R_V and dust grain size remain related in the population synthesis attenuation analysis. We also note that the abundances of additional ISM species listed in Tables 4-6 in Harada et al. (2019) (including CH3OH, H2CO and NNH) show no correlation with the slopes of the extinction curves we obtain.

To further explain these findings, it is crucial to understand the multifaceted role of dust in the ISM. First, the surfaces of dust grains act as catalysts for chemical reactions, particularly in the formation of molecular hydrogen and complex organic molecules (Wakelam et al., 2017; Herbst & van Dishoeck, 2009). Second, dust particles absorb stellar radiation, especially in the ultraviolet and at optical wavelengths, and re-emit this energy in the infrared and sub-millimeter range in the form of thermal emission (Viaene et al., 2016). Third, dust grains participate in heating of the ISM via the photoelectric effect (where they absorb UV photons and eject energetic electrons) as well as through collisions with gas particles (Draine, 1978).

The efficiency of these dust-mediated processes is significantly influenced by the size distribution of dust grains. As noted previously, an increase in R_V shifts the grain size distribution towards larger grains. This shift has several important consequences. Larger grain sizes result in reduced dust opacity, particularly in the UV range, allowing deeper penetra-

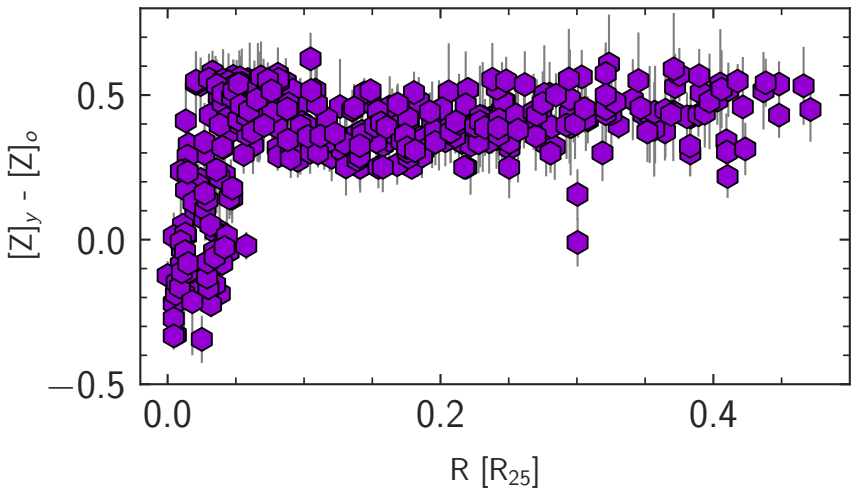

Figure 5.13: The radial gradient of the metallicity difference between the young and old stellar populations. This time, the error bars are explicitly shown.

tion of far-ultraviolet (FUV) radiation into molecular clouds (Weingartner & Draine, 2001; Abel et al., 2008). This leads to elevated FUV radiation energy densities and accelerated gas heating (Wolfire et al., 2022).
On the other hand, FUV photons from neighboring massive stars lead to so-called photodissociation regions (PDRs) at the edges of molecular clouds. It is known that in PDRs the ISM species CCH and CN are predominantly produced through photochemical processes (Martín et al., 2015). CS formation is also favored in PDR environments via ion reactions (Martín et al., 2008; Forrey et al., 2018). Röllig et al. (2013) demonstrated using CLOUDY calculations that larger grains lead to hotter PDRs and consequently lower column densities of H_2, CO, and OH^- compared to scenarios with smaller grains. Although the authors did not explicitly test this for other ISM components, it seems plausible that this trend extends to gas-phase-created species such as CCH, CN, and CS (Sipilä et al., 2020). This would explain the observed correlations. In that sense, Figure 5.6 provides a strong motivation to further investigate the complex interaction between dust grain size and the chemical composition of the ISM.

5.3.2 The Spectral Contribution of the Young and Old Population

In our population synthesis fit we explicitly separate between the contribution of a young and older population to the integrated stellar spectrum. The weights b_y, as defined in Eq. 5.9, describe the relative contribution of the young population to the spectral fit. Their distribution across the galaxy is shown in Figure 5.7 (we have adopted $t^y_{lim} = 0.1$ Gyr for the plot). We find a strong contribution close to the spiral arms and in the center. The inter-arm region, on the other hand, is clearly dominated by older stars. We note that

the contribution of the young stars is slightly shifted away from the spiral arms marked by CO and E(B-V) (see Figure 5.2). This may be the result of disk rotation, spiral pattern speed, and star formation and will certainly be worth further investigation.
The uncertainties of our measurements of the metallicity and age of the young population depend on b_y. The dependence is weak as long as the weights are greater than 0.1. However, once b_y becomes smaller than 0.1, the uncertainties increase and we will not include the corresponding values of metallicities and ages in our discussion and plots. Similarly, the uncertainties for the old population depend on b_o and we will not include the results obtained from the spatial bins with $b_o \leq 0.2$. Errors will be indicated in the plots in the following sections.

5.3.3 Star formation

Figure 5.8 provides spatial maps of ψ_y^{20}, the star formation rate of the young stellar population. We have chosen a maximum age of $t_{lim}^y = 20$ Myr in order to capture the most recent star formation events (see, for instance, Riffel et al. 2021). We clearly see enhanced star formation close to the spiral arms and a giant active star formation region in the southwest of the galaxy at the leading egde outside the spiral arm. We also encounter the well-known nuclear star burst of M83 with strongly enhanced star formation.
In Figure 5.9 we display enlarged maps of the star formation rates in the center. We show the results obtained from full spectral fitting and from Hα flux measurements. For the former, we have chosen $t_{lim}^y = 5$ Myr for reasons explained below. We also include orbits of matter infalling along the bar and around the circumnuclear ring reconstructed from the CO maps shown in Harada et al. (2019). The x_1 orbit types are elongated and aligned with the major axis of the bar and drawn as straight lines in our figures. x_2 orbits, in contrast, are perpendicular to the bar's major axis, often rather circular and typically found inside the Inner Lindblad Resonance (ILR) of the galaxy (Contopoulos & Grosbol, 1989). They both play important roles in the galactic structure and in the evolution of the bar. Harada et al. (2019) argue that at the intersection of both orbit types, molecular gas clouds accumulate and collide, eventually triggering star formation events.
The orbital period of a typical x_2 orbit is 10 Myr (Harada et al., 2019). We therefore select $t_{lim}^y = 5$ Myr for the determination of star formation rates. This is also a time scale that agrees with the ages of the very young stars in the center (see 5.3.4). Extensive star formation is visible throughout the central region within the x_2 orbits. However, we do not see a clearly pronounced minimum of star formation in the region of the dust cavity and the void of molecular gas.
For the sake of testing the method of full-spectrum fitting, it is interesting to compare our star formation results based on stellar population synthesis against the standard method using Hα emission. We use the Kennicutt (1998) relationship between the star formation rate and (dereddened) Hα fluxes in the version updated by Calzetti et al. (2007). We plot the central distribution of star formation rates derived from the Hα fluxes in Figure 5.9 (bottom). We exclude spaxels with signal-to-noise ratios less than 3 in Hα, Hβ, [NII]6583 or [OIII]5007 and regions which lie above the Kewley line (Kewley et al., 2001) in the BPT

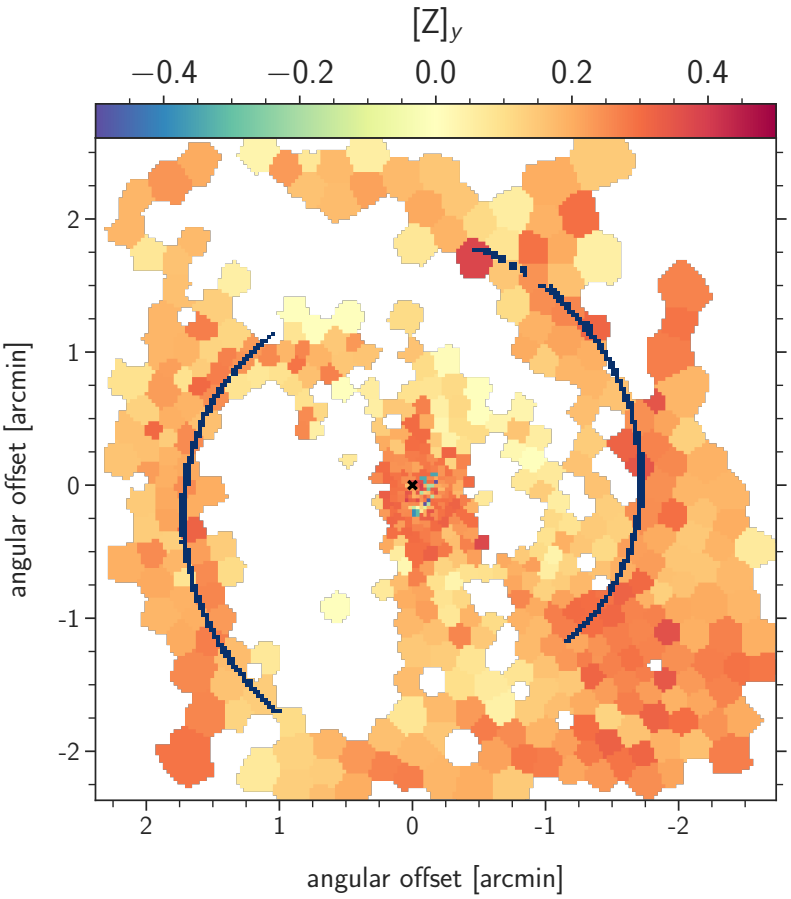

Figure 5.14: Metallicities of the young stellar population. CO spiral arms are indicated as before. Regions with $b_y < 0.1$ were removed in order to exclude results with larger uncertainties (see text).

diagram (i.e. being photoionized by shocks) and we remove the effects of reddening and attenuation of the Hα fluxes by applying the Balmer decrement method and by additional correction for Milky Way foreground extinction.
In general, the distribution of the SFR derived from Hα in the ring and the x_2 orbits is very similar to the structure obtained with population synthesis for the last 5 Myr. We find again very strong star formation activity inside the x_2 orbits. Enhanced star formation activity is also found along the x_1 orbits.

5.3.4 Stellar ages: the young population in the center

Figure 5.10 displays the average age of the young stellar population in the center of M83. We have chosen $t^y_{lim} = 0.1$ Gyr for the calculation, but the mean ages are much younger. We note that the region of maximum star formation and the largest dust content is dominated by very young stars with ages smaller than 10 Myr. The regions with extremely young stars of 5 Myr age coincide with very strong Hα emission. The dust cavity region and the

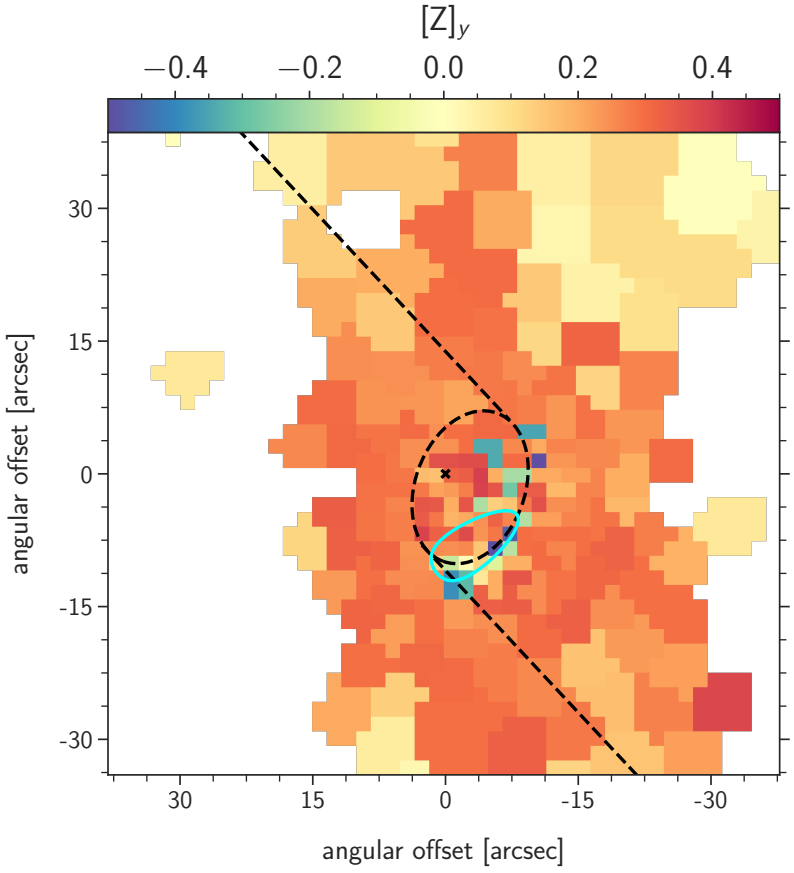

Figure 5.15: Enlarged map of $[Z]_y$ around the center of the galaxy.

eastern part of the x_2 orbit harbor slightly older stars with ages around 7 Myr. Typical age uncertainties are 1 Myr. Thus, we think the age difference is significant. We note that the ages obtained with our population synthesis approach are in good agreement with the spectroscopic study by Bresolin & Kennicutt (2002) of nuclear hot spots around the center of M83.
More generally, in a wider region around the center, the population is still very young with an age smaller than 20 Myr. This is in strong contrast with the outer galactic disk, as we shall see in the next subsection.

5.3.5 Inside-out growth of the galactic disk

As discussed in Paper I the average age of the stellar population gives a good overall impression about the evolution of the galactic disk. Figure 5.11 (top) shows the age map of the total stellar population of M83. We find a strong contribution by young stars in the star-forming regions close to the spiral arms. The remaining parts of the disk show a strong contribution from older stars. Their ages do not seem to vary much. This is consistent with Pessa et al. (2023), who found older stellar populations evenly distributed throughout galactic disks of PHANGS-MUSE galaxies. In M83, there seems to be a slight increase when leaving the center, with a maximum at approximately 0.15 R/R_{25} and then the ages drop again very moderately. As we have found in Paper I for the barred spiral NGC 1365, this might be indicative of galactic inside-out growth. We, therefore, use the same method as in Paper I (Eq. 9) to calculate the lookback time when 85 percent of the mass of the total stellar population has formed. The result is shown in the bottom part of Figure 5.11, which indicates a trend, with outer stars being on average slightly younger. The regression shows a gradient in the time of disk formation of -0.53 ± 0.13 Gyr/kpc or -4.8 ± 1.2 Gyr/R_{25}. This is comparable, given the limits of accuracy, to -4.4 ± 1.3 Gyr/R_{25} found in Paper I for NGC 1365. The inside-out growth may have proceeded similar in both galaxies.

5.4 Results: Stellar Metallicity

5.4.1 Radial metallicity gradients

In a first step, we discuss the metallicity of the young population defined by ages smaller than $t^y_{lim} = 0.1$ Gyr. We display the radial distribution in Figure 5.12 and find two striking features. In the innermost disk and the center, we encounter a significant drop of $[Z]_y$. As we shall see in the next subsection, these lower values of metallicity are confined to a small region in the center of the galaxy. We note that we have encountered a very similar behavior in NGC 1365 (see Paper I).
The distribution further out in the disk ($R \geq 0.04$ R_{25}) is stunningly flat and barely shows a negative metallicity gradient. We notice a weak drop at 0.15 R/R_{25} and then an increase toward smaller and larger radii. A regression fit yields $[Z]_y = 0.20(\pm 0.02) - 0.01(\pm 0.06)$

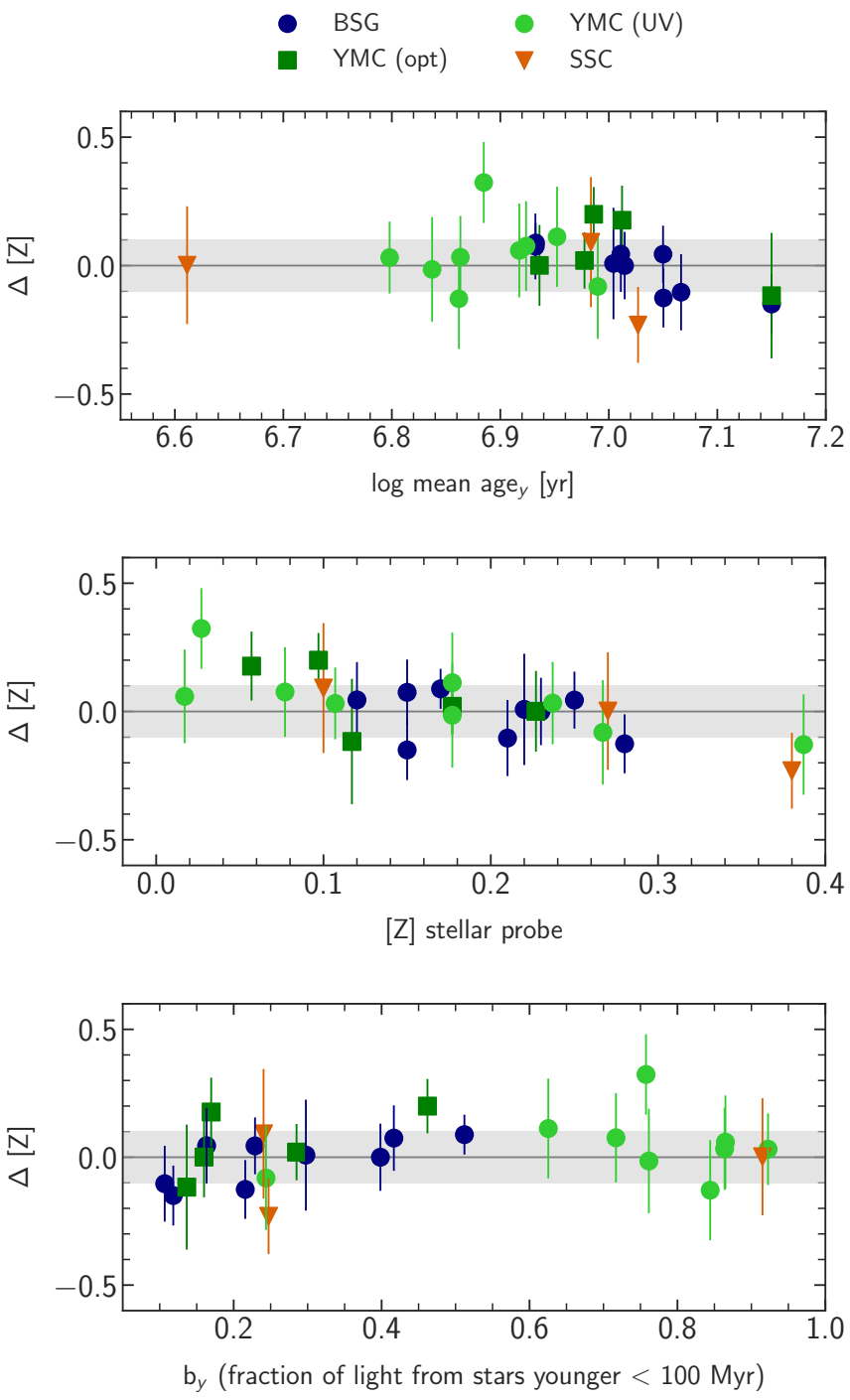

Figure 5.16: Difference Δ[Z] = [Z]$_y$ - [Z]$_{probe}$ between population synthesis and individual stellar source metallicities as a function of the mean flux-weighted age (top), [Z$_y$] (middle) and b$_y$ (bottom). Color coding: dark blue circles: BSG, red triangles: SSC, dark green squares: YMC (optical analysis), light green circles: YMC (UV analysis). Errors result from the addition of stellar source and population synthesis errors in quadrature. The shaded gray strip indicates a difference $\leq \pm 0.1$ and is added for orientation.

R/R_{25}. For comparison, we have also added the radial distribution of H II region oxygen abundances in units of the solar value (Asplund et al., 2009) to our plot of $[Z]_y$. The H II region data were obtained by Grasha et al. (2022) from the M83 TYPHOON survey data cube with the use of HIIphot (Thilker et al., 2000) for identification and LZIFU (Ho et al., 2016) for the measurement of emission line strengths. We have utilized these line strengths and applied the Dopita et al. (2016) strong line calibration for the estimate of oxygen abundances. They confirm the very shallow gradient in this part of the disk, which was already noted by Grasha et al. (2022). For completeness, we also add the H II region metallicities obtained by Bresolin et al. (2005, 2016) with the direct method using weak auroral emission lines and with uncertainties smaller than 0.3 dex.
The flat metallicity distribution in the radial range $0 \leq R/R_{25} \leq 0.5$ was predicted by the chemical evolution model presented in Bresolin et al. (2016). The model is based on the method by Kudritzki et al. (2015) and adopts constant ratios of the galaxy mass loss and the accretion mass gain to the star formation rate. It uses the azimuthally averaged ratios of stellar mass to gas mass for the calculation of the radial metallicity profile. The prediction of this model is shown in Figure 5.12 as well. The metallicity profile simply reflects the average radial ratio of stellar to gas mass. It reproduces the observed metallicity distribution very well, but it does not explain the spatial bins of low metallicity in the center. We note that our IFU study presented here covers only the inner 4 kpc of the galactic disc. The spectroscopic work presented in Bresolin et al. (2016) shows very clearly that the metal content drops towards larger galactocentric distances in a huge extended disk with a metallicity 0.4 dex below solar.
In Figure 5.13 we show the metallicity difference $[Z]_y - [Z]_o$ between the young and old stellar populations. The average value of 0.4 dex in the disk indicates a significant degree of chemical evolution. We note that the distribution is flat, which means that the old population also does not exhibit a gradient. We also note a strong increase in the center. We attribute this to the decline of $[Z]_y$ in the center. We will continue to discuss this further in the next subsection.

5.4.2 Galactic distribution of metallicity

One of the major purposes of this work is the investigation of deviations from simple gradients and from azimuthal homogeneity of the chemical composition of the young stellar population. In Figure 5.14 we show the corresponding spatial map of metallicity. Although the analysis of the result is hampered by the large areas with missing information due to $b_y \leq 0.1$, we can still see a pattern. We see increased metallicity close to the spiral arms, the bar, and around the center together, with a drop between the center and the spiral arms. In addition, the star-forming area southwest of the western spiral shows increased metallicity. We do not encounter regions of lower metallicity in the downstream areas of the spiral arms, as detected in the case of the H II region analysis of the two grand-design barred spirals NGC 1365 and NGC 2997 by Ho et al. (2017, 2018) and Kreckel et al. (2019). Our result agrees with the H II region study by Chen et al. (2024). In the case of a galactic disk without a metallicity gradient, stellar population synthesis fitting is very likely not

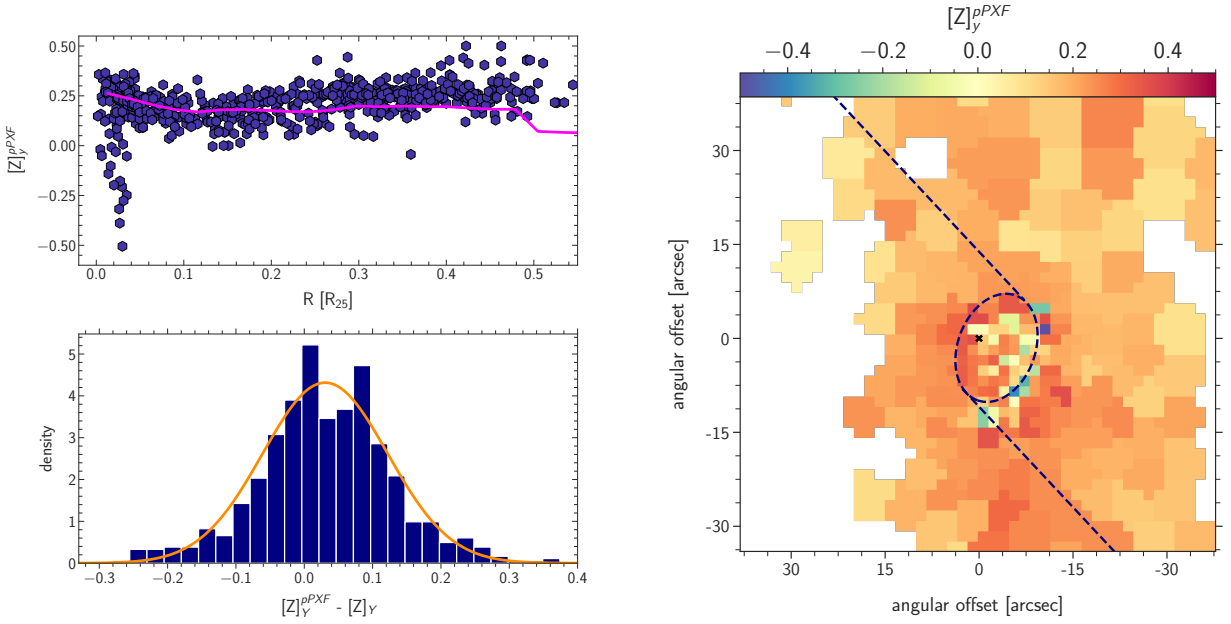

Figure 5.17: Population synthesis with `pPXF`. Top left: Radial gradient of $[Z]_y^{pPXF}$, the chemical evolution model from Bresolin et al. (2016) is shown again in pink to guide the eye. Bottom left: Distribution function of the difference $[Z]_y^{BVLS} - [Z]_y^{pPXF}$, the orange line is a fitted Gaussian function. Right: Central map of $[Z]_y^{pPXF}$

.

sensitive enough to detect these very small subtle variations.

In the following, we discuss the metallicity distribution in the center. Figure 5.15 provides an enlarged map of the $[Z]_y$ distribution in the central region of the galaxy. We find significantly reduced metallicities in the western region of the x_2 orbits where the bar-related x_1 orbits hit the circumnuclear ring. Most striking is the southern part, where low-metallicity spatial bins align exactly along the ring just at the edge of the dust cavity, while the metal content in the dust cavity is higher.

As in Paper I we have carried out detailed tests to check whether the lower $[Z]_y$ are an artifact of the fitting procedure or caused by numerical uncertainty. We compared the minimum spectral fit values χ^2 as a function of $[Z]_y$ and found no systematic difference. Keeping R_V fixed to the Calzetti standard value of 4.05 produces equally low metallicity. In addition, as we show in Section 5.5, applying an independent alternative population synthesis algorithm yields a similar result. We also note that the comparison with the results of detailed spectroscopy of individual stellar sources carried out in Section 5.4.3 indicates that our metallicity diagnostic of $[Z]_y$ is reliable.

We attribute the lower metallicities encountered to the matter inflow of metal-poor gas from the circumgalactic medium leading to the presence of young metal-poor stars. An alternative is interrupted chemical evolution where star formation is stopped by activity of the central AGN for several Gigayears and then resumes with gas ejected by stellar winds from earlier generations of stars. This scenario has been discussed in detail in Paper I. We

also note the most interesting spatial high-resolution 3D near-infrared spectroscopic study by Díaz et al. (2006). This work concludes that a recent dwarf galaxy-like interloper has affected the central region of M83. We plan to investigate the very complex situation in the center of M83 (see also Houghton & Thatte 2008; Knapen et al. 2010; Della Bruna et al. 2022) in follow-up work.

Such peculiar star-forming rings/disks with unexpected metallicity are a recurring observation in the literature. Our findings in NGC 1365 and NGC 5236 align with several other examples, contributing to a growing body of evidence for this phenomenon. Rosado-Belza et al. (2020) find hints for this in the MUSE data of NGC 1300 and NGC 1097. Robbins et al. (2025) describes the central regions of NGC 5806 as having a 'counter-intuitive stellar population' which could be linked to the presence of the AGN and gas flows. NGC 5728 is another example found by Shimizu et al. (2019) who speculate about a recent minor merger as an explanation. Further examples include NGC 7552 (Seidel et al., 2015) as well as several galaxies in the MUSE-Timer sample (including M83) (Bittner et al., 2020; Gadotti et al., 2019). These observations share common characteristics: they occur in barred spiral galaxies and were detected with full-spectral fitting techniques on IFU data. However, we note that these studies do not separately investigate the young stellar population. They also apply luminosity-weighted (or mass-weighted) averages of logarithmic metallicity (see Section 5.6). A follow-up study using our methodology will be very interesting.

5.4.3 Metallicity Comparison: Individual Stellar Sources vs. Population Synthesis

As already mentioned in the introduction, M83 has been subject to detailed quantitative studies of individual luminous stellar sources: BSGs (Bresolin et al., 2016), SSCs (Davies et al., 2017), and YMCs (Hernandez et al., 2018, 2019, 2021) (see Section 1). This provides us with the unique opportunity to compare their metallicities with our population synthesis results for the young stellar population. For all stellar sources within our field of view and in pixels not masked out, we carry out a one-to-one comparison of stellar source metallicity $[Z]_{probe}$ and population synthesis analysis metallicity $[Z]_y$ in the corresponding spatial bin. We exclude bins where the fraction of light coming from the young stellar population is less than 10% and where the results are, therefore, quite uncertain.

Figure 5.16 shows the detailed comparison. We find a very good agreement. The standard deviation of the difference $\Delta Z = Z_y - Z_{probe}$ is 0.12 dex and the mean value is 0.02 dex. There is no trend with the age of the stellar population and the light fraction contributed by young stars to the integrated spectra in each spatial bin. There is a weak indication of a small trend with Z_y, but that hinges mainly on one YMC point at low metallicity. In summary, this comparison demonstrates that the population synthesis approach is an accurate and powerful spectroscopic tool. The consistency between both approaches, spectroscopy of individual stellar probes and the analysis of the spectra of integrated stellar populations, is definitely reassuring.

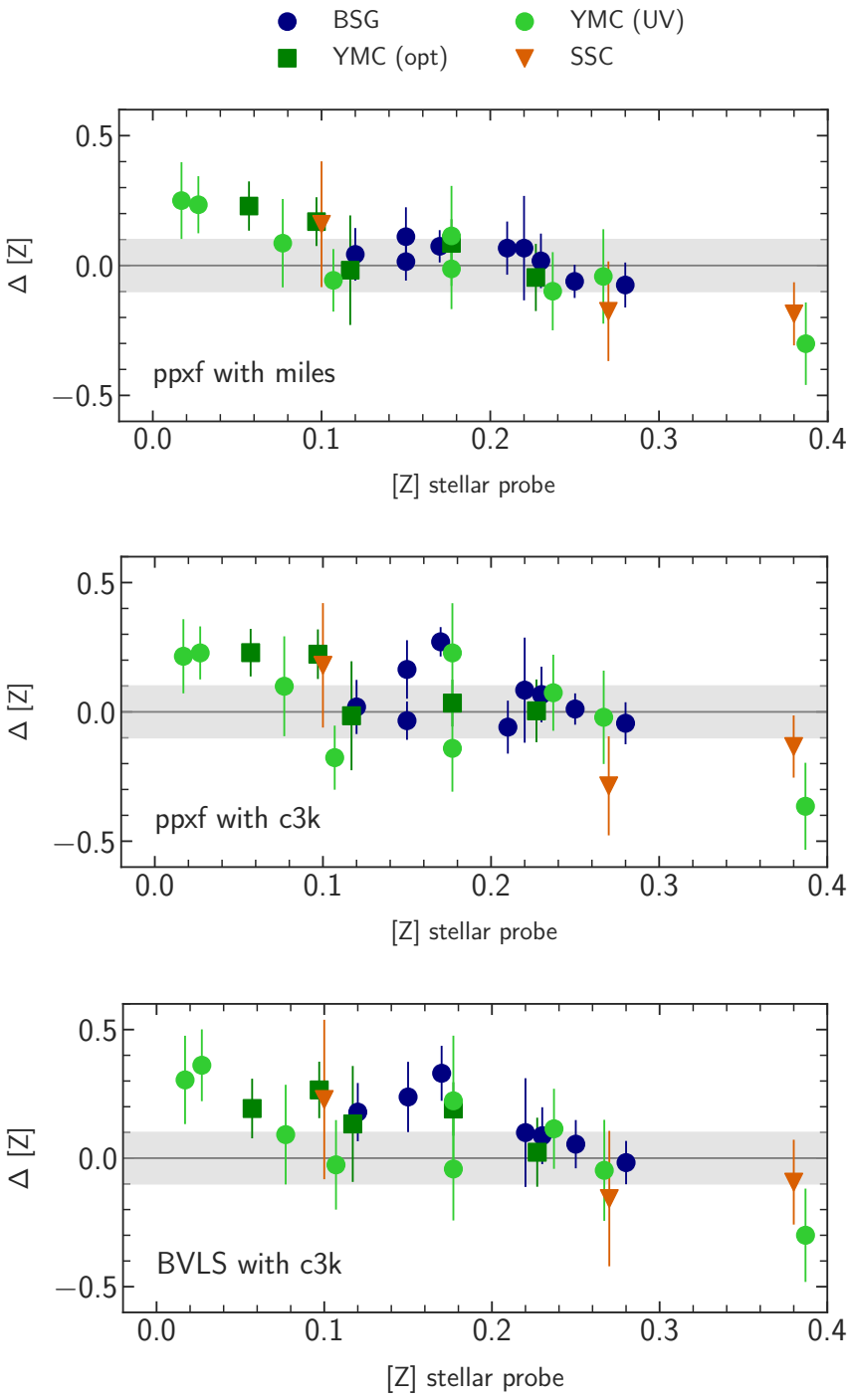

Figure 5.18: Difference $\Delta[\mathrm{Z}]_y - [\mathrm{Z}]_{probe}$ for different population synthesis fit methods and isochrone SSP. Top: `pPXF` with MILES. Middle: `pPXF` with C3K. Bottom: `BVLS` with C3K. Color coding is identical to Figure 5.16

5.5 A comparison between different population synthesis approaches

In the former sections of this work we presented the results obtained with one fitting code (a relatively simple χ^2 minimization technique) and one set of stellar templates. It is interesting and important to repeat the work using alternative approaches. In our discussion we concentrate on metallicity, which according to our experience is more affected by the fitting algorithm than dust properties and ages. We will focus on the metallicity of the young stellar population $[Z]_y$, because this has been the center of our study in the previous sections. This is complementary to previous work, which analyzed old populations in globular clusters (see, for example, Boecker et al. 2020; Gonçalves et al. 2020).
In addition to our `BVLS` method ('bounded variable least-squares', see section 5.2), we also employ the `pPXF` (penalized PiXel-Fitting) fitting code (Cappellari, 2023; Cappellari & Emsellem, 2004) with the Voronoi binned spectra to test the robustness of our approach. The base templates for the fit remain the same as before, i.e. the stellar library, isochrone and IMF are identical to `BVLS`. We also mask out the same emission line regions and use the same wavelength regime. The spectral analysis procedure, inspired by `pPXF`'s GitHub examples[5], follows a multi-step approach. We begin with outlier clipping, as described in Cappellari (2023) Eq. 34, to remove spectral artifacts that could bias the fitting process. This step identifies and removes flux points that deviate by more than $3\,\sigma$ in relative error. An multiplicative polynomial of degree 4 is switched on here allowing for slight continuum correction. Subsequently, a kinematic fit is performed to determine the radial velocity and velocity dispersion of the stellar population. This fit utilizes an additive polynomial of degree 4. The analysis progresses to the stellar population parameters. In this phase, the reddening is also determined, kinematic parameters are kept fixed from before, and the polynomial corrections are disabled to avoid degeneracies. This stage constitutes the primary fit for stellar ages, metallicities, and color excess. Finally, 'wild' bootstrapping is performed. The residuals from the last fit flip their sign at random and are then added to the obtained model fit. `pPXF` is then applied to each of these resampled models, generating distributions of stellar population parameters after 50 steps. This process enables robust uncertainty estimation and helps to identify potential biases or degeneracies in the fit, especially in central bins with a steep intrinsic SED, large extinction, and weak metal lines.
Figure 5.17 summarizes the results obtained with `pPXF` as an alternative to our `BVLS` method. The radial metallicity distribution is very similar to that shown in Figure 5.12, except that the values are slightly larger (~ 0.05 dex). The distribution function of $[Z]_y^{pPXF} - [Z]_y^{BVLS}$ obtained from a spatial bin-by-bin comparison confirms the slight shift. However, most importantly, the standard deviation $\sigma = 0.09$ dex is small and comparable to the uncertainties of the metallicity determination. The central map compared to Figure 5.15 confirms the low metallicites along the southern x_2 orbit, but also shows a few more low metallicity bins in the center inside the x_2 orbit. Although this is a slight quantitative

[5] `https://github.com/micappe/ppxf_examples`

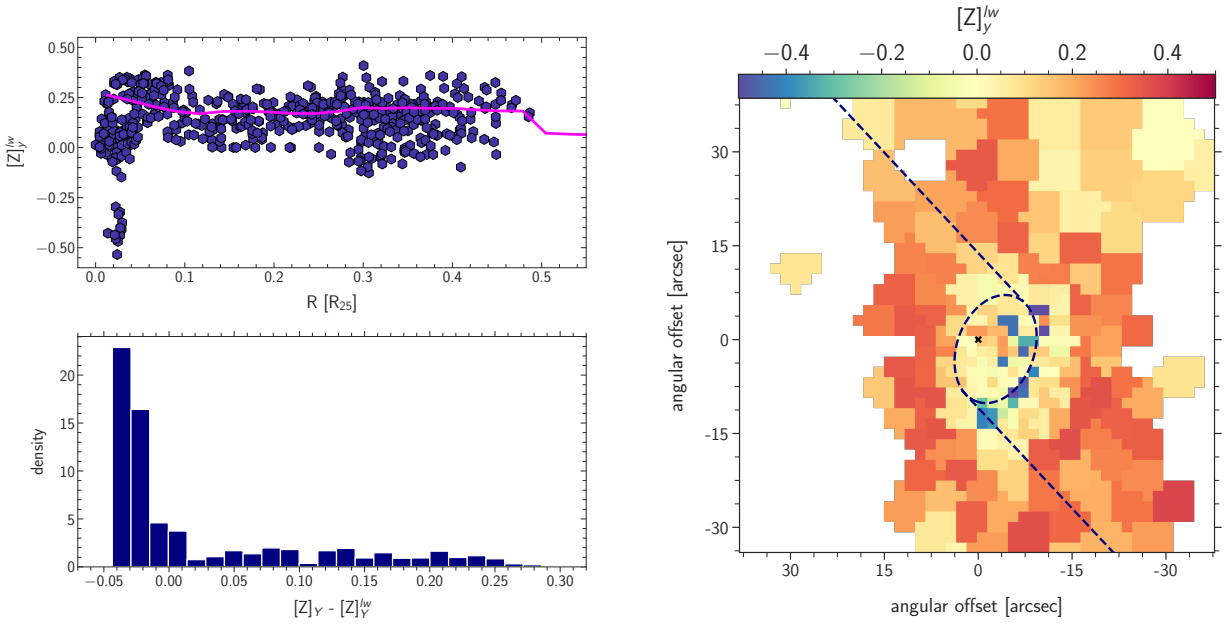

Figure 5.19: Luminosity-weighted metallicity averages. Top left: Radial gradient of $[Z]_y^{lw}$, the chemical evolution model from Bresolin et al. (2016) is shown again in pink to guide the eye. Bottom left: Distribution function of the difference $[Z]_y - [Z]_y^{lw}$. Right: Central map of $[Z]_y^{lw}$ with the same color coding as in Figures 5.15 and 5.17.

difference, it generally confirms the existence of young metal-poor stars in the center.

Figure 5.18 shows the comparison with the metallicities of the stellar probes in a similar way to that carried out with our `BVLS` method in the previous section. The result is equally good. We find a standard deviation of $\Delta[Z] = [Z]_y^{pPXF} - [Z]_{probe}$ of 0.13 and a mean value of 0.02. This confirms the reliability of the population synthesis approach regardless of the fit method applied. We note, however, that the small trend with metallicity seems to be more pronounced than in our use of `BVLS` in Figure 5.16.

As described in Paper I, our isochrone SSPs are calculated from the Flexible Stellar Population Synthesis package (`FSPS`; version 3.2) (Conroy et al., 2009; Conroy & Gunn, 2010a) using the MILES empirical library of stellar spectra (Sánchez-Blázquez et al., 2006) augmented with a comprehensive set of spectra for young massive stars. An alternative option within `FSPS` is the C3K library (Conroy et al., 2019; Byrne et al., 2022) based on theoretical model atmosphere spectra. In order to investigate the impact of the choice of SSPs we have carried a population synthesis analysis using spectra from C3K and the same MIST ioschrone set. This means that the metallicity and age grids remain the same as before. The resulting comparison with metallicities of the stellar probes is also shown in Figure 5.18. Compared with the SSP based on the MILES library, the scatter is larger. We obtain $\sigma = 0.16$ for both the `pPXF` and `BVLS` fitting methods. The mean value of $\Delta[Z]$ is 0.03 dex for `pPXF` and 0.10 dex for `BVLS`, respectively. This means that the choice of the SSP has an influence.

5.6 Luminosity-weighted metallicity averages

In galactic chemical evolution, stellar metallicity is defined as the ratio of the mass of metals confined in stars to the total stellar mass. Eq. 5.7 takes this into account. However, many times and also in our previous work (Sextl et al., 2023, 2024) an alternative, simpler average is used:

$$[Z]^{lw} = \sum_i b_i [Z]_i \tag{5.11}$$

$$[Z]^{lw}_y = \sum_{i_y} b_i [Z]_i. \tag{5.12}$$

As a consequence of Eq. 5.2, this is a V-band luminosity-weighted average of the logarithmic metallicity. Although straightforward and intuitive, this definition of metallicity bears the risk that a relatively small number of stars with high luminosity can bias the average. The luminosities L_i of the SSP isochrones depend on age with a strong and narrow peak between 5 and 8 Myr (see Figures 3 and 4 in Sextl et al. 2023). This peak can influence the luminosity-weighted average, as we will show in the following.
Figure 5.19 shows the luminosity-weighted metallicity of the young population $[Z]^{lw}_y$ obtained with our `BVLS` method. The radial distribution looks very similar to Figure 5.12, however, we notice subtle differences. In the central region and around the position of the spiral arms (0.3 to 0.4 R/R_{25}) we find shifts to lower metallicity. The distribution function of $[Z]^{BVLS}_y - [Z]^{lw}_y$ confirms this impression. The maximum of the distribution is very close to zero, but there is a tail extending to values as large as 0.3 dex, indicating that there are bins where the luminosity-weighted averages are significantly lower. Most of these bins are located in the center, as the central map of $[Z]^{lw}_y$ shows. Compared with Figure 5.15 we now find many more central bins with a lower metallicity. The reason for this result is the presence of young stars with ages between 5 and 8 Myrs with lower metallicity, which contribute more to the luminosity-weighted average of the logarithmic metallicity because of their luminosity. In the linear average of metallicity masses, as given by Eq. 5.7 and Eq. 5.5, these objects do not contribute much. Thus, while Eq. 5.7 describes the correct average in terms of chemical evolution, the luminosity weight in Eq. 5.12 indicates the presence of stars deviating from a homogeneous chemical evolution picture, confirming the presence of a low metallicity inflow.

In our investigation in Paper I of the Great Barred Spiral NGC 1365 we have encountered a confined central region where the metallicity of the young population dropped dramatically and becomes lower than that of the old population. However, this result was based on the application of luminosity-weighted averages. We therefore have repeated the analysis of NGC 1365 calculating the metallicities $[Z]_y$ with the use of equation 5.7 and assuming t^y_{lim} = 1.6 Gyr as in Paper I. The result is shown in Figure 5.20. Although there are quantitative differences from the luminosity-weighted results, the presence of metal-poor young stars in

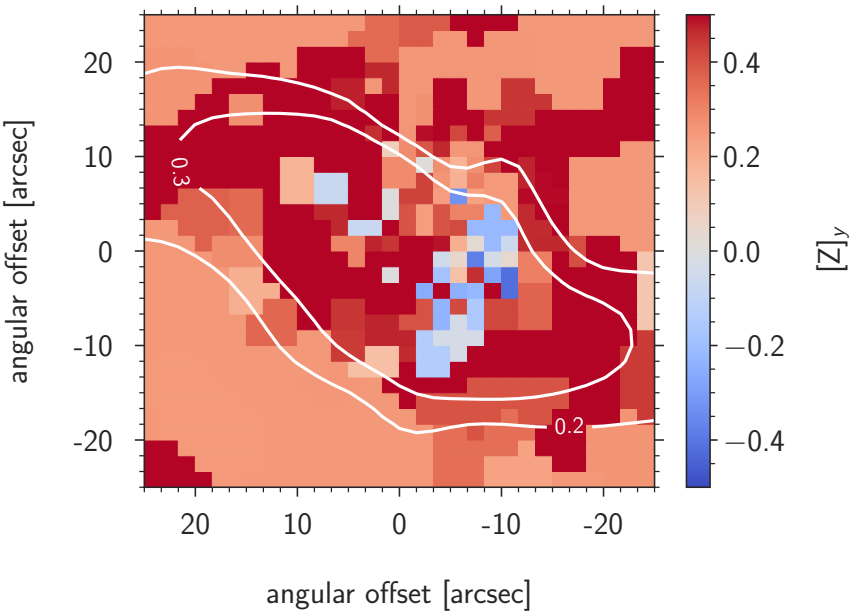

Figure 5.20: Reanalysis of NGC 1365: central map of $[Z]_y$

.

the center is confirmed. In the outer region of NGC1365 around 10 kpc $[Z]_y$ remains the same but the gradient changes from -0.020 ± 0.003 to -0.010 ± 0.003 dex kpc^{-1}.

5.7 The importance of blue wavelength coverage

For our full spectral fitting analysis, we utilize the spectral range of 4000 to 7070 Å, where the TYPHOON spectra have the best signal. As we have already pointed out in Paper I, for the characterization of the young stellar population, this is an important blueward extension compared to the range 4800 to 7000 Å used in corresponding studies of other IFU surveys such as PHANGS-MUSE (see, for instance, Pessa et al. 2023). For young stars, the blue part of the optical regime is crucial. In addition to the steepening SED it contains numerous spectral features sensitive to hot, massive stars (Vazdekis et al., 2016). These features are essential for accurately determining the ages and metallicities of young stellar clusters and recent star formation episodes. In this section, we demonstrate the crucial importance of blue wavelength coverage. We investigate what happens with the characteristics of the young stellar populations, most importantly their metallicity, when parts of the blue optical spectrum are removed in the fit. Is it still possible to successfully characterize the young population with a wavelength coverage starting at 4800 Å?
For this purpose, we fit all spatial Voronoii bins again with the same SSP templates, but with varying wavelength ranges of [4200 Å, 7000 Å], [4400 Å, 7000 Å], [4600 Å, 7000 Å] and [4800 Å, 7000 Å]. Figure 5.21 summarizes the results. In each plot, the metallicity of the young stellar population in each bin is displayed against the baseline fit.

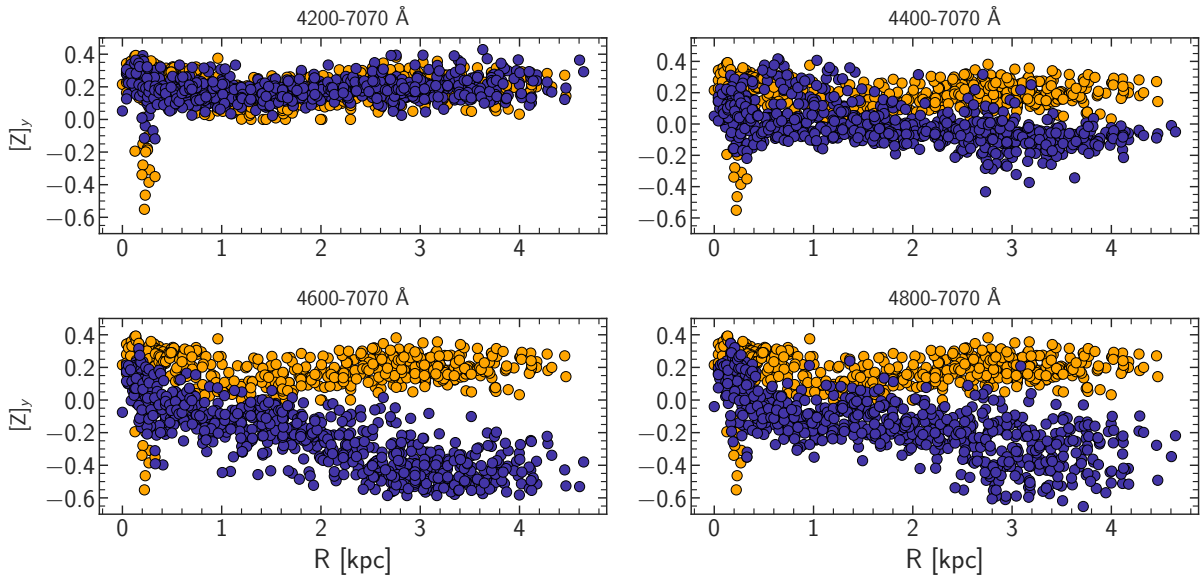

Figure 5.21: Effect of wavelength coverage on the metallicity of the young stellar population (age < 100 Myr). The result from the baseline fit is drawn in each subplot in orange, the result with the wavelength cut in blue. The fitted wavelength is written over the fit each time and the figure margins were kept fixed for comparison.

The plots in the top row exhibit only minor deviations, though these fits already miss prominent spectral features such as He I at 4026 Å and the Fraunhofer e line. However, in the second row with blue wavelengths starting at 4600 Å and 4800 Å, respectively, we start to see significant effects. A metallicity gradient is obtained, which is not real. This is because the reduced wavelength range is less efficient in breaking the age-metallicity degeneracy and begins to produce erroneous metallicities depending on the light fractions and ages of the young population.
This effect is seen in a similar manner in the mock experiments by Lee et al. (2023) with age-divided populations. The authors interpret their findings as a result of a degeneracy not often discussed: a stellar population composed mostly of old stars with a tiny fraction of very young ones can produce a spectrum similar to one with more moderately young stars but still dominated by older stars. The bluer part of the spectrum is crucial to mitigate this.
As a further step, we ran calculations cutting off the blue part of the optical regime as before, but we also extended the wavelength regime towards the red part of the spectrum in order to have in total a 3000 Å range available for the fit. This does not change the situation and leads to identical trends.

The overall conclusion we derive is that age-divided mean stellar populations are sensitive towards the wavelength coverage of the fitted spectra - at least at the relatively low spectral resolution at which the TYPHOON survey operates. To what extent a spectral resolution higher than that reached by the TYPHOON survey ($R = 800$) can improve the

metallicity determination of the young stellar population cannot be answered here. We will investigate this in a follow-up publication.

5.8 Summary

We use a population synthesis full spectral fitting method of TYPHOON 3D spectral data to investigate the inner 4 kpc of the disk of the nearby face-on barred spiral galaxy M83. Since M83 is characterized by intense star formation activity with ongoing star formation bursts, we focus on the young stellar population and the distribution and properties of interstellar dust and its correlation with molecular gas.

The average reddening produced by dust is about 0.2 mag, but we find a strong concentration of dust in the star-forming regions related to the spiral arms, along the bar, and in the center. Close to the center, we detect a dust cavity with a 260 pc diameter similar in size to the local bubble in the Milky Way. The distribution of the ISM molecular gas traced by CO(2-1) emission is correlated with the distribution of dust, supporting the scenario in which molecular gas forms on the surface of dust grains.

We find a wide range of R_V distributed throughout the galactic disk. In the center, we detect an interesting anticorrelation between R_V and the relative column densities of the ISM molecules CCH, CN, and CS. The presence of these molecules is usually attributed to ISM photo-dissociation regions with dust grains of smaller sizes. Our result confirms this.

The population synthesis also allows us to estimate stellar ages. Stars in the central region with strong star formation are very young, with ages of about 5 Myr. The stars in the dust cavity are slightly older with 7 Myr (consistent with Harris et al. (2001) and Jones et al. (2025b)). Outside the central region, we determine the time when 85 percent of the mass of the total stellar population has formed. We find a weak gradient, indicating rapid inside-out growth of the stellar disc.

The young stellar population in the inner 4 kpc of the disk of M83 has a supersolar metallicity $[Z]_y = 0.2$ dex. The radial distribution is flat, without any indication of a negative gradient, and agrees well with the simple chemical evolution model presented in Bresolin et al. (2016). The metallicity of the old population is 0.4 dex lower. In the central region, we find a significant drop of $[Z]_y$. We attribute this to infall of metal poor gas from the circumgalactic medium or a dwarf galaxy interloper that affects subsequent star formation. An alternative is AGN-interrupted chemical evolution as discussed in Paper I.

We check our full spectral fitting method by the comparison with metallicities obtained through the detailed spectroscopic analysis of individual BSGs, SSCs and YMCs. We find good agreement without indications of a systematic effect. To our knowledge, this is the first test of this kind confirming the reliability of the method. In order to further assess the uncertainties we also employed an alternative full spectral fitting algorithm (`pPXF`) as well as an alternative set of single stellar population spectra (C3K), and repeated the analysis. The results were basically confirmed. However, we obtained a small trend with metallicity and a larger scatter with C3K.

In our analysis, we measure the mass of metals confined in the stellar population, which is then used to determine the metallicity. Our research indicates that using a simple luminosity-weighted average of logarithmic metallicity across stellar populations of varying ages can be misleading. This method is particularly problematic when the stellar mix includes a small but bright group of young, metal-poor stars. In such cases, the results may not accurately represent the true metallicity distribution of the entire stellar population.
The analysis of the young stellar population as described above requires a wide spectral coverage of the IFU spectra obtained, most importantly with a far extension to blue wavelengths. We show that restrictions of the optical wavelength range on the blue side have significant effects and introduce large uncertainties.
Our findings have significant implications for studies of galactic chemical evolution and validate the use of integrated light spectroscopy for metallicity determinations in unresolved stellar populations.

6

The Hidden Story of Chemical Evolution in Local Star-Forming Nuclear Rings

Submitted to the Astrophysical Journal on October 10th, 2025

Authors: Eva Sextl, Rolf-Peter Kudritzki

Research Context: In fifth publication, we again apply SPS on spatially resolved spectra of MUSE at the Very Large Telescope (VLT), recognized as one of the world's best IFU spectrographs. Even though its wavelength coverage starts only at 4800 Å, its spectral, spatial resolution and achievable signal-to-noise values are superior to TYPHOON. The presented galaxies NGC 613, NGC 1097, NGC 3351, NGC 7552 were analyzed within MUSE-TIMER, a flagship survey of nuclear rings, and all of them showed peculiar findings in their metallicity which were either dismissed or considered an fitting artifact. Building on the insights gained from previous publications, particularly the distinction between young and old populations and as well as our updated physical definition of metallicity, we revise the results accordingly. We dismiss the idea that the full-spectral fitting technique breaks down in Hα-bright positions on the nuclear rings, a often cited claim in the literature body. In two galaxies of the sample (NGC 7552, NGC 1097), repeated inflow episodes occurred (on a timescale of billion years), so their stellar populations show a mixture of renewed inflow and long-term chemical evolution. This publication builds the cornerstone of the unified idea of a cycle of star-forming nuclear rings presented in chapter 7.

Abstract A VLT/MUSE population synthesis study of metallicities in the nuclear star-forming rings of four disk galaxies (NGC 613, NGC 1097, NGC 3351, NGC 7552) is presented. Disentangling the spectral contributions of young and old stellar populations, we find a large spread of ages and metallicities of the old stars in the nuclear rings. This indicates a persistent infall of metal-poor gas and ongoing episodic star formation over many gigayears. The young stars have metallicities a factor two to three higher than solar in all galaxies except NGC 3351, where the range is from half to twice solar. Previously reported detections of extremely metal poor regions at young stellar age on the rings of these four galaxies are a methodological artifact of the average over all stars, young and old. In addition, it is important to include contributions of very young stars (< 6 Myr) in this environment. For each of the four galaxies, the extinction maps generated through our population synthesis analysis provide support for the infall scenario. They reveal dust lanes along the leading edges of the stellar bars, indicating the flow of interstellar material towards the circumnuclear zone. Prominent stellar clusters show little extinction, most likely because of the onset of stellar winds. Inside and on the nuclear rings, regions that are largely free of extinction are detected.

6.1 Introduction

Nuclear star-forming rings and disks are prominent structures within the central kiloparsec of disk galaxies, where the gas density reaches levels sufficient to trigger intense localized star formation (Knapen, 2005). In many cases, they substantially contribute to the emission of the entire central galaxy region. Their formation is closely tied to the overall dynamical configuration of the host galaxy, especially the presence of large-scale stellar bars and other non-axisymmetric components that induce resonances (such as the Inner Lindblad Resonance) leading to gas accumulation in ring-like morphologies (Athanassoula, 1992; Mazzuca et al., 2006; Verwilghen et al., 2024). These dense gas reservoirs become sites of sustained starburst activity, and the ring often acts as a gas barrier that partially regulates the inward flow towards the nucleus. Over timescales of hundreds of millions of years, nuclear rings contribute to secular galactic evolution by building up stellar mass in the central regions and potentially influencing the growth of pseudo-bulges (inner disks) (Kormendy, J. and Kennicutt, R. C., 2004).

Despite their importance, the chemical evolution of such rings is still poorly understood. Gas-phase abundance measurements based on auroral lines are difficult in these regions because the relevant temperature-sensitive transitions are intrinsically faint and frequently overwhelmed by the bright stellar background (Stasińska, 2005; Díaz et al., 2007). The presence of nuclear activity further complicates the analysis by contaminating nebular emission lines with AGN-related radiation, which alters line ratios and can obscure the signatures of pure star formation (Davies et al., 2014). This effect is particularly relevant in the context of the well-established AGN-starburst connection, where inflowing gas concurrently fuels circumnuclear star formation and but also central supermassive black

hole accretion, leading to intertwined episodes of starburst and AGN activity (Clavijo-Bohórquez et al., 2024).

In the work presented here, we therefore do not focus on emission line analysis but instead on the young and old stellar components themselves. Unlike nebular line methods, which depend heavily on the detectability of temperature-sensitive transitions, stellar spectral features (Balmer lines, Calcium Triplet, iron lines, etc.) remain accessible even in regions with significant interstellar extinction. This allows for constraints on parameters such as ages, initial mass function (IMF) sampling, and metallicities through comparison with population synthesis models (Leitherer et al., 1999; Bruzual & Charlot, 2003).

In our population synthesis analysis of the integrated stellar spectra, we will employ the technique of full spectral fitting (FSF). FSF offers a newer and more powerful way to analyze nuclear SF rings by exploiting the entire stellar spectrum rather than isolated indices, allowing simultaneous constraints on stellar ages, metallicities, and kinematics (Cid Fernandes et al., 2005; Conroy & Gunn, 2010a). By decomposing observed spectra into mixtures of simple stellar populations, FSF disentangles young starburst contributions from older bulge components and reveals star formation histories linked to bar-driven inflows. Despite the tremendous success of this technique, nuclear rings unfortunately show peculiar results. The flagship observational campaigns MUSE TIMER (Gadotti et al., 2019) & PHANGS-MUSE (Emsellem et al., 2022) reported the presence of regions with apparently low metallicity despite exhibiting high Hα luminosities indicating a very young population. The anomalous regions were persistent between different analysis methods, and no adjustment of the fitting procedures was able to remove or reconcile them. In the galaxies NGC 613, NGC 3351, NGC 1097, and NGC 7552, these signatures were especially pronounced (Seidel et al., 2015; Bittner et al., 2020; Pessa et al., 2023; Silva-Lima et al., 2025), but other cases were also found (Shimizu et al., 2019; de Sá-Freitas et al., 2023; Robbins et al., 2025). The sometimes extremely low ([Z]< -0.5) mean metallicities are truly peculiar given their circumnuclear location, where gas and subsequently stars are generally expected to be chemically enriched (Pérez & Sánchez-Blázquez, 2011; Cole et al., 2014).

In this work, we show that for the complicated environment of central SF rings, mean light- or mass-weighted metallicity values obtained as averages over the total stellar population are not sufficient to characterize galactic evolution. We argue that we need another new approach besides 'light' and 'mass' weights to define metallicity. We introduce the 'physical' metallicity $Z_{\rm phys} = M_{metals}/M_{total}$ and show its usefulness in a 1-to-1 comparison with individual stellar probes in the disk of M83. We also disentangle the properties of young and old populations instead of discussing averages over all ages. With this new concept, we can tell another evolutionary story of some of the most prominent nuclear rings in the local universe. Finally, we emphasize the importance of an extensive age grid for spectral fitting templates in the complex environment of nuclear rings. Missing young stellar components in the fit introduces misleading results in nuclear ring studies.

6.2 The galaxy sample

Our sample consists of four nearby barred spiral galaxies that host some of the most prominent circumnuclear star-forming rings in the local universe: NGC 7552, NGC 613, NGC 1097, and NGC 3351. These systems are well-studied archetypes in which the interaction between bars and central star formation has been extensively documented. All four galaxies are included in the TIMER or PHANGS-MUSE survey and their ring like structures are kinematically well established. However, their subsequent analysis with respect to stellar metallicity, ages, and interstellar medium dust content presented significant challenges.

NGC 3351: This barred spiral galaxy hosts a well-defined circumnuclear star-forming ring at a radius of about ~ 300 pc (Swartz et al., 2006). The ring is composed of regularly distributed HII-regions and massive young stellar clusters (Colina et al., 1997; Bresolin & Kennicutt, 2002). The nucleus itself is dominated by an old stellar population, with no evidence of AGN activity (Swartz et al., 2006; Pessa et al., 2023). Gas inflow along the bar appears to efficiently feed the ring, while leaving the very center comparatively quiescent. The regularity and isolation of the nuclear ring make NGC 3351 a relatively 'clean' case for studies of ring star formation.

NGC 1097: Gadotti et al. (2019) noted that despite being the most massive galaxy in the present sample, it exhibits a prominent and extremely young starbursting ring of ~ 800 pc radius. More than 300 HII regions have been resolved in near-infrared imaging (Prieto et al., 2005). The extend of the ring is well-resolved by MUSE, allowing it to be identified with ease in this galaxy. Classified as LINER, NGC 1097 possesses a comparatively faint nucleus that we mask out.

NGC 613: This galaxy hosts a rather asymmetric nuclear ring with an ~ 400 pc radius. Falcón-Barroso et al. (2014) found an unusual large reservoir of molecular gas within ~ 100pc. It harbors a radio jet, an outflow, and an AGN ionization cone in its nuclear region (da Silva et al., 2020). The entire nuclear center shows complex gas kinematics influenced by AGN activity (Silva-Lima et al., 2025). However, we do not detect broad-line region (BLR) features in the spectra.

NGC 7552: This ring is about 200pc in radius. The central nucleus itself lacks starburst or Seyfert-like activity (Forbes et al., 1994; Gadotti et al., 2019). The ring is rich in molecular gas and hosts numerous massive young clusters, making it one of the most extreme star-forming nuclear rings in the nearby universe with a current star formation rate of $= 10 - 15\,\mathrm{M}_\odot\,\mathrm{yr}^{-1}$, (Pan et al., 2013).

6.3 Observations and data retrieval

Our analysis relies primarily on observational data obtained with the Multi Unit Spectroscopic Explorer (MUSE, Bacon et al. (2010, 2014)) on the Very Large Telescope (VLT) in Cerro Paranal, Chile. MUSE is an integral field spectrograph that provides spatially resolved spectra over a nominal wavelength range of 4800 to 9400 Å in steps of 1.25 Å with a spectral resolution of ~ 2.65 Å FWHM. The wide field covers a $60''$ by $60''$ field of view

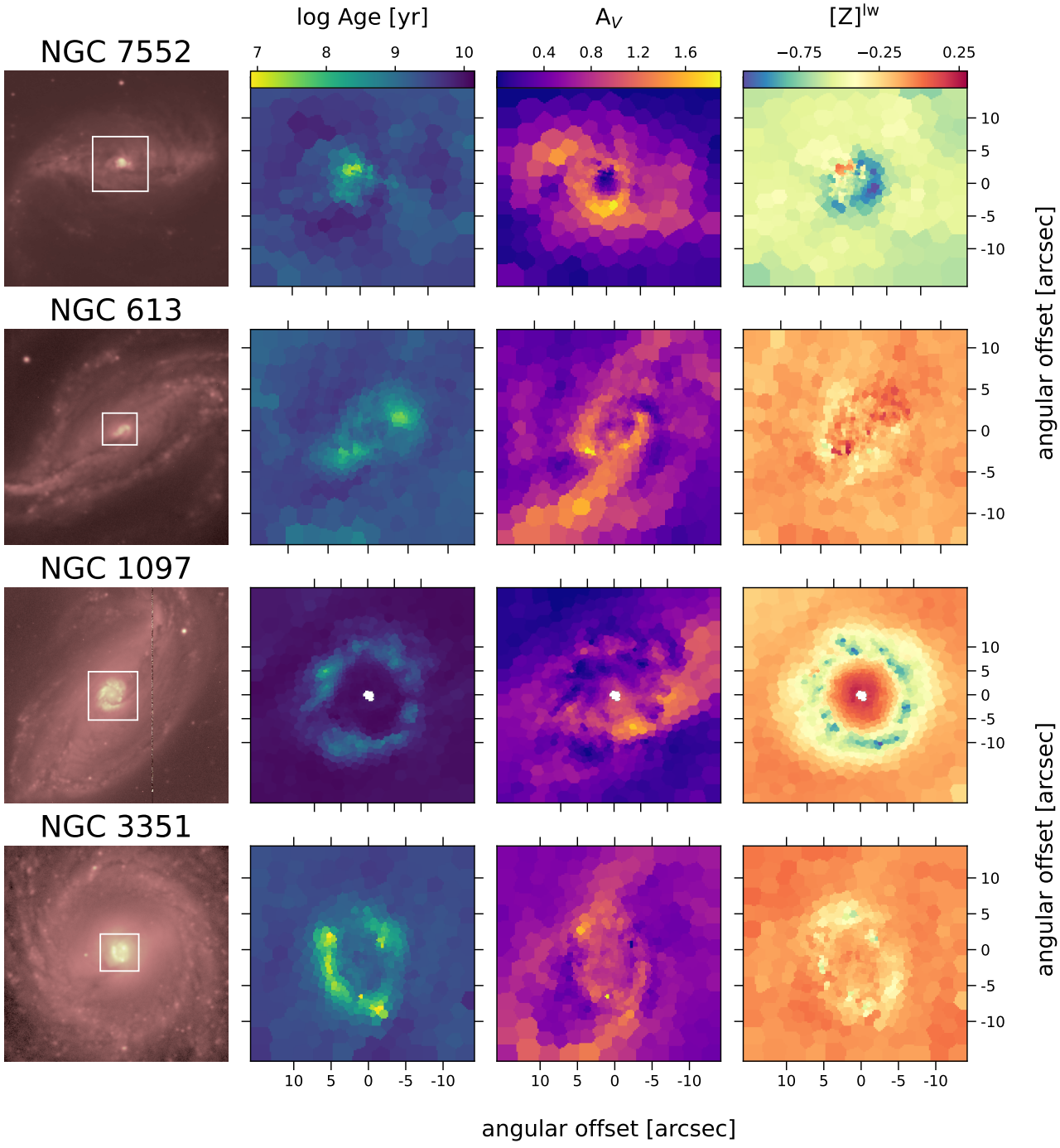

Figure 6.1: First column: B-Band images from the CTIO 1.5m telescope (NGC 7552), CTIO 0.9m telescope (NGC 613), du Pont 2.5m telescope (NGC 1097) and CTIO 1m telescope (NGC 3351). The MUSE FOV used for our FSF fit is marked in white. North is to the top, east is to the left. The following columns show the FOV with results from the FSF fit: mean light-weighted Age, visual extinction A_V and light-weighted total metallicity $[Z]^{lw}$. The color bar at the top holds for all the subplots in the column.

Galaxy	center α (J2000)	center δ (J2000)	stellar mass ($\log M_\odot$)	i (°)	PA (°)	D (Mpc)	spat. scale (pc/arcsec)	AGN?	S/N
NGC 7552	349.044945	-42.584962	10.52	14	54.9	17.2	83	no	200
NGC 613	23.575714	-29.418573	11.09	46	118	17.5	85	yes	130
NGC 1097	41.578937	-30.274717	11.24	46	130	14.5	70	yes	200
NGC 3351	160.990618	11.703659	10.49	45	13	9.96	48	no	200

Table 6.1: Central right ascension and declination coordinates (centroid of the 3.6 μm emission peak) as well as the stellar masses are taken from the Spitzer Survey of Stellar Structure in Galaxies (S4G; Sheth et al. (2010)). Position angles (PA) are measured east of north; i is the inclination, D are distances. The spatial scaling is calculated assuming the given distance. The primary literature references for the other quantities are Bittner et al. (2020) for NGC 7552, Sato et al. (2021) for NGC 613, Onishi et al. (2015) for NGC 1097, and Sun et al. (2024) for NGC 3351.

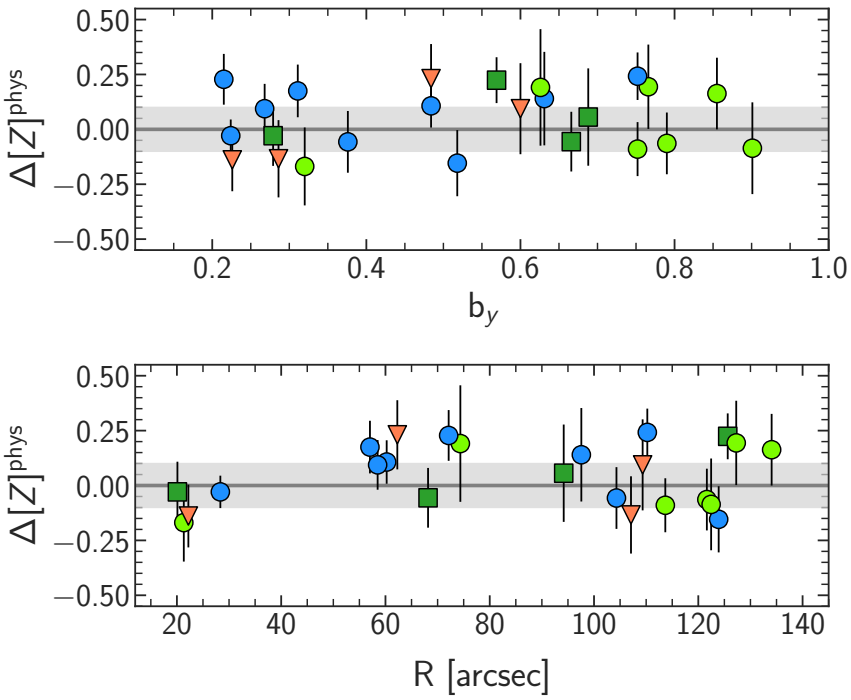

Figure 6.2: Metallicity difference $\Delta[Z]$ between individual stellar probes and population synthesis (see Section 6.5) as a function of the luminosity fraction b_y of young stars (top) and the angular distance from the center (bottom). The different symbols represent differences with respect to BSG (blue circles), SSC (red triangles), YMC with optical analysis (dark green squares), YMC with UV analysis (light green circles). Errors result from the addition of stellar source and population synthesis errors in quadrature. The shaded gray strip indicates a difference ≤ 0.1 dex and is added for orientation.

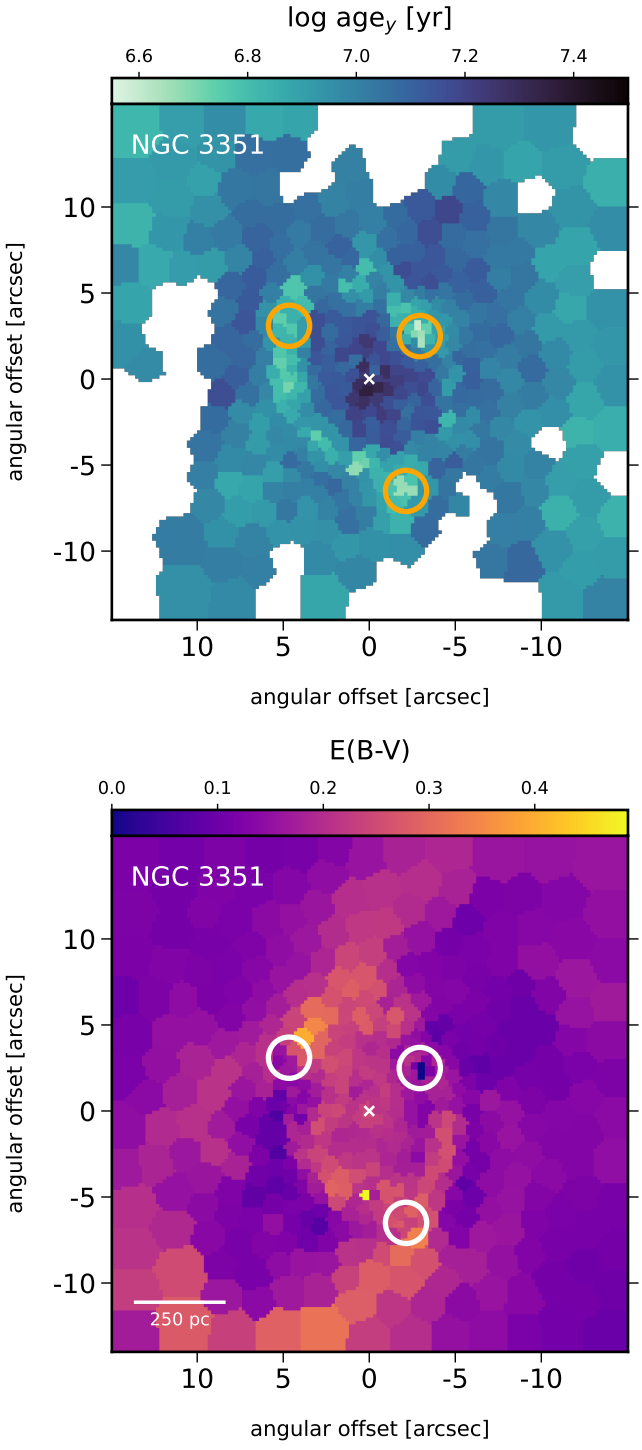

Figure 6.3: The central region of NGC 3351: (top) map of mean ages of the young stellar population; (bottom) interstellar reddening E(B-V). The circles indicate the locations of the three most prominent young stellar clusters highlighted in Fig. 24 of Emsellem et al. (2022) and discussed in the text.

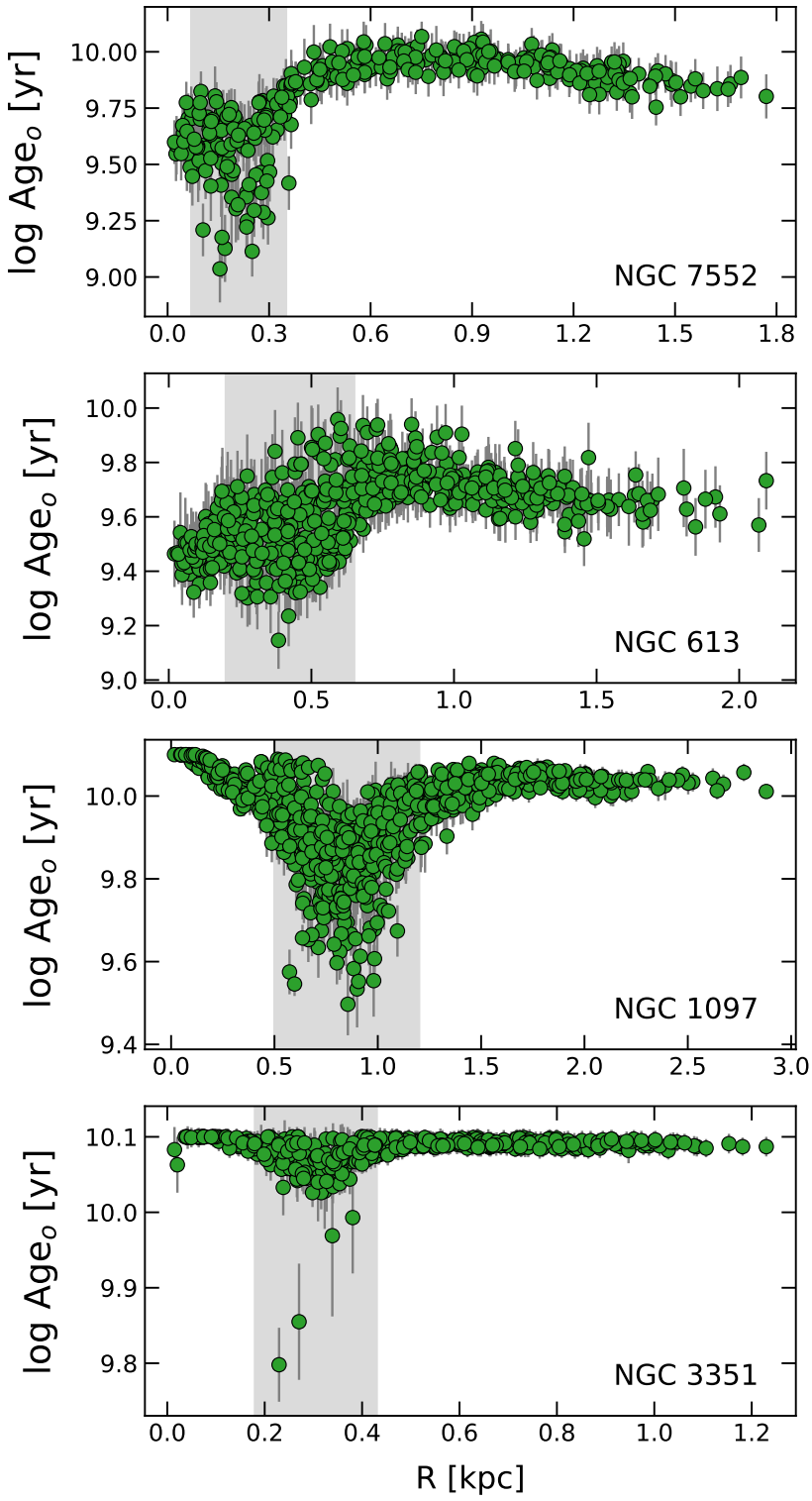

Figure 6.4: Mean ages of the old stellar population as a function of galactocentric distance. The nuclear star forming regions are indicated in gray. From top to bottom: NGC 7552, NGC 613, NGC 1097, NGC 3351.

with 0.2″ spatial sampling, enabling highly detailed mappings of galactic environments (Weilbacher et al., 2020).
For all nuclear rings in our sample, we use the reduced IFU data cubes from the MUSE-DEEP program. At the VLT, observations are always organized into Observing Blocks (OBs), each representing a single pointing with a one-hour maximum exposure time due to operational constraints. Each OB produces a final data cube, referred to as an OB datacube, and these are released individually as part of the 'MUSE collection' in the Science Portal[1]. The MUSE-DEEP program combines multiple such OB datacubes for each target to create a single deep datacube with improved sensitivity. The data reduction in this case follows the standard MUSE pipeline optimized for deep field observations and includes bias subtraction, flat-fielding, wavelength and flux calibration, and sky subtraction. Figure 6.1 shows B-band images for each galaxy in the sample. The subsequently used FOV is indicated in white. They are slightly smaller than the original cubes to better isolate the ring regions.

6.4 Data preparation & Population synthesis technique

As mentioned in the introduction, we make use of the widely adopted FSP technique with Simple Stellar Populations (SSPs) spectra in order to extract physical properties from the observed integrated light spectra. The method essentially models the observed spectrum as a linear superposition of SSP templates, each corresponding to a single-age, single-metallicity stellar population. The SSP sets are synthesized beforehand from theoretical stellar evolution isochrones and corresponding stellar spectra under an assumed initial mass function (IMF) (see Section 6.4.3).
In mathematical turns, a model spectrum M_λ is constructed from a collection of SSPs $f_{\lambda,i}$ with ages t_i and metallicities $[\mathrm{Z}]_i = \log(\mathrm{Z}_i/\mathrm{Z}_\odot)$ as

$$M_\lambda = D_\lambda(R_V, E(B-V)) \left[\sum_{i=1}^{n_{SSP}} b_i f_{\lambda,i}(t_i, [Z]_i) \right]. \tag{6.1}$$

The fit coefficients b_i are determined within the fitting procedure. We note that the SSP spectra (as well as the observed spectra) are normalized to unity in the range of 5500 to 5550 Å, a wavelength regime without prominent emission or absorption features. Due to this normalization, the sum of all coefficients b_i adds up to unity. The b_i are luminosity weighted fit coefficients describing the contribution of the corresponding SSP to the integrated light at the wavelength of normalization (see Sextl et al. 2023, 2024, 2025 for a detailed discussion).
Interstellar dust along the line of sight is accounted for by the term $\mathrm{D}_\lambda(E(B-V))$, whereby the colour excess E(B-V) is also fitted simultaneously. The overall shape of the attenuation

[1] `https://archive.eso.org/scienceportal/home`

curve is chosen in advance. We chose the prescription of Calzetti et al. (2000) with fixed $R_V = 4.05$ due to the star-forming nature of nuclear rings.

6.4.1 Workflow

In practical terms, the fitting process is performed with the `pPXF` algorithm (Cappellari & Emsellem, 2004; Cappellari, 2023). Inspired by the examples provided in `pPXF's` GitHub repository[2], our approach follows several sequential steps which we have already successfully applied to TYPHOON IFU data in the past (Sextl et al., 2025).
When performing full-spectral fitting to reconstruct chemical evolution histories, it is a good practice not to work on the level of individual spectral pixels (spaxels), but to combine several to obtain a higher S/N spectrum. Voronoi binning is widely regarded as the standard approach for this purpose, and we applied it using the vorbin Python package (Cappellari & Copin, 2003). The ultimate S/N values at the wavelengths of normalization for each galaxy are listed in table 6.1.
As a second step, we applied sigma-clipping to remove artifacts and emission lines in the Voronoi spectra, following Eq. (34) of Cappellari (2023). Data points that exceeded the relative error of 3σ were excluded. In this process a multiplicative Legendre polynomial of degree 4 was included to correct for low-order continuum mismatches.
Third, the galaxy stellar kinematics were determined. Velocity and velocity dispersion were constrained in the `pPXF` main routine with an additive polynomial of degree 4. The high spatial and spectral resolution of MUSE would in principle also allow the extraction of higher-order moments (h_3 and h_4), but this lies beyond the scope of the present work. The fitting then proceeded to the derivation of stellar population properties. During this stage, the kinematic parameters are fixed, and polynomial corrections are disabled to avoid degeneracies between continuum adjustments and population parameters. The parameters b_i and $E(B-V)$ are determined simultaneously during this main fit. To obtain an estimate of the uncertainty in the fit, a wild bootstrapping procedure is applied 25 times (Davidson & Flachaire, 2008). The residuals, which are the differences between the Voronoi spectrum and the best-fit model, are randomly multiplied by +1 or -1 to create a new set of perturbations. These perturbed residuals are added back to the original best-fit model to create many simulated spectra, which are then fitted again to see how the fit parameters b_i and subsequently metallicities and ages may vary. This is a proper way to understand how uncertainties in the data (noise in the spectra) propagate into uncertainties in the discussed fitted parameters.

6.4.2 Derivation of physical quantities

Once the parameters b_i are known, physically relevant quantities can be constructed, such as the mean light-weighted age and the mean light-weighted stellar metallicity $[Z]^{\mathrm{lw}}$ of the

[2] `https://github.com/micappe/ppxf_examples`. We also encourage the use the newer .dust-function for the extinction, not the now obsolete .reddening/ .gas-reddening keywords

stellar population in the bin:

$$\log(t)^{\rm lw} = \sum_i b_i \log(t_i) / \sum_i b_i \tag{6.2}$$

$$[Z]^{\rm lw} = \sum_i b_i \log(Z_i/Z_\odot) / \sum_i b_i \tag{6.3}$$

These definitions follow directly from the spectral fit, but can be misleading, as young stellar populations can easily outshine older populations despite a much smaller total mass. The mass-weighted coefficients $\tilde{b_i}$ can show a more nuanced picture and are obtained using the mass-to-light ratio $\gamma_i = \mathrm{M}_i/\mathrm{L}_i(V)$ of each SSP isochrone as follows:

$$\tilde{b_i} = \frac{b_i \gamma_i}{\sum_i b_i \gamma_i}. \tag{6.4}$$

The mass-weighted means for age and metallicity are then calculated in the same way as with equations (2) and (3) but using the coefficients $\tilde{b_i}$ instead of b_i.
However, the definitions of light- or mass-weighted metallicities are misleading when compared with metallicities used in chemical evolution of galaxies or cosmological simulations. Here, metallicity Z is the ratio of the mass of metals M_Z confined in the stellar population divided by the total mass of stars M, $Z = M_Z/M$. Thus, following Sextl et al. (2025) we introduce a physical definition of metallicity:

$$Z_{\rm phys} = \frac{M_Z}{M} = \sum_i \tilde{b_i} Z_i \tag{6.5}$$

$$[Z]^{\rm phys} = \log(Z_{\rm phys}/Z_\odot) \tag{6.6}$$

Note that this definition is *different* from the 'mass-weight' normally found in the literature. We therefore call equation 6.5 the 'physical metallicity' to distinguish the two quantities. Our choice is particularly relevant, as it allows for a *direct* comparison with numerical simulations and is consistent with the conventions typically employed in chemical evolution studies. $[Z]^{\rm phys}$ can then be split into a young and old component as described in the following paragraphs. We will test the capabilities of this new definition in section 6.5 with a 1-to-1 comparison to stellar probes.
To further analyze the chemical evolution history, we separate contributions from the young and old stellar populations. Following again Sextl et al. (2023, 2024, 2025) we introduce a conventional age boundary t^y_{lim} to distinguish between populations dominated by recent star formation activity (young) and those tracing the longer-term assembly history (old). Thus, all SSPs with ages $t_i < t^y_{lim}$ are assigned to the young component, while those with $t_i \geq t^y_{lim}$ comprise the old component. We will use $t^y_{lim} = 0.1$ and 0.3 Gyr, respectively, in the next sections to distinguish between the young and old population.
Metallicities and ages for the young and old populations are then calculated with the above equations, but the sums are carried out only over the old or young SSP, respectively. This separation between the old and young population is used for the calculation of ages and

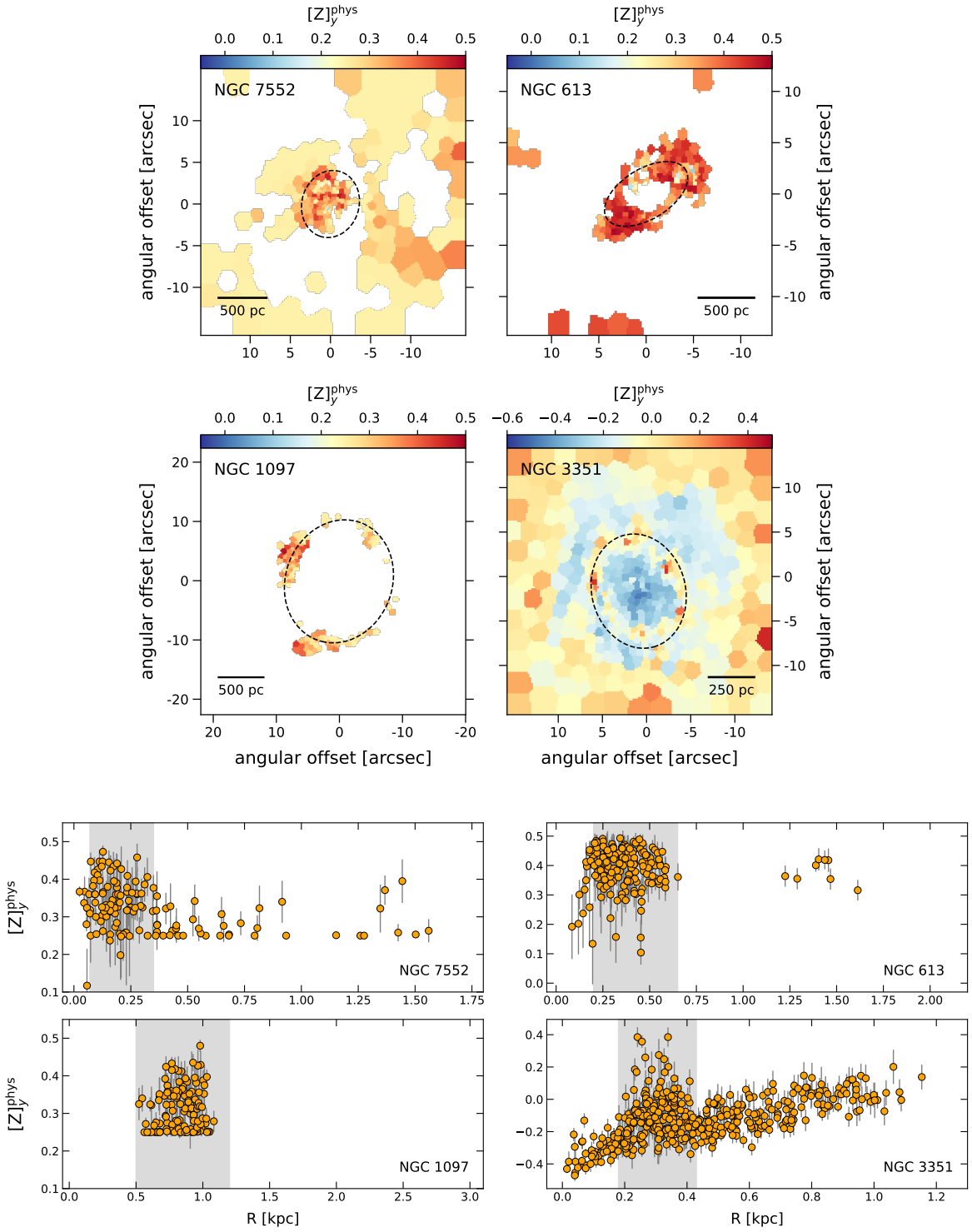

Figure 6.5: Metallicity maps of the young stellar population (top) and radial metallicity distribution including uncertainties (bottom).

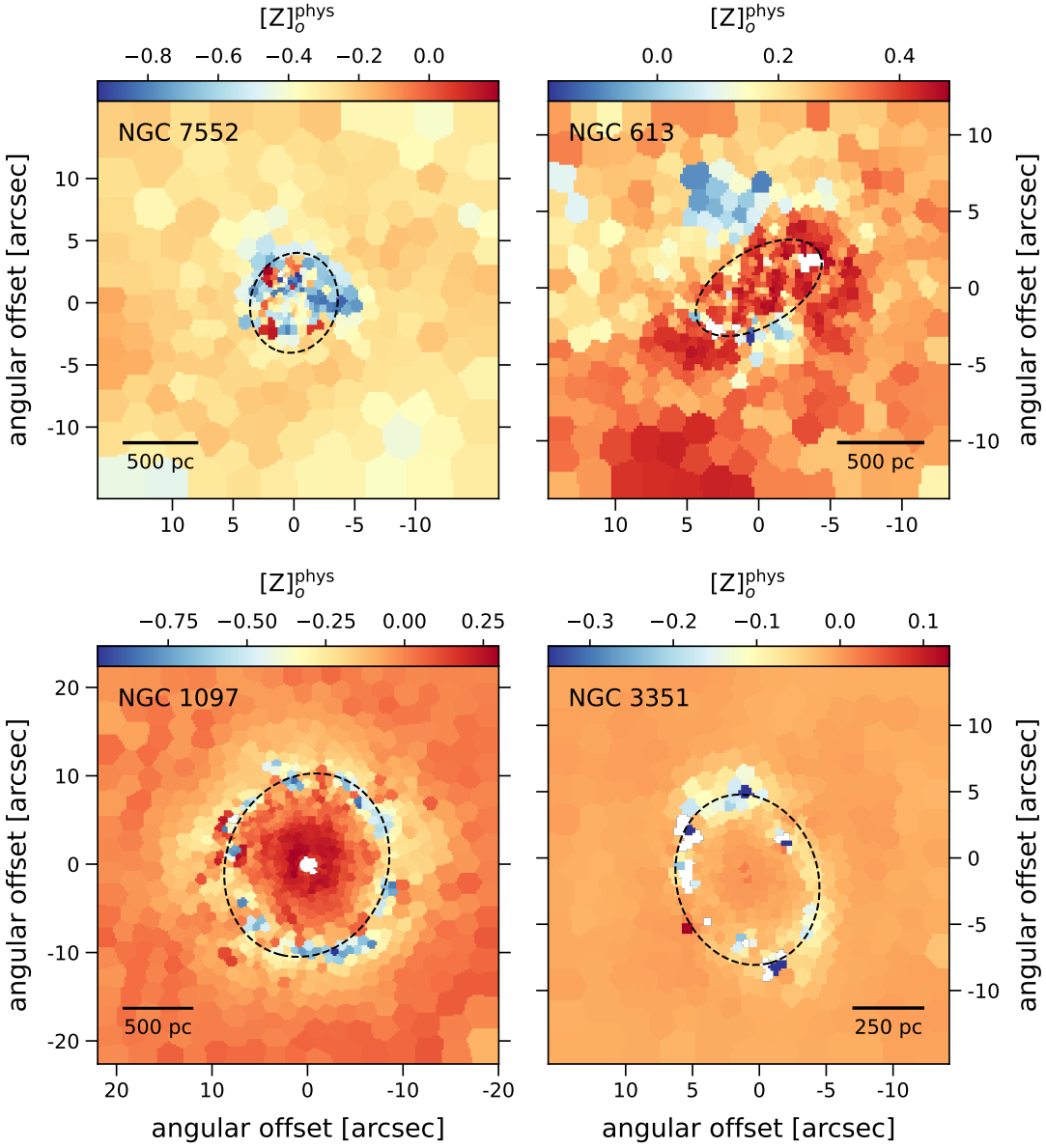

Figure 6.6: Metallicity maps of the old stellar population. For each galaxy, the approximate position of the nuclear ring is shown with a dashed line. Upper row: NGC 7552 (left), NGC 613 (right). Lower row: NGC 1097 (left), NGC 3351 (right)

metallicities. The contribution to the observed spectrum by the two populations is then described by the corresponding sums $b_{\rm young}$ and $b_{\rm old}$, where $b_{\rm young} + b_{\rm old} = 1$ by construction. This division is also applied to the mass-weighted coefficients $\tilde{b_i}$ as defined above. The fractional mass contributions of the two populations were then computed as

$$\tilde{b}_{\rm young} = \sum_{t_i < t^y_{lim}} \tilde{b_i}, \tag{6.7}$$

$$\tilde{b}_{\rm old} = \sum_{t_i \geq t^y_{lim}} \tilde{b_i}. \tag{6.8}$$

This separation highlights the strong discrepancy that often arises between light- and mass-weighted quantities: while the integrated light can be dominated by a relatively small number of very luminous young stars, the bulk of the stellar mass generally resides in the older populations.

6.4.3 A side note on the SSP template set

Apart from the new metallicity definition, we emphasize that, besides the uncertainties inherent to the fitting algorithm itself, full-spectral fitting lives and dies with the choice of templates. Each template set is characterized by the number of ages and metallicities covered as well as the ingredients it was calculated from. The computation of a simple stellar population spectrum then begins with an assumed star formation event in which all stars are formed simultaneously. The adopted stellar initial mass function (IMF) then dictates the relative weighting of stars of different masses. Individual stellar spectra are drawn from an empirical or theoretical stellar library and mapped onto stellar evolutionary tracks, which specify how stars of a given mass and metallicity evolve with time. By integrating all masses and evolutionary stages, one obtains the total flux of the population at a fixed age and metallicity.

We use for these calculations the program FSPS (version 3.2, Flexible Stellar Population Synthesis code, Conroy & Gunn (2010a,b)) which gives the user the choice from different stellar libraries, stellar evolution tracks, and IMFs. For our SSP set, we chose the MILES library (Sánchez-Blázquez et al., 2006), MESA stellar evolution isochrones (Dotter, 2016; Choi et al., 2016) and a Chabrier (Chabrier, 2003) initial mass function. As the empirical MILES library has only a limited number of stars with T > 9000 K (Martins & Coelho, 2007), it is crucial to add additional spectra of hot massive stars (Eldridge et al., 2017), Wolf-Rayet types (Smith et al., 2002), AGB- (Lançon & Wood, 2000), post-AGB (Rauch, 2003) and carbon stars (Aringer et al., 2009). By extending MILES with libraries for hot and post-MS stars, we improve its applicability in the complex environments of nuclear rings. This set, called 'MILES-SSP' was successfully applied and tested in our analysis of the TYPHOON data of M83 and NGC1365 (Sextl et al., 2025, 2024).

In summary, we use a grid with 52 age and ten metallicity values (520 SSPs in total). The metallicities go from [Z] = 0.5 dex in steps of $\Delta[Z] = 0.25$ dex down to [Z] = −1.75 dex. The logarithmic age grid starts at 0.1 Myr ages and goes up to 12.5 Gyr (see also Fig. 2 in Sextl et al. (2023) for an illustration of the grid).

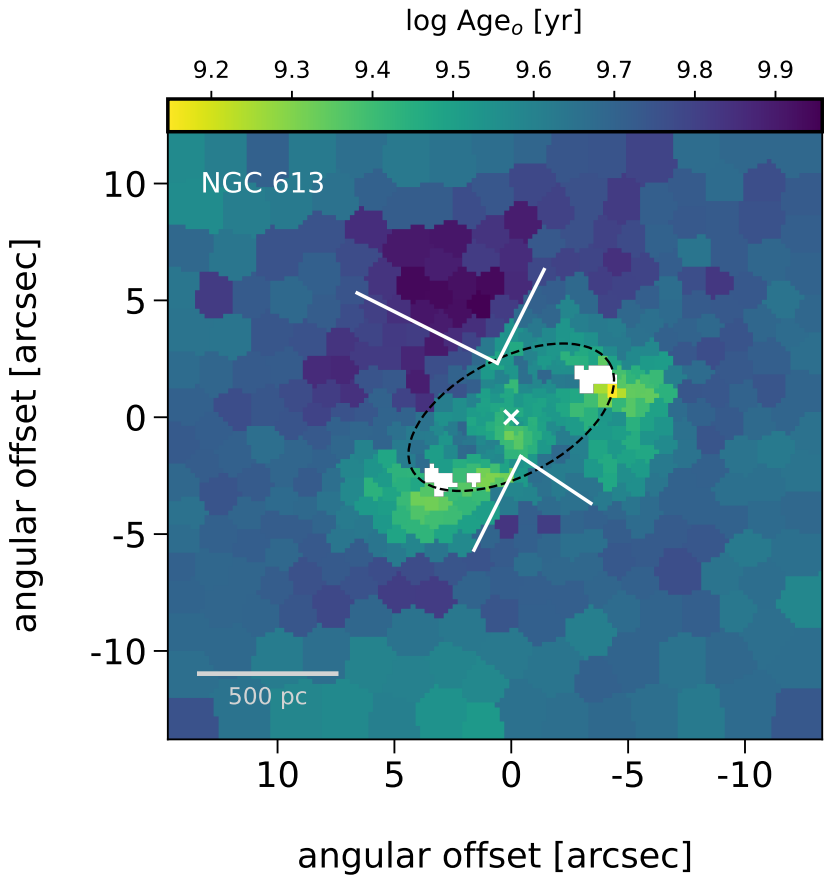

Figure 6.7: Map of the age of the old stellar population of NGC 613. The AGN outflow cone is indicated.

As stated in Sextl et al. (2025), roughly one third of the models are 20 Myr and younger. This is important for the analysis of very young stars and clusters, which we can expect in circumnuclear star-forming rings (ages < 5 Myr as shown in Prieto et al. (2019)). We intentionally do not remove low-metallicity young SSPs to adjust the fit to choose higher metallicities in young populations, as, for example, proposed in de Sá-Freitas et al. (2023); Silva-Lima et al. (2025). In contrast, we will see that the lowest [Z] value is not taken at all by our analysis algorithm and that all regular SF rings in our sample are indeed metal rich or close to solar at the present time. In Section 6.8, we further test the severe consequences of a smaller age grid, removing the youngest SSPs (< 6 Myr and < 30 Myr respectively) and running the fitting procedure again.

6.5 A MUSE metallicity test with young stellar probes in M83

In addition to the galaxies in Table 6.1 MUSE observations are also available for the star forming galaxy M83. This galaxy harbors an asymmetrical nuclear region where Hα emission is irregularly distributed in the center (Gadotti et al., 2019). At a distance of 4.8 Mpc, its proximity makes M83 an excellent target for observations with the MUSE spectrograph, but it has also been a subject of accurate multi-object spectroscopic studies of individual stellar probes. Bresolin et al. (2016) measured the metallicities of individual blue supergiant stars throughout the disk of M83. In addition, young massive clusters in UV and optical (YMCs; Hernandez et al. (2018, 2019, 2021)) and super star clusters in the NIR (SSCs; Davies et al. (2017)) have been investigated spectroscopically. The results of this work offer the unique opportunity to compare the metallicities obtained from these stellar sources with those derived from our MUSE population synthesis analysis.
A similar comparison was carried out by Sextl et al. (2025) using TYPHOON data which have a lower spatial and spectral resolution (1.65″ and 8Å, respectively) but extend to shorter wavelengths (4000Å). Here, we repeat the analysis employing the higher resolution of the MUSE-DEEP data cube. To improve the signal-to-noise ratio for spectral fitting, we combined individual spaxels within the vicinity of each stellar probe to produce integrated spectra representative of those regions. To reduce contamination from individual bright stars, we excluded spaxels within a radius of three pixels centered on each stellar probe. At the TYPHOON pixel scale of 1.65 (Grasha et al., 2022), this adjustment was not required. However, with the much finer spatial resolution of MUSE at 0.2″, the light from a few bright stars can easily dominate the flux within a single pixel, and our fitting-procedure would lead to unreliable results.
The full spectral fitting was then applied to the binned spectrum to infer the stellar population properties surrounding the stellar probes, with particular emphasis on the metallicity $[Z]^{\rm phys}_{\rm 100Myr}$ of the young component (age < 100 Myr). We subsequently compare this fitted metallicity with the independently measured metallicity obtained from the stellar probe. This comparison is quantified in terms of the difference $\Delta[Z] = [Z]_{\rm probe} - [Z]^{\rm phys}_{\rm 100Myr}$, which is illustrated in Figure 6.2. Note that all stellar probes were adjusted to a common baseline of $Z_\odot = 0.142$. Our results reveal a close agreement between the metallicity estimates derived from the full spectral fitting method and those from the stellar probe. The mean value of $\Delta[Z]$ is 0.04 dex and the scatter is 0.14 dex, the latter being the expected result for average errors of 0.1 dex for individual independent values of $[Z]_{\rm probe}$ and $[Z]^{\rm phys}_{\rm 100Myr}$, respectively.

Figure 6.2 demonstrates that MUSE IFU spectra are extremely useful to obtain quantitative information about the young stellar population despite their restricted wavelength range toward the blue. In Sextl et al. (2025) we argued in the opposite direction. However, this was based on the assumption of using low resolution TYPHOON spectra with moderate S/N. As we see now, the MUSE higher spectral resolution and high signal-to-noise ratio compensate for the lack of blue wavelength coverage.

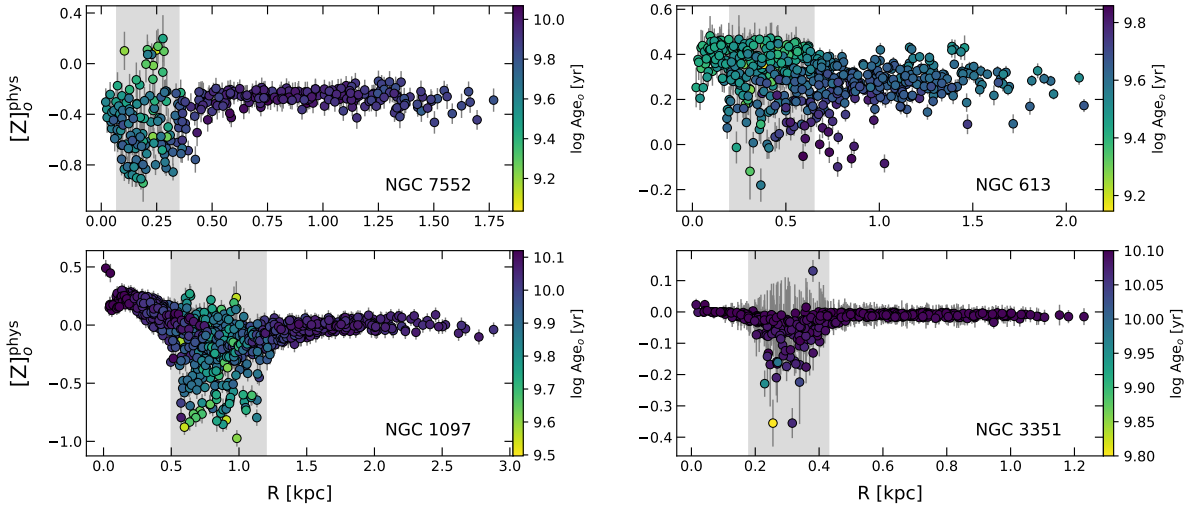

Figure 6.8: Radial metallicity of the old stellar population. Upper row: NGC 7552 (left), NGC 613 (right). Lower row: NGC 1097 (left), NGC 3351 (right). The position of the nuclear ring is again marked in gray. The color coding represents the values of log Age$_o$ [Gyr] which is different for each subfigure.

We also carried out an FSF analysis of the MUSE-DEEP data of the central region of M83. The resulting map of $[Z]^{\rm phys}_{\rm 100Myr}$ is presented and discussed in the Appendix.

6.6 Ages and Extinction

We start with the mean light-weighted ages in our sample (second column in Fig. 6.1). In each system except NGC 7552, the youngest stellar populations trace a clear ring-like morphology, consistent with the location of the nuclear ring inferred from both photometric and spectral diagnostics in the literature. In all four galaxies the contrast between the young star-forming ring and the exterior and interior stellar population is particularly sharp, confirming that these structures are relatively confined in both spatial extent and evolutionary timescale. In NGC 3351, a closer inspection of the regions with log Age < 7 reveals a direct correspondence with the prominent HST-identified clusters younger than 10 Myr (Sun et al., 2024, see also their Fig. 9). For NGC 613, the distribution of young stellar ages closely resembles the HST image presented in Fig. 1 of Falcón-Barroso et al. (2014). Similarly, in NGC 1097, our age map is consistent with the age of young clusters shown in Fig. 1a of Prieto et al. (2019), while in NGC 7552 the general features are in line with those shown in Fig. 7 of Brandl et al. (2012).

In the next section, we discuss stellar metallicity and distinguish between the young and old population. For this purpose, we use $t^y_{lim} = 0.3$ Gyr as age boundary. Below and above this limit, we can calculate the mean ages of the young and old population. As it turns out, the mean ages of the young stars are much lower than the boundary, about 4 to 10 Myr in the nuclear star forming regions. Figure 6.3 gives an example for NGC 3351. The

locations of the three most prominent very young clusters are highlighted, indicating the presence of very young stars.

The average ages of the old stars are significantly higher and in the range of many Gyr as Figure 6.4 demonstrates. Notably, we observe a large dispersion of stellar ages within the nuclear star-forming regions, suggesting an extended period of star formation activity. This finding is consistent with previous studies by Allard et al. (2006); Sarzi et al. (2007); Knapen et al. (2008), which present evidence that star formation in nuclear rings occurs episodically through multiple bursts, with activity sustained over long timescales rather than representing a one-time and short-lived event.

We also note an interesting bimodality with respect to the maximum stellar ages in Figure 6.4. While for NGC 1097 and NGC 3351 the oldest stars in the nuclear rings have an almost similar age as out- and inside, they are significantly younger for NGC 7552 and NGC 613. It seems that in the latter two cases stars have started to form later or older stars have migrated away from the ring.

In FSF, we can also determine the interstellar extinction A_V shown in Fig. 6.1 (third row). The characteristic dust lanes flowing along the leading edges of the stellar bars are observed to connect directly to the nuclear ring, in agreement with predictions from dynamical models of bar-driven inflows (Verwilghen et al., 2024). These dust structures trace the flow of interstellar material from the larger bar region toward the circumnuclear zone, feeding ongoing star formation in the ring. Two aspects seem to be noteworthy: First, the regions of the most prominent cluster in the rings seem to show relatively little reddening and extinction. Figure 6.3 gives an example for the case of NGC 3351. This was already shown in Fig. 24 in Emsellem et al. (2022). However, the authors there speak of a technical artifact in the fit converging to an 'misleading local minimum' with very low $[Z]^{\rm lw}$, young age, and low E(B-V) values, possibly created from a lack of young templates. We will show in the next section that the physical metallicity of the young stars in these regions is close to solar. At the same time, all of our fitting runs indicate indeed low extinction within these regions. From a stellar evolutionary standpoint, this finding is easily explained by the onset of stellar winds from newly formed stars, which effectively disperse the residual parental material from which the clusters originated. Prieto et al. (2019) extracted the gas extinction from the HST recombination map $H\alpha/P\alpha$ of NGC 1097 and came to the same conclusion. Clusters as young as 4 Myr have effectively removed dust from their surroundings. Sun et al. (2024) also reported YMCs that lose their local gas and dust reservoirs at ages between 3 and 6 Myr in NGC 3351. Knutas et al. (2025) found similar timescales in M83 using JWST observations.
As a second peculiar feature, on the rings and inside toward the very nucleus, we consistently detect a region largely free of dust attenuation. The central dust-deficient zone is ubiquitous across the sample, suggesting that the innermost few hundred parsecs are not efficient reservoirs of cold material. This is also the case in NGC1365 (Sextl et al., 2024). For M83, however, a dust cavity is found on the star forming ring (see Sextl et al. 2025), while the rest of the central region shows increased interstellar reddening.

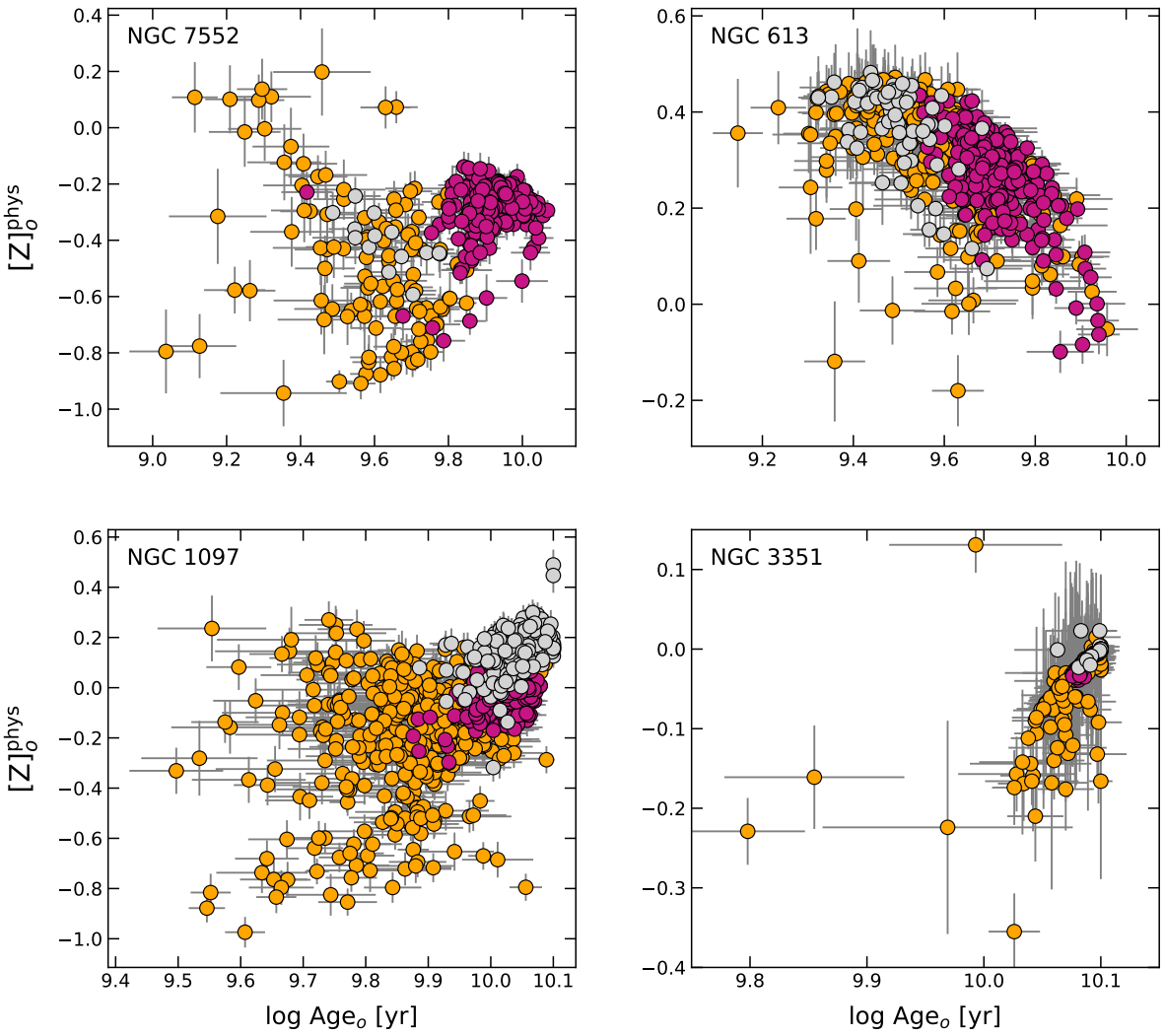

Figure 6.9: Metallicity versus age of the old stellar population. Voronoi bins outside the rings appear in violet red, those on the ring are colored orange, and inner sections are light gray. Upper row: NGC 7552 (left), NGC 613 (right). Lower row: NGC 1097 (left), NGC 3351 (right).

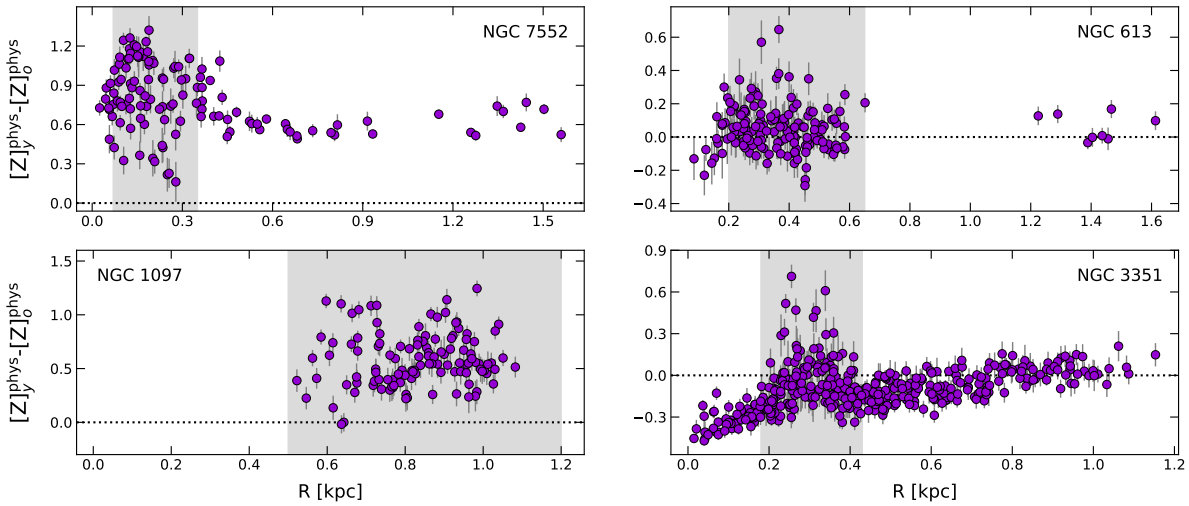

Figure 6.10: Metallicity difference $[Z]_y^{phys}$ - $[Z]_o^{phys}$ versus galactocentric distance. Upper row: NGC 7552 (left), NGC 613 (right). Lower row: NGC 1097 (left), NGC 3351 (right). The dashed line marks the zero line.

6.7 The metallicity of nuclear star forming regions

The fourth row of Fig. 6.1 shows maps of the overall light-weight metallicity $[Z]^{lw}$. We find peculiar drops of $[Z]^{lw}$ in our sample, qualitatively confirming the results of Pessa et al. (2023), Emsellem et al. (2022), Rosado-Belza et al. (2020) and Bittner et al. (2020), although our low values of $[Z]^{lw}$ are less extreme. Even after the inclusion of our very young stellar templates and a nebular continuum correction (see Sextl et al. 2024, 2025), the maps show these features. This was already discussed in the appendix of Pessa et al. (2023) and we will extend the discussion in Section 6.8.

However, we need to keep in mind that what we see here is a mean quantity summarized over an enormously wide range of stellar ages and weighted by stellar light. It is important to understand that the low $[Z]^{lw}$ values found in regions considered 'young' do not directly reflect the intrinsic metallicity of the youngest stars. In such regions often one third or even half of the light still comes from older stellar populations.

Therefore, we calculate [Z] using our physically motivated definition and divide between the young ($\leq$ 0.3 Gyr) and the old population, which significantly alters the picture. Maps of the young stellar population $[Z]_y^{phys}$ are provided for each galaxy in Fig. 6.5. Only regions with a sufficient light fraction of young stars ($b_y > 0.2$) are shown. Voronoi bins that do not meet this criterion are left blank. In addition, Figure 6.5 shows the radial galactocentric distribution of $[Z]_y^{phys}$.

For NGC 1097, NGC 613, NGC 7752 the young component does not fall below solar metallicity. In contrast, many regions show clear super-solar enrichment, with $[Z]_y^{phys} \gtrsim 0.2$ dex. For NGC 7552, we note that this is consistent with the findings reported by Calzetti et al. (2010); Moustakas et al. (2010); Wood et al. (2015), who despite some ambiguities

in the gas-phase metallicity measurements, classify the galaxy as at least solar and likely super-solar.
In NGC 3351, the metallicity of the young population is significantly lower than in the other three galaxies, but we also see clear enrichment in the circumnuclear ring. The regions of the three most prominent young clusters discussed before show solar or somewhat higher metallicity. Generally, the young star metallicity reaches a pronounced local maximum in the ring of NGC 3351. We also note the very clear drop inside the ring where $[Z]_y^{\mathrm{phys}}$ is 0.2 dex lower than outside. Díaz et al. (2007) were able to derive direct HII region abundances on the star forming ring of this galaxy. The authors obtained metallicity values ranging from [Z]$=-0.27 \pm 0.11$ (when using Asplund et al. 2009 as the solar standard) in the eastern segment of the ring up to 0.08 ± 0.09 in the north-western and southern parts. This aligns well with our results for $[Z]_y^{\mathrm{phys}}$ spreading from -0.3 ± 0.1 dex up to 0.3 ± 0.1 dex, especially considering the potential effects of dust depletion of oxygen in HII-regions (Bresolin et al., 2025).

The physical metallicity $[Z]_o^{\mathrm{phys}}$ of the older stellar population ($\geq$ 0.3 Gyr) is shown in Figures 6.6 (maps) and 6.8 (galactocentric distribution). We find an extremely wide range of $[Z]_o^{\mathrm{phys}}$ in the nuclear star forming regions of all four galaxies. Outside these regions, the dispersion of metallicity is significantly smaller. We encounter very low metallicities in the rings of NGC 1097 and NGC 7552.
While the dispersion of $[Z]_o^{\mathrm{phys}}$ outside the nuclear rings is small, the values differ between the four galaxies. $[Z]_o^{\mathrm{phys}}$ is clearly super-solar in NGC 613, solar in NGC 1097 and NGC 3351 and a factor of two below solar in NGC 7552. This must be the result of different evolution histories outside the nuclear rings.
In the case of NGC 613 we notice areas of lower $[Z]_o^{\mathrm{phys}}$ in projected regions perpendicular to the nuclear ring. As Figure 6.7 indicates, these stars have the highest age within the old population encountered in this galaxy (see also Figure 6.9). These areas seem to coincide with the AGN outflow cone (Silva-Lima et al., 2025). Focusing only on the metallicity of the older population in the light-weighted analysis, or considering mean quantities without applying an age cut, does not reveal this distinctive feature. From our viewpoint, the northern cone is projected in front of the stellar ring and is therefore more accessible, while the southern cone lies behind the ring. However, the stars inside the northern cone can only be clearly identified farther out, where the bright stellar ring and its long history of star formation no longer dominates the view. We speculate that the outflow has interrupted star formation for a long period of time and no substantial chemical enrichment was possible.
Figure 6.9 shows $[Z]_o^{\mathrm{phys}}$ as a function of the average age of the old stars in and outside the nuclear star forming regions. The presence of old stars born with very low metallicity over many Gigayears in the cases of NGC 1097 and NGC 7552 is indicative of infall of low metallicity gas over a long period of time. For NGC 613, on the other hand, we see the signature of normal chemical evolution less affected by infall. The old population in the central region of NGC 3351 that we see now was mostly born more than 10 Gyrs ago.
A coarse look at the chemical evolution history is also provided by Figure 6.10, where we plot the metallicity difference between the young and old population as a function of

galactocentric distance. The positive differences indicate normal chemical evolution with the scatter induced by the effects of infall of metal-poor gas of different strengths. NGC 3351, on the other hand, the mostly negative values in the center hint at the most recent strong infall of metal-poor gas.

6.8 Importance of a young template grid

In the sections above, we have pointed out several times that it is crucially important to include the SSP contributions of very young stars with a wide range of possible metallicities. Due to its importance, we use this additional section to address the issue in more detail. We select NGC 3351 and its nuclear ring as an example.

We compare the results of the FSF analysis of the central region of NGC 3351 obtained with three sets of SSPs. The first is identical to the one described in Section 6.4.3. The other two use the same range of metallicities but the ages range from 6 Myr to 12.5 Gyr for set two and 30 Myr to 12.5 Gyr for set three, respectively. For the ages included, the age steps are the same in all three sets.

Figure 6.11 shows the comparison of the total light-weighted metallicities $[Z]^{\rm lw}$. As discussed in Section 7, we encounter spurious regions of low metallicity on the nuclear ring as an artifact of the luminosity-weighted mean over all ages, young and old. However, now we also see the dramatic influence of the contribution of the youngest stars in the sets of SSP. With stars younger than 6 Myr omitted, the metallicities drop to values as low as $[Z]^{\rm lw} = -1.2$. The effect becomes even more extreme when SSP younger than 30 Myr are left out. We encounter extreme regions with $[Z]^{\rm lw} = -1.7$.

The effects shown in Figure 6.11 were already partially discussed in Pessa et al. (2023). We have included the figure here because of the ongoing discussion about the chemical evolution of nuclear rings. However, as we have explained in Section 4.2 the physical relevant description of stellar metallicity is not given by $[Z]^{\rm lw}$ but rather by $[Z]^{\rm phys}$ as defined by equations (5) and (6). Thus, it is important to investigate how the physical metallicities of the young and old stellar populations are affected by the choice of SSPs. Figure 6.12 displays maps of the physical metallicity $[Z]_y^{\rm phys}$ of the young population for the three cases. The differences are equally dramatic, and it is obvious that leaving out the contribution of the youngest stars can cause significant systematic effects. For example, physical metallicities are on average 0.2 dex lower when stars younger than 6 Myr are not included. Differences larger than 1.0 dex are encountered when the contributions of stars younger than 30 Myr are neglected. We have also tested the influence of the SSP sets on the determination of the old population physical metallicities $[Z]_o^{\rm phys}$. We find that the systematic effects are small.

6.9 Summary and conclusions

In our stellar population synthesis of the nuclear star forming regions of four galaxies we use a physical definition of stellar metallicity which is consistent with the study of

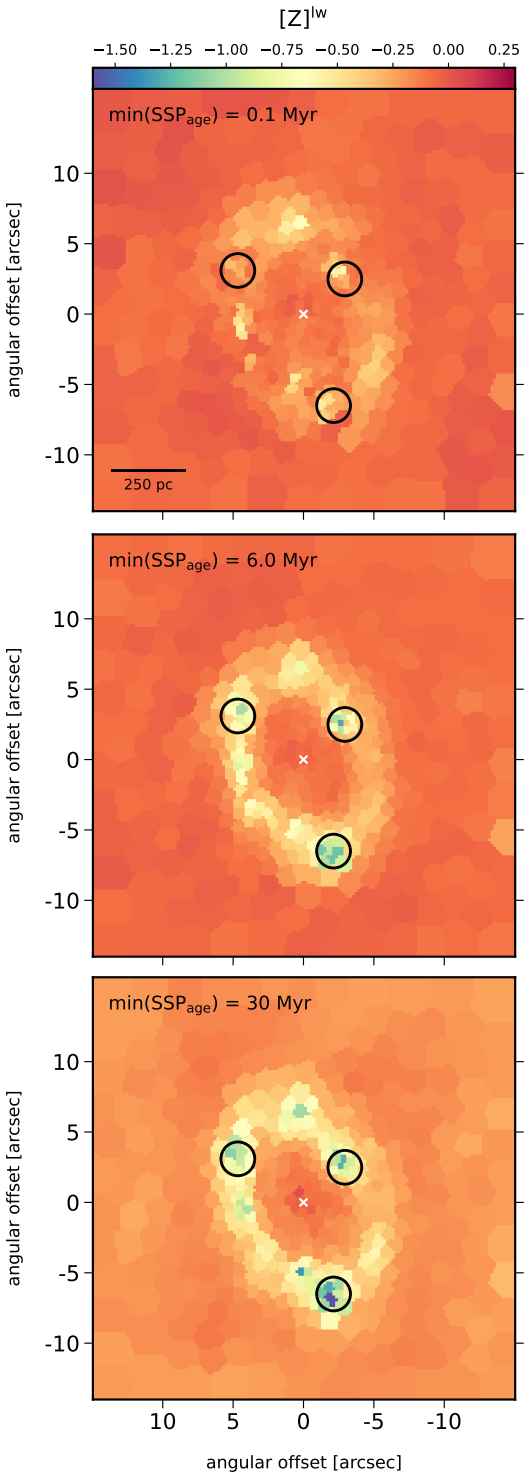

Figure 6.11: Map of total light-weighted metallicity $[Z]^{\rm lw}$ in central region of NGC 3351 obtained with SSP sets of different age ranges: (top) 0.1 Myr to 12.5 Gyr; (middle) 6 Myr to 12.6 Gyr; (bottom) 30 Myr to 12.6 Gyr. The color bar is identical for all subplots. See text.

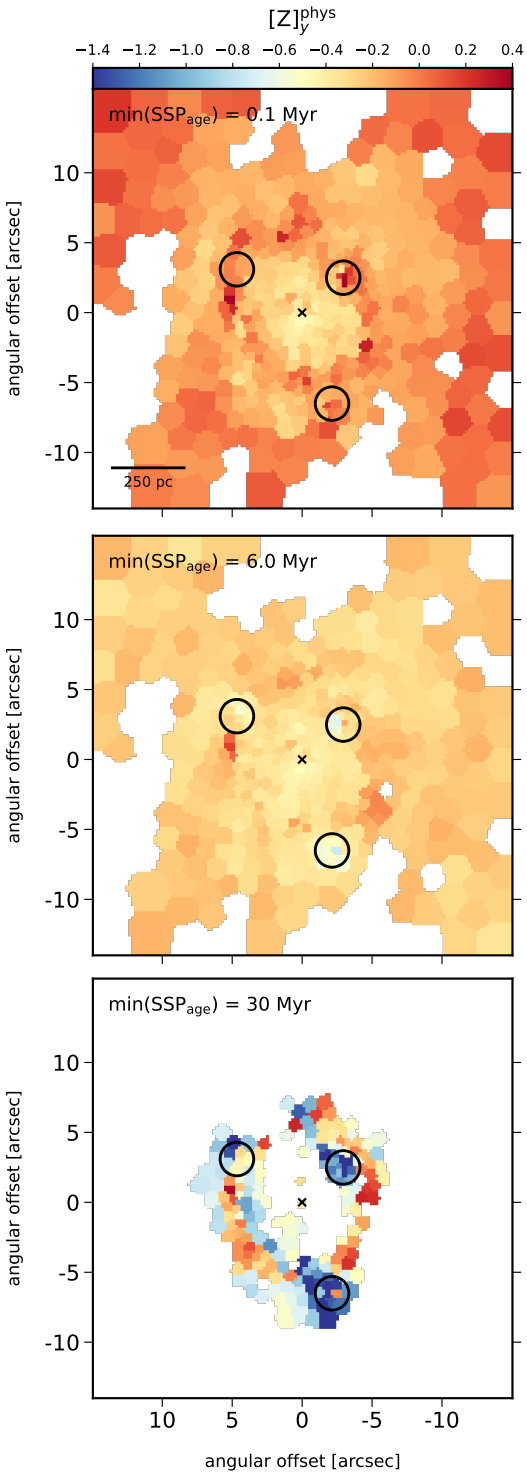

Figure 6.12: Map of physical metallicity $[Z]_y^{phys}$ in central region of NGC 3351 obtained with SSP sets of different age ranges: (top) 0.1 Myr to 12.5 Gyr; (middle) 6 Myr to 12.5 Gyr; (bottom) 30 Myr to 12.5 Gyr. The color bar is identical for all subplots. See text.

chemical evolution. In addition, we disentangle the contributions of young ($\leq$ 0.3 Gyr) and old stars. In this way, we avoid methodological artifacts resulting from the use of conventional luminosity- or mass-weighted averages over stars of all ages, young and old. We also demonstrate that it is crucially important to include the contributions of very young stars in the analysis.
We find that the stellar populations currently forming in the nuclear rings in NGC 613, NGC 1097, and NGC 7752 are super-solar. On the ring of NGC 3351 the metallicities are in a range between half and twice solar, but not as low as a factor of 20 below solar as reported in Bittner et al. (2020). This is in agreement with direct HII region abundance measurements. We also see a clear metallicity enrichment in the case of the ring of NGC 3351. The metallicity distribution in the nuclear ring is similar to the 'onfall' scenario discussed in Friske & Schönrich (2025), Fig. 6.
The ages and metallicities of the old stars indicate continuous star formation in the presence of an inflow of low metallicity gas over many Gyrs in the case of NGC 1097 and NGC 7752. For NGC 613 low metallicity infall appears to be less important. In the case of NGC 3351 the old stars were generated mostly ten Gyrs ago. In the very center, the lower metallicity of the young stars indicates the most recent strong infall of lower-metallicity gas.
The infall scenario is supported by the reddening maps obtained with our population synthesis technique. We find dust lanes tracing the flow of interstellar material toward the circumnuclear zone and providing the material for ongoing star formation. The region inside the nuclear rings is largely free of dust attenuation. On the rings, prominent stellar clusters show little extinction, very likely as a result of the onset of strong stellar winds.
In summary, we conclude that the high spatial and spectral resolution of the MUSE IFU spectrograph combined with the power of an 8m VLT mirror and our technique of stellar population synthesis provide unique means to investigate the nuclear star forming regions of galaxies in the nearby universe.

6.10 Appendix

6.11 The center of M83 with MUSE

Our work focuses on the properties of nuclear rings in the galaxies NGC 7552, NGC 613, NGC 1097, and NGC 3351. In these systems, the young stellar component generally shows metallicities two to three times higher than solar, except in NGC 3351, where values range from approximately half to twice solar. No regions with lower metallicities than this were encountered. That raises a more general question: Does this trend more or less hold for all star-forming nuclear rings, or do individual other cases differ and how are the metallicities distributed?
In our earlier work (Sextl et al., 2025), we investigated the circumnuclear ring of M83 reconstructed from CO maps shown in Harada et al. (2019). We reported a coherent drop in the metallicity of the young stellar population along the southern part of the ring, based on TYPHOON survey data. The IFU-like TYPHOON observations have a coarser spatial

and spectral resolution (1.65″ per spaxel, 8 Å) but extend further into the blue wavelength regime down to 4000Å (Grasha, 2023; Chen et al., 2023). Thus, a comparison with an analysis based on MUSE data is very interesting.
The central region of M83 has also been observed within MUSE-DEEP, offering a rare opportunity to compare full-spectral fitting results from two distinct observational campaigns. For this purpose, we again applied our `pPXF` pipeline now to MUSE data of the central region of M83 and chose our standard template set as described in section 6.4.3.
Figure 6.11.1 shows the metallicity distribution of stars younger than 100 Myr, derived from Voronoi spectra with a S/N of 250. This can be directly compared with Sextl et al. (2025) Figure 17, based on TYPHOON. We again detect the metallicity drop along the southwestern portion of the ring, as well as the slightly sub-solar values west of the optical center. In addition, certain regions east of the center appear slightly metal-poorer in MUSE than in TYPHOON (~ 0.25 dex difference).

These results demonstrate that our revised metallicity definition, combined with a consistent fitting approach, yields results that are broadly comparable across different observational campaigns with different spectrographs, different wavelength regimes, and varying spatial and spectral resolution. They also hint that not all nuclear star-forming rings share the same morphological or chemical characteristics. M83 is distinct in the spatial distribution of the lower metallicity bins. They are not regularly distributed along the ring (regions with $[Z]_y^{\mathrm{phys}} > 0$ dex are found in the south-east). Neither do the regions within the ring appear regular. We find a coherent area in the south, which is relatively enriched, and an irregular distribution around the nucleus.
This fits well with M83's highly peculiar kinematic properties (Della Bruna et al., 2022). Its dynamical center does not coincide with the optical center (Thatte et al., 2000; Díaz et al., 2006), and the location of its elusive AGN remains uncertain (Hernandez et al., 2025). Together, these findings highlight the need to examine galaxies individually, as the metallicity and stellar age distribution within a nuclear ring are shaped by the unique evolutionary history of its host galaxy.

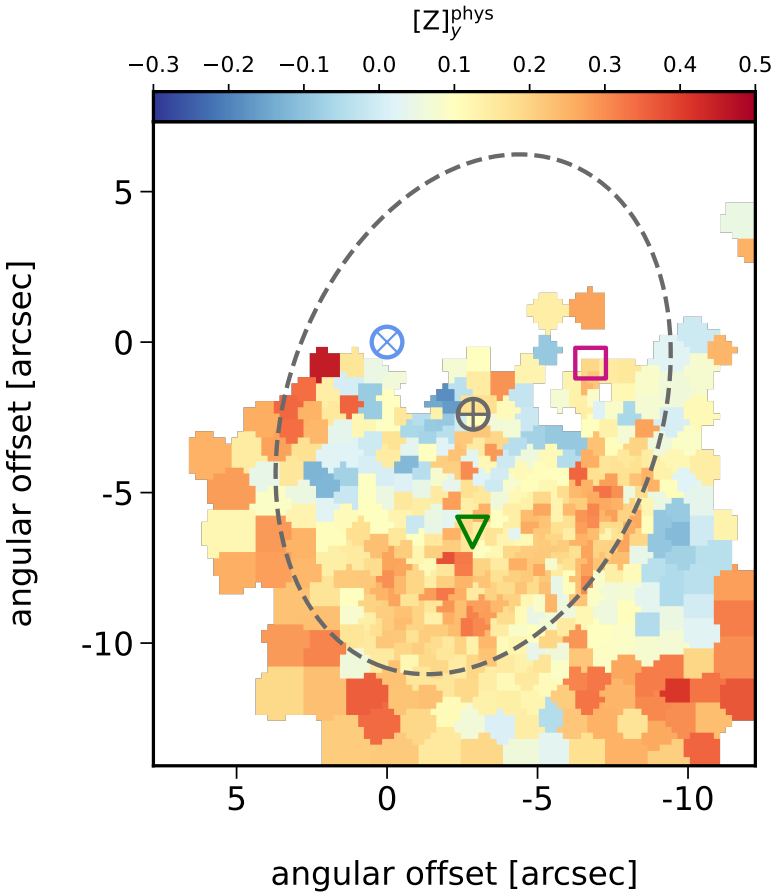

Figure 6.11.1: Metallicity of the young stellar population in the center of M83 with MUSE. Only Voronoi bins with a sufficient young stellar component ($b_y > 0.2$) are shown. The nuclear ring by Harada et al. (2019) reconstructed from CO observations is drawn as dashed ellipse. Its center is determined from the CO velocity field (Muraoka et al., 2009) and shown with a grey plus. The green triangle shows the potential AGN position (pointing P3) from Hernandez et al. (2025) (RA = 204.2530486, Dec = −29.867170, (J2000), priv. comm.). The optical nucleus (Thatte et al., 2000) is shown as a blue cross and the stellar kinematic center (Model A) is shown as violet square (Della Bruna et al., 2022).

7

A Unified Picture and Outlook

This thesis discussed spatially resolved spectroscopic observations from multiple galaxies: NGC 613, NGC 1097, NGC 3351, NGC 7552, M83/NGC 5236, and NGC 1365. They all share a barred morphology, which enables the efficient transport of gas towards their central regions. This gas accumulates at central resonances (for instance a nuclear ring) and becomes compressed, triggering star formation episodes. These dynamics may provide a coherent framework for interpreting the results discussed in this work. The first generations of stars formed after an extensive inflow in these rings tends to be rather metal-poor (down to [Z] ~ -0.9 in NGC 7552), reflecting the original nature of the inflowing gas from outer disk regions or galaxy encounters. Subsequent generations within the star-forming ring show gradual chemical enrichment approaching or exceeding solar metallicity. A prime example for this scenario would be NGC 613. In some galaxies (NGC 7552, NGC 1097), additional later gas inflow episodes occurred (on a timescale of a billion years), so their stellar populations show a mixture of renewed inflow and long-term chemical evolution. In a third category, the latest inflow episode is more recent (a few hundred million years ago), and young low-metallicity stars heavily dominate the integrated spectra of these regions, as seen in M83 and NGC 1365.
Only through our novel approach (combining a rigorous metallicity definition with an age split and suitable templates) has it been possible to disentangle these complex histories and reveal the sustained inflow and episodic star formation in these nuclear rings. In a recently submitted review by Schultheis et al. (2025), the authors speculate that "*Periods during which the galaxy and the bar are starved of gas, and the properties of the inflowing gas (e.g. metallicity), should be imprinted as a fossil record in the star formation history of the NSD [nuclear stellar disk]*" (p. 36). This is exactly what we clearly see with our methodology in SPS.

Obtaining metallicity estimates in outer-disk regions, where the transported gas potentially originates, is generally rather difficult. Within our sample, only some literature about M83 provides evidence in this regard. By means of HII region analysis, Bresolin et al. (2009b) showed that the outer disk beyond 1.0 $R_{25} \approx 9$ kpc until 2.6 $R_{25} \approx 23.4$ kpc has a flat oxy-

gen abundance of ~ 8.2 (equals [Z]≈ -0.5). This matches well with the lowest metallicity values in the center of M83 (Figure 5.12) and confirms our scenario.

For the analyzed galaxies with nuclear rings, we dismissed the extreme low-metallicity values found in the MUSE-TIMER survey, which go down to -1.8 dex in the mean mass- and light-weight at certain positions of the rings. In our analysis, the lowest values for the older populations are down to only $\sim 1/5$ of solar (see Figure 6.9). It is evident that if one limits the analysis to broad age-averaged quantities and relies only on the light- or mass-weighted definitions of SPS, nuclear rings inevitably appear as odd regions. It is then tempting to assume that SPS fails due to degeneracies and that it produces strange artifacts in these complex areas. From our findings, however, it becomes clear that the issue is not a technical failure of SPS, but a methodological one. With our improvements, we demonstrate that star-forming nuclear rings exhibit greater complexity and diversity than previously thought, while remaining consistent and explainable through chemical evolution.

As already mentioned in earlier sections, the study of stacked SDSS spectra of ~ 200000 galaxies motivated us to investigate the age-split and was therefore the first cornerstone of this thesis. Our fitting code in this study, a rather simple χ^2-minimization technique, allowed us to get a full understanding and complete testing of the fitting itself. We also found clear trends of the global galaxy properties (metallicity, age, SFH, extinction, extinction law) as a function of their stellar mass. We conclude that it is highly advantageous to implement an algorithm independently at least once before utilizing the established software packages.
With the key of the kingdom now at hand, it will be possible to reinterpret other galaxies in the literature with peculiar low-metallicity features including NGC 1300 (Rosado-Belza et al., 2020), NGC 5728 (Shimizu et al., 2019) and further examples in PHANGS-MUSE (NGC 1385, NGC 7496, NGC 4535) (Pessa et al., 2023). Also, the 'MAD: The MUSE Atlas of Disks' (Erroz-Ferrer et al., 2019), where only a survey paper has been published, has a rich and mostly unexplored dataset. This survey achieves spatial resolutions of approximately 100 pc, allowing comprehensive mapping of kinematic and interstellar medium characteristics within the inner regions of these galaxies. It was designed with a range of galaxy masses and structural features like bars, rings, and bulges in mind. This can also help to discuss the nature of old stellar populations and to determine the maximum possible age of such structures.
Regarding the general trend towards AI applications, it is perhaps inevitable and not surprising that the first scientific papers are exploring the replacement of traditional stellar population fitting techniques with machine-learning methods. While these approaches enable the extraction of physical properties from probably hundreds of spectra in under a second, these studies have not yet been fully convincing, particularly when we again want to distinguish between young and old populations. What truly impressed us in contrast, was the ability of Generative AI (genAI) to derive spectra from multiple 2D images of galaxies. This super-resolution problem, which initially seemed almost miraculous, is solved with the morphological 2D information in different colors as key. The natural progression now

is to apply our Generative AI method not only to SDSS data but also to the more recent DESI survey (DESI Collaboration et al., 2025). SPS acts here again as a tool to decide whether the genAI succeeded in its task.

However, the most powerful application of SPS in the next decade extends beyond the local universe. While it is essential to first evaluate and fully understand stellar populations in nearby galaxies, the next step is to apply SPS to galaxies in the high-redshift regime. Addressing this requires overcoming several additional challenges: developing improved templates involving significantly different IMF and comprehensive sets of α-abundances, implementing dust modeling that deviates from local models, and carefully considering both data quality and the available wavelength ranges. Among the leading instruments in this field is the James Webb Space Telescope (JWST) with its NIRSpec IFU (Jakobsen et al., 2022). In the future, the Extremely Large Telescope (ELT) is expected to play a significant role, as it includes the High Angular Resolution Monolithic Optical and Near-infrared Integral Field Spectrograph (HARMONI, Thatte et al. (2022)).

Bibliography

Abdalla, F. B., Mateus, A., Santos, W. A., et al. 2008, Mon. Not. Royal Astr. S., 387, 945, doi: 10.1111/j.1365-2966.2008.12881.x

Abel, N. P., van Hoof, P. A. M., Shaw, G., Ferland, G. J., & Elwert, T. 2008, Astrophys. J., 686, 1125, doi: 10.1086/591505

Adebayo, J., Hall, M., Yu, B., & Chern, B. 2023, in The Eleventh International Conference on Learning Representations. https://openreview.net/forum?id=RUzSobdYy0V

Aguerri, J. A. L., Huertas-Company, M., Sánchez Almeida, J., & Muñoz-Tuñón, C. 2012, Astron. & Astrophys., 540, A136, doi: 10.1051/0004-6361/201117632

Alam, S., Albareti, F. D., Allende Prieto, C., et al. 2015, Astrophys. J. Supp. Series, 219, 12, doi: 10.1088/0067-0049/219/1/12

Allard, E. L., Knapen, J. H., Peletier, R. F., & Sarzi, M. 2006, Mon. Not. Royal Astr. S., 371, 1087, doi: 10.1111/j.1365-2966.2006.10751.x

Amari, S., Murata, N., Muller, K. R., Finke, M., & Yang, H. H. 1997, Trans. Neur. Netw., 8, 985–996, doi: 10.1109/72.623200

Amvrosiadis, A., Lange, S., Nightingale, J. W., et al. 2025, Mon. Not. Royal Astr. S., 537, 1163, doi: 10.1093/mnras/staf048

Andreon, S., & Huertas-Company, M. 2011, Astron. & Astrophys., 526, A11, doi: 10.1051/0004-6361/201015610

Andrews, B. H., & Martini, P. 2013, Astrophys. J., 765, 140, doi: 10.1088/0004-637X/765/2/140

Aret, A., Kraus, M., & Šlechta, M. 2016, Mon. Not. Royal Astr. S., 456, 1424, doi: 10.1093/mnras/stv2758

Arimoto, N., & Yoshii, Y. 1987, Astron. & Astrophys., 173, 23

Aringer, B., Girardi, L., Nowotny, W., Marigo, P., & Lederer, M. T. 2009, Astron. & Astrophys., 503, 913, doi: 10.1051/0004-6361/200911703

Arsenault, R. 1989, Astron. & Astrophys., 217, 66

Asari, N. V., Cid Fernandes, R., Stasińska, G., et al. 2007, Mon. Not. Royal Astr. S., 381, 263, doi: 10.1111/j.1365-2966.2007.12255.x

Asplund, M., Grevesse, N., Sauval, A. J., & Scott, P. 2009, A. Review of Astron. and Astrophys., 47, 481, doi: 10.1146/annurev.astro.46.060407.145222

Athanassoula, E. 1992, Mon. Not. Royal Astr. S., 259, 328, doi: 10.1093/mnras/259.2.328

Bacon, R., Copin, Y., Monnet, G., et al. 2001, Mon. Not. Royal Astr. S., 326, 23, doi: 10.1046/j.1365-8711.2001.04612.x

Bacon, R., Accardo, M., Adjali, L., et al. 2010, in Society of Photo-Optical Instrumentation Engineers (SPIE) Conference Series, Vol. 7735, Ground-based and Airborne Instrumentation for Astronomy III, ed. I. S. McLean, S. K. Ramsay, & H. Takami, 773508, doi: 10.1117/12.856027

Bacon, R., Vernet, J., Borisova, E., et al. 2014, The Messenger, 157, 13

Baldry, I. K., Glazebrook, K., Brinkmann, J., et al. 2004, Astrophys. J., 600, 681, doi: 10.1086/380092

Baldwin, C., McDermid, R. M., Kuntschner, H., Maraston, C., & Conroy, C. 2018, Mon. Not. Royal Astr. S., 473, 4698, doi: 10.1093/mnras/stx2502

Baldwin, J. A., Phillips, M. M., & Terlevich, R. 1981, The Publ. of the Astron. S. of the Pac., 93, 5, doi: 10.1086/130766

Ballantyne, D. R., Draper, A. R., Madsen, K. K., Rigby, J. R., & Treister, E. 2011, Astrophys. J., 736, 56, doi: 10.1088/0004-637X/736/1/56

Balogh, M. L., Morris, S. L., Yee, H. K. C., Carlberg, R. G., & Ellingson, E. 1999, Astrophys. J., 527, 54, doi: 10.1086/308056

Baranchuk, D., Rubachev, I., Voynov, A., Khrulkov, V., & Babenko, A. 2022, International Conference on Learning Representations

Bastian, N., Covey, K. R., & Meyer, M. R. 2010, A. Review of Astron. and Astrophys., 48, 339, doi: 10.1146/annurev-astro-082708-101642

Battisti, A. J., Calzetti, D., & Chary, R. R. 2017, Astrophys. J., 840, 109, doi: 10.3847/1538-4357/aa6fb2

Beck, R., Dobos, L., Yip, C.-W., Szalay, A. S., & Csabai, I. 2016, Mon. Not. Royal Astr. S., 457, 362, doi: 10.1093/mnras/stv2986

Bell, G., Hey, T., & Szalay, A. 2009, Science, 323, 1297, doi: 10.1126/science.1170411

Berg, D. A., Skillman, E. D., Croxall, K. V., et al. 2015, Astrophys. J., 806, 16, doi: 10.1088/0004-637X/806/1/16

Berlind, A. A., Quillen, A. C., Pogge, R. W., & Sellgren, K. 1997, Astronom. J., 114, 107, doi: 10.1086/118457

Bezanson, R., van Dokkum, P., & Franx, M. 2012, Astrophys. J., 760, 62, doi: 10.1088/0004-637X/760/1/62

Binney, J. 1978, Comments on Astrophysics, 8, 27

Bittner, A. 2021, PhD thesis, Ludwig-Maximilians University of Munich, Germany

Bittner, A., Sánchez-Blázquez, P., Gadotti, D. A., et al. 2020, Astron. & Astrophys., 643, A65, doi: 10.1051/0004-6361/202038450

Bland-Hawthorn, J., Tepper-Garcia, T., Agertz, O., & Freeman, K. 2023, Astrophys. J., 947, 80, doi: 10.3847/1538-4357/acc469

Blattmann, A., Rombach, R., Ling, H., et al. 2023, in Proceedings of the IEEE/CVF Conference on Computer Vision and Pattern Recognition, 22563–22575

Bochanski, J. J., Hawley, S. L., Covey, K. R., et al. 2010, Astronom. J., 139, 2679, doi: 10.1088/0004-6256/139/6/2679

Boecker, A., Alfaro-Cuello, M., Neumayer, N., Martín-Navarro, I., & Leaman, R. 2020, Astrophys. J., 896, 13, doi: 10.3847/1538-4357/ab919d

Böker, T., Falcón-Barroso, J., Schinnerer, E., Knapen, J. H., & Ryder, S. 2008, Astronom. J., 135, 479, doi: 10.1088/0004-6256/135/2/479

Borne, K. 2010, in American Astronomical Society Meeting Abstracts, Vol. 215, American Astronomical Society Meeting Abstracts #215, 230.01

Bournaud, F., Elmegreen, B. G., & Martig, M. 2009, Astrophys. J. Lett., 707, L1, doi: 10.1088/0004-637X/707/1/L1

Brandl, B. R., Martín-Hernández, N. L., Schaerer, D., Rosenberg, M., & van der Werf, P. P. 2012, Astron. & Astrophys., 543, A61, doi: 10.1051/0004-6361/201117568

Brescia, M., Cavuoti, S., & Longo, G. 2015, Mon. Not. Royal Astr. S., 450, 3893

Brescia, M., Cavuoti, S., Razim, O., et al. 2021, Frontiers in Astronomy and Space Sciences, 8, doi: 10.3389/fspas.2021.658229

Bresolin, F., Gieren, W., Kudritzki, R.-P., et al. 2009a, Astrophys. J., 700, 309, doi: 10.1088/0004-637X/700/1/309

Bresolin, F., Kennicutt, R. C., & Ryan-Weber, E. 2012, Astrophys. J., 750, 122, doi: 10.1088/0004-637X/750/2/122

Bresolin, F., & Kennicutt, Jr., R. C. 2002, Astrophys. J., 572, 838, doi: 10.1086/340371

Bresolin, F., Kudritzki, R.-P., & Urbaneja, M. A. 2022, Astrophys. J., 940, 32, doi: 10.3847/1538-4357/ac9584

Bresolin, F., Kudritzki, R.-P., Urbaneja, M. A., et al. 2016, Astrophys. J., 830, 64, doi: 10.3847/0004-637X/830/2/64

Bresolin, F., Kudritzki, R.-P., Urbaneja, M. A., Sextl, E., & Riess, A. G. 2025, Astrophys. J., 991, 151, doi: 10.3847/1538-4357/adfc4c

Bresolin, F., Ryan-Weber, E., Kennicutt, R. C., & Goddard, Q. 2009b, Astrophys. J., 695, 580, doi: 10.1088/0004-637X/695/1/580

Bresolin, F., Schaerer, D., González Delgado, R. M., & Stasińska, G. 2005, Astron. & Astrophys., 441, 981, doi: 10.1051/0004-6361:20053369

Bressan, A., Chiosi, C., & Tantalo, R. 1996, Astron. & Astrophys., 311, 425, doi: 10.48550/arXiv.astro-ph/9602032

Brinchmann, J., Charlot, S., White, S. D. M., et al. 2004, Mon. Not. Royal Astr. S., 351, 1151, doi: 10.1111/j.1365-2966.2004.07881.x

Bromm, V., & Larson, R. B. 2004, A. Review of Astron. and Astrophys., 42, 79, doi: 10.1146/annurev.astro.42.053102.134034

Bruzual, G., & Charlot, S. 2003, Mon. Not. Royal Astr. S., 344, 1000, doi: 10.1046/j.1365-8711.2003.06897.x

Burstein, D., Faber, S. M., Gaskell, C. M., & Krumm, N. 1984, Astrophys. J., 287, 586, doi: 10.1086/162718

Buta, R., & Combes, F. 1996, Fund. Cos. Phys., 17, 95

Buzzoni, A. 2015, Mon. Not. Royal Astr. S., 449, 296, doi: 10.1093/mnras/stv242

Buzzoni, A., Bertone, E., & Chavez, M. 2009, Astrophys. J. Lett., 703, L127, doi: 10.1088/0004-637X/703/2/L127

Byler, N., Dalcanton, J. J., Conroy, C., & Johnson, B. D. 2017, Astrophys. J., 840, 44, doi: 10.3847/1538-4357/aa6c66

Byrne, C. M., Stanway, E. R., Eldridge, J. J., McSwiney, L., & Townsend, O. T. 2022, Mon. Not. Royal Astr. S., 512, 5329, doi: 10.1093/mnras/stac807

Calabrò, A., Pentericci, L., Feltre, A., et al. 2023, Astron. & Astrophys., 679, A80, doi: 10.1051/0004-6361/202347190

Callanan, D., Longmore, S. N., Kruijssen, J. M. D., et al. 2021, Mon. Not. Royal Astr. S., 505, 4310, doi: 10.1093/mnras/stab1527

Calzetti, D. 2001, The Publ. of the Astron. S. of the Pac., 113, 1449, doi: 10.1086/324269

—. 2013, in Secular Evolution of Galaxies, ed. J. Falcón-Barroso & J. H. Knapen (Cambridge University Press), 419, doi: 10.48550/arXiv.1208.2997

Calzetti, D., Armus, L., Bohlin, R. C., et al. 2000, Astrophys. J., 533, 682, doi: 10.1086/308692

Calzetti, D., Kennicutt, R. C., Engelbracht, C. W., et al. 2007, Astrophys. J., 666, 870, doi: 10.1086/520082

Calzetti, D., Wu, S. Y., Hong, S., et al. 2010, Astrophys. J., 714, 1256, doi: 10.1088/0004-637X/714/2/1256

Camps, P., & Baes, M. 2015, Astron. Comput., 9, 20, doi: 10.1016/j.ascom.2014.10.004

—. 2020, Astron. Comput., 31, 100381, doi: 10.1016/j.ascom.2020.100381

Cappellari, M. 2017, Mon. Not. Royal Astr. S., 466, 798, doi: 10.1093/mnras/stw3020

—. 2023, Mon. Not. Royal Astr. S., 526, 3273, doi: 10.1093/mnras/stad2597

Cappellari, M., & Copin, Y. 2003, Mon. Not. Royal Astr. S., 342, 345, doi: 10.1046/j.1365-8711.2003.06541.x

Cappellari, M., & Emsellem, E. 2004, The Publ. of the Astron. S. of the Pac., 116, 138, doi: 10.1086/381875

Cappellari, M., Emsellem, E., Krajnović, D., et al. 2011, Mon. Not. Royal Astr. S., 413, 813, doi: 10.1111/j.1365-2966.2010.18174.x

Cardelli, J. A., Clayton, G. C., & Mathis, J. S. 1989, Astrophys. J., 345, 245, doi: 10.1086/167900

Cardiel, N., Gorgas, J., Sánchez-Blázquez, P., et al. 2003, Astron. & Astrophys., 409, 511, doi: 10.1051/0004-6361:20031096

Cardoso, L. S. M., Gomes, J. M., & Papaderos, P. 2017, Astron. & Astrophys., 604, A99, doi: 10.1051/0004-6361/201630378

Cardoso, L. S. M., Gomes, J. M., Papaderos, P., et al. 2022, Astron. & Astrophys., 667, A11, doi: 10.1051/0004-6361/202243856

Carrillo, A., Jogee, S., Drory, N., et al. 2020, Mon. Not. Royal Astr. S., 493, 4094, doi: 10.1093/mnras/staa397

Cattaneo, A., Dekel, A., Faber, S. M., & Guiderdoni, B. 2008, Mon. Not. Royal Astr. S., 389, 567, doi: 10.1111/j.1365-2966.2008.13562.x

Cavuoti, S., Brescia, M., D'Abrusco, R., Longo, G., & Paolillo, M. 2014, Mon. Not. Royal Astr. S., 437, 968, doi: 10.1093/mnras/stt1961

Cezario, E., Coelho, P. R. T., Alves-Brito, A., Forbes, D. A., & Brodie, J. P. 2013, Astron. & Astrophys., 549, A60, doi: 10.1051/0004-6361/201220336

Chabrier, G. 2003, The Publ. of the Astron. S. of the Pac., 115, 763, doi: 10.1086/376392

Charlot, S., & Fall, S. M. 2000, Astrophys. J., 539, 718, doi: 10.1086/309250

Chen, B. H., Goto, T., Kim, S. J., et al. 2021, Mon. Not. Royal Astr. S., 501, 3951, doi: 10.1093/mnras/staa3865

Chen, Q.-H., Grasha, K., Battisti, A. J., et al. 2023, Mon. Not. Royal Astr. S., 519, 4801, doi: 10.1093/mnras/stac3790

Chen, Q.-H., Grasha, K., Battisti, A. J., et al. 2024, Mon. Not. Royal Astr. S., 534, 883, doi: 10.1093/mnras/stae2119

Chen, T., Kornblith, S., Norouzi, M., & Hinton, G. 2020, in International conference on machine learning, PMLR, 1597–1607

Chen, X. Y., Liang, Y. C., Hammer, F., et al. 2010, Astron. & Astrophys., 515, A101, doi: 10.1051/0004-6361/200913894

Chiappini, C., Matteucci, F., & Romano, D. 2001, Astrophys. J., 554, 1044, doi: 10.1086/321427

Choi, J., Dotter, A., Conroy, C., et al. 2016, Astrophys. J., 823, 102, doi: 10.3847/0004-637X/823/2/102

Cid Fernandes, R., Asari, N. V., Sodré, L., et al. 2007, Mon. Not. Royal Astr. S., 375, L16, doi: 10.1111/j.1745-3933.2006.00265.x

Cid Fernandes, R., Mateus, A., Sodré, L., Stasińska, G., & Gomes, J. M. 2005, Mon. Not. Royal Astr. S., 358, 363, doi: 10.1111/j.1365-2966.2005.08752.x

Cid Fernandes, R., Mateus, A., Sodré, L., Stasinska, G., & Gomes, J. M. 2011a, STARLIGHT: Spectral Synthesis Code, Astrophysics Source Code Library, record ascl:1108.006. http://ascl.net/1108.006

Cid Fernandes, R., Stasińska, G., Mateus, A., & Vale Asari, N. 2011b, Mon. Not. Royal Astr. S., 413, 1687, doi: 10.1111/j.1365-2966.2011.18244.x

Cid Fernandes, R., Pérez, E., García Benito, R., et al. 2013, Astron. & Astrophys., 557, A86, doi: 10.1051/0004-6361/201220616

Cikota, A., Deustua, S., & Marleau, F. 2016, Astrophys. J., 819, 152, doi: 10.3847/0004-637X/819/2/152

Ciotti, L., & Ostriker, J. P. 2007, Astrophys. J., 665, 1038, doi: 10.1086/519833

Clark, C. J. R., Verstocken, S., Bianchi, S., et al. 2018, Astron. & Astrophys., 609, A37, doi: 10.1051/0004-6361/201731419

Clavijo-Bohórquez, W. E., de Gouveia Dal Pino, E. M., & Melioli, C. 2024, Mon. Not. Royal Astr. S., 535, 1696, doi: 10.1093/mnras/stae487

Cole, D. R., Debattista, V. P., Erwin, P., Earp, S. W. F., & Roškar, R. 2014, Mon. Not. Royal Astr. S., 445, 3352, doi: 10.1093/mnras/stu1985

Colina, L., García Vargas, M. L., Mas-Hesse, J. M., Alberdi, A., & Krabbe, A. 1997, Astrophys. J. Lett., 484, L41, doi: 10.1086/310766

Combes, F. 2021, Galaxies: Formation and Evolution (Wiley-ISTE, London), doi: 10.1002/9781119818007

Comerón, S., Knapen, J. H., Beckman, J. E., et al. 2010, Mon. Not. Royal Astr. S., 402, 2462, doi: 10.1111/j.1365-2966.2009.16057.x

Comte, G. 1981, Astron. & Astrophys. Supp., 44, 441

Conroy, C., & Gunn, J. E. 2010a, FSPS: Flexible Stellar Population Synthesis, Astrophysics Source Code Library, record ascl:1010.043

—. 2010b, Astrophys. J., 712, 833, doi: 10.1088/0004-637X/712/2/833

Conroy, C., Gunn, J. E., & White, M. 2009, Astrophys. J., 699, 486, doi: 10.1088/0004-637X/699/1/486

Conroy, C., Naidu, R. P., Zaritsky, D., et al. 2019, Astrophys. J., 887, 237, doi: 10.3847/1538-4357/ab5710

Contopoulos, G., & Grosbol, P. 1989, Astron. & Astrophys. Rev., 1, 261, doi: 10.1007/BF00873080

Contopoulos, G., & Papayannopoulos, T. 1980, Astron. & Astrophys., 92, 33

Corbelli, E., Braine, J., Bandiera, R., et al. 2017, Astron. & Astrophys., 601, A146, doi: 10.1051/0004-6361/201630034

Cordts, M., Omran, M., Ramos, S., et al. 2016, in Proceedings of the IEEE conference on computer vision and pattern recognition, 3213–3223

Cowie, L. L., Songaila, A., Hu, E. M., & Cohen, J. G. 1996, Astronom. J., 112, 839, doi: 10.1086/118058

Csizi, B., Tortorelli, L., Siudek, M., et al. 2024, Astron. & Astrophys., 689, A37, doi: 10.1051/0004-6361/202449838

Cummings, J. D., Kalirai, J. S., Tremblay, P. E., Ramirez-Ruiz, E., & Choi, J. 2018, Astrophys. J., 866, 21, doi: 10.3847/1538-4357/aadfd6

Curti, M., Hayden-Pawson, C., Maiolino, R., et al. 2022, Mon. Not. Royal Astr. S., 512, 4136, doi: 10.1093/mnras/stac544

Cutri, R. M., Skrutskie, M. F., van Dyk, S., et al. 2003, VizieR Online Data Catalog: 2MASS All-Sky Catalog of Point Sources (Cutri+ 2003), VizieR On-line Data Catalog: II/246. Originally published in: University of Massachusetts and Infrared Processing and Analysis Center, (IPAC/California Institute of Technology) (2003)

da Silva, P., Menezes, R. B., & Steiner, J. E. 2020, Mon. Not. Royal Astr. S., 492, 5121, doi: 10.1093/mnras/staa007

da Silva, R., Crestani, J., Bono, G., et al. 2022, Astron. & Astrophys., 661, A104, doi: 10.1051/0004-6361/202142957

D'Agostino, J. J., Poetrodjojo, H., Ho, I. T., et al. 2018, Mon. Not. Royal Astr. S., 479, 4907, doi: 10.1093/mnras/sty1676

Damineli, A., Kaufer, A., Wolf, B., et al. 2000, Astrophys. J. Lett., 528, L101, doi: 10.1086/312441

Daniel, K. J., & Wyse, R. F. G. 2015, Mon. Not. Royal Astr. S., 447, 3576, doi: 10.1093/mnras/stu2683

Darg, D. W., Kaviraj, S., Lintott, C. J., et al. 2010, Mon. Not. Royal Astr. S., 401, 1552, doi: 10.1111/j.1365-2966.2009.15786.x

Davé, R., Finlator, K., & Oppenheimer, B. D. 2011, Mon. Not. Royal Astr. S., 416, 1354, doi: 10.1111/j.1365-2966.2011.19132.x

Davidson, R., & Flachaire, E. 2008, Journal of Econometrics, 146, 162, doi: https://doi.org/10.1016/j.jeconom.2008.08.003

Davies, B., Origlia, L., Kudritzki, R.-P., et al. 2009a, Astrophys. J., 694, 46, doi: 10.1088/0004-637X/694/1/46

—. 2009b, Astrophys. J., 696, 2014, doi: 10.1088/0004-637X/696/2/2014

Davies, B., Kudritzki, R.-P., Lardo, C., et al. 2017, Astrophys. J., 847, 112, doi: 10.3847/1538-4357/aa89ed

Davies, R. L., Rich, J. A., Kewley, L. J., & Dopita, M. A. 2014, Mon. Not. Royal Astr. S., 439, 3835, doi: 10.1093/mnras/stu234

Dayal, P., Ferrara, A., & Dunlop, J. S. 2013, Mon. Not. Royal Astr. S., 430, 2891, doi: 10.1093/mnras/stt083

de Melo, C. M., Torralba, A., Guibas, L., et al. 2022, Trends in cognitive sciences, 26, 174

de Sá-Freitas, C., Gadotti, D. A., Fragkoudi, F., et al. 2023, Astron. & Astrophys., 678, A202, doi: 10.1051/0004-6361/202347028

de Vaucouleurs, G. 1991, Science, 254, 1667

del Burgo, C., & Allende Prieto, C. 2018, Mon. Not. Royal Astr. S., 479, 1953, doi: 10.1093/mnras/sty1371

Della Bruna, L., Adamo, A., Amram, P., et al. 2022, Astron. & Astrophys., 660, A77, doi: 10.1051/0004-6361/202142315

DESI Collaboration, Aghamousa, A., Aguilar, J., et al. 2016a, arXiv e-prints, arXiv:1611.00036, doi: 10.48550/arXiv.1611.00036

—. 2016b, arXiv e-prints, arXiv:1611.00037, doi: 10.48550/arXiv.1611.00037

DESI Collaboration, Abdul-Karim, M., Adame, A. G., et al. 2025, arXiv e-prints, arXiv:2503.14745, doi: 10.48550/arXiv.2503.14745

Dey, B., Andrews, B. H., Newman, J. A., et al. 2022, Mon. Not. Royal Astr. S., 515, 5285, doi: 10.1093/mnras/stac2105

Díaz, Á. I., Terlevich, E., Castellanos, M., & Hägele, G. F. 2007, Mon. Not. Royal Astr. S., 382, 251, doi: 10.1111/j.1365-2966.2007.12351.x

Díaz, R. J., Dottori, H., Aguero, M. P., et al. 2006, Astrophys. J., 652, 1122, doi: 10.1086/507886

D'Isanto, A., & Polsterer, K. L. 2018, Astron. & Astrophys., 609, A111, doi: 10.1051/0004-6361/201731326

Djorgovski, S., & Davis, M. 1987, Astrophys. J., 313, 59, doi: 10.1086/164948

Do, T., Kerzendorf, W., Winsor, N., et al. 2015, Astrophys. J., 809, 143, doi: 10.1088/0004-637X/809/2/143

Doorenbos, L., Cavuoti, S., Longo, G., et al. 2022, arXiv e-prints, arXiv:2211.05556, doi: 10.48550/arXiv.2211.05556

Doorenbos, L., & Sextl, E. 2024, Code for "Galaxy spectroscopy without spectra: Galaxy properties from photometric images with conditional diffusion models", v1, Zenodo, doi: 10.5281/zenodo.13938724

Doorenbos, L., Torbaniuk, O., Cavuoti, S., et al. 2022, Astronomy & Astrophysics, 666, A171

Dopita, M. A., Kewley, L. J., Sutherland, R. S., & Nicholls, D. C. 2016, Astrophys. Space Science, 361, 61, doi: 10.1007/s10509-016-2657-8

Dopita, M. A., Blair, W. P., Long, K. S., et al. 2010, Astrophys. J., 710, 964, doi: 10.1088/0004-637X/710/2/964

Dotter, A. 2016, Astrophys. J. Supp. Series, 222, 8, doi: 10.3847/0067-0049/222/1/8

Draine, B. T. 1978, Astrophys. J. Supp. Series, 36, 595, doi: 10.1086/190513

Duarte Puertas, S., Vilchez, J. M., Iglesias-Páramo, J., et al. 2017, Astron. & Astrophys., 599, A71, doi: 10.1051/0004-6361/201629044

Duchêne, G., & Kraus, A. 2013, A. Review of Astron. and Astrophys., 51, 269, doi: 10.1146/annurev-astro-081710-102602

Dwek, E. 2005, in American Institute of Physics Conference Series, Vol. 761, The Spectral Energy Distributions of Gas-Rich Galaxies: Confronting Models with Data, ed. C. C. Popescu & R. J. Tuffs (AIP), 103–122, doi: 10.1063/1.1913921

Efremov, Y. N., & Elmegreen, B. G. 1998, Mon. Not. Royal Astr. S., 299, 588, doi: 10.1046/j.1365-8711.1998.01819.x

Ekström, S., Georgy, C., Eggenberger, P., et al. 2012, Astron. & Astrophys., 537, A146, doi: 10.1051/0004-6361/201117751

Eldridge, J. J., Stanway, E. R., Xiao, L., et al. 2017, Publ. Astron. Soc. Australia, 34, e058, doi: 10.1017/pasa.2017.51

Eldridge, J. J., & Vink, J. S. 2006, Astron. & Astrophys., 452, 295, doi: 10.1051/0004-6361:20065001

Emsellem, E., Renaud, F., Bournaud, F., et al. 2015, Mon. Not. Royal Astr. S., 446, 2468, doi: 10.1093/mnras/stu2209

Emsellem, E., Schinnerer, E., Santoro, F., et al. 2022, Astron. & Astrophys., 659, A191, doi: 10.1051/0004-6361/202141727

Erroz-Ferrer, S., Carollo, C. M., den Brok, M., et al. 2019, Mon. Not. Royal Astr. S., 484, 5009, doi: 10.1093/mnras/stz194

Erwin, P. 2024, Mon. Not. Royal Astr. S., 528, 3613, doi: 10.1093/mnras/stad3944

Erwin, P., Vega Beltrán, J. C., & Beckman, J. E. 2001, in Astronomical Society of the Pacific Conference Series, Vol. 249, The Central Kiloparsec of Starbursts and AGN: The La Palma Connection, ed. J. H. Knapen, J. E. Beckman, I. Shlosman, & T. J. Mahoney, 171, doi: 10.48550/arXiv.astro-ph/0112056

Faber, S. M., & Jackson, R. E. 1976, Astrophys. J., 204, 668, doi: 10.1086/154215

Falco, E. E., Impey, C. D., Kochanek, C. S., et al. 1999, Astrophys. J., 523, 617, doi: 10.1086/307758

Falcón-Barroso, J., Böker, T., Schinnerer, E., Knapen, J. H., & Ryder, S. 2007, The Messenger, 130, 40

Falcón-Barroso, J., Ramos Almeida, C., Böker, T., et al. 2014, Mon. Not. Royal Astr. S., 438, 329, doi: 10.1093/mnras/stt2189

Falcón-Barroso, J., Sánchez-Blázquez, P., Vazdekis, A., et al. 2011, Astron. & Astrophys., 532, A95, doi: 10.1051/0004-6361/201116842

Feinstein, A., Marraco, H. G., & Muzzio, J. C. 1973, Astron. & Astrophys. Supp., 12, 331

Fisher, D. B., Bolatto, A. D., Glazebrook, K., et al. 2022, Astrophys. J., 928, 169, doi: 10.3847/1538-4357/ac51c8

Fitzpatrick, E. L. 1999, The Publ. of the Astron. S. of the Pac., 111, 63, doi: 10.1086/316293

Fitzpatrick, E. L., & Massa, D. 2007, Astrophys. J., 663, 320, doi: 10.1086/518158

Forbes, D. A., Kotilainen, J. K., & Moorwood, A. F. M. 1994, Astrophys. J. Lett., 433, L13, doi: 10.1086/187536

Forrey, R. C., Babb, J. F., Stancil, P. C., & McLaughlin, B. M. 2018, Mon. Not. Royal Astr. S., 479, 4727, doi: 10.1093/mnras/sty1739

Foster, J. B., Mandel, K. S., Pineda, J. E., et al. 2013, Mon. Not. Royal Astr. S., 428, 1606, doi: 10.1093/mnras/sts144

Fouesneau, M. 2022, pyphot, 1.4.3, Zenodo, doi: 10.5281/zenodo.7016774

Franchetto, A., Mingozzi, M., Poggianti, B. M., et al. 2021, Astrophys. J., 923, 28, doi: 10.3847/1538-4357/ac2510

Frick, P., Stepanov, R., Beck, R., et al. 2016, Astron. & Astrophys., 585, A21, doi: 10.1051/0004-6361/201526796

Friske, J. K. S., & Schönrich, R. 2025, Astron. & Astrophys., 701, A140, doi: 10.1051/0004-6361/202554932

Fuhrmann, K., Chini, R., Kaderhandt, L., & Chen, Z. 2017, Astrophys. J., 836, 139, doi: 10.3847/1538-4357/836/1/139

Gadotti, D. A., Sánchez-Blázquez, P., Falcón-Barroso, J., et al. 2019, Mon. Not. Royal Astr. S., 482, 506, doi: 10.1093/mnras/sty2666

Gadotti, D. A., Bittner, A., Falcón-Barroso, J., et al. 2020, Astron. & Astrophys., 643, A14, doi: 10.1051/0004-6361/202038448

Galárraga-Espinosa, D., Garaldi, E., & Kauffmann, G. 2023, Astron. & Astrophys., 671, A160, doi: 10.1051/0004-6361/202244935

Gallais, P., Rouan, D., Lacombe, F., Tiphene, D., & Vauglin, I. 1991, Astron. & Astrophys., 243, 309

Gallazzi, A., Charlot, S., Brinchmann, J., White, S. D. M., & Tremonti, C. A. 2005, Mon. Not. Royal Astr. S., 362, 41, doi: 10.1111/j.1365-2966.2005.09321.x

Garn, T., & Best, P. N. 2010, Mon. Not. Royal Astr. S., 409, 421, doi: 10.1111/j.1365-2966.2010.17321.x

Gazak, J. Z., Kudritzki, R., Evans, C., et al. 2015, Astrophys. J., 805, 182, doi: 10.1088/0004-637X/805/2/182

Ge, J., Mao, S., Lu, Y., Cappellari, M., & Yan, R. 2019, Mon. Not. Royal Astr. S., 485, 1675, doi: 10.1093/mnras/stz418

Genovali, K., Lemasle, B., Bono, G., et al. 2014, Astron. & Astrophys., 566, A37, doi: 10.1051/0004-6361/201323198

Genzel, R., Tacconi, L. J., Lutz, D., et al. 2015, Astrophys. J., 800, 20, doi: 10.1088/0004-637X/800/1/20

Goddard, D., Thomas, D., Maraston, C., et al. 2017, Mon. Not. Royal Astr. S., 466, 4731, doi: 10.1093/mnras/stw3371

Goddard, Q. E., Bresolin, F., Kennicutt, R. C., Ryan-Weber, E. V., & Rosales-Ortega, F. F. 2011, Mon. Not. Royal Astr. S., 412, 1246, doi: 10.1111/j.1365-2966.2010.17990.x

Goldschmidt, M. 1863, Mon. Not. Royal Astr. S., 23, 243, doi: 10.1093/mnras/23.8.243

Gonçalves, G., Coelho, P., Schiavon, R., & Usher, C. 2020, Mon. Not. Royal Astr. S., 499, 2327, doi: 10.1093/mnras/staa3051

González Delgado, R. M., García-Benito, R., Pérez, E., et al. 2015, Astron. & Astrophys., 581, A103, doi: 10.1051/0004-6361/201525938

González-Payo, J., Caballero, J. A., Gorgas, J., et al. 2024, Astron. & Astrophys., 689, A302, doi: 10.1051/0004-6361/202450048

Gordon, K. D., Calzetti, D., & Witt, A. N. 1997, Astrophys. J., 487, 625, doi: 10.1086/304654

Götberg, Y., de Mink, S. E., Groh, J. H., Leitherer, C., & Norman, C. 2019, Astron. & Astrophys., 629, A134, doi: 10.1051/0004-6361/201834525

Grasha, K. 2023, in IAU Symposium, Vol. 373, Resolving the Rise and Fall of Star Formation in Galaxies, ed. T. Wong & W.-T. Kim, 234–241, doi: 10.1017/S174392132200429X

Grasha, K., Chen, Q. H., Battisti, A. J., et al. 2022, Astrophys. J., 929, 118, doi: 10.3847/1538-4357/ac5ab2

Gray, R. O., & Corbally, J., C. 2009, Stellar Spectral Classification (Princeton University Press)

Groves, B., Kreckel, K., Santoro, F., et al. 2023, Mon. Not. Royal Astr. S., 520, 4902, doi: 10.1093/mnras/stad114

Guo, Y., Jogee, S., Finkelstein, S. L., et al. 2023, Astrophys. J. Lett., 945, L10, doi: 10.3847/2041-8213/acacfb

Han, Z.-W., Ge, H.-W., Chen, X.-F., & Chen, H.-L. 2020, Research in Astronomy and Astrophysics, 20, 161, doi: 10.1088/1674-4527/20/10/161

Harada, N., Sakamoto, K., Martín, S., et al. 2019, Astrophys. J., 884, 100, doi: 10.3847/1538-4357/ab41ff

Harris, J., Calzetti, D., Gallagher, John S., I., Conselice, C. J., & Smith, D. A. 2001, Astronom. J., 122, 3046, doi: 10.1086/324230

He, K., Zhang, X., Ren, S., & Sun, J. 2016, in Proceedings of the IEEE conference on computer vision and pattern recognition, 770–778

Heavens, A., Panter, B., Jimenez, R., & Dunlop, J. 2004, Nature, 428, 625, doi: 10.1038/nature02474

Henghes, B., Thiyagalingam, J., Pettitt, C., Hey, T., & Lahav, O. 2022, Mon. Not. Royal Astr. S., 512, 1696, doi: 10.1093/mnras/stac480

Herbst, E., & van Dishoeck, E. F. 2009, A. Review of Astron. and Astrophys., 47, 427, doi: 10.1146/annurev-astro-082708-101654

Herbst, W. 1976, Astrophys. J., 208, 923, doi: 10.1086/154681

Hernandez, S., Larsen, S., Trager, S., Kaper, L., & Groot, P. 2018, Mon. Not. Royal Astr. S., 473, 826, doi: 10.1093/mnras/stx2397

Hernandez, S., Larsen, S., Aloisi, A., et al. 2019, Astrophys. J., 872, 116, doi: 10.3847/1538-4357/ab017a

Hernandez, S., Aloisi, A., James, B. L., et al. 2021, Astrophys. J., 908, 226, doi: 10.3847/1538-4357/abd6c4

Hernandez, S., Jones, L., Smith, L. J., et al. 2023, Astrophys. J., 948, 124, doi: 10.3847/1538-4357/acc837

Hernandez, S., Smith, L. J., Jones, L. H., et al. 2025, Astrophys. J., 983, 154, doi: 10.3847/1538-4357/adba5d

Herrmann, K. A., Ciardullo, R., Feldmeier, J. J., & Vinciguerra, M. 2008, Astrophys. J., 683, 630, doi: 10.1086/589920

Hickox, R. C., & Alexander, D. M. 2018, A. Review of Astron. and Astrophys., 56, 625, doi: 10.1146/annurev-astro-081817-051803

Hirota, A., Egusa, F., Baba, J., et al. 2018, Publ. Astron. Soc. Japan, 70, 73, doi: 10.1093/pasj/psy071

Ho, I. T., Kudritzki, R.-P., Kewley, L. J., et al. 2015, Mon. Not. Royal Astr. S., 448, 2030, doi: 10.1093/mnras/stv067

Ho, I. T., Medling, A. M., Groves, B., et al. 2016, Astrophys. Space Science, 361, 280, doi: 10.1007/s10509-016-2865-2

Ho, I. T., Seibert, M., Meidt, S. E., et al. 2017, Astrophys. J., 846, 39, doi: 10.3847/1538-4357/aa8460

Ho, I. T., Meidt, S. E., Kudritzki, R.-P., et al. 2018, Astron. & Astrophys., 618, A64, doi: 10.1051/0004-6361/201833262

Ho, J., Jain, A., & Abbeel, P. 2020, Advances in Neural Information Processing Systems, 33, 6840

Ho, J., Saharia, C., Chan, W., et al. 2022, The Journal of Machine Learning Research, 23, 2249

Holmberg, E. 1958, Meddelanden fran Lunds Astronomiska Observatorium Serie II, 136, 1

Holwerda, B. W., & Keel, W. C. 2013, Astron. & Astrophys., 556, A42, doi: 10.1051/0004-6361/201321455

Holwerda, B. W., Wu, J. F., Keel, W. C., et al. 2021, Astrophys. J., 914, 142

Hou, J. L., Prantzos, N., & Boissier, S. 2000, Astron. & Astrophys., 362, 921, doi: 10.48550/arXiv.astro-ph/0007164

Houghton, R. C. W., & Thatte, N. 2008, Mon. Not. Royal Astr. S., 385, 1110, doi: 10.1111/j.1365-2966.2008.12893.x

Hoyle, B. 2016, Astronomy and Computing, 34

Hoyle, B., Rau, M. M., Paech, K., et al. 2015, Mon. Not. Royal Astr. S., 452, 4183, doi: 10.1093/mnras/stv1551

Hubble, E. P. 1926, Astrophys. J., 64, 321, doi: 10.1086/143018

Hunt, L. J., Pimbblet, K. A., & Benoit, D. M. 2024, Mon. Not. Royal Astr. S., 529, 479, doi: 10.1093/mnras/stae479

Innes, R. T. A. 1917, Circular of the Union Observatory Johannesburg, 40, 331

Irwin, J. A. 2007, Astrophysics: Decoding the Cosmos (Wiley)

Ivezić, Ž., Kahn, S. M., Tyson, J. A., et al. 2019, Astrophys. J., 873, 111, doi: 10.3847/1538-4357/ab042c

Jakobsen, P., Ferruit, P., Alves de Oliveira, C., et al. 2022, Astron. & Astrophys., 661, A80, doi: 10.1051/0004-6361/202142663

Jałocha, J., Bratek, Ł., Kutschera, M., & Skindzier, P. 2010, Mon. Not. Royal Astr. S., 406, 2805, doi: 10.1111/j.1365-2966.2010.16887.x

Jang, I. S., Hatt, D., Beaton, R. L., et al. 2018, Astrophys. J., 852, 60, doi: 10.3847/1538-4357/aa9d92

Jarrett, T. H., Chester, T., Cutri, R., Schneider, S. E., & Huchra, J. P. 2003, Astronom. J., 125, 525, doi: 10.1086/345794

Jimenez, R., Bernardi, M., Haiman, Z., Panter, B., & Heavens, A. F. 2007, Astrophys. J., 669, 947, doi: 10.1086/521323

Jones, G. T., Byrne, C. M., & Stanway, E. R. 2025a, Mon. Not. Royal Astr. S., 543, 167, doi: 10.1093/mnras/staf1462

Jones, L. H., Hernandez, S., Smith, L. J., et al. 2025b, Astrophys. J., 987, 142, doi: 10.3847/1538-4357/adce71

Kacharov, N., Neumayer, N., Seth, A. C., et al. 2018, Mon. Not. Royal Astr. S., 480, 1973, doi: 10.1093/mnras/sty1985

Kaiser, N., Aussel, H., Burke, B. E., et al. 2002, in Society of Photo-Optical Instrumentation Engineers (SPIE) Conference Series, Vol. 4836, Survey and Other Telescope Technologies and Discoveries, ed. J. A. Tyson & S. Wolff, 154–164, doi: 10.1117/12.457365

Kang, X., Chang, R., Kudritzki, R.-P., Gong, X., & Zhang, F. 2021, Mon. Not. Royal Astr. S., 502, 1967, doi: 10.1093/mnras/stab147

Kang, X., Kudritzki, R.-P., & Zhang, F. 2023, Astron. & Astrophys., 679, A83, doi: 10.1051/0004-6361/202347677

Kauffmann, G., Heckman, T. M., Tremonti, C., et al. 2003, Mon. Not. Royal Astr. S., 346, 1055, doi: 10.1111/j.1365-2966.2003.07154.x

Kennicutt, Robert C., J. 1998, Astrophys. J., 498, 541, doi: 10.1086/305588

Kewley, L. J., & Dopita, M. A. 2002, Astrophys. J. Supp. Series, 142, 35, doi: 10.1086/341326

Kewley, L. J., Dopita, M. A., Sutherland, R. S., Heisler, C. A., & Trevena, J. 2001, Astrophys. J., 556, 121, doi: 10.1086/321545

Kewley, L. J., & Ellison, S. L. 2008, Astrophys. J., 681, 1183, doi: 10.1086/587500

Kewley, L. J., Jansen, R. A., & Geller, M. J. 2005, The Publ. of the Astron. S. of the Pac., 117, 227, doi: 10.1086/428303

Kewley, L. J., Nicholls, D. C., & Sutherland, R. S. 2019, A. Review of Astron. and Astrophys., 57, 511, doi: 10.1146/annurev-astro-081817-051832

Khederlarian, A., Newman, J. A., Andrews, B. H., et al. 2024, Mon. Not. Royal Astr. S., 531, 1454, doi: 10.1093/mnras/stae1189

Kim, J., Chevance, M., Kruijssen, J. M. D., et al. 2021, Mon. Not. Royal Astr. S., 504, 487, doi: 10.1093/mnras/stab878

Kingma, D. P., & Ba, J. 2015, International Conference on Learning Representations

Kippenhahn, R., Weigert, A., & Weiss, A. 2013, Stellar Structure and Evolution, 2nd edn. (Springer Berlin, Heidelberg), doi: 10.1007/978-3-642-30304-3

Klochkova, V. G. 2019, Astrophysical Bulletin, 74, 475, doi: 10.1134/S1990341319040138

Knapen, J. H. 2005, Astron. & Astrophys., 429, 141, doi: 10.1051/0004-6361:20041909

Knapen, J. H., Allard, E. L., Mazzuca, L. M., Sarzi, M., & Peletier, R. F. 2008, in Astrophysics and Space Science Proceedings, Vol. 4, Mapping the Galaxy and Nearby Galaxies, ed. K. Wada & F. Combes, 125, doi: 10.1007/978-0-387-72768-4_18

Knapen, J. H., Sharp, R. G., Ryder, S. D., et al. 2010, Mon. Not. Royal Astr. S., 408, 797, doi: 10.1111/j.1365-2966.2010.17180.x

Knutas, A., Adamo, A., Pedrini, A., et al. 2025, apj, 993, 13, doi: 10.3847/1538-4357/ae018c

Kobayashi, C., & Nomoto, K. 2009, Astrophys. J., 707, 1466, doi: 10.1088/0004-637X/707/2/1466

Koda, J., Hirota, A., Egusa, F., et al. 2023, Astrophys. J., 949, 108, doi: 10.3847/1538-4357/acc65e

Koleva, M., Prugniel, P., Bouchard, A., & Wu, Y. 2009, Astron. & Astrophys., 501, 1269, doi: 10.1051/0004-6361/200811467

Koleva, M., Prugniel, P., Ocvirk, P., Le Borgne, D., & Soubiran, C. 2008, Mon. Not. Royal Astr. S., 385, 1998, doi: 10.1111/j.1365-2966.2008.12908.x

Kormendy, J. and Kennicutt, R. C. 2004, A. Review of Astron. and Astrophys., 42, 603, doi: https://doi.org/10.1146/annurev.astro.42.053102.134024

Kreckel, K., Ho, I. T., Blanc, G. A., et al. 2019, Astrophys. J., 887, 80, doi: 10.3847/1538-4357/ab5115

Kremer, J., Stensbo-Smidt, K., Gieseke, F., Pedersen, K., & Igel, C. 2017, IEEE Intelligent Systems, 32, 16, doi: 10.1109/MIS.2017.40

Kroupa, P. 2001, Mon. Not. Royal Astr. S., 322, 231, doi: 10.1046/j.1365-8711.2001.04022.x

Kroupa, P., Gjergo, E., Jerabkova, T., & Yan, Z. 2026, in Encyclopedia of Astrophysics, Vol. 2, 173–210, doi: 10.1016/B978-0-443-21439-4.00035-3

Kudritzki, R.-P., Bresolin, F., Urbaneka, M. A., & Sextl, E. 2025, arXiv e-prints, arXiv:2510.20652, doi: 10.48550/arXiv.2510.20652

Kudritzki, R. P., Castro, N., Urbaneja, M. A., et al. 2016, Astrophys. J., 829, 70, doi: 10.3847/0004-637X/829/2/70

Kudritzki, R.-P., Ho, I. T., Schruba, A., et al. 2015, Mon. Not. Royal Astr. S., 450, 342, doi: 10.1093/mnras/stv522

Kudritzki, R.-P., & Puls, J. 2000, A. Review of Astron. and Astrophys., 38, 613, doi: 10.1146/annurev.astro.38.1.613

Kudritzki, R.-P., Teklu, A. F., Schulze, F., et al. 2021a, Astrophys. J., 910, 87, doi: 10.3847/1538-4357/abe40c

—. 2021b, Astrophys. J., 922, 274, doi: 10.3847/1538-4357/ac32cf

Kudritzki, R.-P., Urbaneja, M. A., Bresolin, F., et al. 2024, Astrophys. J., 977, 217, doi: 10.3847/1538-4357/ad9279

—. 2008, Astrophys. J., 681, 269, doi: 10.1086/588647

Kudritzki, R.-P., Urbaneja, M. A., Gazak, Z., et al. 2012, Astrophys. J., 747, 15, doi: 10.1088/0004-637X/747/1/15

Lacerda, E. A., Sánchez, S. F., Cid Fernandes, R., et al. 2020, Mon. Not. Royal Astr. S., 492, 3073

Lançon, A., & Wood, P. R. 2000, Astron. & Astrophys. Supp., 146, 217, doi: 10.1051/aas:2000269

Lapi, A., Pantoni, L., Boco, L., & Danese, L. 2020, Astrophys. J., 897, 81, doi: 10.3847/1538-4357/ab9812

Lardo, C., Davies, B., Kudritzki, R. P., et al. 2015, Astrophys. J., 812, 160, doi: 10.1088/0004-637X/812/2/160

Larson, R. B. 1969, Mon. Not. Royal Astr. S., 145, 405, doi: 10.1093/mnras/145.4.405

Lee, J. H., Pak, M., Jeong, H., & Oh, S. 2023, Mon. Not. Royal Astr. S., 521, 4207, doi: 10.1093/mnras/stad814

Leitherer, C., Schaerer, D., Goldader, J. D., et al. 1999, Astrophys. J. Supp. Series, 123, 3, doi: 10.1086/313233

Lépine, J. R. D., Acharova, I. A., & Mishurov, Y. N. 2003, Astrophys. J., 589, 210, doi: 10.1086/374596

Lequeux, J., Peimbert, M., Rayo, J. F., Serrano, A., & Torres-Peimbert, S. 1979, Astron. & Astrophys., 500, 145

Leroy, A. K., Walter, F., Brinks, E., et al. 2008, Astronom. J., 136, 2782, doi: 10.1088/0004-6256/136/6/2782

Leroy, A. K., Sandstrom, K. M., Lang, D., et al. 2019, Astrophys. J. Supp. Series, 244, 24, doi: 10.3847/1538-4365/ab3925

Li, H., Mao, S., Cappellari, M., et al. 2018, Mon. Not. Royal Astr. S., 476, 1765, doi: 10.1093/mnras/sty334

Li, N., & Thakar, A. R. 2008, Computing in Science and Engineering, 10, 18, doi: 10.1109/MCSE.2008.6

Li, Z., Shen, J., & Kim, W.-T. 2015, Astrophys. J., 806, 150, doi: 10.1088/0004-637X/806/2/150

Lima, E. V. R., Sodré, L., Bom, C. R., et al. 2022, Astronomy and Computing, 38, 100510, doi: 10.1016/j.ascom.2021.100510

Lindblad, P. O. 1999, Astron. & Astrophys. Rev., 9, 221, doi: 10.1007/s001590050018

Lintott, C., Schawinski, K., Bamford, S., et al. 2011, Mon. Not. Royal Astr. S., 410, 166, doi: 10.1111/j.1365-2966.2010.17432.x

Lintott, C. J., Schawinski, K., Slosar, A., et al. 2008, Mon. Not. Royal Astr. S., 389, 1179, doi: 10.1111/j.1365-2966.2008.13689.x

Liu, C., Kudritzki, R.-P., Zhao, G., et al. 2022, Astrophys. J., 932, 29, doi: 10.3847/1538-4357/ac69cc

Lo Faro, B., Buat, V., Roehlly, Y., et al. 2017, Mon. Not. Royal Astr. S., 472, 1372, doi: 10.1093/mnras/stx1901

López Fernández, R., Cid Fernandes, R., González Delgado, R. M., et al. 2016, Mon. Not. Royal Astr. S., 458, 184, doi: 10.1093/mnras/stw260

Lower, S., Narayanan, D., Leja, J., et al. 2020, Astrophys. J., 904, 33, doi: 10.3847/1538-4357/abbfa7

Lundmark, K. 1927, Nova Acta Regiae Soc. Sci. Upsaliensis Ser. V, 1

MacArthur, L. A., González, J. J., & Courteau, S. 2009, Mon. Not. Royal Astr. S., 395, 28, doi: 10.1111/j.1365-2966.2009.14519.x

Maeder, A. 1987, Astron. & Astrophys., 173, 247

Magrini, L., Coccato, L., Stanghellini, L., Casasola, V., & Galli, D. 2016, Astron. & Astrophys., 588, A91, doi: 10.1051/0004-6361/201527799

Maíz Apellániz, J., Trigueros Páez, E., Bostroem, A. K., Barbá, R. H., & Evans, C. J. 2017, in Highlights on Spanish Astrophysics IX, 510–510. https://arxiv.org/abs/1610.01031

Mandel, K. S., Narayan, G., & Kirshner, R. P. 2011, Astrophys. J., 731, 120, doi: 10.1088/0004-637X/731/2/120

Mannucci, F., Cresci, G., Maiolino, R., Marconi, A., & Gnerucci, A. 2010, Mon. Not. Royal Astr. S., 408, 2115, doi: 10.1111/j.1365-2966.2010.17291.x

Maraston, C. 2005, Mon. Not. Royal Astr. S., 362, 799, doi: 10.1111/j.1365-2966.2005.09270.x

Maraston, C., & Strömbäck, G. 2011, Mon. Not. Royal Astr. S., 418, 2785, doi: 10.1111/j.1365-2966.2011.19738.x

Maraston, C., Strömbäck, G., Thomas, D., Wake, D. A., & Nichol, R. C. 2009, Mon. Not. Royal Astr. S., 394, L107, doi: 10.1111/j.1745-3933.2009.00621.x

Marino, R. A., Rosales-Ortega, F. F., Sánchez, S. F., et al. 2013, Astron. & Astrophys., 559, A114, doi: 10.1051/0004-6361/201321956

Martín, S., Requena-Torres, M. A., Martín-Pintado, J., & Mauersberger, R. 2008, Astrophys. J., 678, 245, doi: 10.1086/533409

Martín, S., Kohno, K., Izumi, T., et al. 2015, Astron. & Astrophys., 573, A116, doi: 10.1051/0004-6361/201425105

Martín-Navarro, I., de Lorenzo-Cáceres, A., Gadotti, D. A., et al. 2024, Astron. & Astrophys., 684, A110, doi: 10.1051/0004-6361/202348060

Martins, F., Hillier, D. J., Paumard, T., et al. 2008, Astron. & Astrophys., 478, 219, doi: 10.1051/0004-6361:20078469

Martins, L. P., & Coelho, P. 2007, Mon. Not. Royal Astr. S., 381, 1329, doi: 10.1111/j.1365-2966.2007.11954.x

Mateus, A., Sodré, L., Cid Fernandes, R., et al. 2006, Mon. Not. Royal Astr. S., 370, 721, doi: 10.1111/j.1365-2966.2006.10565.x

Matheson, T., Fan, X., Green, R., et al. 2013, arXiv e-prints, arXiv:1311.2496, doi: 10.48550/arXiv.1311.2496

Mazzuca, L. M., Knapen, J. H., Veilleux, S., & Regan, M. W. 2008, Astrophys. J. Supp. Series, 174, 337, doi: 10.1086/522338

Mazzuca, L. M., Sarzi, M., Knapen, J. H., Veilleux, S., & Swaters, R. 2006, Astrophys. J. Lett., 649, L79, doi: 10.1086/508461

Mei, S., Holden, B. P., Blakeslee, J. P., et al. 2009, Astrophys. J., 690, 42, doi: 10.1088/0004-637X/690/1/42

Méndez-Delgado, J. E., Esteban, C., García-Rojas, J., Kreckel, K., & Peimbert, M. 2023, Nature, 618, 249, doi: 10.1038/s41586-023-05956-2

Menéndez-Delmestre, K., Sheth, K., Schinnerer, E., Jarrett, T. H., & Scoville, N. Z. 2007, Astrophys. J., 657, 790, doi: 10.1086/511025

Merritt, D. 1993, Science, 259, 1867, doi: 10.1126/science.259.5103.1867

Miller, A. A., Bloom, J. S., Richards, J. W., et al. 2015, Astrophys. J., 798, 122, doi: 10.1088/0004-637X/798/2/122

Mitchell, P. D., Lacey, C. G., Baugh, C. M., & Cole, S. 2013, Mon. Not. Royal Astr. S., 435, 87, doi: 10.1093/mnras/stt1280

Mollá, M., Díaz, Á. I., Ascasibar, Y., & Gibson, B. K. 2017, Mon. Not. Royal Astr. S., 468, 305, doi: 10.1093/mnras/stx419

Mollá, M., Wekesa, S., Cavichia, O., et al. 2019, Mon. Not. Royal Astr. S., 490, 665, doi: 10.1093/mnras/stz2537

Morton, D. C. 1991, Astrophys. J. Supp. Series, 77, 119, doi: 10.1086/191601

Moustakas, J., Kennicutt, Jr., R. C., Tremonti, C. A., et al. 2010, Astrophys. J. Supp. Series, 190, 233, doi: 10.1088/0067-0049/190/2/233

Muñoz-Mateos, J. C., Sheth, K., Gil de Paz, A., et al. 2013, Astrophys. J., 771, 59, doi: 10.1088/0004-637X/771/1/59

Muraoka, K., Kohno, K., Tosaki, T., et al. 2009, Publ. Astron. Soc. Japan, 61, 163, doi: 10.1093/pasj/61.2.163

Najarro, F., Figer, D. F., Hillier, D. J., Geballe, T. R., & Kudritzki, R. P. 2009, Astrophys. J., 691, 1816, doi: 10.1088/0004-637X/691/2/1816

Najarro, F., Figer, D. F., Hillier, D. J., & Kudritzki, R. P. 2004, Astrophys. J. Lett., 611, L105, doi: 10.1086/423955

Napolitano, N. R., D'Ago, G., Tortora, C., et al. 2020, Mon. Not. Royal Astr. S., 498, 5704, doi: 10.1093/mnras/staa2409

Neistein, E., van den Bosch, F. C., & Dekel, A. 2006, Mon. Not. Royal Astr. S., 372, 933, doi: 10.1111/j.1365-2966.2006.10918.x

Nersesian, A., van der Wel, A., Gallazzi, A., et al. 2024, Astron. & Astrophys., 681, A94, doi: 10.1051/0004-6361/202346769

Nevin, R., Blecha, L., Comerford, J., & Greene, J. 2019, Astrophys. J., 872, 76, doi: 10.3847/1538-4357/aafd34

Newman, J. A., & Gruen, D. 2022, A. Review of Astron. and Astrophys., 60, 363, doi: 10.1146/annurev-astro-032122-014611

Ng, A. 2017, Train / Dev / Test sets, Coursera

Nogueras-Lara, F., Schödel, R., Gallego-Calvente, A. T., et al. 2020, Nature Astronomy, 4, 377, doi: 10.1038/s41550-019-0967-9

Ocvirk, P., Pichon, C., Lançon, A., & Thiébaut, E. 2006, Mon. Not. Royal Astr. S., 365, 74, doi: 10.1111/j.1365-2966.2005.09323.x

O'Donnell, J. E. 1994, Astrophys. J., 422, 158, doi: 10.1086/173713

Oh, S., Oh, K., & Yi, S. K. 2012, Astrophys. J. Supp. Series, 198, 4, doi: 10.1088/0067-0049/198/1/4

Onishi, K., Iguchi, S., Sheth, K., & Kohno, K. 2015, Astrophys. J., 806, 39, doi: 10.1088/0004-637X/806/1/39

Origlia, L., Oliva, E., Maiolino, R., et al. 2013, Astron. & Astrophys., 560, A46, doi: 10.1051/0004-6361/201322586

Oyarzún, G. A., Bundy, K., Westfall, K. B., et al. 2019, Astrophys. J., 880, 111, doi: 10.3847/1538-4357/ab297c

Padmanabhan, N., Schlegel, D. J., Finkbeiner, D. P., et al. 2008, Astrophys. J., 674, 1217, doi: 10.1086/524677

Pagel, B. E. J. 2009, Nucleosynthesis and Chemical Evolution of Galaxies, 2nd edn. (Cambridge University Press)

Pan, H.-A., Lim, J., Matsushita, S., Wong, T., & Ryder, S. 2013, Astrophys. J., 768, 57, doi: 10.1088/0004-637X/768/1/57

Panter, B., Jimenez, R., Heavens, A. F., & Charlot, S. 2008, Mon. Not. Royal Astr. S., 391, 1117, doi: 10.1111/j.1365-2966.2008.13981.x

Pantoni, L., Lapi, A., Massardi, M., Goswami, S., & Danese, L. 2019, Astrophys. J., 880, 129, doi: 10.3847/1538-4357/ab2adc

Parikh, T., Thomas, D., Maraston, C., et al. 2021, Mon. Not. Royal Astr. S., 502, 5508, doi: 10.1093/mnras/stab449

Pasquet, J., Bertin, E., Treyer, M., Arnouts, S., & Fouchez, D. 2019, Astron. & Astrophys., 621, A26, doi: 10.1051/0004-6361/201833617

Paulino-Afonso, A., Sobral, D., Darvish, B., et al. 2020, Astron. & Astrophys., 633, A70, doi: 10.1051/0004-6361/201834244

Paxton, B., Bildsten, L., Dotter, A., et al. 2011, Astrophys. J. Supp. Series, 192, 3, doi: 10.1088/0067-0049/192/1/3

Peng, Y., Maiolino, R., & Cochrane, R. 2015, Nature, 521, 192, doi: 10.1038/nature14439

Pérez, I., & Sánchez-Blázquez, P. 2011, Astron. & Astrophys., 529, A64, doi: 10.1051/0004-6361/201015002

Pessa, I., Schinnerer, E., Sanchez-Blazquez, P., et al. 2023, Astron. & Astrophys., 673, A147, doi: 10.1051/0004-6361/202245673

Pettini, M., & Pagel, B. E. J. 2004, Mon. Not. Royal Astr. S., 348, L59, doi: 10.1111/j.1365-2966.2004.07591.x

Pierce, C. M., Lotz, J. M., Primack, J. R., et al. 2010, Mon. Not. Royal Astr. S., 405, 718, doi: 10.1111/j.1365-2966.2010.16502.x

Pilyugin, L. S., & Grebel, E. K. 2016, Mon. Not. Royal Astr. S., 457, 3678, doi: 10.1093/mnras/stw238

Pilyugin, L. S., & Thuan, T. X. 2005, Astrophys. J., 631, 231, doi: 10.1086/432408

—. 2011, Astrophys. J. Lett., 726, L23, doi: 10.1088/2041-8205/726/2/L23

Prieto, M. A., Fernandez-Ontiveros, J. A., Bruzual, G., et al. 2019, Mon. Not. Royal Astr. S., 485, 3264, doi: 10.1093/mnras/stz579

Prieto, M. A., Maciejewski, W., & Reunanen, J. 2005, Astronom. J., 130, 1472, doi: 10.1086/444591

Quillen, A. C., Frogel, J. A., Kuchinski, L. E., & Terndrup, D. M. 1995, Astronom. J., 110, 156, doi: 10.1086/117503

Racca, G. D., Laureijs, R., Stagnaro, L., et al. 2016, in Society of Photo-Optical Instrumentation Engineers (SPIE) Conference Series, Vol. 9904, Space Telescopes and Instrumentation 2016: Optical, Infrared, and Millimeter Wave, ed. H. A. MacEwen, G. G. Fazio, M. Lystrup, N. Batalha, N. Siegler, & E. C. Tong, 99040O, doi: 10.1117/12.2230762

Raghavan, D., McAlister, H. A., Henry, T. J., et al. 2010, Astrophys. J. Supp. Series, 190, 1, doi: 10.1088/0067-0049/190/1/1

Rajpurohit, A. S., Allard, F., Rajpurohit, S., et al. 2018, Astron. & Astrophys., 620, A180, doi: 10.1051/0004-6361/201833500

Ramesh, A., Pavlov, M., Goh, G., et al. 2021, in International Conference on Machine Learning, PMLR, 8821–8831

Rauch, T. 2003, Astron. & Astrophys., 403, 709, doi: 10.1051/0004-6361:20030412

Reichardt, C., Jimenez, R., & Heavens, A. F. 2001, Mon. Not. Royal Astr. S., 327, 849, doi: 10.1046/j.1365-8711.2001.04768.x

Reines, A. E., Nidever, D. L., Whelan, D. G., & Johnson, K. E. 2010, Astrophys. J., 708, 26, doi: 10.1088/0004-637X/708/1/26

Remple, B. A. 2025, PhD thesis, Ludwig-Maximilians University of Munich, Germany. http://nbn-resolving.de/urn:nbn:de:bvb:19-350505

Rémy-Ruyer, A., Madden, S. C., Galliano, F., et al. 2014, Astron. & Astrophys., 563, A31, doi: 10.1051/0004-6361/201322803

Renzo, M., Zapartas, E., Justham, S., et al. 2023, Astrophys. J. Lett., 942, L32, doi: 10.3847/2041-8213/aca4d3

Richardson, C. T., Allen, J. T., Baldwin, J. A., et al. 2016, Mon. Not. Royal Astr. S., 458, 988, doi: 10.1093/mnras/stw100

Rickards Vaught, R. J., Sandstrom, K. M., Belfiore, F., et al. 2024, Astrophys. J., 966, 130, doi: 10.3847/1538-4357/ad303c

Riffel, R., Mallmann, N. D., Ilha, G. S., et al. 2021, Mon. Not. Royal Astr. S., 501, 4064, doi: 10.1093/mnras/staa3907

Robbins, S. L., Raimundo, S. I., & Malkan, M. A. 2025, Astrophys. J., 980, 64, doi: 10.3847/1538-4357/ada294

Roberts, M. S., & Haynes, M. P. 1994, A. Review of Astron. and Astrophys., 32, 115, doi: 10.1146/annurev.aa.32.090194.000555

Roediger, J. C., & Courteau, S. 2015, Mon. Not. Royal Astr. S., 452, 3209, doi: 10.1093/mnras/stv1499

Röllig, M., Szczerba, R., Ossenkopf, V., & Glück, C. 2013, Astron. & Astrophys., 549, A85, doi: 10.1051/0004-6361/201118190

Rombach, R., Blattmann, A., Lorenz, D., Esser, P., & Ommer, B. 2022, in Proceedings of the IEEE/CVF Conference on Computer Vision and Pattern Recognition, 10684–10695

Ronneberger, O., Fischer, P., & Brox, T. 2015, in Medical Image Computing and Computer-Assisted Intervention–MICCAI 2015: 18th International Conference, Munich, Germany, October 5-9, 2015, Proceedings, Part III 18, Springer, 234–241

Rosado-Belza, D., Falcón-Barroso, J., Knapen, J. H., et al. 2020, Astron. & Astrophys., 644, A116, doi: 10.1051/0004-6361/202039530

Rosas-Guevara, Y., Bonoli, S., Puchwein, E., Dotti, M., & Contreras, S. 2025, Astron. & Astrophys., 698, A20, doi: 10.1051/0004-6361/202453160

Roškar, R., Debattista, V. P., Quinn, T. R., Stinson, G. S., & Wadsley, J. 2008, Astrophys. J. Lett., 684, L79, doi: 10.1086/592231

Saharia, C., Chan, W., Saxena, S., et al. 2022, Advances in Neural Information Processing Systems, 35, 36479

Salaris, M., & Cassisi, S. 2005, Evolution of Stars and Stellar Populations (John Wiley & Sons, Ltd)

Salim, S., & Narayanan, D. 2020, A. Review of Astron. and Astrophys., 58, 529, doi: 10.1146/annurev-astro-032620-021933

Salpeter, E. E. 1955, Astrophys. J., 121, 161, doi: 10.1086/145971

Sana, H., de Mink, S. E., de Koter, A., et al. 2012, Science, 337, 444, doi: 10.1126/science.1223344

Sánchez, S. F., Rosales-Ortega, F. F., Iglesias-Páramo, J., et al. 2014, Astron. & Astrophys., 563, A49, doi: 10.1051/0004-6361/201322343

Sánchez-Blázquez, P., Ocvirk, P., Gibson, B. K., Pérez, I., & Peletier, R. F. 2011, Mon. Not. Royal Astr. S., 415, 709, doi: 10.1111/j.1365-2966.2011.18749.x

Sánchez-Blázquez, P., Peletier, R. F., Jiménez-Vicente, J., et al. 2006, Mon. Not. Royal Astr. S., 371, 703, doi: 10.1111/j.1365-2966.2006.10699.x

Sánchez-Blázquez, P., Rosales-Ortega, F. F., Méndez-Abreu, J., et al. 2014, Astron. & Astrophys., 570, A6, doi: 10.1051/0004-6361/201423635

Sánchez-Menguiano, L., Sánchez, S. F., Pérez, I., et al. 2020, Mon. Not. Royal Astr. S., 492, 4149, doi: 10.1093/mnras/staa088

—. 2016, Astron. & Astrophys., 587, A70, doi: 10.1051/0004-6361/201527450

—. 2018, Astron. & Astrophys., 609, A119, doi: 10.1051/0004-6361/201731486

Sandage, A. 1975, in Galaxies and the Universe, ed. A. Sandage, M. Sandage, & J. Kristian (University of Chicago Press), 1

Sanders, R. L., Shapley, A. E., Jones, T., et al. 2021, Astrophys. J., 914, 19, doi: 10.3847/1538-4357/abf4c1

Sarzi, M., Allard, E. L., Knapen, J. H., & Mazzuca, L. M. 2007, Mon. Not. Royal Astr. S., 380, 949, doi: 10.1111/j.1365-2966.2007.12177.x

Sato, K., Miyamoto, Y., Kuno, N., et al. 2021, Publ. Astron. Soc. Japan, 73, 1019, doi: 10.1093/pasj/psab060

Schaefer, A. L., Croom, S. M., Allen, J. T., et al. 2017, Mon. Not. Royal Astr. S., 464, 121, doi: 10.1093/mnras/stw2289

Schawinski, K., Urry, C. M., Simmons, B. D., et al. 2014, Mon. Not. Royal Astr. S., 440, 889, doi: 10.1093/mnras/stu327

Schaye, J., Crain, R. A., Bower, R. G., et al. 2015, Mon. Not. Royal Astr. S., 446, 521, doi: 10.1093/mnras/stu2058

Schinnerer, E., Emsellem, E., Henshaw, J. D., et al. 2023, Astrophys. J. Lett., 944, L15, doi: 10.3847/2041-8213/acac9e

Schlafly, E. F., & Finkbeiner, D. P. 2011, Astrophys. J., 737, 103, doi: 10.1088/0004-637X/737/2/103

Schuldt, S., Suyu, S. H., Cañameras, R., et al. 2021, Astron. & Astrophys., 651, A55, doi: 10.1051/0004-6361/202039945

Schultheis, M., Sormani, M. C., & Gadotti, D. A. 2025, arXiv e-prints, arXiv:2509.04562, doi: 10.48550/arXiv.2509.04562

Searle, L., & Sargent, W. L. W. 1972, Astrophys. J., 173, 25, doi: 10.1086/151398

Seidel, M. K., Cacho, R., Ruiz-Lara, T., et al. 2015, Mon. Not. Royal Astr. S., 446, 2837, doi: 10.1093/mnras/stu2295

Sellwood, J. A., & Binney, J. J. 2002, Mon. Not. Royal Astr. S., 336, 785, doi: 10.1046/j.1365-8711.2002.05806.x

Setton, D. J., Dey, B., Khullar, G., et al. 2023, Astrophys. J. Lett., 947, L31, doi: 10.3847/2041-8213/acc9b5

Sextl, E., Kudritzki, R.-P., Weller, J., Urbaneja, M. A., & Weiss, A. 2021, Astrophys. J., 914, 94, doi: 10.3847/1538-4357/abfafa

Sextl, E., Kudritzki, R.-P., Zahid, H. J., & Ho, I. T. 2023, Astrophys. J., 949, 60, doi: 10.3847/1538-4357/acc579

Sextl, E., Kudritzki, R.-P., Burkert, A., et al. 2024, Astrophys. J., 960, 83, doi: 10.3847/1538-4357/ad08b3

Sextl, E., Kudritzki, R.-P., Bresolin, F., et al. 2025, Astrophys. J., 987, 138, doi: 10.3847/1538-4357/addec2

Shaw, A. M. 2006, Astrochemistry: from astronomy to astrobiology (Wiley)

Sheth, K., Regan, M., Hinz, J. L., et al. 2010, The Publ. of the Astron. S. of the Pac., 122, 1397, doi: 10.1086/657638

Shimizu, T. T., Davies, R. I., Lutz, D., et al. 2019, Mon. Not. Royal Astr. S., 490, 5860, doi: 10.1093/mnras/stz2802

Shirazi, M., Brinchmann, J., & Rahmati, A. 2014, Astrophys. J., 787, 120, doi: 10.1088/0004-637X/787/2/120

Shlosman, I., Frank, J., & Begelman, M. C. 1989, Nature, 338, 45, doi: 10.1038/338045a0

Si, J. M., Luo, A. L., Li, Y. B., et al. 2021, VizieR Online Data Catalog (other), 0730, J/other/SCPMA/57

Silva-Lima, L. A., Gadotti, D. A., Martins, L. P., et al. 2025, Mon. Not. Royal Astr. S., 540, 2787, doi: 10.1093/mnras/staf837

Sipilä, O., Zhao, B., & Caselli, P. 2020, Astron. & Astrophys., 640, A94, doi: 10.1051/0004-6361/202038353

Skibba, R. A., Bamford, S. P., Nichol, R. C., et al. 2009, Mon. Not. Royal Astr. S., 399, 966, doi: 10.1111/j.1365-2966.2009.15334.x

Smith, L. J., Norris, R. P. F., & Crowther, P. A. 2002, Mon. Not. Royal Astr. S., 337, 1309, doi: 10.1046/j.1365-8711.2002.06042.x

Sobel, D. 2016, The glass universe: how the ladies of the Harvard Observatory took the measure of the stars (New York, New York: Viking)

Sparre, M., Whittingham, J., Damle, M., et al. 2022, Mon. Not. Royal Astr. S., 509, 2720, doi: 10.1093/mnras/stab3171

Spinrad, H., & Taylor, B. J. 1972, Astrophys. J., 171, 397, doi: 10.1086/151291

Spitoni, E. 2015, Mon. Not. Royal Astr. S., 451, 1090, doi: 10.1093/mnras/stv1008

Spitoni, E., Calura, F., Mignoli, M., et al. 2020, Astron. & Astrophys., 642, A113, doi: 10.1051/0004-6361/202037879

Spitoni, E., Cescutti, G., Minchev, I., et al. 2019, Astron. & Astrophys., 628, A38, doi: 10.1051/0004-6361/201834665

Spitoni, E., Gioannini, L., & Matteucci, F. 2017a, Astron. & Astrophys., 605, A38, doi: 10.1051/0004-6361/201730545

Spitoni, E., Vincenzo, F., & Matteucci, F. 2017b, Astron. & Astrophys., 599, A6, doi: 10.1051/0004-6361/201629745

Stark, P., & Parker, R. 1995, Computational Statistics, 10, 129–141

Stasińska, G. 2005, Astron. & Astrophys., 434, 507, doi: 10.1051/0004-6361:20042216

Stasińska, G., Costa-Duarte, M. V., Vale Asari, N., Cid Fernandes, R., & Sodré, L. 2015, Mon. Not. Royal Astr. S., 449, 559, doi: 10.1093/mnras/stv078

Stoughton, C., Lupton, R. H., Bernardi, M., et al. 2002, Astronom. J., 123, 485, doi: 10.1086/324741

Strateva, I., Ivezić, Ž., Knapp, G. R., et al. 2001, Astronom. J., 122, 1861, doi: 10.1086/323301

Sun, J., He, H., Batschkun, K., et al. 2024, Astrophys. J., 967, 133, doi: 10.3847/1538-4357/ad3de6

Swartz, D. A., Yukita, M., Tennant, A. F., Soria, R., & Ghosh, K. K. 2006, Astrophys. J., 647, 1030, doi: 10.1086/504680

Tabatabaei, F. S., Weiß, A., Combes, F., et al. 2013, Astron. & Astrophys., 555, A128, doi: 10.1051/0004-6361/201321487

Taormina, M., Kudritzki, R.-P., Puls, J., et al. 2020, Astrophys. J., 890, 137, doi: 10.3847/1538-4357/ab6bd0

Teimoorinia, H., Jalilkhany, M., Scudder, J. M., Jensen, J., & Ellison, S. L. 2021, Mon. Not. Royal Astr. S., 503, 1082, doi: 10.1093/mnras/stab466

Thainá-Batista, J., Cid Fernandes, R., Herpich, F. R., et al. 2023, Mon. Not. Royal Astr. S., 526, 1874, doi: 10.1093/mnras/stad2698

Thatte, N., Tecza, M., & Genzel, R. 2000, Astron. & Astrophys., 364, L47, doi: 10.48550/arXiv.astro-ph/0009392

Thatte, N. A., Melotte, D., Neichel, B., et al. 2022, in Society of Photo-Optical Instrumentation Engineers (SPIE) Conference Series, Vol. 12184, Ground-based and Airborne Instrumentation for Astronomy IX, ed. C. J. Evans, J. J. Bryant, & K. Motohara, 1218420, doi: 10.1117/12.2628834

The, P. S., Bakker, R., & Tjin A Djie, H. R. E. 1980, Astron. & Astrophys., 89, 209

Thilker, D. A., Braun, R., & Walterbos, R. A. M. 2000, Astronom. J., 120, 3070, doi: 10.1086/316852

Thomas, A. D., Dopita, M. A., Kewley, L. J., et al. 2018, Astrophys. J., 856, 89, doi: 10.3847/1538-4357/aab3db

Thomas, D., Maraston, C., & Bender, R. 2003, Mon. Not. Royal Astr. S., 339, 897, doi: 10.1046/j.1365-8711.2003.06248.x

Thomas, D., Maraston, C., Bender, R., & Mendes de Oliveira, C. 2005, Astrophys. J., 621, 673, doi: 10.1086/426932

Thomas, R., Le Fèvre, O., Zamorani, G., et al. 2019, Astron. & Astrophys., 630, A145, doi: 10.1051/0004-6361/201935813

Tinsley, B. M. 1968, Astrophys. J., 151, 547, doi: 10.1086/149455

Tissera, P. B., Rosas-Guevara, Y., Sillero, E., et al. 2022, Mon. Not. Royal Astr. S., 511, 1667, doi: 10.1093/mnras/stab3644

Tortorelli, L., McCullough, J., & Gruen, D. 2024, Astron. & Astrophys., 689, A144, doi: 10.1051/0004-6361/202450694

Trager, S. C., Worthey, G., Faber, S. M., Burstein, D., & González, J. J. 1998, Astrophys. J. Supp. Series, 116, 1, doi: 10.1086/313099

Tremonti, C. A., Heckman, T. M., Kauffmann, G., et al. 2004, Astrophys. J., 613, 898, doi: 10.1086/423264

Trussler, J., Maiolino, R., Maraston, C., et al. 2020, Mon. Not. Royal Astr. S., 491, 5406, doi: 10.1093/mnras/stz3286

Tully, R. B., Rizzi, L., Shaya, E. J., et al. 2009, Astronom. J., 138, 323, doi: 10.1088/0004-6256/138/2/323

Urbaneja, M. A., Kudritzki, R. P., Gieren, W., et al. 2017, Astronom. J., 154, 102, doi: 10.3847/1538-3881/aa79a8

Valdes, F., Gupta, R., Rose, J. A., Singh, H. P., & Bell, D. J. 2004, Astrophys. J. Supp. Series, 152, 251, doi: 10.1086/386343

Vale Asari, N., Stasińska, G., Cid Fernandes, R., et al. 2009, Mon. Not. Royal Astr. S., 396, L71, doi: 10.1111/j.1745-3933.2009.00664.x

Vallini, L., Witstok, J., Sommovigo, L., et al. 2024, Mon. Not. Royal Astr. S., 527, 10, doi: 10.1093/mnras/stad3150

van Dokkum, P. G. 2008, Astrophys. J., 674, 29, doi: 10.1086/525014

van Mierlo, S. E., Caputi, K. I., & Kokorev, V. 2023, Astrophys. J. Lett., 945, L21, doi: 10.3847/2041-8213/acb773

Vazdekis, A., Koleva, M., Ricciardelli, E., Röck, B., & Falcón-Barroso, J. 2016, Mon. Not. Royal Astr. S., 463, 3409, doi: 10.1093/mnras/stw2231

Venturi, G., Nardini, E., Marconi, A., et al. 2018, Astron. & Astrophys., 619, A74, doi: 10.1051/0004-6361/201833668

Verwilghen, P., Emsellem, E., Renaud, F., et al. 2024, Astron. & Astrophys., 687, A53, doi: 10.1051/0004-6361/202348772

Viaene, S., Baes, M., Bendo, G., et al. 2016, Astron. & Astrophys., 586, A13, doi: 10.1051/0004-6361/201527586

Vink, J. S., de Koter, A., & Lamers, H. J. G. L. M. 2001, Astron. & Astrophys., 369, 574, doi: 10.1051/0004-6361:20010127

Wakelam, V., Bron, E., Cazaux, S., et al. 2017, Molecular Astrophysics, 9, 1, doi: https://doi.org/10.1016/j.molap.2017.11.001

Walter, F., Brinks, E., de Blok, W. J. G., et al. 2008, Astronom. J., 136, 2563, doi: 10.1088/0004-6256/136/6/2563

Weilbacher, P. M., Palsa, R., Streicher, O., et al. 2020, Astron. & Astrophys., 641, A28, doi: 10.1051/0004-6361/202037855

Weinberg, D. H., Andrews, B. H., & Freudenburg, J. 2017, Astrophys. J., 837, 183, doi: 10.3847/1538-4357/837/2/183

Weingartner, J. C., & Draine, B. T. 2001, Astrophys. J. Supp. Series, 134, 263, doi: 10.1086/320852

Westfall, K. B., Cappellari, M., Bershady, M. A., et al. 2019, Astronom. J., 158, 231, doi: 10.3847/1538-3881/ab44a2

Westmoquette, M., Smith, L., & Iii, J. 2011, Mon. Not. Royal Astr. S., 414, 3719, doi: 10.1111/j.1365-2966.2011.18675.x

Whitaker, K. E., van Dokkum, P. G., Brammer, G., et al. 2013, Astrophys. J. Lett., 770, L39, doi: 10.1088/2041-8205/770/2/L39

Whitmore, B. C., Chandar, R., Rodríguez, M. J., et al. 2023, Astrophys. J. Lett., 944, L14, doi: 10.3847/2041-8213/acae94

Wiersma, R. P. C., Schaye, J., & Smith, B. D. 2009, Mon. Not. Royal Astr. S., 393, 99, doi: 10.1111/j.1365-2966.2008.14191.x

Wilkinson, D. M., Maraston, C., Goddard, D., Thomas, D., & Parikh, T. 2017, Mon. Not. Royal Astr. S., 472, 4297, doi: 10.1093/mnras/stx2215

—. 2021, FIREFLY: Chi-squared minimization full spectral fitting code, Astrophysics Source Code Library, record ascl:2108.010. http://ascl.net/2108.010

Wilkinson, D. M., Maraston, C., Thomas, D., et al. 2015, Mon. Not. Royal Astr. S., 449, 328, doi: 10.1093/mnras/stv301

Witt, A. N., & Gordon, K. D. 1996, Astrophys. J., 463, 681, doi: 10.1086/177282

—. 2000, Astrophys. J., 528, 799, doi: 10.1086/308197

Wolf, M. 1908, Publikationen des Astrophysikalischen Instituts Koenigstuhl-Heidelberg, 3, 109

Wolfire, M. G., Vallini, L., & Chevance, M. 2022, A. Review of Astron. and Astrophys., 60, 247, doi: 10.1146/annurev-astro-052920-010254

Woo, J., Walters, D., Archinuk, F., et al. 2024, Mon. Not. Royal Astr. S., 530, 4260, doi: 10.1093/mnras/stae1114

Wood, C. M., Tremonti, C. A., Calzetti, D., et al. 2015, Mon. Not. Royal Astr. S., 452, 2712, doi: 10.1093/mnras/stv1471

Worthey, G. 1994, Astrophys. J. Supp. Series, 95, 107, doi: 10.1086/192096

Worthey, G., Faber, S. M., Gonzalez, J. J., & Burstein, D. 1994, Astrophys. J. Supp. Series, 94, 687, doi: 10.1086/192087

Worthey, G., & Ottaviani, D. L. 1997, Astrophys. J. Supp. Series, 111, 377, doi: 10.1086/313021

Wu, F., Bu, Y., Zhang, M., et al. 2023, Astronom. J., 166, 88, doi: 10.3847/1538-3881/acdcfb

Wu, J. F., & Peek, J. E. G. 2020, arXiv e-prints, arXiv:2009.12318, doi: 10.48550/arXiv.2009.12318

Yates, R. M., Kauffmann, G., & Guo, Q. 2012, Mon. Not. Royal Astr. S., 422, 215, doi: 10.1111/j.1365-2966.2012.20595.x

Yoachim, P., Roškar, R., & Debattista, V. P. 2012, Astrophys. J., 752, 97, doi: 10.1088/0004-637X/752/2/97

Yuan, F.-T., Argudo-Fernández, M., Shen, S., et al. 2018, Astron. & Astrophys., 613, A13, doi: 10.1051/0004-6361/201731865

Yuan, F.-T., Burgarella, D., Corre, D., et al. 2020, in Panchromatic Modelling with Next Generation Facilities, ed. M. Boquien, E. Lusso, C. Gruppioni, & P. Tissera, Vol. 341, 201–205, doi: 10.1017/S174392131900276X

Zahid, H. J., Dima, G. I., Kudritzki, R.-P., et al. 2014, Astrophys. J., 791, 130, doi: 10.1088/0004-637X/791/2/130

Zahid, H. J., Geller, M. J., Fabricant, D. G., & Hwang, H. S. 2016, Astrophys. J., 832, 203, doi: 10.3847/0004-637X/832/2/203

Zahid, H. J., Kudritzki, R.-P., Conroy, C., Andrews, B., & Ho, I. T. 2017, Astrophys. J., 847, 18, doi: 10.3847/1538-4357/aa88ae

Zahid, H. J., Yates, R. M., Kewley, L. J., & Kudritzki, R. P. 2013, Astrophys. J., 763, 92, doi: 10.1088/0004-637X/763/2/92

Zánmar Sánchez, R., Sellwood, J. A., Weiner, B. J., & Williams, T. B. 2008, Astrophys. J., 674, 797, doi: 10.1086/524940

Zeraatgari, F. Z., Hafezianzadeh, F., Zhang, Y., et al. 2024, Mon. Not. Royal Astr. S., 527, 4677, doi: 10.1093/mnras/stad3436

Zhang, F., Han, Z., Li, L., & Hurley, J. R. 2004, Astron. & Astrophys., 415, 117, doi: 10.1051/0004-6361:20031268

Zhang, Y., Ling, H., Gao, J., et al. 2021, in Proceedings of the IEEE/CVF Conference on Computer Vision and Pattern Recognition, 10145–10155

Zheng, Z., Li, C., Mao, S., et al. 2019, Astrophys. J., 873, 63, doi: 10.3847/1538-4357/ab03d2

Zucker, C., Goodman, A. A., Alves, J., et al. 2022, Nature, 601, 334, doi: 10.1038/s41586-021-04286-5

Zurlo, A., Gratton, R., Pérez, S., & Cieza, L. 2023, European Physical Journal Plus, 138, 411, doi: 10.1140/epjp/s13360-023-04041-x

Acknowledgments

First and foremost, my deepest gratitude goes to my supervisor, Prof. Rolf-Peter Kudritzki, whose wise guidance, patience and research experience as a grandmaster of spectroscopy, were invaluable throughout this journey. The quality of a thesis stands and falls also with a good supervisor and one must not take an excellent supervisor for granted, especially after been burnt once. I would also like to extend my sincere thanks to Prof. Andreas Burkert, Prof. Klaus Dolag and the members of the DRAGONS team lead by Dr. Rhea-Silvia Remus for insightful questions, their curiosity and thoughtful suggestions which helped to enhance the quality of the work.
I am also grateful to the whole staff at the University Observatory Munich for their technical support and their patience in navigating the sometimes complex administrative processes.

This thesis was made possible by the generous funding provided by the Excellence Cluster Origins. It is fostering an outstanding interdisciplinary research environment that explores the origin and development of the Universe and the emergence of life. We were all pleased to learn of its successful renewal for the next funding period starting 2026.

I also deeply appreciate my partner's constant motivation and for reminding me to celebrate small victories along the way, all while navigating his own demanding PhD journey.

I would like to express my heartfelt thanks to my father, who, had to entrust me with the responsibility of the family farm due to illness in early 2024. He still did his best to support me whenever possible. To my mother, I am forever grateful for her tireless organization and support that kept everything running smoothly when I needed it most. Special appreciation goes to my grandmother, who has made certain that our farmstead remains the most beautiful and well-kept in all of Rottal-Inn.
I owe my deepest thanks to the Moser family, Untereschlbach for their guidance and support in converting my fields to organic principles. Their experience, patience, and genuine devotion to farming in harmony with nature have meant more to me than I can say. Together, we believe that choosing organic over conventional farming is not just a business decision, but an investment in the future.

This thesis is as much theirs as it is mine: A reflection of the many hands, hearts, and minds that helped shape it. Thank you all for your kindness, patience, and support.